IMPACT OF NATURAL AND ANTHROPOGENIC AEROSOLS ON CLOUDS AND RADIATIVE PROPERTIES OVER WEST AFRICA

BY

DAJUMA, ALIMA
(MET/15/5745)

SEPTEMBER, 2019

IMPACT OF NATURAL AND ANTHROPOGENIC AEROSOLS ON CLOUDS AND RADIATIVE PROPERTIES OVER WEST AFRICA

By

DAJUMA Alima
(BSc, UFHB, CÔTE D'IVOIRE MSc, UAM, NIGER)
(MET/15/5745)

A THESIS IN THE DEPARTMENT OF METEOROLOGY AND CLIMATE SCIENCE IN PARTNERSHIP WITH THE WEST AFRICAN SCIENCE SERVICE CENTER ON CLIMATE CHANGE AND ADAPTED LAND USE (WASCAL) SUBMITTED TO THE SCHOOL OF POSTGRADUATE STUDIES, IN PARTIAL FULFILLMENT OF THE REQUIREMENTS FOR THE AWARD OF THE DEGREE OF DOCTOR OF PHILOSOPHY IN METEOROLOGY AND CLIMATE SCIENCE OF THE FEDERAL UNIVERSITY OF TECHNOLOGY, AKURE, ONDO STATE, NIGERIA.

SEPTEMBER, 2019

DECLARATION

I hereby declare that this Thesis was written by me and is a correct record of my own research work. It has not been presented in any previous application for any degree of this or any other University. All citations and sources of information are clearly acknowledged by means of references.

Candidate's Name: DAJUMA Alima

Signature …… Date: 19th September 2019

CERTIFICATION

We certify that this Thesis entitled “Impact of Natural and Anthropogenic Aerosols on Clouds and Radiative properties over West Africa” is the outcome of the research carried out by Dajuma Alima in the Department of Meteorology and Climate Science, Federal University of Technology Akure, Nigeria.

Major Supervisor’s Name: Prof. K.O. Ogunjobi

Signature: …… Date: 19th September 2019

Co-Supervisor’s Name: Prof. Véronique Yoboué

Signature  Date: 19th September 2019

Co-Supervisor’s Name: Dr. Bernhard Vogel

Signature  Date: 19th September 2019

AKNOWLEDGEMENTS

This Ph.D programme is fully supported by the German Ministry of Education and Research (BMBF) through the West African Science Service Centre on Climate Change and Adapted Land Use (WASCAL). I am therefore grateful to WASCAL for granting me the financial support for the study and research visit to Karlsruhe Institute of Technology (KIT), Germany.

I sincerely thank the executive Director and the staff of WASCAL Head office, Accra, Ghana and the Director, Prof. K.O. Ogunjobi and staff of WASCAL GRP-WACS, FUTA, Nigeria for their support throughout this PhD work. I also appreciate Prof. J. A. Omotosho and Prof. A. A. Balogun, the Head of Meteorology Department and climate science for their cooperation.

I am also grateful to my supervisor Prof. K.O. Ogunjobi, Nigeria, for his collaboration, contribution, advices, and comments to improve this work. Thanks a lot.

My sincere gratitude also goes to my Co-supervisor, Prof. Véronique Yoboué, for being not only a supervisor but a mother. Thanks a lot for your help and assistance.

I am sincerely grateful to Dr. Bernhard Vogel and his wife Dr. Heike Vogel for hosting me at KIT and providing all the facility during my stay. Thank you Bernhard for your valuable contribution to this work. I also thank all the colleagues from the working group of Aerosol and Reactive traces gases (ART) as well as IMK-TRO team. I really felt at home.

I want to acknowledge the full cluster resources for the simulations supported by the ART working group for meteorology and climate research, with granted access to the HPC resources ForHLR 1.

I appreciate the support of Dynamics-Aerosol-Chemistry-Cloud Interactions in West Africa (DACCIWA) through collaborations with Prof. Peter Knippertz. Thanks a lot for your constructive criticism.

I also thank Prof. Arona Diedhiou for his great support in the research and all the opportunities.

My thanks go to all my family members for their support, encouragements and patience throughout this thesis.

I express my gratitude to friends especially Dr. Keita Sekou, Doumbia Madina, Zouzoua Maurin, Fofana Mohamed, and colleagues from FUTA WACS and LAPA Abidjan for their support. A special regard to Faye Aissatou, WASCAL colleague with whom I have shared experiences and friendship.

I thank all Professors and Doctors at staff of LAPA in Abidjan, especially Prof. Eric-Pascal Zahiri, Prof. Vafi Doumbia and my elders Dr. Silué Siélé, Dr. Kouakou Kouadio, Dr. Touré N'Datchoh Evelyne, and Dr. Bamba Adama for their useful advices, supports and encouragements.

Thank you Allah for given me the strength throughout this whole journey.

DEDICATION

This thesis is dedicated to my Late supervisor Prof. Abdourahamane KONARÉ, my late Father DAJUMA Labaran Baba and my late grand-mother Awa TOURÉ.

May ALLAH accept you in his Paradise Al Firdaus.

ABSTRACT

Using a high-resolution regional climate model COSMO-ART, the impact of natural and anthropogenic aerosols loads on radiative and cloud optical properties over West Africa is assessed through sensitivity experiments.

Based on a monthly climatology, model simulations compare satisfactory with wind fields from reanalysis data, cloud observations, daily average particulate matter (PM), temperature, relative humidity and satellite retrieved CO mixing ratio. However, COSMO-ART shows a slight overestimation of spatial distribution of CO mixing ratio compared to satellite observation.

Regarding the atmospheric composition, COSMO-ART shows good representation with the observation of aerosol mass concentration in upwind marine and urban outflow, whereas it underestimates the observed aerosols in the regional background.

Evaluating two emission inventories datasets; simulation conducted with DACCIWA emissions performed better than with EDGAR emissions for the chemistry. However, aerosols compounds are mostly underestimated by COSMO-ART except for NO_3 using EDGAR inventory.

Focusing on a case study of 02 July 2016, using CO as an indicator for biomass burning plume, individual mixing events south of the coast of Côte d'Ivoire due to midlevel convective clouds injecting parts of the biomass burning plume into the boundary layer were identified. Idealized tracer experiments suggested that about 20% of the CO mass from the 2–4km layer are mixed below 1km within two days over the Gulf of Guinea.

Quantifying the impact of biomass burning aerosols on cloud and radiation, it is found that 27% increase of cloud droplets number concentration (CDNC) over the Gulf of Guinea and 7.5% over the whole simulated domain spatially averaged. A reduction of 50 W m^{-2} of surface shortwave (SW) radiation and 20 W m^{-2} respectively over the Gulf

of Guinea (3–4ºN; 9 ºW –1ºE) and over the study domain (3–11ºN; 9 ºW –1ºE) spatially averaged for all sky conditions. The maximum increase of surface concentration for 05-06 July 2016 case study due to biomass burning aerosols is 154 μg m^{-3} for CO, 27 μg m^{-3} for O_3 and 6–7 μg m^{-3} for PM which agrees with WRF-CHEM simulation.

Same investigation was done to quantify the impact of local source anthropogenic aerosols on clouds and radiation. 90% of the CDNC are from anthropogenic aerosols and a shift of median clouds radius from 12 to 10 μm as result of anthropogenic aerosols. Regarding the surface SW, a decrease of up to 60 W m^{-2} is simulated over the study domain as a result of anthropogenic aerosol. A reduction of monsoon wind speed of about 1.2 m s^{-1} occurred as a result of anthropogenic aerosols.

The impact of future anthropogenic emissions increase is examined under two RCP 2.6 8.5 scenarios. All pollutants are projected to increase more or less, over the whole West African region except for BC which shows some decrease in Nigeria part of Ghana and Niger. Looking at local scale, coastal cities (Abidjan and Accra) is predicted to exceed the World Health Organization (WHO) with respect to NO_x and O_3.

In conclusion, the results of this study underscore the need to investigate the impact of aerosols (anthropogenic, biomass burning) on the cloud properties and radiative budget on a longer time scales and a need for air quality monitoring over the region especially over the coastal cities.

RÉSUMÉ

Dans cette étude, nous évaluons l'impact des aérosols d'origine naturelle et anthropique sur le bilan radiatif et les propriétés des nuages en Afrique de l'Ouest. Elle est menée en simulant de différentes manières l'interaction aérosol-radiation d'une part et d'autre part aérosol-nuages pendant le mois de Juillet 2016 avec le modèle climatique haute résolution COSMO-ART (Consortium for small-scale modelling- Aerosol and Reactive Trace gas). En moyenne, les simulations du modèle reproduisent de façon réaliste la dynamique atmosphérique sur l'Afrique de l'Ouest, notamment, les champs de vent, de température et d'humidité relative. En outre, les matières particulaires (PM) et le rapport de mélange du monoxyde de carbone (CO) simulés par le modèle se comparent de façon satisfaisante aux observations. Néanmoins, nous enregistrons une légère surestimation du rapport de mélange de CO. Concernant la composition chimique de l'atmosphère, les simulations produisent une bonne représentation des concentration massiques d'aérosols mesurées sur le domaine marin, des flux sortants des villes urbaines. Cependant, elles sous-estiment les concentrations au niveau régional. Afin d'évaluer différents inventaires d'émissions, nous avons inter-comparé des simulations réalisées à partir de deux inventaires d'émissions, de DACCIWA et EDGAR. Il en ressort que les simulations avec l'inventaire d'émissions de DACCIWA donnent une meilleure correspondance avec les observations.

Par ailleurs, à l'exception de NO_3, les concentrations des particules d'aérosols, simulées en utilisant les inventaires d'EDGAR, sont sous-estimées.

L'analyse du cas du 02 July 2016, en utilisant CO comme indicateur du panache des feux de biomasse, révèle que les nuages convectifs sont à l'origine du transport vertical du panache des feux de biomasse depuis les moyennes altitudes jusqu'au niveau de la couche limite au Sud de la Côte d'Ivoire. En outre, les simulations basées sur des cas

idéalisées de traceurs montrent qu'environ 20% de la masse de CO localisés entre les altitudes 4 km et 2 km est transporté en dessous de 1 km d'altitude sur le Golfe de Guinée après deux jours de simulation.

Nous avons quantifié l'impact des aérosols issus des feux de biomasse sur la couverture nuageuse et le rayonnement solaire. Les résultats montrent qu'une augmentation de 27% des concentrations des gouttelettes de nuages a été constatée au-dessus du Golfe de Guinée et de 7,5% sur l'ensemble de la zone d'intérêt. Nous remarquons une réduction de 50 W m^{-2} et de 20 W m^{-2} du rayonnement en surface de courte longueur ondes est simulée respectivement au-dessus du Golfe de Guinée (3–4ºN ; 9ºW–1ºE) et sur l'ensemble du domaine d'étude (3–11ºN ; 9ºW –1ºE) en moyenne spatiale pour toutes les conditions du ciel (couvert et dégagé).

Au travers de ces simulations, nous avons quantifié l'impact des aérosols provenant des feux de biomasse sur la composition chimique de l'atmosphère. Nous enregistrons après deux jours de simulations, une augmentation maximale des concentrations en surface du CO, de l'ozone, des matières particulaires de taille inférieure à 1, 2,5 et 10 µm respectivement de 154 µg m^{-3}, 27 µg m^{-3} et 6–7 µg m^{-3}.

Aussi, nous avons abordé l'impact des aérosols d'origine anthropiques de source locale sur des paramètres météorologiques, notamment le trafic, les feux domestiques, l'industrie, les émissions des centrales thermiques, les feux de déchets. Les résultats montrent une augmentation d'environ 90 % du nombre de gouttelettes de nuages due aux aérosols anthropiques. Il en découle une diminution de la taille de ces gouttelettes de 12 à 10 µm. En outre, en moyenne spatiale, le rayonnement en surface de courte longueur ondes est réduite jusqu'à 60 W m^{-2}. L'analyse de la distribution spatiale de la vitesse des vents de mousson révèle une réduction de 1,2 m s^{-1}.

Par ailleurs, des simulations basées sur deux scenarios climatiques d'inventaire d'émissions en 2050 notamment RCP 2.6 et 8.5 ont été réalisées. L'objectif était d'analyser l'impact de l'augmentation future des émissions d'origine anthropique sur la composition atmosphérique.

Les résultats suggèrent une augmentation de tous les polluants sur l'Afrique de l'Ouest à l'exception du carbone suie (BC) qui diminuerait au Nigeria, au Ghana et au Niger. En outre, les concentrations d'Ozone et d'oxyde de nitrogène (NO_x) dans certaines villes de l'Afrique de l'Ouest comme Abidjan et Accra excèderaient les seuils fixés par l'Organisation mondiale de la santé (OMS).

En conclusion, les résultats de cette étude mettent en exergue la nécessité d'établir un réseau de surveillance de la qualité de l'air en Afrique de l'Ouest particulièrement dans les villes côtières ou le niveau de pollution est plus élevé.

CONTENTS

LIST OF FIGURES

LIST OF TABLES

LIST OF ACRONYMS

ABL: Atmospheric Boundary Layer

ACI: Aerosol Cloud Interactions

ADE: Aerosols Direct Effect

AEJ: African Easterly Jet

AERONET: Aerosols Robotic Network

AI: Atlantic Inflow

AIE: Aerosol Indirect Effect

AMMA: African Monsoon Multidisciplinary Analysis

AOD: Aerosol Optical Depth

AOT: Aerosol Optical Thickness

AR5: Fifth Assessment Report 5

ARI: Aerosols Radiation Interaction

ATR: Avion de Transport Regional

AVHRR: Advanced Very High-Resolution Radiometer

AWB: Abidjan Waste Burning

BAS: British Antarctic Survey

BBA: Biomass Burning Aerosols

BC: Black Carbon

BVOC: Biogenic Volatile Organic

CALIPSO: Cloud-Aerosol Lidar and Infrared Pathfinder Satellite Observations

CAMS: Copernicus Atmosphere Monitoring Service

CCN: Cloud Condensation Nuclei

CCSM: Community Climate System Model

CDNC: Cloud Droplets Number Concentration

CMIP5: Coupled Model Intercomparison Project Phase 5

CO: Carbon Monoxide

CO2: Carbon dioxide

COSMO-ART: Consortium for Small-scale Modelling- Aerosols and Reactive Trace gases

DACCIWA: Dynamics-Aerosol-Chemistry-Cloud Interactions in West Africa

DJF: December-January-February

DLR: Deutsches Zentrum für Luft- und Raumfahrt

DMS: Dimethyl sulfide

DMSO: Dimethyl Sulfoxide

DWD: Deutscher Wetterdienst

ECDF: Empirical Cumulative Distribution Function

ECMWF: European center for Medium-range Weather Forecasts

EDGAR HTAP_v2: Emission Database for Global Atmospheric Research, Hemispheric Transport of Air Pollution version 2

EDGAR: Emission Database for Global Atmospheric Research

ERF: Effective Radiative Forcing

ETS: Equitable Threat Score

EUMETSAT: European Organization for the Exploitation of Meteorological Satellites

FADE: Factor ADE

FAIE: Factor AIE

FRP: Fire Radiative Power

GCM: Global Climate Models

GFAS: Global Fire Assimilation System

GFED: Global Fire Emissions Database

GRAALS: General Radiative Algorithm Adapted to Linear-type Solutions

hPa: hectopascal

HSS: Heidke skill Score

HWSD: Harmonized World Soil Database

ICON: ICOsahedral Non-hydrostatic

IFS: Integrated Forecasting System

IMERG-GPM: Integrated Multi-satelliteE Retrievals for Global Precipitation Measurement

IOP: Intensive Observations Period

IPCC: Intergovernmental Panel in Climate Change

ITCZ: Inter-tropical Convergence Zone

ITD: Inter Tropical Discontinuity

JAS: July-August-September

JASO: July-August-September-October

JJA: June-July-August

LAI: Leaf Area Index

LLCs: Low-level clouds

LUT: Look-up Tables

LW: Longwave

LWP: Liquid Water Path

MADEsoot: Modal Aerosol Dynamics Model for Europe extended by Soot

MCS: Mesoscale Convective System

MI: Maritime Inflow

MODIS: Moderate Resolution Imaging Spectroradiometer

MOPITT: Measurements of Pollution in the Troposphere

MSG: Meteosat Second Generation

Mt: Megatons

NASA: National Aeronautics and Space Administration

NH: Northern Hemisphere

NH3: Ammonium

NLLJ: Nocturnal Low-Level Jet

NLLS: Nocturnal Low-Level Stratus

nm: nanometer

NMVOC: Non-Methane Volatile Organic Compound

NO2: nitrogen dioxide

NO_x: nitrogen oxide

NWP: Numerical Weather Prediction

OC: Organic Carbon

PAPA: Photolysis Model

PBL: Planetary Boundary Layer

PFT: Plant Functional Types

PM: Particulate matter

POD: Probability of Detection

POFD: Probability of False Detection

POM: Primary Organic Matter

ppb: part per billion

ppm: part per million

ppmv: part per million by volume

RADM2: Regional Acid Deposition Model Version 2

RADMKA: Regional Acid Deposition Model Version Karlsruhe

RCM: Regional climate models

RCP: Representative Concentration Pathway

RegCM: Regional Climate Model

RK: Runge-Kutta

RMSE: Root Mean Square Error

RTE: radiative transfer equation

SAFIRE: Service des Avions Français Instrumentés pour la Recherche en Environnement

SEVIRI: Spinning Enhanced Visible and Infrared Imager

SH: Southern Hemisphere

SHL: Saharan heat low

SO2: Sulfur dioxide

SODEXAM: Société d'Exploitation et de Développement Aéroportuaire, Aéronautique et Météorologique

SSA: Single Scattering Albedo

SST: Sea surface temperature

STRATOZ: Stratospheric Ozone Experiment

SW: Shortwave

SWA: southern West Africa

SYN: Synergistic effect of ADE and AIE

TEJ: Tropical Easterly Jet

Tg: Teragram

TKE: turbulent kinetic energy

TMMS: Two Moment Microphysics Scheme

TOA: Top of the Atmosphere

TROPOZ: Tropospheric Ozone Experiment

TS: Threat Score

UNEP: United Nations Environment Programme

UNO: United Nations Organization

USDA: United States Department of Agriculture

UTC: Universal Time Coordinated

VBS: Volatility basic set

VOC: Volatile Organic compounds.

WAM: West African Monsoon

WRF-Chem: Weather Research and Forecasting -Chemistry

Yr: year

CHAPTER ONE

INTRODUCTION

1.1 Background to the Study

Aerosols are tiny liquid and solid particles presents in the atmosphere. They are emitted directly in the atmosphere by manmade activities or naturally released by surface known as primary aerosols (e.g. soot, sea salt, dust). Secondary aerosol rather results from photochemical processes through nucleation of gas precursors (e.g. mixture of sulfate, ammonium, nitrate, organic matter and water). They grow by condensation and coagulation with other particles and extend from few nanometers to hundred micrometers of diameter. Aerosols become clouds droplets or ice crystals by condensational growth of water vapor onto the particles. This happens as a result of adiabatic cooling in an updraft when a moist air is supersaturated with respect to water. Some particles can grow quickly to form clouds droplets but it depends on the size, water content and chemical composition of the aerosols (Kerkweg *et al.,* 2003). Further growth of clouds droplets occurs by collision and coalescence of the droplets which efficiency depends on the size distribution. Aerosols affect the global energy budget by scattering and absorption of radiation (Schulz *et al.*, 2006). Radiation drives a lot of processes in the atmosphere that govern the global climate and weather. Additionally, aerosols also determine the initial size of cloud, serving as cloud condensation nuclei or ice nuclei. Aerosol changes induce change in cloud radiative effects, thus affecting the whole atmospheric circulation. Consequently, aerosols to some extent affect precipitation by changing cloud microphysics (lifetime, size, height, spatial coverage). Owing to the non-linearity of aerosol effects on cloud microphysics, aerosol-cloud interaction is the least understood process in the atmosphere. This makes it difficult to quantify the impact of aerosols on clouds as well as precipitation (Stevens and Feingold,

2009; Tao *et al.*, 2012; Deetz *et al.*, 2018). On the other hand, climate models suffered from capturing interaction between various components of large range of scales (Seinfeld *et al.*, 2016). For instance, aerosol numerical prediction seems to be hampered by several errors due to the complex aerosols processes and their sensitivity to the atmospheric meteorological conditions (Benedetti *et al.,* 2018). This might explain the buffered cloud and precipitation response to aerosol as suggested by (Stevens and Feingold, 2009). One the other hand, observational networks are limited to some extent because of larges range of scale and the fact that various measuring systems tend to address different scales. In short, aerosol particles from their formation to their implication into radiation, clouds and precipitation through chemical and physical processes have to be fully understood in order to quantify their potential impact on the state of the atmosphere.

Although, these past decades, a lot of studies have focused on the impact of aerosol on the climate, there is still a lot of challenges to quantify accurately the impact of aerosol on the climate due the complexity in the relevant processes involved. Especially in West Africa, a lot of studies have been dedicated to the impact of aerosol mainly dust aerosol on the climate and West African monsoon dynamics (e.g. Miller *et al.,* 2004; Yoshioka *et al.*, 2007 ; Ogunjobi *et al.*, 2007; Konare *et al.,* 2008; Solmon *et al.*, 2008; *Stanelle et al.*, 2010; Zhao *et al.*, 2011; Raji *et al.*, 2017; N'Datchoh *et al.*, 2018). In addition the African Monsoon Multidisciplinary Analysis (AMMA, Redelsperger *et al.*, 2006) has improved our understanding of the West African monsoon variability and its interaction with dust aerosols but with focus over the Sahel. For instance Tulet et *al.* (2008) showed that long-range dust transport over the Gulf of Guinea generated an Aerosol Optical Thickness (AOT) greater than four (4) in Nigeria during a dust even occurred in March 2006. Dust impacts the vertical structure of the atmosphere by modifying the

atmospheric stability and the potential temperature in the boundary layer below 2 km. Chaboureau *et al*. (2007) demonstrated that the use of a prognostic dust aerosols scheme improve the forecast of convective activities observed by Meteosat Second Generation (MSG) satellites over the Sahel during AMMA campaign. Regarding the radiative forcing of aerosol, several studies have highlighted the scattering effect of mineral dust in Niamey and Djougou respectively -56 W m^{-2} and -45 W m^{-2} on daily average during dry season 2006 (Milton *et al.*, 2008; Mallet *et al.*, 2008). Recently, the Dynamics-Aerosol-Chemistry-Cloud Interactions in West Africa (DACCIWA, Knippertz *et al.*, 2015) have shift attention over southern West Africa (SWA), mainly on coastal region over the Gulf of Guinea. As a result of accelerated urbanization and industrialization, SWA undergoes an unprecedent local pollution. On top of the local pollution occurring, long-range transport of dust from Sahel and Sahara Desert, and biomass burning aerosol from Central and southern Africa affects the atmospheric composition (Knippertz *et al.*, 2017). Deetz *et al.* (2018) showed that increasing aerosols over SWA leads to a reduction of the propagation velocity of a coastal front called Maritime Inflow (MI) and a weakening of the Nocturnal Low-Level Jet (NLLJ) and a delay of 1-2 hours of stratus to cumulus transition during summer monsoon using COSMO-ART. Associated to NLLJ, nocturnal low level stratus and stratocumulus (NLLS) deck form over SWA (Schrage and Fink, 2012 ;van der Linden *et al*., 2015; Adler *et al*., 2017; Deetz *et al.,* 2018). The mechanism of formation and dissolution of the NLLS, and transition to cumulus clouds is well documented in (Adler *et al.*, 2019; Babic *et al.*, 2019). Moreover, long-range transport of biomass burning aerosol from Central and southern Africa have been observed in the Planetary Boundary Layer (PBL) over SWA as well as upwind marine of the SWA coastal cities but the mechanism by which these aerosols get mixed into the PBL is still unclear (Brito *et al*., 2018; Haslett *et al*., 2019). Menut *et al.* (2018)

showed through modelling that long-range transport of biomass burning aerosols increase the level of pollution in the urban cities such as Lagos and Abidjan. These biomass burning aerosols modified the cloud microphysical properties over SWA by reducing their size and increasing the number concentration of cloud droplets (Haslett *et al*., 2019). It is obvious that biomass burning aerosols will also affect the incoming surface radiation as well as the climate over the region therefore it need to be investigated.

Despite all the efforts done to understand the effects of aerosols on the West African climate, there is still a lot of open questions. It remains unclear the implication of anthropogenic aerosols in the formation of nocturnal low levels clouds over SWA during summer monsoon. According to Taylor *et al.* (2019), the existing background aerosol in the SWA boundary layer due to biomass burning plumes from Central Africa is likely to dampen any effect of increasing local emissions on cloud-aerosol interactions as emission is expected to continue rising as population grows.

1.2 Problem of statement

The interest of air pollution in West Africa has grown substantially in recent years. Recent studies have been dedicated to study aerosol (natural and anthropogenic) effects on the climate over West Africa (Raji *et al*., 2017; N'Datchoh *et al.*, 2018; Deetz *et al.*, 2018). The contribution of each source individually (e.g. natural, biomass burning, local pollution) on South West Africa (SWA) clouds and radiation as well as West African Monsoon (WAM) dynamics have not yet been fully investigated. Moreover, previous studies (e.g. Deetz *et al*., 2018) used global anthropogenic aerosol datasets, (Emission Database for Global Atmospheric Research (EDGAR), 2010) which are not specific to SWA. New anthropogenic emissions inventories (Keita, 2018) have been developed in the framework of DACCIWA which take into account the specificities of SWA cities

and are more recents, reflecting the atmospheric chemistry of the region. In addition, observational studies during DACCIWA have measured high concentration of biomass burning aerosol over SWA from long range transport (Brito *et al.*, 2018; Flamant *et al.*, 2018; Taylor *et al.*, 2019; Haslett *et al.,* 2019). This is what motivated the scope of this study.

This study therefore investigates impact of natural, biomass burning aerosols from Southern and Central Africa and local anthropogenic pollution on the state of the atmosphere over South West Africa using COSMO-ART.

Moreover, it investigates the implications of convective clouds in downwards transport of biomass burning aerosols from mid-tropospheric height into the PBL over the Gulf of Guinea and SWA.

This study evaluates different emission datasets and compares it with observations in order to improve the air quality forecast over the region.

1.3 Research justification

As far as climate change is concerned, increasing anthropogenic activities (e.g. industrialization, local pollution, biomass burning) have induced a growing interest of aerosol research in the field of atmospheric science. Till date, natural aerosol (e.g. dust) from the Saharan and biomass burning are being considered as major source of aerosols over West Africa. However, a study conducted by Andreae and Merlet (2001) showed that domestic fires are important source of gaseous and particulate matter in Africa. Particularly in West Africa, Liousse *et al.* (2014) demonstrated in a regional emission inventory that domestic fire is the principal source of pollutant, followed by traffic. Increasing population in West Africa is unprecedent, with increasing megacities along the Guinea coast due to urbanization. Consequently, anthropogenic emissions will

continue to increase. Keita (2018) elaborated the regional emissions inventory in Africa of nitrogen oxide (NO_x) and Black Carbon (BC) in 2015.

NO_x is highly emitted over cities along the coast in SWA as a result of anthropogenic emissions, except Nigeria where emissions are also observed in the Northern part of the country. Same observation for BC but with low values compared to NO_x emissions. Developing countries in West Africa are the most affected by climate change. Till date, two big projects have been carried over West Africa in order to understand the interaction between WAM system and the atmospheric composition. The African Monsoon Multidisciplinary Analysis (AMMA, Redelsperger *et al.,* 2006) and DACCIWA (Knippertz *et al*., 2015). The former focus on the Sahel while the latter drew attention on coastal region over the Gulf of Guinea referring as SWA. A huge data sets from modelling, ground observations, satellites and aircraft have been compiled through DACCIWA to address issues related to aerosol influence on clouds, radiation as well as WAM dynamics.

Moreover, Low-level clouds (LLCs) over SWA are common features during summer monsoon (Schrage and Fink, 2012; van der Linden *et al*., 2015). In the framework of DACCIWA, studies revealed that a considerable aerosol fraction in the monsoon layer in SWA is water and significantly alter the Aerosol optical depth (AOD) (Deetz *et al.*, 2018; Haslett *et al.*, 2018). Deetz *et al*. (2018) showed that increasing aerosol amount lead to a reduction of the propagation velocity of a coastal front know as Maritime Inflow (MI), a weakening of the NLLJ and a delay of 1–2h of stratus to cumulus transition over southern West Africa during the summer monsoon season using COSMO-ART. However, SWA is characterized by a mixture of pollutants from different sources during the summer monsoon as highlighted by Knippertz *et al*. (2017): natural sources such as dust from Sahel and Sahara Desert, sea salt from the Gulf of

Guinea, and biogenic aerosols from vegetation and biomass burning aerosol from Central and southern Africa. This work will contribute to understand the role of anthropogenic aerosols in Low-Level Clouds (LLCs) formation over SWA during summer monsoon and improve their representation in climate models over SWA.

1.4 Aim and Objectives

The aim of this study is to quantify the impact of natural and anthropogenic aerosols on the clouds and radiative properties over West Africa:

The objectives of the study are to:

(i) determine the spatio-temporal variability and vertical profile of aerosol and trace gases and identify contribution from different sources (local pollution, biomass burning, natural);

(ii) evaluate different anthropogenic emissions datasets (DACCIWA, EDGAR) impacts on clouds and radiation and compare with previous studies (modeling, observations);

(iii) quantify effects aerosol-radiation and aerosol-cloud interactions on the state of the atmosphere; and

(iv) assess the impact of future anthropogenic pollutants on the state of the atmosphere.

CHAPTER TWO

LITERATURE REVIEW

This chapter summarizes recent research studies on aerosol characteristics as well as their impacts on clouds and radiation through both observations and modeling studies during summer monsoon period, highlighting aerosols contribution from different sources (Saharan dust, urban sources, biomass burning). A description of West African Monsoon (WAM) is given in the section below, which is a special feature of the region during this period of the year.

2.1 West African Monsoon (WAM)

It is defined by two main features. The ITCZ, and the Jets; African Easterly Jet and Tropical Easterly Jet (AEJ and TEJ). Figure 2.1 presents the meridional-pressure section illustrating the West African Monsoon circulation. ITCZ is the convergence zone of two air masses. The first one is a cool and humid southwesterly flow, from the Ocean called Monsoon and the second one is a hot and dry northeasterly flow from the continent called Harmattan. This convergence will create a rising air accompanied by clouds formation. The air masses as well as the ITCZ also called Inter Tropical Discontinuity (ITD) over land move due to the pressure gradients. The differential pressure gradient between cool and moist air from Ocean and dry and hot air from the continent acts to maintain the low-level southerly monsoon flow. The strength of the monsoon flow is monitored by the thermal depression zone called Saharan heat low (SHL) located between (18 °N to 30 °N). When it goes high in latitude, it creates a northward push of the ITD and vice-versa when it goes down to the equator. As a result, precipitation migrates from Guinea coast to the Sahel as a result of the south-north migration of the ITCZ (Sultan and Janicot, 2003).

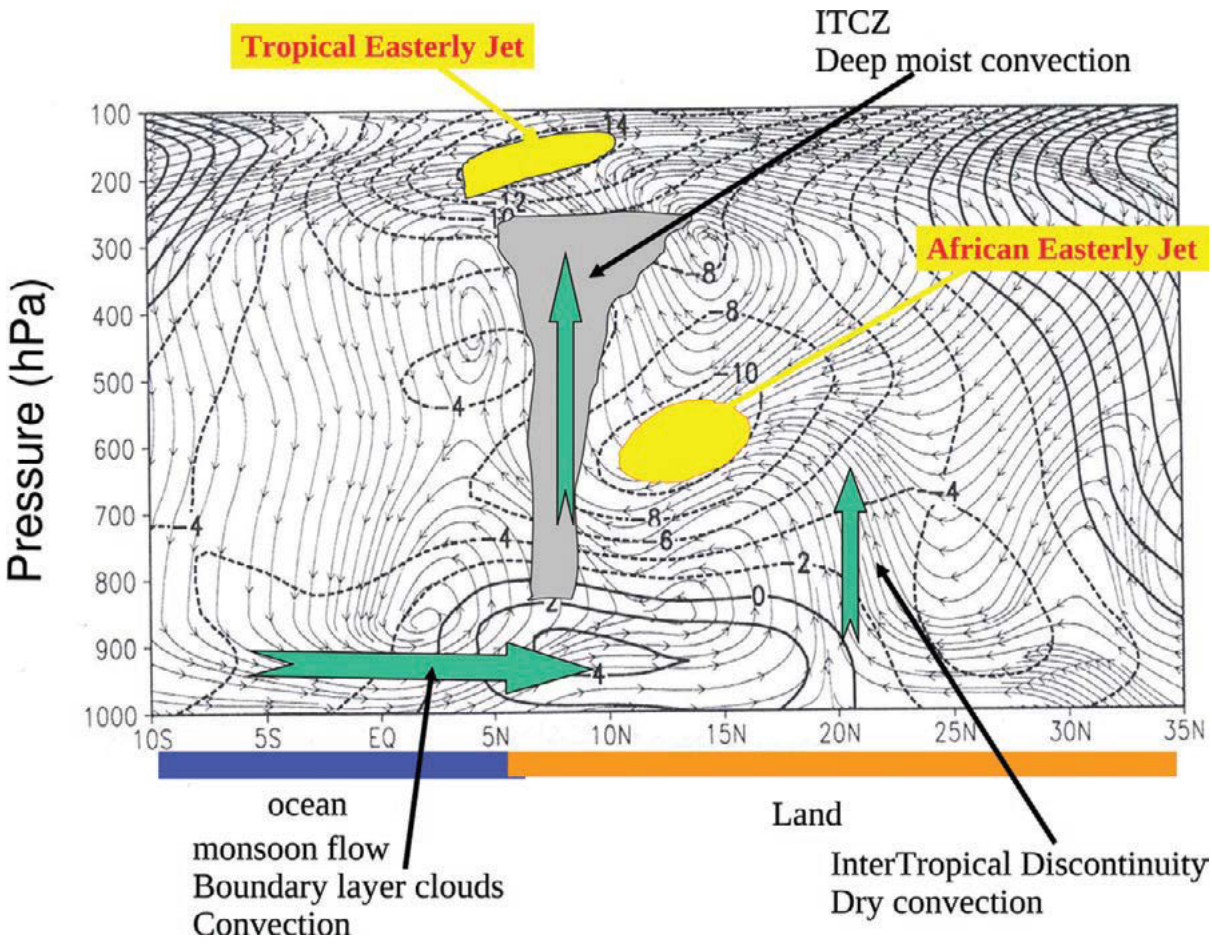

Figure 2.1: Mean Meridional Circulation (streamlines) and associated mean Zonal Wind (m/s in contours) over West Africa during the summer season adopted from Hourdin *et al*. (2010).

The WAM is also intimately related to the African Easterly Jet (AEJ), a mid-tropospheric flow centered around 600-700 hPa at a latitude of around 15° N (e.g. Burpee, 1972; Parker *et al*., 2005; Cook, 1999; Thorncroft and Blackburn, 1999). It results from the strong baroclinicity across the ITD together with the contrasts in moist convection south of the ITD and dry convection north of the ITD (Lafore *et al*., 2011). The AEJ is linked to the formation of African Easterly waves (Thorncroft and Hoskins, 1994; Diedhiou *et al*., 1999), favorable to the development of Mesoscale Convective Systems (MCS), which produce 80 % of the precipitation over the Sahel (Mathon *et al*., 2002). Regarding the TEJ, it is a summer-time upper-tropospheric (100–200hPa) easterly wind between 5° and 20° N. It originates in the South Asian Monsoon system over Bay of Bengal, extends westwards to Africa and decays over the tropical Atlantic Ocean (Lemburg *et al*., 2019). The relationship between TEJ and the rainfall is a causal one. Nicholson (2009) suggested that a strong TEJ can enhance rainfall by increased upper-level divergence. WAM, as a key feature of SWA, it determines the meteorological and climate over the region.

2.2 Aerosol, clouds characteristics over West Africa

These last decades, a lot of research have been devoted to aerosol, radiation, cloud, their interactions and effects on weather, climate and precipitation through observations, modeling, remote sensing techniques. In the following, aerosol composition and cloudiness over SWA will be introduced, aerosols impact on radiation, clouds and climate will be reviewed in general and particularly over SWA.

2.2.1 Local anthropogenic sources of pollution in West Africa

Air pollution is a problem in SWA with increasing emissions from various sources. For instance, coastal cities development in SWA is leading to more traffic and therefore fuel consumption increases anthropogenic emissions in the West-African context (Doumbia

et al., 2018). Previous studies from Andreae and Merlet (2001) have showed that domestic fire for cooking purpose in Africa appear to be one of the largest source of primarily emitted gaseous and particulate matter. Traffic is identified as the second largest sources of anthropogenic aerosols in West Africa (Liousse *et al*., 2014). Marais and Wiedinmyer (2016) demonstrated through regional emissions inventories for Africa that car traffic, industries, oil extraction, domestic fires, and waste burning are the major sources of anthropogenic emissions. Anthropogenic activities are predicted to surpass biomass and become the first largest source of pollution in 2030 (Liousse *et al*., 2014). Most people rely on crop residue, fuelwood, charcoal kerosene, and backup generators for energy in Africa. At a regional scale, a recent emission inventory was developed in the framework of DACCIWA with an updated fuel consumption data by Keita (2018). West African region is the largest emitter of BC (386.4 Gg), Organic Carbon (OC) (2794.4 Gg), CO (33483.7 Gg) and Non-Methane Volatile Organic Compound (NMVOC) (5759.3 Gg) in 2015, representing 29%, 38%, 35% and 36% of total emissions in Africa, respectively. Regarding the sectors, domestic sources and waste burning are the largest emitters of emitters of BC, OC and NMVOC. Abidjan waste burning (AWB) site receives the waste of the district of Abidjan since 50 years, currently more than 1 millions tons of waste per year (Adjiri *et al*., 2015). Domestic fires include smoking meat and fish, grilling of peanuts, and domestic cooking. As a result of combustion, carbonaceous aerosols are among the major components of $PM_{2.5}$ in urbanized areas (Zhang *et al*., 2007).

In the framework of DACCIWA project, a lot of effort have been made to give an accurate state of the atmospheric composition (aerosol and trace gases) over southern West Africa. Through in situ observations, Bahino *et al.* (2018), showed that domestic fires and traffic are the biggest sources of gaseous pollutants in Abidjan (Côte d'Ivoire)

while in Cotonou (Benin), the two-wheel vehicles from traffic sector is the highest source of pollution. Measurement of trace gases nitrogen dioxide (NO_2), ammonia (NH_3), and sulfur dioxide (SO_2) with concentration up to 90 part per billion (ppb), 20 ppb and 6 ppb respectively, in Abidjan (Côte d'Ivoire) in winter 2015/2016 have been observed. SO_2 is predominantly from traffic while NH_3 from domestic fires. NO_2 predominant source is industries, followed by traffic and domestic fires. Concerning aerosols, Djossou *et al.* (2018) found that the highest Particulate Matter with diameter smaller than 2.5 µm ($PM_{2.5}$) concentration of 145 µg m^{-3} were located close to domestic fires places in Abidjan. A background concentration measured by the French Service des Avions Français Instrumentés pour la Recherche en Environnement (SAFIRE) ATR-42 aircraft during the DACCIWA campaign showed a fairly polluted region in SWA (outside the urban plumes) with an averaged Particulate Matter with diameter smaller than 1 µm (PM_1) concentration of 5.9 µg m^{-3} dominated by secondary organic compounds that contributes 53% to the total aerosol mass (Brito *et al*., 2018). Focusing on urban pollution plumes (outflow of Abidjan, Accra and Lomé), PM_1 concentration was 11.9 µg m^{-3} with an average CO concentration of 176 ppb (Brito *et al.*, 2018).

In addition, another source of anthropogenic emissions is from gas flaring along the coast of the Gulf Guinea with Nigeria identified as the second largest gas flaring country (Elvidge *et al*., 2016). This flaring emission releases typical pollutants such as CO_2, SO_2, BC and NO_x. Elvidge *et al*. (2009) showed using satellites products that gas flaring in Africa represent 31% of the flared gas in the world with only Nigeria accounting for 14%. The adverse environmental effects of gas flaring on the Nigerian Niger Delta have led to a government decision to extinct gas flaring (Ite and Ibok, 2013). Though an attempt to stop gas flaring is not yet effective, there was a decrease of 25 % flaring emissions in West Africa from 2014 to 2015 as highlighted by Deetz and Vogel (2017).

It is worth noting that anthropogenic emissions do not only increase the level of pollution over the region but they also have impact on the radiation, weather, climate and likewise the prevailing meteorological condition also plays a role in shaping the anthropogenic aerosols distribution. Flamant *et al*. (2018) showed that land–sea surface temperature gradients between the northern part of the Gulf of Guinea and the continent as well as orography over Ghana and Togo play important role for the distribution of aerosols and gases over coastal West African region based on a case study. Large scale pollution distribution observed at the coast of SWA up to 1.5 km are essentially related to emissions from Lomé, with moderate contribution from Accra and Cotonou based on a case study (1–2 July 2016) (Flamant *et al*., 2018). From the surface to the top of the planetary boundary layer (PBL), anthropogenic pollution emitted at the coast are transported by northeastward monsoon flows before moving further inland (Knippertz *et al.*, 2017). Deroubaix *et al*. (2018) quantified the relative contribution of different sources (i.e., emissions from several large coastal cities) to the air quality in Savè. It is shown that a systematic diurnal cycle exists with high surface concentrations of pollutants from 18:00 to 22:00 UTC attributed to pollution transport from coastal city of Cotonou (Benin).

Due to the high humidity in SWA region, recent studies based on modeling and observations, have revealed that a considerable fraction of aerosol in the monsoon layer is water and significantly alter the aerosol optical depth (Deetz *et al.*, 2018; Haslett *et al*., 2018).

2.2.2 Remote Source of Pollution in West Africa

Dust represents the most important source of aerosol mass for the atmosphere (Seinfeld and Pandis, 2008). The world largest source of mineral dust aerosols is Africa (Laurent *et al*., 2008), with Saharan desert dust emissions of about 1150 Mt yr^{-1} (Tanaka and

Chiba, 2006; Shao *et al*., 2011). Dust is regularly transported throughout the all year (Marticorena *et al*., 2011). Dust aerosol has four main trajectories. It is transported southward from the Saharan Desert toward the Sahel and the Gulf of Guinea. It is also transported westward toward the Atlantic Ocean, northward to Europe, and eastward which is relatively minor. The particle size, number and mass concentrations of Saharan dust during three successive Harmattan seasons in 1996, 1997 and 1998 in southern Ghana (6°40′N, 1°34′W) was reported by (Afeti and Resch, 2000). Dust transport in SWA is most dominant during winter via Harmattan (Ogunjobi *et al*., 2007; Ogunjobi *et al*., 2008; Awadzi and Breuning-Madsen, 2011). But late spring and early summer is also period when dust load over West Africa particularly in Sahelian and Sub-Sahelian Countries (Engelstaedter and Washington, 2007). Flamant *et al*. (2009) showed that in late spring and early summer dust is subsequently transported from Bodélé southwest towards the Sahel and the Gulf of Guinea. According to the authors, the ITD acts to raise the aerosol layer over the southwesterly monsoon flow and into the AEJ core which contributes to the rapid westward transport across the continent. There is evidence of long-range transport of dust from Saharan/Sahelian region toward West African coastal regions but mostly in the northern part of the region. Marticorena *et al*. (2010) showed that dust event in summer are primarily related to local dust emissions by Mesoscale Convective Systems (MCSs).

During DACCIWA campaign, ATR 42 flight conducted on 2 July revealed a presence of dust layer in the region of Savè (Benin ~ 8°N) (Flamant *et al*., 2018). Flamant *et al*. (2018) highlighted that during the DACCIWA aircraft measurement, dust was forecasted by the European center for Medium-range Weather Forecasts (ECMWF) Copernicus Atmosphere Monitoring Service-Integrated Forecasting System (CAMS-IFS) to be mainly north of 8°N (latitude of Savè) and southward transport over the

Soudanian zone and was clearly modulated by major synoptic-scale features (Knippertz *et al*., 2017).

Ogunjobi *et al.* (2007) showed that the development of a synoptic scale ridge largely induces a large-scale regional influence of Harmattan dust in Nigeria. The authors highlighted that the mobilization and transport of dust requires a threshold of high wind speed. Knippertz *et al*. (2017) showed through observed Aerosol Optical Depth (AOD) at 550 nm the presence of dust at the coast (around 6° N) before the onset of the monsoon (1–21 June 2016) and retreats to the North of 8° N after the onset (22 June–20 July 2016). A modelling study conducted by Deroubaix *et al*. (2018) has revealed that desert dust contribution to the Guinea Gulf coast decreases from ~38% in May to ~ 5% in July during summer monsoon 2006.

Biomass burning fires in West Africa occurs during winter time whereas wide areas in Central and southern Africa are burned as a result of agricultural activities in summer time (between June and September) each year. The smoke aerosol from biomass burning is mainly composed of reactive species such as CO, hydrocarbons, NO_x, absorbing black carbon (BC) particles and fine organic carbon (OC) particles, whose proportions vary according to vegetation type, oxygen availability, and combustion phase (Andreae and Merlet, 2001). It has been discovered by Marenco (1990) during Stratospheric Ozone Experiment (STRATOZ) and Tropospheric Ozone Experiment (TROPOZ) airborne campaign that large CO concentrations are presents in the mid-Atlantic as well over West Africa as evidence of lofting of biomass burning. The plumes arising from agricultural burning fumes mix in 3–4 km deep boundary layer over Africa as a result of convergence, then overrides moister and cooler air before it is advected westward over the Atlantic Ocean (Chatfield *et al.*, 1998). In another studies, it is shown that biomass burning plumes from Central and southern Africa are transported each year

during the WAM season and carried westward by a jet located at 700 hPa between 2 and 4km (Barbosa *et al.*, 1999; Mari *et al*., 2008). Real *et al*. (2010) found ozone plumes in mid and upper troposphere over the Gulf of Guinea as a result of long-range transport of biomass burning from Central Africa. Mari *et al*. (2008) demonstrated using backward trajectories that the intrusion of biomass burning in the upper troposphere of the Gulf of Guinea and Northern hemisphere is controlled by the active and break phases of the southern hemisphere AEJ during summer monsoon.

Biomass burning is an important source of aerosols and trace gases, with an estimated burned biomass of 3260 to 10450 Tg a^{-1} for tropical areas (Barbosa *et al*., 1999). (Hao and Liu (1994) estimated the amount of 2500 Tg a^{-1} (46% of the tropics total) for tropical Africa to which the savanna contributes up to 1600 Tg a^{-1} (30% of the tropics total). Number and size distributions of biomass burning aerosols are dominated by the accumulation mode (Haslett *et al*., 2019). Likewise, according to Menut *et al*. (2018) biomass burning from Central and southern Africa increased the level of air pollution in urban cities such as Lagos and Abidjan (approximately 150 µg m^{-3} for CO, 10–20 µg m^{-3} for O_3, and 5 µg m^{-3} for $PM_{2.5}$) through modeling study (WRF-Chem). The contribution of biomass burning $PM_{2.5}$ concentration from Central Africa increases from ~ 10% in May to ~ 52 % in July (Deroubaix *et al*., 2018). Haslett *et al*. (2019) found in southern West Africa boundary layer a significant accumulation mode aerosol concentration both over the ocean and continent with similar chemical properties. The authors suggested that the upstream (Ocean) aerosols is originated from Central Africa biomass burning and demonstrated that these aerosols render cloud optical properties but less sensitive to precipitation. However, the mechanism by which the biomass burning get mixed into the boundary layer is unclear.

2.2.3 Cloudiness over West Africa

Cloud is the component of the atmosphere controlling the hydrological cycle. During the monsoon season , SWA experiences a complex pattern of cloud types with a pronounced diurnal cycle (Hill *et al*., 2016). The meteorological conditions of SWA during summer monsoon is characterized by frequent Nocturnal Low-Level Stratus (NLLS) and stratus deck over the region (e.g. Schrage and Fink, 2012; Schuster *et al.*, 2013); van der Linden *et al*., 2015; Adler *et al.*, 2017). According to the above-mentioned studies, the NLLS cloud base is between 200–400 m above ground level increasing in the course of the morning. At around 9 UTC, the NLLS maximum is reached and the stratus deck on average covers the southern half of Côte d'Ivoire, the southwestern part of Ghana and Nigeria. Those above-mentioned studies were done through climate modeling and remote sensing data analysis. In the framework of DACCIWA, during June–July 2016 observations from in-situ measurements from radiosonde, ceilometer, cloud radar and energy balance stations have been collected to shed light on cloud microphysics over West Africa. It appears that these NLLS formation is closely linked a NLLJ, a feature within the monsoon flow with a core wind speed around 7–11 m s^{-1} within (200-300°) southwesterly sector at about 350 m height, same height where the NLLS form indicated by (Dione *et al.*, 2019). The NLLJ develops nearly every night being strong between 21:00 and 02:00 UTC and dissipates gradually after sunrise at around 06:00 UTC observed over SWA measurements sites (Kumasi, Savè and Ile Ife) by Kalthoff *et al*. (2018). Though, Using Intensive Observations Periods (IOPs) from mid-June to end of July 2016, the relevant processes and parameters for the formation of NLLS were highlighted. It is found that energy balance at the Earth's surface, depth and strength of the monsoon flow, Harmattan and AEJ conditions, cold air advection and the presence of mid and upper clouds are key factors for NLLS formation. The mechanisms in the cloud formation has been described by

Dione *et al*. (2019) as follows:

(i) advection of cold air, associated with the monsoon flow, and more abruptly with the Maritime inflow and the NLLJ;

(ii) radiative cooling that occurs at the end of the day, which cools and stabilizes the surface layer;

(iii) turbulent mixing that occurs at the NLLJ core flanks, which can distribute the cooling from the surface up to the cloud layer height;

According to Adler *et al*. (2019) different nocturnal phases exist during the temporal evolution of Low-Level Clouds (LLCs) at Savè based on IOPs. The authors found that a surface inversion forms after sunset when the horizontal wind speed in the Monsoon layer is weak (stable phase). The jet phase starts with the arrival of the Maritime inflow (MI) during which a LLJ wind profile and differential horizontal cold air advection are prominent. Once saturation is reached LLC form either as stratus or stratus fractus at first. The MI is a coastal front stationary during the day due to turbulence which propagate inland after 16 UTC after the mixing of the planetary boundary layer has reduced (Adler *et al*., 2017; Deetz *et al*., 2018). The contribution of each process in the formation of LLC have been documented in Babic *et al.* (2019) by analyzing the complete diurnal cycle of the LLC. The horizontal cold-air advection contributes to 72% in the formation of LLC while radiative cooling and sensible heat flux divergence contribute to 16 and 12% respectively. It is worth noting that climate models struggle to represent the low-level cloudiness (Knippertz *et al*., 2011; Hannak *et al*., 2017) which lead to an overestimation of solar surface irradiance compared to station measurements. Kniffka *et al*. (2019) through sensitivity experiments with ICOsahedral Non-hydrostatic (ICON) model showed that rainfall over West Africa depends logarithmically on the

optical thickness of low clouds, as these control the diurnal evolution of the planetary boundary layer, vertical stability and finally convection.

From all the above-mentioned clouds and aerosols are the most important component controlling the earth energy budget, the hydrological cycle through their radiative effects yet there are a lot of uncertainties to quantify their interactions and its subsequent effects on the state of the atmosphere.

2.3 Impact of Aerosols on Radiation

Aerosol impact on radiation refers to aerosols direct effect (ADE), describing the interactions between aerosol and radiation through scattering and absorption of radiation fluxes. According to the Intergovernmental Panel in Climate Change Assessment report 5 (IPCC, AR5, IPCC, 2013) estimated the global effective radiative forcing by Aerosols Direct effect (ADE) as -0.45 W m^{-2} (-0.95 to +0.05) W m^{-2}.

It is well known that there are three main sources of aerosol in the atmosphere: Desert dust, smoke from biomass burning and anthropogenic air pollution. This section will evaluate the impact of each aerosol type on radiation with respect to their source from global to regional scale through observations and modelling studies.

2.3.1 Dust

Dust aerosol exerts a cooling effect at surface due to extinction of shortwave radiation. Dust radiative impact evaluated using GCMs showed that the cooling effect is larger over the Northern Atmosphere (NH) than in the Southern Atmosphere (SH) (Zhao *et al*., 2015). The authors also highlighted that this leads to reduction in evaporation over low latitudes of NH compared to SH. As a result, precipitation will decrease in arid and semi-arid region in NH due to dust aerosol radiative impact. In another study by Lau *et al*. (2009), it is shown that Saharan dust absorbs solar radiation, warms the layer of the atmosphere, cools the earth surface by reducing incoming radiation received at the

surface. On the other hand, the dust impact on longwave radiation does the opposite. It cools the atmosphere and warms the surface. It increases the static stability of the atmosphere and that inhibits precipitation.

Using satellites observation, the overall aerosol effects (dust, smoke, anthropogenic) is evaluated on shallow clouds development over Atlantic ocean for three months (June–August 2002) by (Kaufman *et al*., 2005). It results from their studies that the radiative aerosol effect at the top of the atmosphere due the aerosol effect shallow clouds is 11 W m^{-2} where 2/3 of it is due to aerosols induced cloud changes and 1/3 is due to aerosol direct radiative forcing. The total aerosol radiative forcing in the North Atlantic is -8 to -14 W m^{-2}. The shallow cloud cover increases systematically by 0.2-0.4 with increasing aerosols column concentration, accompanied by reduction on cloud droplets size by 10-30%. Aerosol induced radiative forcing can cause change in local energy balance and in circulation thus, causing changes in the atmospheric thermal profile (Ramaswamy, 1998). Most of the limitation accounted in modelling the global effect of aerosol is the lack of capability of the GCMs to resolve fine scales dynamical processes of the aerosols due to their coarse resolution. Also, the lack of knowledge on spatial distribution and vertical profile of the aerosol hampers the accuracy to estimate its radiative forcing. Even though GCMs are coupled with aerosol module, the aerosol model is offline treated due to the expensive cost of online treatment, thus a lot of feedback effects are not accounted for.

Regional Climate Models (RCM)s show better agreement with observations as they are able to resolve fine scales processes such as cloud, convection compared to GCMs. A lot of studies have been devoted to study the radiative properties of dust over West Africa. Konare *et al*. (2008) found a dust radiative shortwave forcing of -5 to -10

W m^{-2} using a regional climate model (RegCM) to simulate 38 summer monsoon seasons (1969-2006), and a reduction of precipitation over Sahel region due to dust aerosols. The dust longwave radiative forcing was not accounted in Konare *et al*. (2008). Another study of Raji *et al*. (2017) showed that the dust induced longwave (LW) radiative forcing exerted an atmospheric cooling during December–January–February (DJF) season. The LW radiative forcing of 4.3 W m^{-2} at the Top of the Atmosphere (TOA) is maximum during June–July–August (JJA) season with the core over the source region (Bodélé). Solmon *et al*. (2008) investigating dust radiative forcing (both shortwave and longwave) found two counteractive effects on precipitation: a reduction of monsoon intensity in the lower troposphere due to dust surface cooling and an elevated heat pump in the higher troposphere caused by the dust diabatic warming. The former leads to a reduction of precipitation while the latter an increase in precipitation. According to this study, the overall effect induces a reduction of precipitation mostly over Sahel on average by 8%. N'Datchoh *et al.* (2018) focusing on dust impact on the WAM dynamics demonstrated that dust load into the atmosphere lead to a westward shift with a slight strengthening of AEJ core over tropical Atlantic and weakening of both TEJ and monsoon flux penetration over land which corroborate with previous findings (Konare *et al*., 2008; Camara *et al*., 2010). The effect of dust strongly reduces the temperature especially near surface and humidity at mid-levels (Camara *et al*., 2010). Stanelle *et al*. (2010) investigated the impact of two dust events over West Africa using COSMO-ART. The shortwave radiative forcing of dust at the surface was linearly correlated with the Aerosol Optical Depth (AOD). For an AOD at 450 nm of 1, the average shortwave radiation reduction amounts of -140 W m^{-2} with a decrease of up to 4K in 2-meter temperature was found during noon. Regarding the LW radiative effect of mineral dust, it was nonlinear with an average increase of 70 W m^{-2} for an AOD at

450 nm of 1. Bangert *et al*. (2012) modeling the radiative forcing of dust by using COSMO-ART found up to 80 W m^{-2} reduction of incoming shortwave radiation and surface temperature decrease of -0.2 to -0.5 K. Over Northern Indian, a modelling study of Lau *et al*. (2017) focusing on aerosol-monsoon interaction highlighted that the mineral dust transport and radiative heating-induced dynamical feedback processes have major impacts on the large-scale monsoon circulation. Dust is recognized to reduce precipitation, decrease incoming shortwave radiation and temperature at the surface over the Sahel region of West Africa. It also induced a warming effect of the atmosphere, thus increase the daytime atmospheric stability and reduce it at nighttime (Zhao *et al*., 2011).

2.3.2 Biomass Burning

Biomass burning aerosol is getting much attention as it has detrimental effects on radiation and climate. Biomass burning is a practice widely observed in the tropics because of increasing deforestation practices in Brazil's Amazon basin and land clearing for agricultural activities in South America, Southeast Asia, and Africa (Seiler *et al*., 1980). Previous studies estimated that 114 Tg of smoke from biomass burning is released into throughout the year of which 80% is in the tropics (Penner *et al*., 1992; Hao and Liu, 1994). It is one of the major sources of carbonaceous aerosols mainly Primary Organic Matter (POM) and Black Carbon (BC). Jiang *et al*. (2016) quantified the global mean direct radiative effect of all fire aerosols (POM and BC) to be 0.155 W m^{-2} mainly due to fire BC absorption (0.25 W m^{-2}) while POM induces a small overall effect of (-0.005 to +0.4 W m^{-2}). Strong positive direct radiative effect is found in the Artic and in the oceanic regions west of South Africa and South America as a result of amplified absorption of fire BC. Huang *et al*. (2016) studied the aerosol-radiation interaction on precipitation during the biomass burning season in East China. During

that biomass burning event in June 2012, absorbing aerosols trapped significant part of solar radiation in the atmosphere reducing the surface incoming radiation, followed by low surface sensible and latent heat fluxes. By stabilizing the atmosphere below BC laden plumes, it tends to dissipate daytime cloud and suppress precipitation over Nanjing (China). BC absorption depends on its aging and exerts a strong positive radiative on the atmosphere (Peng *et al.*, 2016). A modelling study of Walter *et al.* (2016) investigated the impact of Canadian forest fires occurred in July 2010 on SW and temperature. Downwelling surface SW was found to reduced up to 50 % below the plume and a decrease of up to 6 K of 2-m temperature. There was a strong change in atmospheric stability within the biomass burning plume.

Pani *et al*. (2016) estimated the direct aerosol radiative effects of biomass burning aerosol over northern Indochina from observed grounds measurements of aerosols optical properties. It was found that the overall mean aerosol radiative forcing was -8 W m^{-2} and -31.4 W m^{-2} at TOA and surface respectively. BC radiative forcing was estimated to +10.7 and -18.1 W m^{-2} at TOA and surface respectively. The radiative forcing from biomass burning in tropical South America is investigated by Liu (2005). The direct radiative forcing of -16.5 W m^{-2} over the smoke area was simulated. Biomass burning aerosol affects significantly the surface radiation flux. A study from Pereira *et al*. (1999) demonstrated that there is a large deviation of observed surface radiation estimates between ground measurements and satellites estimates where the biomass burning occurs. The estimated surface fluxes from satellites is 4 times larger than in the sites located within the biomass burning under clear sky condition and 2 times larger under all sky condition.

Thornhill *et al.* (2018) analyzed 30 years simulations using the Met Office Unified Model to assess the impact of American biomass burning aerosol on the regional

climate. Using a difference of simulation between high case biomass burning emissions minus low case, it is found that the downwelling clear-sky and all sky shortwave radiation at the surface decreased by 13.77 W m^{-2} and 7.37 W m^{-2} respectively. Regarding the upwelling shortwave radiation at the TOA, it increased by 3.32 W m^{-2} in clear sky but decreased by 1.36 W m^{-2} when cloud radiative effect is included. SW heating rates increase in the aerosol layer by 18% in the high emissions case.

Roeckner *et al*. (2006) studied the impact of carbonaceous aerosol emission on the regional climate change. They simulated 2 periods: pre-industrial run (1980–2000) and two twentieth centuries 2001 and 2050. Increase of BC absorption of solar radiation induced surface cooling in region of low latitudes (Brazil tropical Atlantic, northern India, Central and southern Africa). The authors hypothesized that cooling of tropical Atlantic can be related to increase carbonaceous aerosol which have their origin in the biomass burning region on Central Africa.

In Africa, biomass burning occurs in dry season (December–March) over West Africa and during wet season (July–October) over Central and southern Africa each year. Huang *et al*. (2013) investigated the impact of direct radiative forcing of BC on WAM precipitation using global models. The authors found a reduction in precipitation in WAM region due to the radiative effect of BC during dry season. They demonstrated that aerosol from Africa significantly reduce convective precipitation particularly in boreal cold season when biomass burning smoke is prevailing. They have highlighted that biomass burning can affect local weather and climate over West Africa to some extent. Biomass burning in Central and southern Africa contribute to 30 % of global biomass burning aerosol by mass (Van Der Werf *et al*., 2010). Large quantities of these biomass burning plumes are transported over the southeastern Atlantic Ocean by the predominant circulation (Barbosa *et al.*, 1999; Mari *et al*., 2008; Zuidema *et al*., 2016;

Lu *et al*., 2018). In a modelling study by Lu *et al*. (2018), fire events in southern Africa induce changes in shortwave radiative budget and alter longwave radiative energy over southeastern Atlantic Ocean. Likewise, long-range biomass burning aerosol reaches the Gulf of Guinea and SWA coastal cities, it also increases the aerosol concentration over the region (e.g. Mari *et al*., 2008; Menut *et al*., 2018; Deroubaix *et al*., 2018; Brito *et al*., 2018; Flamant *et al*., 2018; Haslett *et al.*, 2019).

However, its implication on WAM dynamics and regional climate impact is not yet investigated.

2.3.3 Local anthropogenic aerosols

Anthropogenic aerosols being one of the major sources of submicron aerosols have increased the aerosol load in the atmosphere from preindustrial time till now.

Anthropogenic aerosol burden since the beginning of the industrialization has possibly induced a reduction in solar irradiation at the surface (the so-called solar dimming) (Feichter *et al*., 2004; Liepert *et al*., 2004). Using GCMs, Quaas *et al*. (2004) quantified the impact of greenhouse gases and aerosol direct effect on radiation. Sulfate aerosol was used as proxy for anthropogenic aerosols and it was found that sulfate aerosol strongly cools the atmosphere through its negative radiative forcing. Wang *et al.* (2014) investigated the impact of fine particle pollution on the meteorology during severe haze episode in January 2013 in China. Using online coupled meteorology chemistry model, it was found that high $PM_{2.5}$ significantly reduce the maximum daily average solar radiation up to 53%, leading to a more stable PBL in Beijing. Another study of the impact of haze event in Nanjing megacity (China) is analyzed using regional climate models WRF-Chem by Li *et al*. (2017). The scattering dominant anthropogenic haze aerosol exerts a negative forcing, followed by a decrease in irradiance and surface temperature by 130 W m^{-2} and 1.1–1.4 ° C respectively.

An evaluation of regional anthropogenic aerosols effects associated with 2000-1950 difference in aerosols emissions using GCMs over Eastern Asia is conducted by Guo *et al*. (2013). The simulation revealed that direct radiative effect of BC is a major contributor to changes in Eastern Asian monsoon system while that of the sulfate does not alter the monsoon system over the region.

RCM model is used to investigate the direct radiative impacts of anthropogenic aerosols on the Indian summer monsoon (Das *et al*., 2016). Simulated surface shortwave radiation of -6 W m^{-2} was found over northeast India followed by a reduction in surface temperature as a result of the dimming effect of anthropogenic aerosols. In a modelling study of Wang *et al*. (2015), the response of anthropogenic aerosol to the state of atmosphere is simulated at a global scale. It is found that -0.23 W m^{-2} cooling at TOA associated with 2010-1970 difference in anthropogenic aerosols emissions. Shortwave radiation reduction of -0.31 W m^{-2} due to aerosol scattering and cloud reflectivity and longwave radiation change of +0.008 W m^{-2} due to increase in high clouds and column water in the troposphere.

In West Africa, the radiative effect of local anthropogenic aerosol only is not yet fully investigated. During AMMA project, Mallet *et al*. (2008) investigated the aerosol radiative forcing over Djougou (northern Benin) during dry season (January–February). A reduction of 61. 5 ± 12.9 W m^{-2} in surface solar radiation, an increase of

43. 1 ± 10.5 W m^{-2} in the atmospheric solar absorption and an increase of

18. 4 ± 3.1 W m^{-2} in the reflected solar radiation at the TOA. Using RegCM, the direct effect of both natural and anthropogenic aerosols over West and Central Africa during WAM is investigated (Salah *et al.*, 2018). Comparing different parametrizations scheme of auto-conversion, the aerosol induced radiative forcing is found to vary between -5 to -25 W m^{-2}.

From all above- mentioned, all the models and observations agree that aerosols exert has a negative radiative forcing except BC and to some extent dust which exert a positive forcing at the TOA. Though aerosol physical, chemical and optical properties are highly variables and source of uncertainties exist in quantifying the aerosol effect on the Earth global budget, the model parametrization of aerosol direct effect has strongly improved compared to aerosol indirect effect (Myhre *et al*., 2013).

2.4 Impact of Aerosols on Clouds

Aerosol impact on cloud refers also to Aerosol Indirect Effect (AIE). In IPCC AR5 the effective radiative forcing from AIE is estimated as –0.45 (–1.2 to 0.0) W m^{-2}. AIE is the most uncertain in term of radiative forcing (IPCC, 2013). There is low scientific confidence associated to the parametrization of AIE in atmospheric models due to their complexity and multiple of counteracting mechanism (Myhre *et al*., 2013). Oversimplification of parameters due to limited computational resources is a problem in simulating AIE because the related effects cover scales from nanometers to kilometers with similar importance to quantify the impacts on the state of atmosphere. Another reason is the variety of cloud types and the complex responses to variation of the aerosols (Bangert, 2012). Difficulties to quantify AIE has hampered the capability of models to quantify aerosols impact on precipitation formation. (Stevens and Feingold (2009) pointed out that the impact of aerosol variation on clouds and precipitations is highly non-linear due to feedback mechanisms with cloud microphysics, cloud dynamics, and the environment of the cloud. As a consequence, an increase in CCN can either increase or decrease precipitation depending on the cloud type and the environment. The poor understanding of AIE according to Fan *et al.* (2016) is related to the insufficient model representation of the updraft intensity and cloud properties, the difficulties to distinguish between actual aerosol impacts and natural variability, clouds

microphysical parametrizations and the subgrid-scale cloud parameterization in GCMs. In a complex climate regime such as WAM, the analysis of AIE must be done for a particular cloud regime with fine scale model (e.g. convection permitting) to be able to address AIE (e.g. Stevens and Feingold, 2009; Fan *et al*. 2016).

This section assesses the first and second AIE. The first AIE, related to warm clouds states that increasing aerosol leads to an increase in cloud albedo with increasing CCN and reduces cloud droplet size with constant liquid water path (Twomey, 1977). The second AIE describes an increase CCN associated with increase cloud lifetime which leads to the suppression of precipitation (Albrecht, 1989).

From global to regional scale, the AIE will be reviewed through modelling studies as well as observations for dust, biomass burning and anthropogenic aerosols.

2.4.1 Impact of Dust Aerosols

On a global scale, dust aerosols are found to decrease precipitation through the reduction of evaporation over low latitudes of northern hemisphere which lead to precipitation decrease in arid and semi-arid region in the northern hemisphere (Zhao *et al.*, 2015). In a modeling study of Lau *et al*. (2009) using GCMs, Saharan dust affects the atmospheric water cycle of West Africa. The overall dust radiative forcing (SW and LW) increase the static stability of the atmosphere and that inhibits moist convection. As warms air lifts, the moist influx air from eastern Atlantic and Gulf of Guinea into the Sahel region is reinforced. It overrides cooler air mass near the surface, that enhance rainfall in the eastern Atlantic ITCZ off the coast of West Africa and shift rainfall more over land in WAM region.

Solomos *et al*. (2011) studied the effect of mineral dust and sea salt particles on clouds and precipitation. Simulated cloud formation is delayed in the polluted case compared

to clean case over the Mediterranean. They found a non-linear precipitation response to aerosol variation and suggested that large uncertainties still exist in modelling AIE.

Regional simulation through WRF-Chem analyzed the mineral dust impact on cloud formation in a Saharan outflow region (Smoydzin *et al*., 2012). The authors found that the temporal and spatial distribution of precipitation is slightly shifted with no impact on the total amount of precipitation. Dust acting as giant CCN on precipitation formation was not significant in the mixed cloud phase based on their simulation.

Dust enhances the formation of ice crystal highlighted by Gu *et al*. (2012). African Dust was found to act as ice nuclei in remote region over Florida through observations (DeMott *et al*., 2003). However, the ability of dust to act as ice nuclei depends on its chemical composition. Therefore, its radiative forcing could be positive or negative depending on its composition (Sokolik and Toon, 1999).

In West Africa particularly during summer monsoon, dust induces a decrease of precipitation over Sahel region as highlighted by previous studies (Konare *et al*., 2008; Camara *et al*., 2010; N'Datchoh *et al*., 2018).

Satellites data analyses suggested that large amount of dust aerosols release from dust events is found to inhibits precipitation (Rosenfeld *et al*., 2002). During a field campaign over the eastern Atlantic, Jenkins *et al*. (2008) demonstrated that Saharan dust lead to invigoration of rain bands associated with tropical cyclogenesis.

2.4.2 Impact of Biomass Burning Aerosols

Biomass burning aerosols appear to significantly affects precipitation and clouds optical and microphysical properties. For instance, carbonaceous aerosols (i.e. BC) from Central Africa biomass burning plumes favor stratiform clouds formation below the BC layer over the tropical Atlantic and amplifies surface cooling (Roeckner *et al.*, 2006).

Considering all biomass burning aerosols, the global mean cloud radiative effect is estimated to -0.70 W m^{-2} from which BC and POM contributes to 41% and 70% respectively (Jiang *et al*., 2016).

At regional scale, WRF-Chem is used to simulate biomass burning event in mid-June over East China (Huang *et al*., 2016). On one hand, black carbon load in the atmosphere tend to dissipate daytime cloud and suppress the convective precipitation over the region. On the other hand, heating aloft increase upper level convective activity and then favored convergence carrying in moist air, thereby enhancing the nocturnal precipitation in the downwind aerosol of biomass burning plumes. Thornhill *et al*. (2018) simulated the impact of South American biomass burning aerosol on the climate for 30 years using that regional climate model. The main findings of their work were that increasing aerosols particularly in dry year reduce precipitation which may trigger drought. The position of the South Atlantic high pressure is modified by increase of biomass burning aerosol and the strength of the southward low-level jet to the east of the Andes is increased.

In West Africa, Huang *et al.* (2013) investigated the implication of BC in the WAM dynamics in boreal cold season when biomass burning smoke is prevailing. The authors found a reduction in cloud amount, cloud top height and surface precipitation due to high BC aerosols load. Their results suggested that BC effect on precipitation is nonlinear and BC radiative forcing is responsible for precipitation decrease over the region.

Lu *et al.* (2018) using a combination of satellites observations and simulations (WRF-Chem) showed that biomass burning from southern Africa can significantly enhance the brightness of stratocumulus over the southeastern Atlantic Ocean. Their results verified the Twomey effect as biomass burning burden result in cloud brightening by reducing

the cloud droplet size. They also modulate the diurnal cycle of cloud water path and cover.

2.4.3 Impact of Local Anthropogenic Aerosols

In contrast to biomass burning and dust aerosols which happened seasonally, anthropogenic air pollution occurs every day throughout the year. Therefore, it affects the local, regional and global climate and weather. A study of Teller and Levin (2006) through numerical experiments using cloud model showed that polluted clouds (with high CCN concentrations) produced less precipitation compared to clean clouds (with low CCN concentrations). The results demonstrated that initiation of precipitation is delayed and lifetimes of the clouds are longer. Adding more ice nuclei (e.g. mineral dust particles) reduce the amount of precipitation on the ground. Polluted clouds are higher in altitude and have a wider spatial cover than the clean clouds. Indirect anthropogenic aerosol effect using a GCM was evaluated by Quaas *et al*. (2004). Decrease of high-level cloud cover through a cooling of atmosphere and increase of low-level cloud cover are simulated as a result of anthropogenic aerosol burden. The lifetime of low-level cloud is quantified to 0.5 min day^{-1} $decade^{-1}$ for the simulated period (1903-1989). From preindustrial to present day a net AIE of -1.67 W m^{-2} with a global mean surface cooling of 1.12 K, precipitation decrease of 3.36% K^{-1} (Chen *et al.*, 2012). Projection till year 2100 of a net AIE is estimated to -0.58 W m^{-2} with a cooling of surface temperature to 0.47 K and precipitation predicted to decrease by 1.7 %. This result showed a potential decrease of AIE in the future and agree with other studies (Unger *et al*., 2009). Aerosol cloud lifetime effect is investigated through GCM simulation of Liquid Water Path (LWP) under increasing CCN (Zhang *et al*., 2015). Focusing on tropical convective clouds, Lee and Feingold (2013) found 9% difference in precipitation between high and

low case aerosols and pointed out that convective mass flux, temporal evolution and frequency distribution of condensed water path are much sensitive to aerosol change.

Statistical analysis of between derived aerosol concentration and clouds droplets from satellites observations (CALIPSO and MODIS) are evaluated for six year (2005-2010) (Costantino and Bréon, 2013). It was found that aerosols increase reduce clouds droplets radius, and increase CCN leading to more water retention through precipitation (drizzle) suppression in marine environment (Albrecht, 1989). Aerosol enhances low-level cloud cover through their analysis.

Regional climate models simulated with COSMO-ART was used to investigate aerosol impact on post-frontal convective cumulus clouds developed after the passage of a cold front over Germany (Rieger *et al.*, 2014). Their study showed a decrease of precipitation with increasing aerosol concentration for an averaged domain covered by convective clouds. They compared a prescribed against a prognostic aerosols distribution and found that simulated aerosol distribution significantly changes the cloud properties.

A study from Lee (2012) investigated the effects of aerosol on clouds and suggested that aerosol induced-changes in the larger-scale circulation. According to this study, aerosol increase invigorates the MCSs in the domain by increasing latent heat from the freezing of cloud liquid, thus updrafts, as a result precipitation is enhanced over the domain.

GCMs is used to simulate the anthropogenic response of Asian summer monsoon by Guo *et al*. (2013). The response is evaluated by comparing simulations driven by aerosol emissions representative of 1950 and 2000. It is found that precipitation decreases significantly of which 80% is attributed to changes in convective precipitation. As shown in Salzmann *et al*. (2014), using the Coupled Model Intercomparison Project Phase 5 (CMIP5), average precipitation decreases in the South and Southeast Asian

region as a result of anthropogenic aerosol increase. Using the CMIP6 scenarios, forcing estimates of anthropogenic aerosol and its associated Twomey effect is evaluated by (Fiedler *et al*., 2019). The radiative forcing of anthropogenic aerosol is estimated from high- and low-end scenarios in the mid-2090s by performing ensembles of simulations. The effective radiative forcing (ERF) associated with change in Twomey effect is to -0.39 W m^{-2} and -0.92 W m^{-2}.

Recently, Deetz *et al*. (2018) showed that increasing aerosols over SWA leads to a reduction of the propagation velocity of a coastal front called Maritime Inflow (MI) and a weakening of the Nocturnal Low-Level Jet (NLLJ) and a delay of 1-2 hours of stratus to cumulus transition during summer monsoon using COSMO-ART.

Overall, aerosol has significant effect both on radiation and clouds. The ADE carried less uncertain compared to AIE because cloud feedback in still not resolved in climate models. Since last decade, emphasis on AIE has been made to quantify aerosol-cloud interaction but the effect is still not very clear. Meanwhile AIE is a critical factor to improve precipitation forecast, which is important in developing countries such as West Africa regions which are rainfed dependent for agricultural purpose.

2.5 Gap identified

From the literature review, five aspect become apparent as far as aerosol, radiation and clouds interactions are concerned:

(i) there are more studies on dust direct effect on West Africa with a focus on Sahel whereas dust indirect effect on the West Africa monsoon system and clouds is missing,

(ii) the impact of local anthropogenic aerosol and remote biomass burning aerosols from Central southern Africa individually on the climate over West

Africa is not yet fully investigated, their radiative effect and their implication on Low Level Clouds occurrence is not yet quantified,

(iii) the process by which long-range transport of biomass burning aerosol get mixed into the boundary layer over the Gulf of Guinea and West African cities is fairly understood,

(iv) aerosol-precipitation interaction through clouds in still uncertain in the climate modelling,

(v) direct effect of local anthropogenic aerosol is not yet investigated over West Africa.

CHAPTER THREE

DATA AND METHODS

3.1 Introduction to COSMO-ART

COSMO-ART stands for Consortium for Small scale Models – Aerosols and Reactive Traces gases (Vogel *et al*., 2009). It is an online coupled regional model allowing to account for interaction between weather, climate and aerosols. This implies that the resolved grids point for both meteorological and atmospheric variables are identical. The provided outputs for both variables are given at the same timestep without any spatial and temporal interpolation. This allows to considered feedback between meteorology, gas phase chemistry and particulate matter.

COSMO-ART has been used over West Africa since 2010 to simulate two dust storms (March 2006 and June 2007) and their atmospheric feedbacks (Stanelle *et al*., 2010). Model results, compared with AMMA observations showed that the model performed well by capturing the location of the dust front in general, only for some few stations, the model simulated the arrival of the front a few hours later compared to the observation. Comparing the observed and modeled radiation fluxes in Niamey, the model performed well when the dust radiation interaction is accounted for. Besides that, A linear relationship between the AOD 450 nm and the surface net shortwave radiation was simulated with a reduction of -140 W m^{-2} and a relative increase of +70 W m^{-2} of longwave radiation during noon. As a result, a near surface temperature decrease of 4 K was seen at noon.

Olaniyan *et al*. (2015) used COSMO to simulate the daily evolution of the West African Monsoon (WAM) and its characteristics for the first half of 2015. Their results revealed that COSMO is able to predict the daily evolution of the WAM daily variability including the onset of raining season and the dry spells. A spatial correlation of 0.64

between the observations and the model forecast highlighting that the model underestimates the rainfall amount over that period.

During the DACCIWA project, COSMO-ART was used for aerosol and gas phase chemistry forecast during the measurement campaign with different spatial resolutions (28 km, 5 km and 2.5 km). The objective was to assess and validate the model with ground based and aircraft observation as well as meteorological field during the whole campaign period (June–July 2016). Good agreement was found regarding the Nocturnal Low-Level Stratus clouds (NLLS) spatial extent, base and top height between COSMO-ART and ground-based observation in Savè and previous studies from Schuster *et al*. (2013) and Deetz (2017). Regarding the spatiotemporal distribution of aerosol and trace gases, COSMO-ART overestimates the AOD compared to MODIS and Copernicus Atmosphere Monitoring Service (CAMS) mainly the anthropogenic AOD. One raison is the uncertainties related to the emissions inventories (Liousse *et al.*, 2014; Keita, 2018) used by COSMO-ART. Whereas, for the mineral dust AOD, the agreement is reached. Deetz (2017) highlighted that the high-resolution model configuration (2.5 km) improve cold bias observed in solar radiation and cloud representation as well as precipitation in the model.

Deetz *et al*. (2018) using COSMO-ART showed a weakening of the West African monsoon flow and nocturnal low-level jet associated with a delay of 1 to 2h in the stratus to cumulus cloud transition due to increasing aerosols. In other studies, by the same authors, aerosol optical depth and size distribution are modified by water uptake due to the high relative humidity of SWA during summer monsoon (Deetz *et al*., 2018). Increasing submicron (coarse mode) aerosol particle by 2 (4) leads to an increase in mean aerosol optical depth from 0.2 to 0.7. The latter finding was from modeling studies with COSMO-ART and was validated by observations during DACCIWA measurement

campaign by Haslett *et al*. (2018). As stated earlier, COSMO-ART is a coupled model. It is based on COSMO (www.cosmo-model.org), a numerical weather prediction, model used by the operational weather forecast of the Deutscher Wetterdienst (DWD). The next section gives a description of the numerical weather prediction model, and its different components including the dynamical core and the physical parametrization.

3.2 COSMO

COSMO is a compressible, non-hydrostatic regional model use for prediction. It is based on primitive thermo-hydrodynamical equations describing in a moist atmosphere, formulated in a rotated geographical coordinate system, and a generalized terrain following height coordinate. This section will detail the dynamical core, the numerics and various physical parametrization, as well as the land surface model used.

3.2.1 Model dynamics and numerics

The basic dynamical equations are prognostic Eulerian equations for the momentum, heat, total mass, mass of water, and the equation of state. COSMO-ART considers different type of hydrometeors as cloud water, water vapor, ice crystals, graupel, hail. The following equations are described in a spherical coordinate:

$$\begin{cases} \dfrac{\partial u}{\partial t} + v.\nabla u - \dfrac{\tan\phi}{r}uv + \dfrac{1}{r}uw = -\dfrac{1}{\rho r\cos\phi}\dfrac{\partial p}{\partial \lambda} + 2\Omega(v\sin\phi - w\cos\phi) + M_u & (3.1) \\ \dfrac{\partial v}{\partial t} + v.\nabla v - \dfrac{\tan\phi}{r}u^2 + \dfrac{1}{r}vw = -\dfrac{1}{\rho r}\dfrac{\partial p}{\partial \phi} - 2\Omega u\sin\phi + M_v & (3.2) \\ \dfrac{\partial w}{\partial t} + v.\nabla w - \dfrac{u^2+v^2}{r} = -\dfrac{1}{\rho}\dfrac{\partial p}{\partial r} - g + 2\Omega u\cos\phi + M_w & (3.3) \\ \dfrac{\partial p}{\partial t} + v.\nabla p = -\dfrac{c_p}{c_v}p\nabla.v + \dfrac{R}{c_v}Q_h + \dfrac{c_p}{c_v}Q_m & (3.4) \\ \dfrac{\partial T}{\partial t} + v.\nabla T = \dfrac{1}{\rho c_v}(-p.\nabla v) + Q_h + Q_m & (3.5) \\ p = \rho R_d(1 + (\dfrac{R_v}{R_d} - 1)q_v - q_c - q_s - q_i - q_g)T & (3.6) \end{cases}$$

From equation (3.1) – (3.6), the following definitions are given: t: time; p: pressure; T: temperature; Ω constant angle velocity of earth rotation; q_i, q_v, q_s, q_g, q_c are respectively

the mass fraction (mixing ratio) of ice, water vapor ,snow, graupel and cloud water; g: acceleration of gravity; r:= radius, λ: azimuthal angle; ρ: total density of air; M_x: turbulence flux of x; ϕ: polar angle; c_p: specific heat at constant pressure; c_v: specific heat of moist air at constant volume; R_d, R_v: gas constants for dry air and water vapor; Q_m: the impact of changes in the concentration of humidity constituents on the pressure tendency; Q_h: the diabatic heat production per unit of volume of air; u, v are the horizontal component of the wind and w: the vertical wind component.

As the equations system are non-linear, finite difference method is applied to solve them. The model variables (e.g. temperature) are horizontally and vertically staggered on an Arakawa-C Lorenz rectangular grid with scalar at the center of the grid box and the normal velocity component defined on the corresponding box faces. The dynamical core used in COSMO is the Runge-Kutta (RK) in addition to the Leapfrog-scheme (Klemp and Wilhelmson, 1978). It is based on the time-splitting approach of Wicker and Skamarock (2002). The dynamical variables (wind, pressure perturbation and temperature) from a base state are split into slow and fast part due to computational cost. Following Wicker and Skamarock (2002), the tendency of the slow processes (buoyancy, Coriolis, horizontal advection) is calculated and added in each sub step of the fast processes (vertical advection, vertical and horizontal sound waves, horizontal gravity waves). For the tracer transport, the finite volume scheme (Bott scheme) is used as it satisfies the mass conservation.

3.2.2 Vertical structure

The vertical structure applied in COSMO is a terrain following coordinate system as in the vertical coordinate with geometrical height, the lowest surface is constant. The terrain-following coordinate is conformed to the orography (e.g. of pressure-based Sigma coordinate for hydrostatic models and the Gal-Chen coordinate (Gal-chen and

Somerville, 1975) for the non-hydrostatic models). In COSMO, the vertical coordinate denoted ξ is prescribed to be independent of time and the surface of constant ξ are fixed in physical space. The different option for the coordinate system is either a base-state pressure-based height coordinate or Gal-Chen height coordinate.

3.2.3 Physical parametrization

Parametrization accounts for the effects of subgrid/subscale processes (radiation, cloud physics, turbulence, convection) on the resolved variables.

3.2.3.1 Radiation

Radiation is a molecular process which are not resolved explicitly by the models due to spatial and temporal resolution. Radiation is a key component for numerical weather prediction (NWP) because it determines the energy budget of the Earth as the ultimate source of energy of the Earth atmosphere system. To capture the radiative processes in NWP, a radiative transfer equation (RTE) is developed under the assumption of a plane parallel and horizontally homogeneous atmosphere and follow the radiation scheme of Ritter and Geleyn (1992). With regard to directional distribution of radiances, it assumes only upward and downward fluxes knows as the two-stream methods, reducing it to only one dimension. The two-stream method for the RTE is solved in 3 spectral intervals in the solar band and 5 in the thermal band, expanding from 0.25 to 104.5 μm considering the diffuse upward and downwards fluxes and the direct solar flux. The table below shows the spectral interval used for the radiative transfer scheme. Within each layer, the effect of the following optical constituent on the radiation transfer through that layer is considered: cloud water droplets, cloud ice crystals, water vapor, ozone, carbon dioxide and other minor trace gases (O_2, CH_4) and aerosols (dust, sea salt, soot).

Table 3.1: Spectral intervals employed in the radiative transfer scheme of COSMO (after Ritter and Geleyn (1992))

Interval limit	Spectral range	Optically actives constituents
0.25-0.70	Solar	O_3, O_2, H_2O, clouds & aerosols
0.7-1.53	Solar	H_2O, CO_2, O_2, clouds & aerosols
1.53-4.64	Solar	H_2O, CO_2, CH_4, N_2O, clouds & aerosols
4.64-8.33	Thermal	H_2O, CO_2, CH_4, N_2O, clouds & aerosols
8.33-9.01 & 10.31-12.5	Thermal	H_2O, CO_2, N_2O, clouds & aerosols
9.01-10.31	Thermal	O_3, CO_2, N_2O, H_2O, clouds & aerosols
12.50-20.00	Thermal	CO_2, N_2O, H_2O, clouds & aerosols
20.00-104.5	Thermal	H_2O, clouds & aerosols

3.2.3.2 Turbulence

It is a small-scale process by which heat and momentum are transfer from the Earth's surface to the free atmosphere. Thus, it is a crucial process for NWP. The subgrid scale turbulent diffusion is parametrized based on a K-theory which relates the subgrid scale flux F_ψ to the gradient of a scalar quantity ψ and the diffusion coefficient K for the transport in this following equation:

$$F_\psi = -K_\psi . \nabla \psi \tag{3.7}$$

Where K_ψ is the is the diffusion coefficient and $-\nabla_\psi$ is the thermodynamic forcing function for the flux. In COSMO model, the vertical turbulent transport scheme is based on the second order closure at hierarchy level 2.5 following Mellor and Yamada (1974). It contains a prognostic turbulent kinetic energy (TKE) equation. It includes a moist turbulence scheme which is a subgrid scale saturation adjustment using conserved variables with respect to condensation/evaporation. The method applied is a generalized boundary layer approximation mainly a single column scheme but it is extendable to horizontal shear contributions. It is a separated turbulence scheme which interact with other subgrid scale circulation. It represents the core of the surface to atmosphere transfer scheme. The main assumption behind its parametrization is that turbulence is isotropic, normally distributed and only one characteristic length scale at each grid point, forced by shear and buoyancy.

3.2.3.3 Convection

It is a subgrid scale phenomenon that determines the vertical structure of the temperature and the moisture field of the atmosphere. It can be explicitly resolved otherwise it need to be parametrized. In COSMO, theses convection types are considered: deep, shallow and mid-level convection. The convection scheme applied is the Tiedtke mass-flux scheme according to Tiedtke (1989) which uses a mass-flux approach to represent moist

convection in numerical models. More detailed on the scheme can be found in Tiedtke (1989). It consists of a set of differential equations for convective updraughts and downdraughts. Turbulent entrainment and detrainment are different depending on the type of convection. Updraught mass flux at the cloud base is linked to the sub-cloud layer moisture convergence (divergence of the subgrid scale and resolved scale moisture fluxes integrated from the surface to cloud base). Downdraught mass flux at the level of free sinking (where the downdraught originates) is proportional at the cloud base. Evaporation of convective precipitation in the sub-cloud layer is considered. Shallow non-precipitation convection is treated based on a simplified Tiedkte (1989) scheme which incorporates some assumptions (e.g. on the convection vertical extent). Particularly for our study, the simulation was done at high resolution with convection explicitly resolved by the COSMO-ART.

3.2.3.4 Land surface model (TERRA)

It provides the temperature and specific humidity at the ground, thus considers the surface energy budget which determined the Planetary Boundary Layer (PBL) development. For the ground temperature, it uses an optimized two-layer model for its calculation through the equation of heat conduction according to Jacobsen and Heise (1982). Whereas the soil water content is predicted for two, three or more layers. Soil parameters (heat capacity, water storage capacity) from TERRA strongly depend on the soil texture separated into five classes: sandy, sandy loam, loamy clay and clay. The important parameters are soil moisture and type, vegetation, surface roughness and land-use class, snow coverage. The soil model TERRA is split into two parts: the first part deal with a one-layer vegetation for the evapotranspiration after (Dickinson, 1984) and the second with heat and water transfer in the soil and predict the soil temperature and water content. A more detailed parametrization of source and sink term for soil moisture

and temperature is described in Majewski and Schrodin (1994). Urban areas are considered modified surface roughness, leaf area index, plant coverage.

For the ocean we used a prescribed surface temperature. For the fresh water lakes, a lake model named Flake (Mironov *et al*., 2010) is applied using a parametrized scheme. It predicts the vertical temperature structure and mixing conditions in lakes of various depths on the time scales expanding from a few hours to many years.

3.2.3.5 Cloud microphysics

Cloud microphysics are central for atmospheric models as they determine the accuracy for precipitation forecast. Also, they represent the major sources of uncertainties in climate modeling regarding the aerosol-cloud radiation (Penner *et al*., 2011; Rosenfeld *et al*., 2019). There are grid scales clouds and subgrid scales cloudiness. When deep convection is resolved, the parametrization is not needed. Updrafts and downdrafts are resolved and formation of precipitation is simulated by clouds microphysics. The cloud formation is determined by the equilibrium between the water vapor and liquid. The mechanisms by which air cooled are: radiative effect, mixing and uplift. At a constant pressure, radiative cooling occurs when air radiates energy it cools down but the amount of water vapor remains unchanged. Thus, the temperature drops vapor pressure drops and become saturated, then cloud forms (e.g. fog). For the cloud formation through mixing, it happens when two air parcels, a nearly warmer moist air and a cooler dry air in its surrounding environment. As the warm air mixes with the drier air, the parcel grows and the average temperature and water vapor pressure of the mixed parcel decreases and get close to the environmental values, as it continues, it becomes saturated and a mixing cloud form. In contrast to the former two mechanisms, the uplift happens at constant energy (adiabatic). It is an adiabatic ascent driven by convection when less dense air mass override more dense air, it cools and becomes saturated, thus clouds are

formed (e.g. air flowing over a mountain). The cloud formation usually happens under heterogenous nucleation (e.g. water condenses onto existing aerosols particles called cloud condensation nuclei (CCN)). The supersaturation equilibrium between a water vapor and an aqueous solution droplet is described by the Köhler theory (Köhler, 1936) which is the combination of two effects: The Kelvin and the Raoult effect. The Kelvin effect refers to the high-water vaper pressure over a curved surface compared to flat surface whereas the Raoult effect states that a solution droplet reduces the water vapor pressure compare to a pure water droplet. The Köhler equation is described as followed:

$$s_{seq} = \frac{A}{D_D} - \frac{B}{D_D^3}; \tag{3.8}$$

$$A = \frac{4\varsigma M_w}{RT\rho_w} \tag{3.9}$$

$$B = \frac{\upsilon_s M_w \rho_s D_P^3}{M_s \rho_w} \tag{3.10}$$

Where D_D : Droplet diameter; D_P: Aerosol diameter; ς: surface tension of water; M_w/M_s: Molecular mass water/ aerosol; R: Universal gas constant; T: Temperature; υ_s : Specific volume of aerosol particles; ρ_s/ρ_w: Density of aerosol particle/ water

In the equation (3.8), the A/D_D is the Kelvin effect and B/D^3_D is the Raoult term. The following figure illustrates the Köhler curve for a ammonium sulfate aerosol for different particle diameters (Figure 3.1). The particle diameter decreases with increasing curvature thus, increasing water vapor pressure (Kelvin effect) and the small the droplet, the higher the concentration of the solute, thus less water vapor pressure (Raoult effect). Increasing droplet diameter leads to a decrease of both curvature and mass concentration thus, the curve converges toward s_{seq}=0.

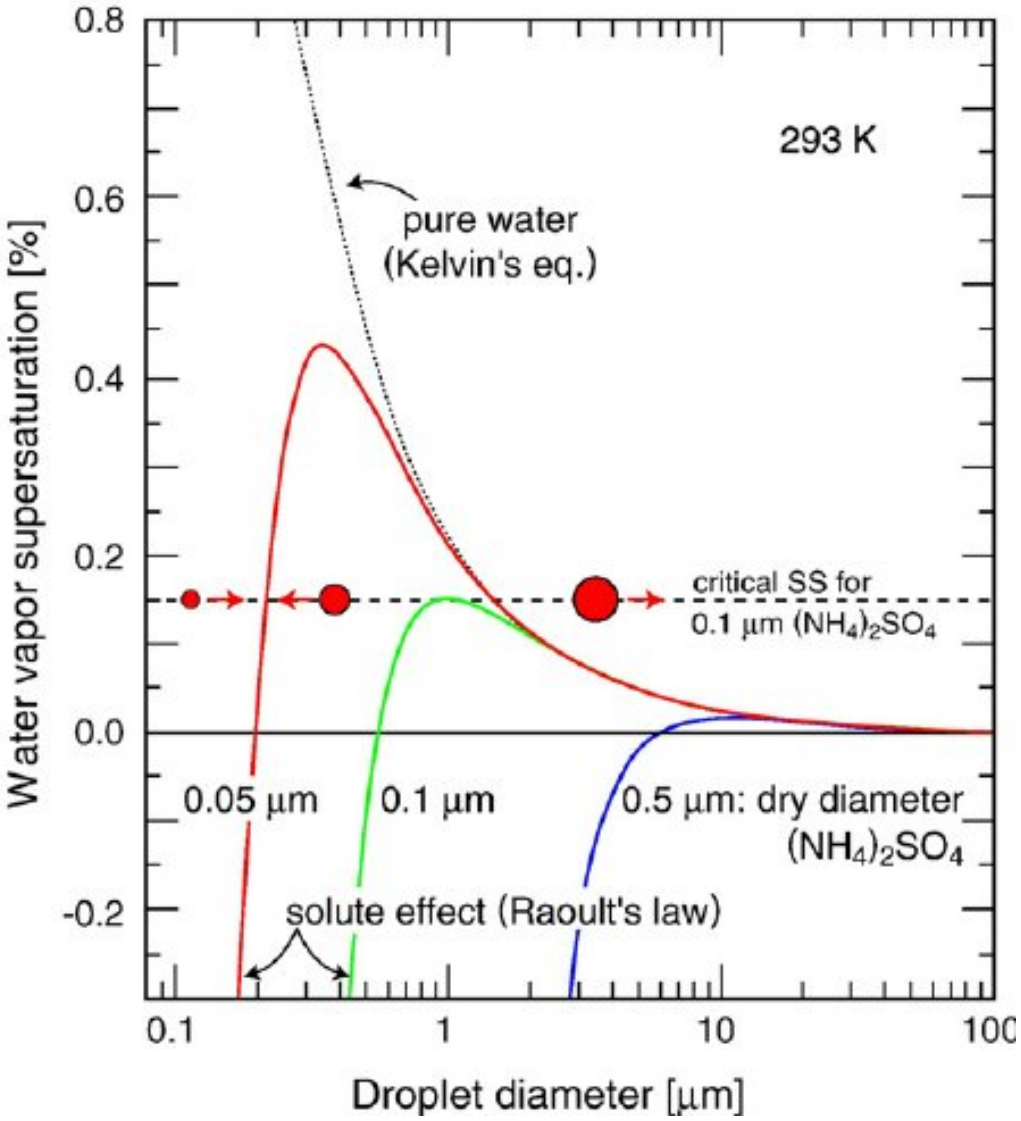

Figure 3.1: Köhler curves showing the equilibrium water vapor supersaturation at 293 K for droplets of pure water (dotted curve) and for droplets containing various masses of dissolved (NH4)2SO4 (solid curves) vs. diameter of the droplet with dry diameter of 0.005 µm (solid red), 0.1 µm (solid green) and 0.5 µm (solid blue) (Andreae and Rosenfeld, 2008).

The critical supersaturation is reached at a point where the derivative of (3.8) is equaled to zero. The point corresponds to a critical diameter.

$$\frac{ds_{seq}}{d_{D_D}} = 0 \qquad \rightarrow \qquad D_c = (\frac{3B}{A})^{1/2} \qquad s_c = (\frac{4A^3}{27B})^{1/2} \tag{3.11}$$

As soon as the droplet diameter exceeds D_c, the activation of CCN into clouds droplets occurs by depositional growth and collision, cloud droplets size become large enough and form raindrops. The activation parametrization is after Abdul-Razzak and Ghan (2000). In COSMO-ART, to account for aerosol size distribution and chemical composition in the activation process, a parametrization after Fountoukis and Nenes (2005) is applied assuming an ideal solution of aerosols particles. The basic assumptions behind the cloud microphysical parametrizations is the simplification of the type of hydrometeors, only few are considered: cloud droplets. Raindrops, cloud ice, snow and graupel. It is assumed that thermodynamic equilibrium between cloud droplets and water vapor. This implies that the condensation/evaporation of cloud droplets can be treated diagnostically by a saturation adjustment scheme. To avoid an underestimation of updraft velocity, thus CDNC, Bangert (2012), introduced the consideration of subgrid scale updrafts at the cloud base which is added to the simulated grid-scale updraft velocity (w). w is computed after Seinfeld and Pandis (2008). Particle activation occurs either in case of newly formed clouds or by vertical transport into the cloud base (Bangert, 2012). In case of new clouds, the CCN parametrization used directly the number of activated aerosols for this time step or in case of an existing cloud, the advection and turbulent diffusion into the cloud are considered. A bulk microphysics scheme after Seifert and Beheng (2006) is used which is derived from a spectral model by integration named Two Moment Microphysics Scheme (TMMS). TMMS includes prognostics mass mixing ratio and number concentration of cloud water, rain water,

cloud ice, graupel and snow. The autoconversion, accretion and self-collection are parametrized after Seifert and Beheng (2001). The budget equation for the mixing ratio of cloud water (x_c) and the number concentration of cloud droplets (N_c) are given as follows:

$$\frac{\partial}{\partial t} x_c = ADV_m + DIFF_m + COND_m - AU_m - ACC_m + MELT_m + ICEP_m \quad (3.12)$$

$$\frac{\partial}{\partial t} N_c = ADV_N + DIFF_N + ACT - AU_N - ACC_N - SC_N + MELT_N + \frac{\rho_h}{m_c} ICEP_m \quad (3.13)$$

Where ADV_m and ADV_N are the tendencies due to advection; $DIFF_m$ and $DIFF_N$ are the tendencies due to diffusion, $COND_m$ is the tendency due to condensation of water waper, AU_m and AU_N, ACC_m and ACC_N and SC_N are the tendencies due to autoconversion, accretion and selfcollection, $\overline{m}_c = x_c N_c^{-1} \rho_h$ is the mean droplet mass and ρ_h is the density of humid air. $MELT_m$ and $MELT_N$ are the tendencies due to melting of cloud ice. In our study, only warm clouds phase is considered.

3.3 ART

ART is designed to focus on the impact of aerosol on radiation and clouds. ART is a combination of three models comprising:

- chemistry model transport called Regional Acid Deposition Model Version Karlsruhe (RADMKA) model describing the mathematical treatment of chemical reaction involved,
- Photolysis Model (PAPA) computing the photolysis frequencies based on the available energy using the General Radiative Algorithm Adapted to Linear-type Solutions (GRAALS) radiation scheme (Ritter and Geleyn, 1992).

- The Aerosol dynamical model Modal Aerosol Dynamics Model for Europe extended by Soot (MADEsoot) which explicitly resolved the aerosol dynamical processes by a lognormal approximation of the number density of a given aerosols population.

3.3.1 Regional Acid Deposition Model Version Karlsruhe Model

It based on Regional Acid Deposition Model Version 2 (RADM2) mechanism (Stockwell *et al*., 1990). It comprises 56 transported species, 23 radicals, 172 reactions. The inorganic substances (17 stables species and 4 radicals) are treated explicitly whereas the organic compounds (26 stables species and 16 radicals) are combined based on their molecular structure and treated in a condensed form (Athanasopoulou *et al*., 2013). The following compounds N_2, O_2 and CH_4 are kept constant but are involved in the chemical reaction. The mathematical description of the chemical reaction is given as follows:

$$\frac{\partial \overline{c_i}}{\partial t} = \sum_{j=1}^{J} \nu_{ij} k_j \prod_{m=1}^{I} (\overline{c_m})^{r_{jm}} - \sum_{j=1}^{J} \mu_{ij} k_j \prod_{i \neq m=1}^{I} (\overline{c_m})^{s_{jm}} (\overline{c_i})^{s_{ji}} \tag{3.14}$$

Here, c_i is the concentration of a substance i, j is the number of reactions,

i the number of substances, ν_{ij} and μ_{ij} the stochiometrical coefficient of the i-th substance in the j-th reaction, k_i is the reaction of the j-th reaction and r_{jm} and s_{jm} the reaction order of the m substance in the j-th reaction. An example for the equation ozone:

$$\begin{aligned} \frac{\partial [O_3]}{\partial t} = {} & j_1[NO_2] + j_8[NO_3] - k_2[O^3P][NO_2] \\ & - k_5[O^1D][H_2O] - k_6[O_3][NO] - k_7[O_3][HO] \\ & - k_8[O_3][HO_2] - k_{17}[O_3][NO_2] - k_{84}[OL_2][O_3] \\ & - k_{85}[OLT][O_3] - k_{86}[OLI][O_3] - k_{87}[ISO][O_3] \end{aligned} \tag{3.15}$$

The non-linearity of the equation leads to the use of numerical solution method for linearization. The numerical solution is given as follows:

$$\frac{\partial \overline{c_i}}{\partial t} = P_i - L_i + Q_i \tag{3.16}$$

Here P_i and L_i are the production and loss term and Q_i the exchange rate.

3.3.2 Photolysis PAPA model

The photolysis is the absorption of a photon (hν) by a molecule A to get to an exited state A^*. The photolysis frequency $J_i(\tau)$ is the integral of the product of spectral absorption cross section $\sigma(\lambda)$, spectral absorption cross section , $\phi(\lambda)$, spectral quantum yield and $I_A(\tau, \lambda)$, actinic flux over all wavelengths.

$$J_i(\tau) = \int_{\lambda_a}^{\lambda_b} I_A(\tau,\lambda).\sigma_i(\lambda).\phi_i(\lambda)\, d\lambda \tag{3.17}$$

τ is the optical thickness;

$$\tau(Z) = \int_0^z b_a(Z') + b_s(Z')\, dZ' \tag{3.18}$$

b_a: absorption coefficient, b_s: extinction coefficient

the actinic flux $I_A(\tau, \lambda)$, is the integral of radiation density over the complete solid angle. The equation describing the actinic flux is given as follows:

$$I_A(\tau,\lambda) = \int L(\tau,\Omega,\lambda)\, d\Omega = \int_0^{2\pi}\int_{-1}^{1} L(\tau,\varphi,\mu,\lambda)\, d\mu\, d\varphi \tag{3.19}$$

The unit is expressed in W/m^2 or $N_Q/(s\ m^2)$, N_Q= number of light quanta

τ=optical thickness, λ=wavelength, Ω=solid angle, φ= azimuth angle, μ=cos Θ, Θ=zenith angle.

3.3.3 MADEsoot

With a focus on tropospheric aerosol, the aerosol dynamical MADEsoot module

(Vogel *et al*., 2006) comprises 7 types of aerosols: dust, sea salt, primary and secondary aerosols, Black Carbon (BC), sulfate, nitrate, ammonium and water. They are separated into soluble particles (sulfate, ammonium, primary and secondary organic matter, sea salt, and water), mixed insoluble and soluble with coated BC particles and insoluble (dust and BC). A modal approach is used for the treatment of aerosols comprising 12 modes. Table 3.2 summarizes the different modes, chemical composition, mixing state, the initial mean diameter and standard deviation.

The aerosol population is represented by a number of particles per cubic meter (m^3) air in the size between dp and dp+ddp n(dp)ddp.

The total number (N_P), surface (S_P) and volume (V_P) density are given respectively as follows under the assumption of spherical aerosol particles:

$$N_P = \int_0^\infty n(dp)ddp \tag{3.20}$$

$$S_P = \int_0^\infty n_s(dp)\,ddp = \int_0^\infty \pi d_P^2 n(dp)\,ddp \tag{3.21}$$

$$V_P = \int_0^\infty n_V(dp)\,ddp = \int_0^\infty \frac{\pi}{6} d_P^3 n(dp)\,ddp \tag{3.22}$$

Table 3.2: Mixing state initial diameter for mass/number concentration and standard deviation of the individual mode of aerosol particles.

Mode	**Chemical composition and mixing state**	**Initial diameter (μm) Mass/number**	**Standard deviation**
If	SO_4^{2-}, NO_3^-, NH_4^+, H_2O, SOA (internally mixed)	0.03/0.01	1.7
Ic	SO_4^{2-}, NO_3^-, NH_4^+, H_2O, SOA (internally mixed)	0.3/0.07	1.7
Jf	SO_4^{2-}, NO_3^-, NH_4^+, H_2O, SOA (internally mixed)	0.03/0.08	2.0
Jc	SO_4^{2-}, NO_3^-, NH_4^+, H_2O, SOA (internally mixed)	0.3/0.08	2.0
S	Soot	0.17/0.08	1.4
C	Direct PM_{10} emissions	6/1	2.5
Cseasa	Sea salt mode A	0.69/0.2	1.9
Cseasb	Sea salt mode B	0.85/2	2.0
Cseasc	Sea salt mode C	27.93/12	1.7
Csoila	Dust mode A	1.5/0.64	1.7
Csoilb	Dust mode B	6.7/3.5	1.6
Csoilc	Dust mode C	14.2/8.7	1.5

In COSMO-ART, the number density of the aerosols is approximated through a log-normal distribution following Whitby (1978) defined as:

$$n_l(\ln dp) = \frac{N_{Pl}}{\sqrt{2\pi}\ln\sigma_{g,l}} \exp(-\frac{(\ln dp - \ln d_{g.l})^2}{2\ln^2\sigma_{g,l}}) \tag{3.23}$$

Where l is the mode of the aerosol particle, N_{Pl} is the number density of the mode l, $d_{g,l}$ is the median diameter and $\sigma_{g,l}$ is the geometric standard deviation. It is defined as follows:

$$\ln\sigma_{g,l} = (\frac{1}{N_{Pl}}\int_0^\infty n_l(dp)(\ln dp - \ln d_{g,l})^2\, ddp)^{\frac{1}{2}} \tag{3.24}$$

The standard deviation is kept constant while the mean diameter varies based on the chemical processes involved.

Thus, the three equations needed for the atmospheric models is the time variation of the mean diameter, the number density and the geometric standard deviation.

Generally, the moment of distribution is expressed by:

$$M_k = \int_0^\infty d_P^k n(dp) ddp \tag{3.25}$$

By deduction, the total number (N_P), surface (S_P) and volume (V_P) density correspond to the zero, the second, and the third moment of distributions as defined:

$$N_P = \int_0^\infty n(dp) ddp = M_0 \tag{3.26}$$

$$S_P = \int_0^\infty n_s(dp)\, ddp = \int_0^\infty \pi d_P^2 n(dp)\, ddp = \pi M_2 \tag{3.27}$$

$$V_P = \int_0^\infty n_V(dp)\, ddp = \int_0^\infty \frac{\pi}{6} d_P^3 n(dp)\, ddp = \frac{\pi}{6} M_3 \tag{3.28}$$

From equation (3.12) M_k becomes:

$$M_k = \int_0^\infty d_P^k n(dp) ddp = N_{Pl} d_{g,l}^k \exp(\frac{k^2}{2} \ln^2 \sigma_{g,l}) \quad (3.29)$$

The time variation of the mean diameter ($\partial d_g/\partial t$), the number density ($\partial N/\partial t$), and the geometrical standard deviation ($\partial \sigma_{g,l}/\partial t$) are resolved and expressed as follows:

$$N_{Pl} = M_{0,l}$$

$$\ln^2 \sigma_{g,l} = \frac{1}{3} \ln(\frac{M_{0,l} M_{3,l}^2}{M_{2,l}^3}) \quad (3.30)$$

$$d_{g,l} = M_{0,l}^{-5/6} M_{2,l}^{-3/2} M_{3,l}^{-3} \quad (3.31)$$

It is worth noting that in COSMO-ART only two moments are considered. The 0th moment corresponding to the number density and the 3rd moment corresponding to the mass density.

For each mode defined is Table 3.2, prognostic equation for mass and number density are solved.

For consistency with the treatment of temperature and humidity within COSMO-ART, the number and mass density are normalized with the total number density of air molecules N and with the total mass concentration of humid air ρ, (Vogel *et al.*, 2009) respectively:

$$\psi_{0,l} = \frac{M_{0,l}}{N} \quad (3.32)$$

and

$$\psi_{n,l} = \frac{m_{n,l}}{\rho} \quad (3.33)$$

$m_{n,l}$ represents the mass concentration of the chemical compound n of the aerosol.

For example, the prognostic equation solved for the normalized number density of mode if is given as follows:

$$\frac{\partial \hat{\psi}_{0,if}}{\partial t} = \underbrace{-\hat{v}.\nabla \hat{\psi}_{0,if}}_{1} \underbrace{-\bar{v}_{sed,0,if} \frac{\partial \hat{\psi}_{0,if}}{\partial z}}_{2} + \underbrace{\frac{1}{\rho} \nabla.F^{\hat{\psi}_{0,if}}}_{3} \quad (3.34)$$
$$\underbrace{-\overline{W}_{0.if}}_{4} \underbrace{-\overline{C}_{a0,if,if}}_{5} \underbrace{-\overline{C}_{a0,if,jf}}_{6} \underbrace{-\overline{C}_{a0,if,ic}}_{7} \underbrace{-\overline{C}_{a0,if,jc}}_{8}$$
$$\underbrace{-\overline{C}_{a0,ifs}}_{9} \underbrace{+\overline{N}_{u0}}_{10}$$

The first term of equation (3.34) refers to the advection component, $\hat{v}$ being the mean wind speed vector. The second term is the sedimentation with $\bar{v}_{sed,0,if}$ the sedimentation velocity of the zeroth moment of the mode l. (3) describes the turbulent diffusion with $\nabla.F^{\hat{\psi}^{0,if}}$ the turbulent flux for zeroth moment of the mode l. (4) is the wet deposition $-\overline{W}_{0,if}$ (loss of particles by precipitation scavenging). (5-9) $-\bar{C}_{a0,f1,f2}$ refers to changes of the zeroth moment due to coagulation respectively between if and if, ic, jf, jc and s term, (10) is the nucleation.

The full set of equation of all the five modes is given in Vogel *et al*. (2009). As the following substances SO_4^{-2}, NO_3^-, NH_4^+ and water are in thermodynamic equilibrium, only the mass density of SO_4^{-2} is numerical solved and the rest are derived from the equilibrium theory of (Fountoukis and Nenes, 2005). The relevant process modifying the aerosols distribution which are nucleation, coagulation, condensation, sedimentation, deposition (dry and wet), atmospheric transport and emissions are detailed in the next section.

3.3.3.1 Nucleation

It refers to gas-to particles conversion. It is the process of secondary aerosol formation and it is calculated through the Volatility basic set (VBS) scheme developed by Athanasopoulou *et al*. (2013). It incorporates 9 secondary organic aerosol precursors: higher alkanes, terminal and internal alkenes, toluene, xylenes, cresol for anthropogenic,

a-pinene, limonene and isoprene for biogenic. The above-mentioned species are oxidized by the hydroxyl radical (OH), ozone and nitrate radical (NO_3) through reactions forming semi-volatile product grouped by their effective saturation concentration C^* into four species with the C^* of 1, 10, 100 and 1000 $\mu g/m^3$ at 298 K. Further detailed are described in Athanasopoulou *et al*. (2013). Regarding the inorganic particles within COSMO-ART, they are in the if and ic mode through binary homogenous nucleation of sulfuric acid (H_2SO_4) and water.

3.3.3.2 Coagulation

Coagulation refers to the collision of aerosols particles with submicron size with others. In COSMO-ART, Brownian motion is the only form of coagulation accounted for. There are two situations when coagulation happens: (1) particles formed in intramodal coagulation stay in their origin mode, (2) particles formed in intermodal coagulation end up having the mode with the larger median diameter. The intermodal coagulation changes only the number density not the mass density.

3.3.3.3 Condensation

Condensation refers to change of water from vapor into liquid water, occurring in the atmosphere when warm air rises, cools and reaches a saturation equilibrium. In COSMO-ART, all submicron are subjected to condensation and only the mass density is altered not the number density. The particle growth condensation rate follows the that of (Whitby and McMurry, 1997).

3.3.3.4 Sedimentation and deposition

There are ways by which aerosols are removed from the atmosphere. Sedimentation and dry deposition are parametrized in COSMO-ART following respectively Binkowski and Shankar (1995) and (Ackerman *et al*., 2008). All the submicron and coarse particles are

do sediment at different sedimentation rate. Regarding the wet deposition through cloud and precipitation, it is parametrized according to Rinke (2008).

The following figure summarizes the aerosol particles growth processes.

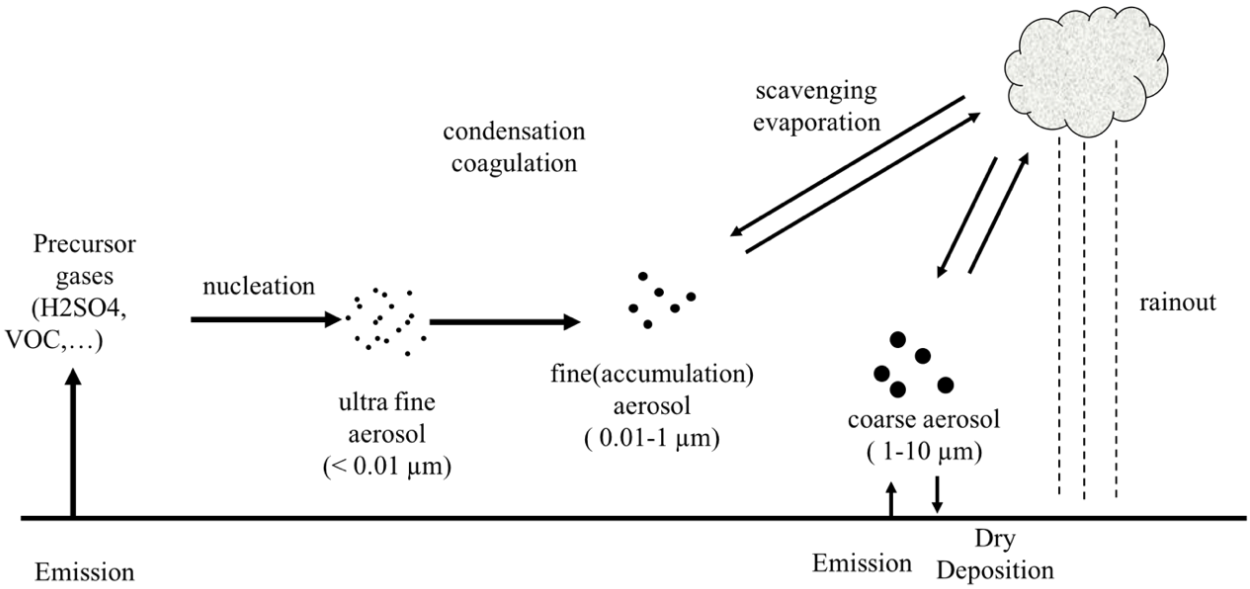

Figure 3.2: Schematic of aerosols and its dynamical processes in the atmosphere.

3.3.4 Emissions

Southern West Africa is influenced by a mixture of different sources of aerosols, therefore different types of emissions are considered.

3.3.4.1 Mineral Dust emissions

Mineral dust consists of oxides and carbonates resulting from agricultural soil and quartz sand. There are mainly from northern Africa including Bodélé depression, the Nubian desert, the Lybian desert and partly the Sahelian region (Mali, Mauritania, Niger). These sources produce roughly some thousands of Megatons of dust yearly (Ginoux *et al*., 2004; Tanaka and Chiba, 2006). The seasonal variation of long-range transport of dust over West Africa has been well documented (Kaufman *et al*., 2005; Ogunjobi *et al*., 2007; Knippertz and Todd, 2012; Ogunjobi *et al*., 2012) . Dust emissions mechanism is described by three processes according to Shao *et al.* (2011): aerodynamic lift, saltation bombardment and disaggregation. More details on the dust scheme realization can be found in Shao (2004); Shao *et al*. (2011). Dust parametrization (dust scheme) used in COSMO-ART is after Vogel *et al*. (2006) which have been improved in several ways by Rieger *et al*. (2017). The basic inputs for the dust scheme are the friction velocity, the soil moisture, vegetation cover, land use data, soil types from Harmonized World Soil Database (HWSD, 2012) and particles size distribution from Shao *et al*. (2011). The output being dust emission ($\mu g\ m^{-2}\ s^{-1}$) in a form of lognormal distribution for different mode (see table 3.2) and the threshold friction velocity. In COSMO-ART, Deetz (2017) set the tuning c_{white} of dust to 0.75 for simulation realization over West Africa based on AOD comparison between COSMO-ART and MODIS observation over the Saharan area. c_{white} is a tuning factor used to compute the saltation flux after Whitby (1978). More details on the parametrization can be found in Deetz (2017).

3.3.4.2 Sea salt emissions and Dimethyl sulfide (DMS)

Sea salt is mainly composed of chloride (55%) and sodium (30.6%) followed by sulfate (7.7%) and some magnesium, calcium, potassium and some organic and iodine traces (Seinfeld *et al*., 1998). The annual global emissions of sea salt is estimated to 8.91 10^{15} g yr^{-1} between validity size range of (0.1–10) μm in dry diameter according (Grythe *et al*., 2014). In COSMO-ART, sea salt is emitted in different sizes: as film droplets (0.02–1 μm); jet droplets (1–9 μm), spume droplets (9–28 μm) parametrized respectively by Mårtensson *et al*. (2003); Monahan *et al*. (1986) and Smith *et al*. (1993). 10 m horizontal wind speed is used for the parametrization of the three modes and only NaCl, Na_2SO_4, and H_2SO_4 were considered for sea salt species. Their mean (for mass and number) diameter and standard deviation are indicated in Table 3.2. Sea salt is assumed to be emitted as dry matter. The impact of salinity in the emission is not considered and the sea surface temperature effect is accounted only on the film droplet mode.

DMS ($(CH_3)_2S$) is emitted by phytoplankton or bacterial transformation of dimethyl sulfoxide (DMSO). The DMS emissions datasets are prescribed from monthly climatology of DMS fluxes after Lana *et al.* (2011) and it is assumed that DMS emissions depend only on 10 m horizontal wind speed.

3.3.4.3 Biogenic emissions

Biogenic aerosol sources are from vegetation, produced by photosynthesis. The total Biogenic Volatile Organic (BVOC) emissions are estimated to 1000 Tg yr^{-1} according to Guenther *et al*. (2012). BVOC is a precursor of ozone expressed in the following reaction:

$$VOC + NO_x + hv \longrightarrow O_3 + \text{products} \quad (3.35)$$

The BVOC parametrization is realized in COSMO-ART after Guenther *et al*. (2012) which depends on the temperature, radiation, leaf age, Leaf Area Index (LAI) and Plant

Functional Types (PFT)s obtained from (Community Climate System Model (CCSM), 2015) at a grid size of 0.05º. Five PFTs are considered in West Africa region: broadleaf evergreen tropical tree, broadleaf deciduous tropical tree, cool grass, warm grass and crop. Only Isoprene, alpha-Pinene and Limonene are considered in COSMO-ART. Isoprene emission depends on both temperature and radiation whereas the monoterpenes (alpha-Pinene, Limonene) emissions depend only on temperature. A LAI (LAI fraction that is lit by sun) reduction is applied via Dai *et al*. (2004) to avoid an overestimation of BVOC emissions from tropical evergreen forests. The emission rate of BVOC species at each grid point is calculated as follows:

$$E_i = \sum_j \varepsilon_{ij} \cdot \chi_j \qquad (\mu g\ m^{-2}\ h^{-1}) \tag{3.36}$$

Where $\varepsilon_{ij}$is the emission factor at standard condition for vegetation type j; χ_j is the emission activity factor accounting for processes controlling emission responses (temperature, radiation, leaf age). The emissions factors for COSMO-ART BVOC's computed for West Africa after Guenther *et al*. (2012) are detailed in Deetz (2017).

3.3.4.4 Biomass burning emissions

Biomass burning (BB) is one of the major sources of aerosols in Africa after Saharan dust. In the form of submicron accumulation mode BB pollutants are mainly composed of Organic Carbon (OC) and Black Carbon (BC) aerosols and carbon monoxide (CO), hydrocarbon and nitrogen oxide (NOx), as gaseous pollutants. Biomass burning activities occurs in Africa in a seasonal basis as it is associated with the movement of the ITCZ (Swap *et al*., 2002; N'Datchoh *et al*., 2015) as a result of agricultural purpose. In West Africa it occurs between December and March each year (N'Datchoh *et al*., 2015) whereas in Central and southern Africa it occurs from June to September each year (Barbosa *et al*., 1999; Mari *et al*., 2008). Figure 3.2 shows the spatial distribution of global biomass emissions (g C m^{-2} yr^{-1}) from Global Fire Emissions Database

(GFED). Two distinct areas of high emissions are visible over Africa (Figure 3.2), the West Africa band spreading from West to East over the Soudanian region occurring during dry season and the Southern Hemisphere Central Africa emission occurring during wet season. The wet season and dry season refer here to the season over West Africa corresponding to the opposite in Central Africa.

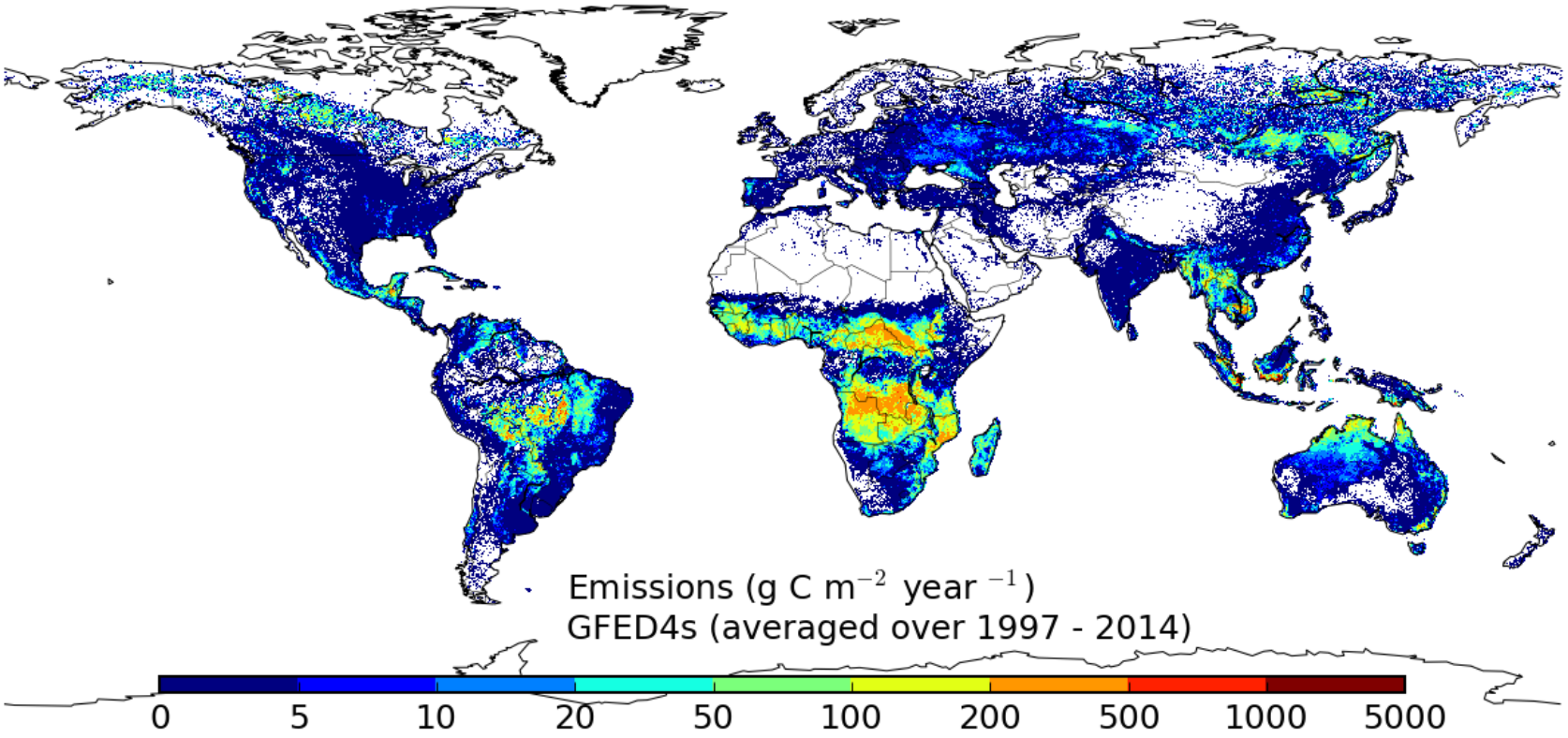

Figure 3.3: Global Fire emissions averaged between 1997 and 2014 from (http://www.globalfiredata.org/index.html)

For our modeling purpose, fire emission which also refers to biomass burning emission is derived from Global fire Assimilation System (GFASv1.2, Kaiser *et al*., 2012) at 0.1º grid size on a daily basis. The fire radiative power (FRP, W m^{-2}) and mean emissions fluxes (kg m^{-2} s^{-1}) of species are read hourly by the model. There are then use as an input to a plume rise model to calculate the lower and upper limit of the fire emission plume (Walter *et al*., 2016). The authors implemented a diurnal cycle for heat flux and emissions (Freitas *et al*., 2006; Zhang and Kondragunta, 2008) in which the maximum fire activity occurs between 10 to 15 local solar time. As Walter *et al*. (2016) implemented the biomass burning emission for forests vegetation type, Deetz (2017) extended it to savanna, forest and grassland as West Africa is characterized by different type of vegetation cover. The uplift parameter, vertical velocity at the surface, the density difference (plume – environment) and the temperature in the plume at the surface are used to derive the vertical mass distribution of the plume. The top plume height is reached if $w < 1$ m s^{-1} and the bottom height is computed using 30 W m^{-2} fire intensity (e.g. for the tropical forest). For more details on the representation of plume rise model in COSMO-ART are described in Walter *et al*. (2016).

3.3.4.5 Anthropogenic emissions

Anthropogenic aerosols (Organic matter, black carbon, SO_4, NH_4, NO_3, PM_{10}) are read from external datasets such as Emission Database for Global Atmospheric Research, Hemispheric Transport of Air Pollution version 2 , (EDGAR HTAP_v2) (Edgar, 2010) or DACCIWA (Dynamic-Aerosol-Chemistry-Clouds Interactions in West Africa) from (Keita, 2018) emissions inventories for anthropogenic emissions. Both inventories are monthly mean climatology, thus there is no diurnal cycle included in the data. Regarding the EDGAR emissions, it has been complemented by a flaring emission data to suit

better the condition over West Africa by Deetz and Vogel (2017). A reason being that the flaring emission from EDGAR was done based on a rural population proxy data six year back and neglected all offshore flares (Deetz, 2017). The flaring emissions are point sources emissions and there are read by COSMO-ART. DACCIWA emission (2015) is more recent compared to EDGAR (2010) and it has been realized only over Africa region whereas EDGAR is at a global scale. DACCIWA is a regionally updated emissions as it encompasses for all the specificities of African region (Figure 3.3). Both datasets have been used for this study. Figure 3.3 shows the BC spatial distribution from all anthropogenic sources (traffic, industry, waste burning, domestic fire, flaring) in 2015 derived from DACCIWA emissions. West Africa emits most of the BC aerosol with Nigeria as the major contributor both southern and northern part of the country, followed by the Gulf of Guinea region (southern part of the Côte d'Ivoire, Ghana, Togo, Benin, Guinea) and southern Burkina Faso. This is mainly as a result of anthropogenic activities. Eastern Africa also show considerable amount of BC emissions and the least contribution is from central Africa.

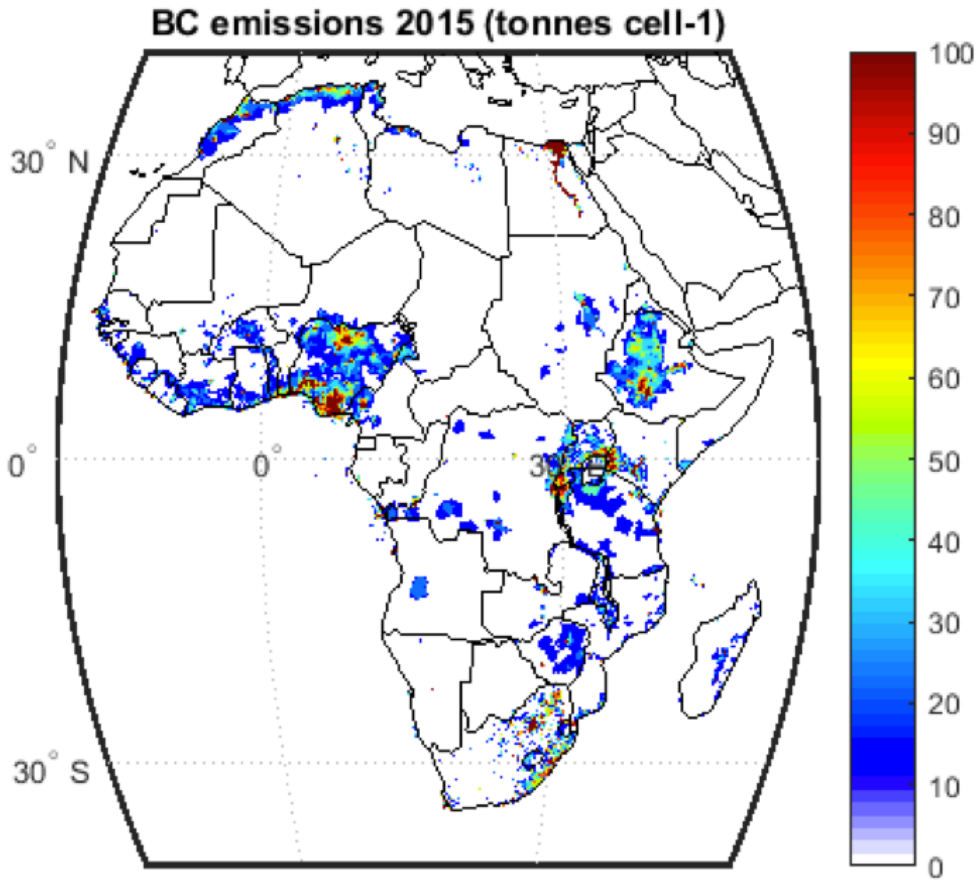

Figure 3.4: Spatial distribution of Black Carbon (BC) from (fossil fuel combustion, domestic fire, wastes burning, flaring) in 2015 (Keita, 2018).

3.3.5 Aerosol feedback in COSMO-ART

ADE (Aerosol direct effect) and AIE (Aerosol Indirect effect) are both considered for the purpose of this study. As far as the ADE is concerned, it is the impact of aerosol on the reflected, scattered radiation. It is computed using optical thickness of 8 Aerosols components in 3 (5) spectral internal of shortwave (longwave) with General Radiative Algorithm Adapted to Linear-type Solutions (GRAALS) radiation scheme (Ritter and Geleyn, 1992). In addition, the radiative properties of active trace gases are accounted for as well as for the optical thickness of present clouds.

The radiative indices were derived from Seinfeld and Pandis (2008) for water, sea salt, mineral dust, carbon and sulfuric acid. Then a Mie scattering algorithm is applied using the single scattering albedo ω, the specific extinction coefficient $b_{\_ext}$ and the asymmetry parameter g. From a priori Mie calculation (ω', $b_{\_ext}$', g') combined into a Look-up Tables (LUT), COSMO-ART computes the ω, $b_{\_ext}$, and g for the prevailing aerosol concentration (prognostic mode specific aerosol mass) over all the 8 wavelengths band. The detailed equation of those parameters ω, $b_{\_ext}$, and g are found in Vogel *et al*. (2009). A scaling factor is used in COSMO-ART to assess the sensitivity of ADE.

AIE is assessed through aerosol activation mechanism (from aerosol to cloud droplet formation) which has been described earlier under Cloud microphysics section. As ADE, AIE is also scaled by a factor in COSMO-ART. Both factors (for ADE and AIE) do not change the aerosol distribution but only the total number.

3.4 Methods

The high regional climate model COSMO-ART is used to conducted a set of experiments for the purpose of this study. This section describes the experiments performed, the simulated domains as well as the simulation setup.

3.4.1 Study domains

Southern West Africa (SWA) referring as region of West Africa located over the Gulf of Guinea is one of the regions where data scarcity has hampered scientific progress on air quality and aerosols impact on weather and climate. It appears to be one of the region of the world to experience the fastest population growth (Lamarque *et al.*, 2005). Megacities are increasing over the region as a result of urbanization and progress toward development has led to industrialization. As a result, local pollution is increasing over the region affecting the air quality, as well as the weather and the climate of the region. Moreover, long-range transport of aerosol from other sources add to the aerosol burden already existing over the region.

Côte d'Ivoire and Ghana are located in SWA. The key domain ranges from 3° –10.8° N; 9° W–1° E, encompassing Côte d'Ivoire (Figure 3.4), the Gulf of Guinea and Western part of Ghana, including Abidjan (Côte d'Ivoire), Accra and Kumasi (Ghana). A part from Kumasi, Accra and Abidjan are located along the coast and are the economic capital of those countries. These cities are among the five most populated in SWA according to UNO (2018) as a result of urbanization. Abidjan is the second most populated city in SWA after Lagos with a population of 5 millions, followed by Kumasi with 2.7 millions and the fifth one is Accra with 2.3 millions of inhabitants. Côte d'Ivoire as well as other SWA countries (Ghana, Togo, Benin, and Nigeria) have same climatic features (raining and dry seasons). Côte d'Ivoire is characterized by two typical zones. Dense and humid evergreen tropical forest in the South and savanna and grassland in the North. The south part is characterized by two raining seasons: a small and big raining season. The latter (big raining season) is intense and longer with a peak rainfall around June. In year 2016 over the coastal zone, according to Société d'Exploitation et de Développement Aéroportuaire, Aéronautique et Météorologique

(SODEXAM, 2017), the annual cumulative rainfall was 1530 mm, a reduction of 8.2 % compared to the reference period of 1981-2010 (1666.5 mm). During the same year seasonal rainfall in Abidjan was reduced by 29 % during July–August–September-October (JASO) season. In the North, they experience only one raining season with a maximum around August. While rainfall is decreasing in the southern part of the country, the northern part is experiencing an increase of 5% annual cumulative rainfall (1324.7 mm) compared to the reference period (1261.1 mm) (SODEXAM, 2017). Meanwhile as far as temperature is concerned, this year (2016) was the hottest (26.78° C) in Côte d 'Ivoire since 1961 compared to the reference period (25.6° C).

3.4.2 Simulation Setup

Two domains are used for our study with the nesting option (two ways nesting). First domain is D1 (18°W–26.6°E; 20°S–24.6°N) covering a large area including the fire areas from Central Africa and the Saharan where mineral dust is originated. The nested domain D2 (9°W–1°E; 3°–10.8°N), mostly covering Cote d'Ivoire and Ghana (Figure 3.4). Table 3.3. presents an overview of the simulation setup. Convection parametrization is not applied in this study as it is assumed that at 5 km and 2.5 km the model performs quite better. The ADE climatology was after Tegen *et al*. (1997) and 1700 cm^{-3} was prescribed over the continent for the AIE climatology according to Segal and Khain (2006).

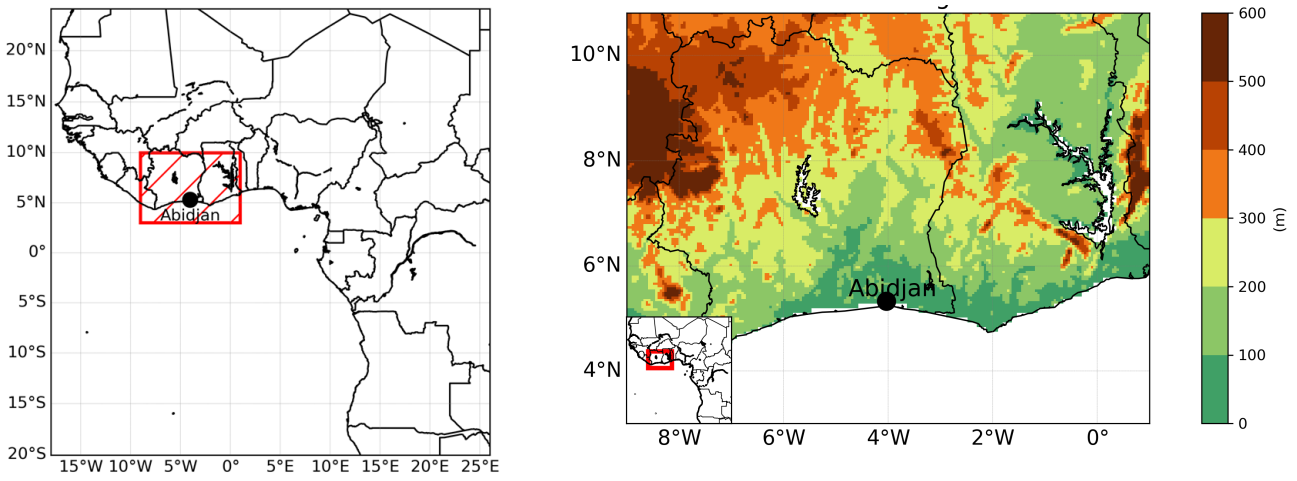

Figure 3.5: Study Map of outer domain D1 (left panel) and nested domain D2 over Côte d'Ivoire and Ghana (right panel). D1 is nested into a global model ICON and D2 is nested into D1.

Table 3.3.: Overview of the simulation setup

Characteristics	**Description**
Period	29June-31July2016
Simulation domains	D1:18°W26.6°E; 20°S-24.6°N; D2: 9°W-1°E; 3°S-10.8°N
Resolution	D1: 5 km; D2: 2.5 km
Vertical level	D1: 50 levels; D2: 80 levels
Meteorological boundary and initial conditions	ICON (Icosahedral Nonhydrostatic) model operation forecast from German Weather Service
Aerosols/chemistry boundary conditions	MOZART (Model for OZone and Related chemical Tracers)
Convection	Explicitly resolved
Cloud Microphysics	Two Moment Microphysics Scheme (TMMS)
ADE	D1: Climatology; D2: Prognostic
AIE	D1: Prescribed CCN; D2: Prognostic

3.4.3 Experimental Analysis

This section summarizes the set of experiments realized for the purpose of this study.

3.4.3.1 Biomass burning experiment

In order to assess the effect of biomass burning over the study domain, two sets of simulations were carried out: one with biomass burning emissions (call hereafter FIRE) and another one where biomass burning emissions were neglected (hereafter No FIRE) for the period of investigation.

3.4.3.2 Tracers experiment

An artificial tracer experiment is an idealized case study. The presence of remote biomass burning emission from Central Africa into the PBL of West Africa triggered the question of by which mechanism these emissions transported primarily aloft by a jet get mixed downward into the PBL. Convective clouds have been identified as a mean by which biomass burning located aloft get into the PBL and the tracer experiment here is realized to quantified the percentage of the mass concentration of the tracer used that mixed from the free troposphere into the PBL. We used CO as an inert tracer and a surrogate for biomass burning emissions. The deposition velocity is set to zero and chemistry switched off in order to account only for meteorological atmospheric transport processes. The interaction between gas phase chemistry, aerosol dynamics and the meteorology is neglected. A constant profile of 1 ppmv were set at the height where the maximum concentration of the biomass burning plume is observed (i.e. 2–4 km) and 0 below and above that layer.

3.4.3.3 Anthropogenic experiment

Similar to the biomass burning experiment, two sets of simulations were involved: one with anthropogenic emissions (call hereafter ANTHRO) and another one where anthropogenic emission were not used (hereafter No ANTHRO).

3.4.3.4 AIE and ADE case study realizations

To assess the sensitivity of the Aerosols Indirect Effect (AIE) on the clouds and radiative properties, as well as Aerosols Direct Effect (ADE), a namelist parameter FAIE and FADE was added in COSMO-ART within this study that allows to scale the aerosol number concentration. This method is known as factorial method and it is after Montgomery (2005). It has been applied by Deetz *et al*. (2018) in a case study realization using COSMO-ART to determine the sensitivity of the WAM dynamics to aerosols change. The contribution of AIE and ADE as well as the synergetic (SYN) can be separated. Using n=2 as a factorial number due to the consideration of only 2 parameters (AIE, ADE), the following equations describe their relative contribution:

$$SS_{AIE} = \frac{1}{4}(AIE_{1.0}ADE_{1.0} + AIE_{1.0}ADE_{0.1} - AIE_{0.1}ADE_{1.0} - AIE_{0.1}ADE_{0.1})^2 \quad (3.38)$$

$$SS_{ADE} = \frac{1}{4}(AIE_{1.0}ADE_{1.0} + AIE_{0.1}ADE_{1.0} - AIE_{1.0}ADE_{0.1} - AIE_{0.1}ADE_{0.1})^2 \quad (3.39)$$

$$SS_{SYN} = \frac{1}{4}(AIE_{1.0}ADE_{1.0} - AIE_{1.0}ADE_{0.1} - AIE_{0.1}ADE_{1.0} + AIE_{0.1}ADE_{0.1})^2$$

$$SS_{TOT} = SS_{AIE} + SS_{ADE} + SS_{SYN} \quad (3.40)$$

Where SS_{AIE}, SS_{ADE}, SS_{SYN} and SS_{TOT} are respectively the contribution from AIE, ADE, SYN and total.

3.4.3.5 Future scenarios experiment

To assess the impact of future anthropogenic emissions, we used IPCC RCP 2.6 and 8.5 climate scenarios for near future (2050). Because the ratio is not uniform over the whole domain, the emissions were scaled differently for each grid box. And because they are not on the same horizontal resolution the RCP emissions were re-gridded onto the same

horizontal resolution as the emission inventory. Therefore, the grid of scale factors from the RCP scenarios could be applied to the grid of emission data.

3.5 Data

Several datasets have been used in this study encompassing input datasets for COSMO-ART initial and boundary conditions, ground-based and aircraft measurement datasets, satellite retrieved observations and reanalysis. An introduction of the overall dataset will be presented in this section.

3.5.1 Initial and boundary data

These datasets are prepared and read into a preprocessor called INT2LM-ART. The latter interpolates data from several sources (point data, model output, gridded observation and satellite products), to COSMO-ART grid. Table 3.4 summarizes the initial and boundary data from different source.

3.5.2 Satellites observed data

The space-borne platforms data used in this study are from Moderate Resolution Imaging Spectroradiometer (MODIS) instrument on board of EOS Terra satellite where we retrieve cloud products. Measurement of Pollution in the Troposphere (MOPITT) satellite from NASA Terra satellite for CO surface mixing ratio. Precipitation products was derived from Global Precipitation Measurement Integrated Multi satellite Retrievals (GPM-IMERG) and Tropical Rainfall Measuring Mission (TRMM) products both from NASA using different algorithm. Advanced Very High-Resolution Radiometer (AVHRR) satellite data from the Pathfinder AVHRR SST dataset was used for Sea Surface Temperature retrieval. Spinning Enhanced Visible and InfraRed Imager (SEVIRI) cloud visible image from EUMETSAT (from NAScube http://nascube.univ-lille1.fr). Table 3.5 presents an overview of these products.

Table 3.4: Overview of initial and boundary data used by COSMO-ART.

Data	**Resolution (km)**	**Type based**	**References**
Mean DMS fluxes	100	ground	Lana *et al.* (2011)
Soil types	1	Ground	HWSD (2012)
ICON Meteorology boundary (D1)	13	Model	Zängl *et al*. (2015)
MOZART Atmospheric/Chemistry boundary (D1)	280x213	Model	Emmons *et al*. (2009)
EDGAR HTAP_v2 Anthropogenic emissions (D1, D2)	10	Ground	EDGAR (2010)
DACCIWA Anthropogenic emissions (D1, D2)	10	Ground	Keita (2018)
Flaring emissions	0.7	Satellite	Deetz and Vogel (2017)
Land Use Classes	0.2	Satellite	GlobCover (2009)
Biomass burning	10		GFAS v2 (Kaiser *et al*., 2012)
Plant functional types	5	Satellite	CCMS (2015)

Table 3.5: Overview of satellite data used for model evaluation.

Data	**Spatial resolution (km)**	**Temporal Resolution (min)**	**References**
TRMM	25	180	Huffman *et al*. (2007)
GPM-IMERG	10	30	Huffman *et al*. (2018)
MOPITT	22	4320	Clerbaux *et al*. (2008)
MODIS	10	1440	Platnick *et al*. (2017)
EUMETSAT, SEVIRI	3	60	NasCube (2016)
AVHRR	25	1440	Reynolds *et al*. (2007)

3.5.3 ERA-interim reanalysis data

Monthly mean ERA-Interim reanalysis data from the European Centre for Medium-Range Weather Forecasts (ECMWF) are used for this study (Dee *et al.*, 2011). It includes a forecast model to which a data assimilation scheme of 12 hourly cycles was applied in advancing forward.

3.5.4 DACCIWA ground and aircraft measurement data

DACCIWA field campaign took place in June–July 2016 in West Africa region, mainly over the Gulf of Guinea region (Knippertz *et al*., 2015). This period captures the WAM season for this particular year. Knippertz *et al*. (2017) identified the different phases of the monsoon: the Pre-onset period (1–21 June 2016) characterized by maximum rainfall in the coastal band including the onset period from 16–26 June 2016. The post onset period from 22 June–20 July, with a shift of the rainfall band northward (7.5º N) and a maximum of nocturnal low-level stratus (NLLS) fraction over the region. The recovery period was defined from 21–26 July 2016.

The ground-based measurement from 13 June–31 July 2016 and the aircraft measurement expanded from 27 June –17 July 2016. Basic meteorological fields (near surface temperature, relative humidity, surface radiation, precipitation, wind speed and direction), and aerosol fields (CO mixing ratio, aerosol mass and number concentration, Ozone mixing ratio) was gathered as well as profiles of cloud liquid water, aerosol profiles, from both aircraft and measurements.

CHAPTER FOUR

RESULTS AND DISCUSSION

This section is dedicated to the results and discussion of the model simulations. The model evaluation over West Africa will be described in section 4.1, Atmospheric composition and meteorological condition over the investigated domain will be presented in section 4.2. Section 4.3 analyses the impact of different aerosol sources (biomass, local pollution) on the state of the atmosphere. Section 4.4 evaluates different emission datasets and compare them with observations. Finally, the last section (4.5) assess the increasing future emissions using RCP_s scenarios (RCP 2.6 and 8.5) over the study domain.

4.1 Model Evaluation

In the following, observational data from satellites measurement (MODIS, IMERG-GPM, MOPITT, MSG/SEVIRI), ground-based and aircraft measurements from DACCIWA campaign and AERONET observations are used to assess the model performance in reproducing the atmospheric composition and meteorological quantities locally over Abidjan (Côte d'Ivoire), Accra (Ghana) and Kumasi (Ghana) and regionally over West Africa.

4.1.1 Meteorological quantities over West Africa cities

As one of the coastal cities over West Africa, Abidjan is the capital city of Côte d'Ivoire, experiencing urbanization and industrialization, and identified as the second most populated cities in West Africa after Lagos (UNO, 2018). In the framework of DACCIWA campaign, Abidjan belongs to the urban sites where air pollution measurement was conducted. Figure 4.1. presents a temporal evolution of observed temperature and relative humidity against modeled results with COSMO-ART. The

comparison is made from 01 to 15 July 2016 and observation are derived from DACCIWA field observation. COSMO-ART is well corelated with the observation given a correlation coefficient of about 0.87 (0.85) for temperature (relative humidity). The model slightly overestimates the observed surface temperature with a root mean square error (RMSE) of 0.74 ºC and a bias of 0.07. Regarding the relative humidity, the RMSE is estimated to 4.50% with an error bias of 0.21.

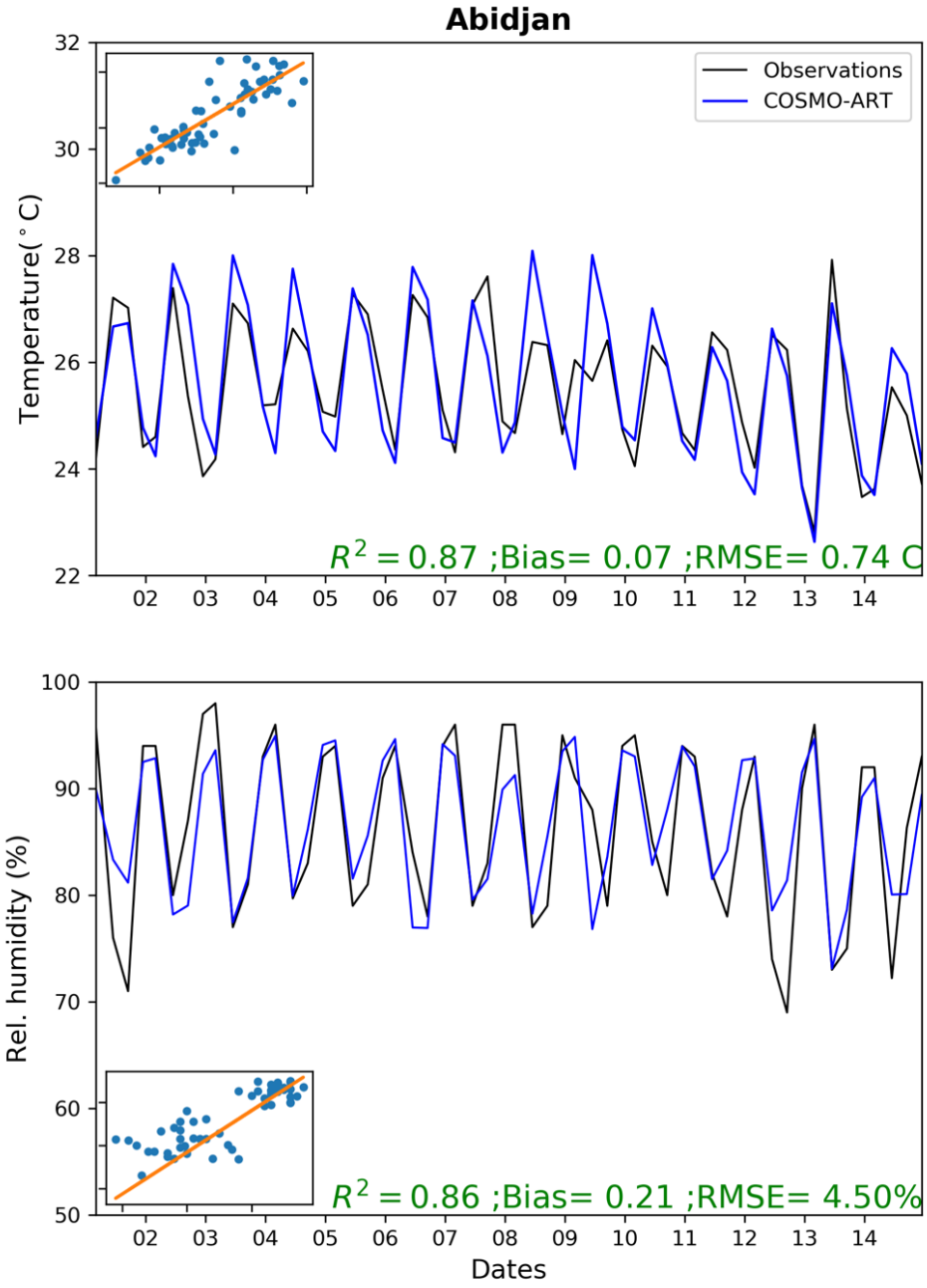

Figure 4.1: Times series of temperature and relative humidity as observed in Abidjan (black) and modeled (blue) for period ranging from 01 to 15 July 2016.

Precipitation is one of the most important meteorological quantity in West Africa, particularly in Côte d'Ivoire due to its high socio-economic impact. The country depends highly on rainfed agricultural resources. For that reason, precipitation trend is also analyzed in our study. Due to its high variability, it has been analyzed in Abidjan and three others West African cities (Accra, Save and Kumasi) based on the availability of observed data. Figure 4.2 shows daily precipitation for the four aforementioned cities throughout the month of July 2016, characterizing the post onset phase (22 June to 20 July 2016) and the recovery phase (27–31 July 2016) of the rainy season according to Knippertz *et al*. (2017). During the post-onset phase, precipitation is reduced as observed by both satellites retrieved data and in situ measurements but some isolated rainy events are still observed. Whereas COSMO-ART shows precipitation during the whole month of July 2016 for all the sites. Thus, the model shows the highest number of precipitations events. The recovery phase depicts high precipitation patterns as observed by DACCIWA in situ measurements. The peak of precipitation during that period is not well captured by COSMO-ART and GPM, except for Accra where the model displays comparable values with in-situ measurement. One reason could be that in-situ measurement is point observation, whilst the extraction of precipitation from both COSMO-ART and GPM are based on pixels. The modeled (observed) standard deviation precipitation is 0.82 (2.46), 1.84 (2.33), 1.76 (13.42) and 3.37 (2.46) for Abidjan, Accra, Kumasi and Savè respectively. The modeled (observed) average precipitation is 0.74 (0.85), 1.76 (0.82), 1.6 (3.71) and 2.75 (0.85) for Abidjan, Accra, Kumasi and Savè respectively. The high standard deviation is observed for Kumasi precipitation which is due to the peak precipitation of 73 mm seen on 06 July 2016. The overall standard deviation is higher in the observed values than the modeled ones except for Savè. The reason being that precipitation occurs mainly during the recovery phase

(after 25 July 2016). Deetz (2017) observed a mean modeled precipitation for Savè of 2.9 mm for June-July 2016 which is similar to the modeled precipitation (2.7 mm) for July 2016. However, the difference is significant for the observed precipitation in Savè which is 0.85 mm for this study against 4.4 mm (Deetz, 2017). The author computed the mean observed precipitation for June-July 2016 which covers period from the onset to recovery phase. In this study, the simulated precipitation is restricted to only July 2016. The Table of contingency summarizes (Table 4.2) the evaluation of observed precipitation (in situ measurement) against modeled precipitation for Abidjan, Accra, Kumasi and Savè.

The following metrics are quantified: Equitable threat score (ETS), Heidke skill score (HSS), Hit, False Alarm, Misses, correct rejected, Probability of False Detection (POFD), Probability of Detection (POD) and Threat score (TS). Their definitions are found in the section below. The skill scores values of ETS, HSS and TS are unbounded with negatives for Abidjan, Kumasi and Savè except for Accra. Negative values imply that the model is less skillful, thus there is a lot of shortcomings in predicting precipitation with COSMO-ART. The best TS (ETS) skill is obtained only for Accra with 0.35 (0.17). The HSS is very low meaning that the COSMO-ART forecast is quite similar to a random forecast.

4.1.2 Skill Scores

Those measurements/metrics are used to assess the performance of COSMO-ART with respect to precipitation. The four basic measures of the Contingency Table are hit (a), false alarm (b), misses (c) and correct rejected (d). which are then used to compute the metrics. The latter are computed based on a, b, c and d in the following:

$$\begin{cases} TS = \dfrac{a}{a+b+c} \\ ETS = \dfrac{(a-a_r)}{a+b+c-a_r} \\ with \qquad a_r = \dfrac{(a+b)(a+c)}{n} \\ POFD = \dfrac{b}{b+d} \\ POD = \dfrac{a}{a+c} \\ HSS = \dfrac{2(ad-bc)}{(a+c)(c+d)+(a+b)(b+d)} \end{cases} \tag{4.1}$$

n is the number of events.

The perfect skill for TS, ETS, POD, POFD, and HSS is 1 whilst zero (0) correspond to no skill level. The TS account for hits, misses and false alarm whilst correct forecast is not considered. The ETS is the TS including the hits due to random forecast. POD is sensitive to misses events and hits, only whilst POFD is sensitive to false alarm and correct rejected.

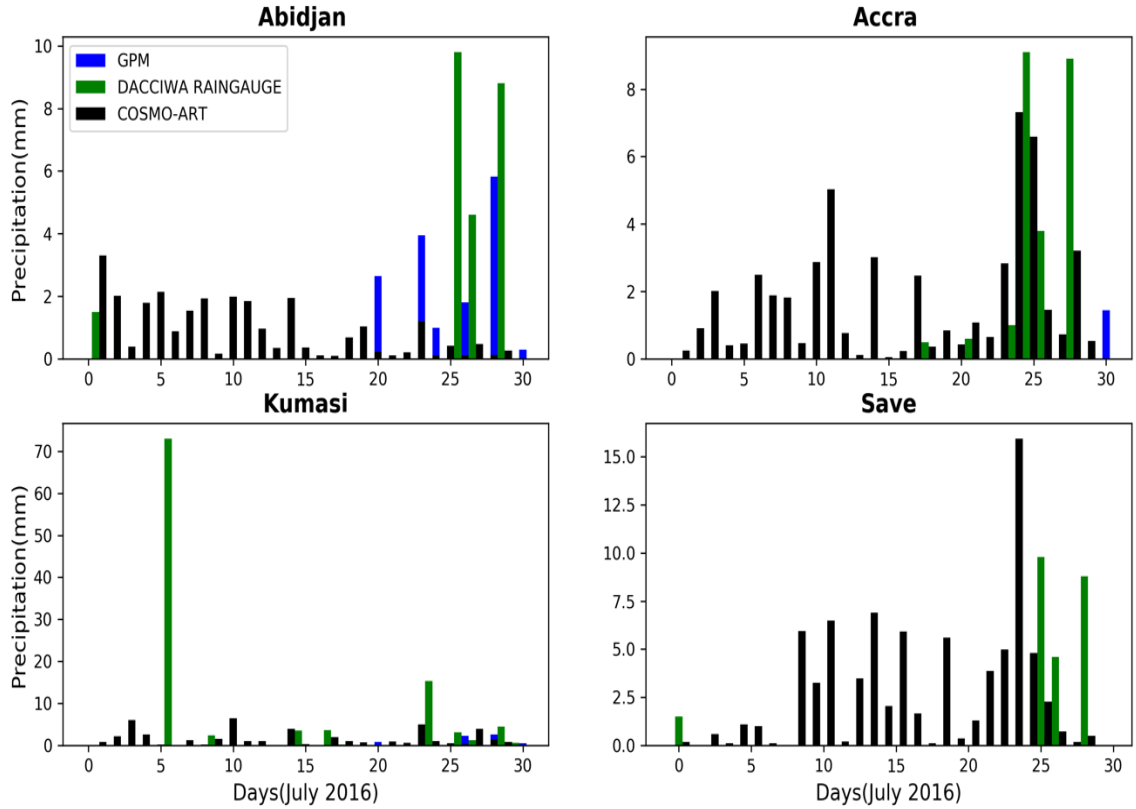

Figure 4.2: Daily precipitation comparison between Satellite products (GPM, blue), rain gauges in situ measurement (DACCIWA, green) and modeled (COSMO-ART, black) for July 2016.

Table 4.1: Basic Table of Contingency

Event Forecast	Event Observed	
	Yes	No
Yes	Hit	False Alarm
No	Misses	Correct rejected

Table 4.2: Table of Contingency of precipitation based on 29 days for July month between in situ observed and modeled precipitation for four cities in West Africa.

Metrics	COSMO-ART/Abidjan	COSMO-ART/Accra	COSMO-ART/Save	COSMO-ART/Kumasi
ETS	-0.11	0.17	-0.05	-0.31
HSS	-0.05	0.1	-0.02	-0.13
Hit	0	0.07	0.03	0
False Alarm	0.103	0.27	0.41	0.24
Misses	0.79	0.62	0.48	0.51
Correct rejected	1	0.8	0.92	1
POFD	0	0.66	0.33	0
POD	0	0.18	0.06	0
TS	-0.11	0.35	-0.13	-0.31

4.1.3 Meteorological features over West Africa region

The simulated wind speed and streamlines at 925 and 700 hPa are compared with ERA-Interim re-analysis in Figure 4.3. The wind is southeasterly in the southern hemisphere and turns southwesterly along the Guinea Coast after crossing the equator. This low-level monsoon flow advects relatively cool and moist air from the Gulf of Guinea onto the continent. In July the precipitation maximum is located around 10°N (e.g. Janicot *et al*., 2008), and westerlies penetrate far north into the continent and over the adjacent Atlantic Ocean. Apart from a slightly northward shifted turning point, COSMO-ART agrees well with ERA-Interim in terms of the overall structure of the low-level flow field. However, there are some prominent differences in wind speed. ERA-Interim shows highest wind speeds in the southern hemisphere and a slow down towards West Africa as well as a clear minimum over Central Africa. COSMO-ART shows a stronger monsoon flow and also significantly higher winds over Central Africa. Maxima reach 15 m s^{-1} for both for model and reanalysis. COSMO-ART shows a domain average of 6 m s^{-1}, 1.4 m s^{-1} higher than ERA-Interim. The wind field at 700 hPa is characterized by a broad easterly flow across most of the considered domain. A maximum is found over the Sahel known as the African Easterly Jet (AEJ), which typically peaks around 600 hPa (Parker *et al*., 2005) and is the result of the large meridional temperature gradient at low levels (Cook, 1999; Wu *et al*., 2009). The AEJ is well represented in COSMO-ART with a maximum wind speed of 10.9 m s^{-1} as compared to 13.0 m s^{-1} in ERA-Interim. Easterlies are also enhanced near the equator with weaker flow over the Guinea Coast to the north. There are some subtle differences between COSMO-ART and ERA-Interim here, with the model showing a larger northward component over the ocean and slightly stronger winds. COSMO-ART also displays more fine structure in the southern hemisphere, where winds are overall weaker.

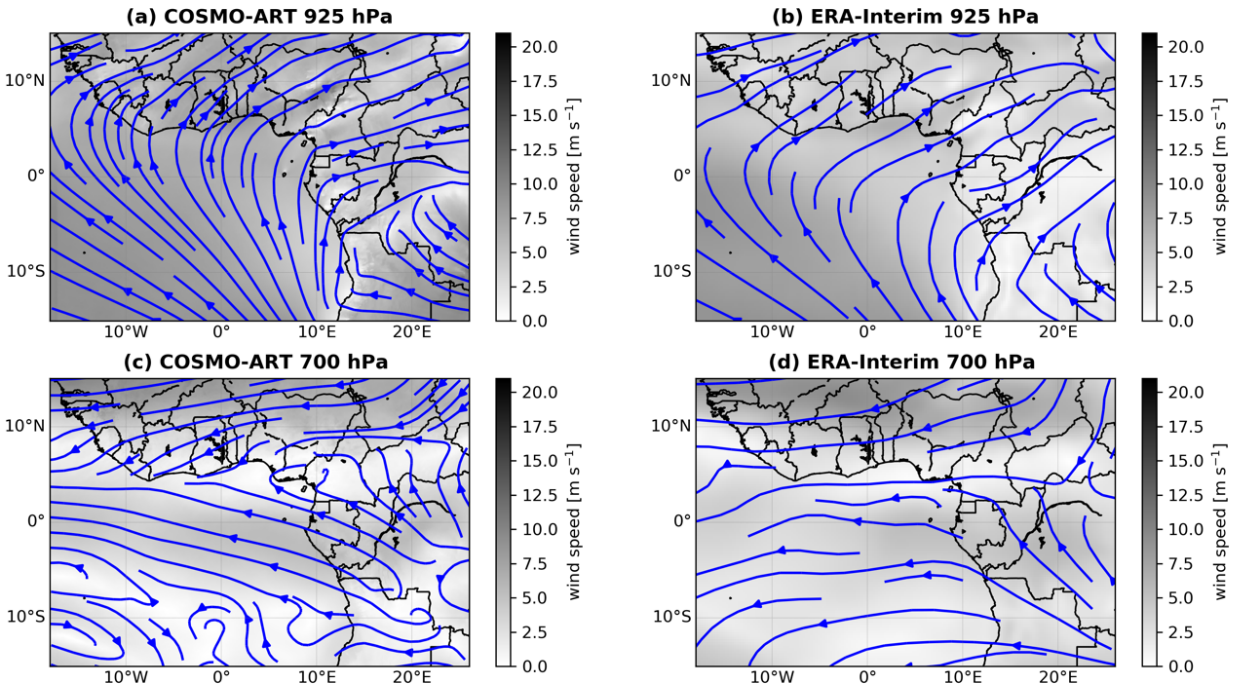

Figure 4.3: Average wind speed (grey shading) and streamlines at 925hPa (top) and 700hPa (bottom) simulated with COSMO-ART (left) and in ERA-Interim re-analysis (right) for July 2016. The scaling is different in top and bottom panels.

Regarding the observed cloud cover fraction, MODIS products was used to evaluate the model performance in cloud representation for July 2016 climatology (Figure 4.4). Côte d'Ivoire is characterized by a cloudy summer feature with values ranging from 70 to almost 100% which agrees well with the climatology found by Hill *et al*. (2016). Despite the difficulty of cloud representation in the atmospheric model due to their coarse resolution (Hannak *et al*., 2017), COSMO-ART nicely reproduces the cloud fraction mainly over land. Cloud cover maxima stretch from southwestern Ghana to northeastern Côte d'Ivoire, along the Atakora chain at the border of Ghana and Togo, and over the Guinea Highlands of Liberia and Sierra Leone with satisfactory agreement between the two datasets. Towards the Sahel cloud fraction decreases markedly in COSMO-ART but much less so in MODIS, which has a rather prominent minimum over central Côte d'Ivoire. Cloud cover is clearly overestimated by the model over the Gulf of Guinea with two local minima upwind of Abidjan and Accra, which may be related to coastal upwelling and are hard to verify with MODIS due to the coarser resolution.

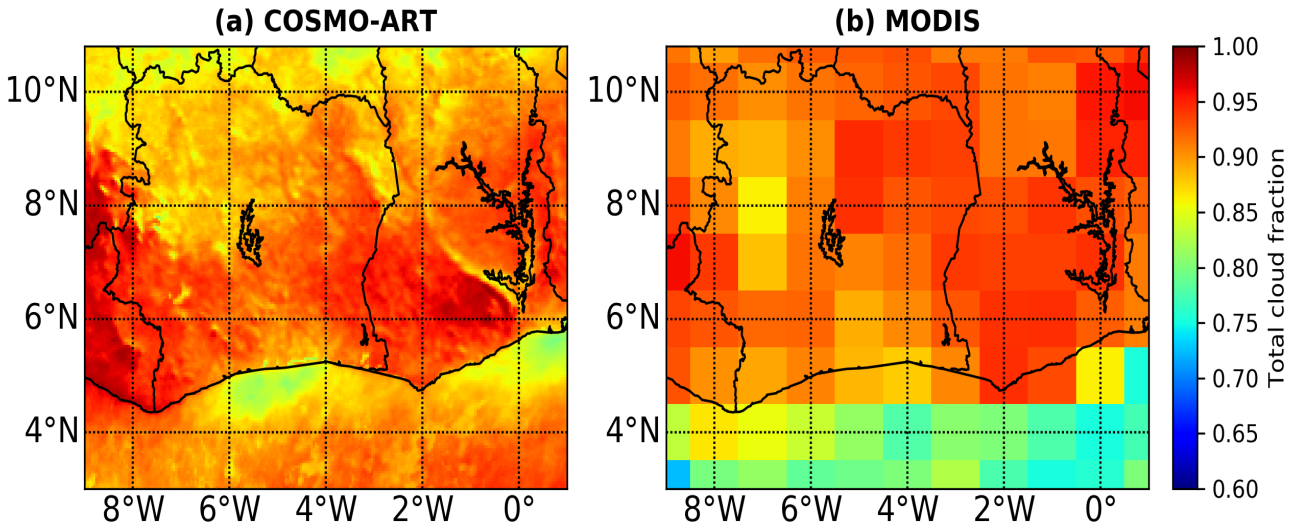

Figure 4.4: Monthly mean total cloud fraction for July 2016 over domain D2 as simulated with COSMO-ART (a) and observed by MODIS (b).

4.1.4 Atmospheric quantities over West Africa

In this section, the atmospheric composition is quantified locally over Abidjan and regionally over West Africa. Figure 4.5 shows the daily averaged of the near surface modeled particulate matter (PM) concentration with different size diameters (PM_1, $PM_{2.5}$ and PM_{10}) compared with observation from DACCIWA field campaign. The simulated PM agrees well with the observed for all PM except for PM_1 where the model slightly overestimated its concentration by 7 µg. m^{-3}. PM_1 aerosol concentrations are highly dominated by anthropogenic sources which emissions calculations suffered from lot of uncertainties related to the data used and methods for computation (Liousse *et al*., 2014; Keita, 2018). It is worth noting that the PM_{10} concentration reaches 25.2 µg.m^{-3}, whilst $PM_{2.5}$ reaches 23µg.m^{-3} close to the WHO daily mean limit for $PM_{2.5}$. Therefore, the level of pollution over West Africa, particular over the coastal cities is alarming. Adon *et al*. (2019) found that all PM concentration measured in three different sites over Abidjan are well above the WHO annual and daily limit during wet and dry season under DACCIWA air pollution measurement campaign.

Figure 4.6 presents a regional distribution of CO mixing ratio over West Africa. The simulated CO mixing ratio is compared to observations from MOPITT spaceborne measurement. Overall the spatial patterns of CO concentration are reasonably captured by the model. Some areas have too frequent cloud contamination and do not allow the computation of a representative monthly mean (white shading in Figure 4.6b). Over Central Africa widespread burning is evident with a larger magnitude and spatial extent in the model as compared to satellite. From there a plume of enhanced concentrations stretches northwestward in both datasets, but again fields in COSMO-ART are somewhat larger and therefore reach more remote parts of the Atlantic Ocean. This also supports a potential overestimation of the important of pollution from Central Africa

into West Africa in the model. In addition, COSMO-ART simulates marked pollution plumes over Nigeria associated with Lagos, the oil fields in the Niger Delta (flaring activities), and the population center around the Sahelian city of Kano, which are hard to verify due to clouds. Emissions from other large cities (e.g. Accra, Kumasi, Abidjan) appear relatively weak in COSMO-ART. This may be at least partly due to uncertainties in standard emission inventories (Liousse *et al*., 2014).

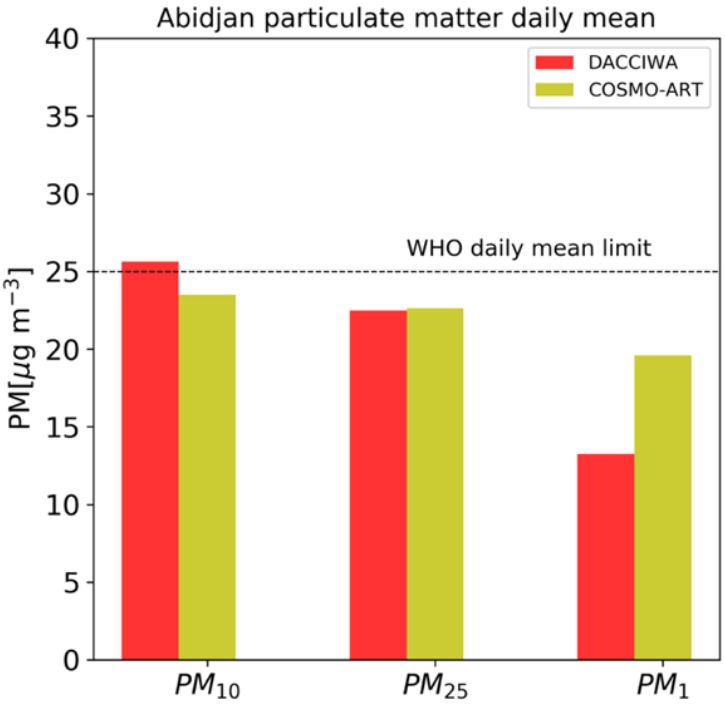

Figure 4.5: Daily average of observed (red) particulate matter respectively PM_{10}, $PM_{2.5}$ and PM_1 with COSMO-ART (yellow) on 07 July 2016.

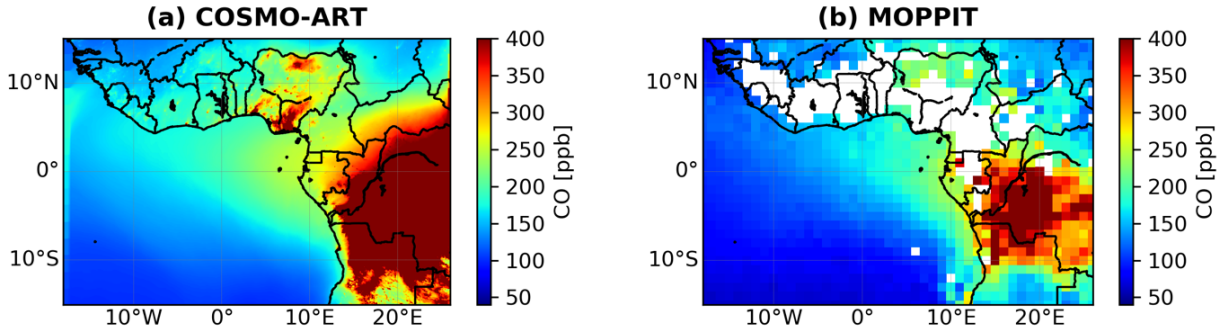

Figure 4.6: Monthly mean surface CO concentrations for July 2016 as simulated by COSMO-ART (left) and as observed by MOPPIT (right).

In the framework of DACCIWA, Haslett *et al*. (2019) compiled the aircraft measurement of the aerosol composition of West Africa over three regimes: coastal cities plumes, the regional background and the marine monsoon layer (below 1.9 km). Figure 4.7 shows the flight path of the three aircrafts during the campaign; the German Deutsches Zentrum für Luft- und Raumfahrt (DLR) Falcon 20, the French Service des Avions Français Instrumentés pour la Recherche en Environnement (SAFIRE) ATR-42 and the British Antarctic Survey (BAS) Twin Otter. Sulfate (SO_4), nitrate (NO_3), ammonium (NH_4) and organic aerosol compound mass and number concentration measured by sensors on board of the aircrafts are displayed in Figure 4.9 as compared with COSMO-ART. The aerosol mass concentration is dominated by large fraction of organic aerosol, followed by sulfate, ammonium and nitrate. The aerosol mass fraction observed (modeled) is 6.3 (4.45) µg m^{-3} over the marine domain, 11.52 (10.85) µg m^{-3} over the city plume and 1.90 (7.5) µg m^{-3} over the regional background. The inconsistency between the model and the observation over the region could be due to the fact that over land, the model still has difficulties to simulate coastal circulation. Kniffka *et al*. (2019) recently found that models have large errors at the immediate coast. Haslett *et al*. (2019) argued that the possible reasons responsible for this large difference are: (i) the progression of the marine air far north is not well represented in the model, which support the findings of Kniffka *et al*. (2019); overestimated losses in the model due to vertical mixing being strong over land and (iii) the model computed a daily average whilst the flights activities occur at different times of the day. Regarding the point (ii), indeed there are some vertical mixing of the biomass burning aerosol located aloft (2 km altitude) into the monsoon layer by clouds Dajuma *et al*. (2019, in review) which are then being transported northwards over land by southerlies winds. Over land,

the daytime mixing being stronger will likely mixed the aerosols to the surface where it affects people.

Moreover, from this study, regional emissions from DACCIWA campaign was compared with global emissions dataset from EDGAR. Both emissions were used to carried out simulation with COSMO-ART (see section 4.4). It appears that the EDGAR emission underestimated the organic aerosol fraction, as well as the sulfur, nitrogen dioxide traces gases compared to that of DACCIWA emissions. The similarity of aerosol characteristics (aged accumulation mode) found in both marine and regional background (away from urban influence) suggests that there are both from the same source (Haslett *et al*., 2019), mainly the long-range transport of biomass burning. The organic aerosol fraction alone represents 60 % of the aerosol mass, which is the most abundant aerosol fraction released by biomass burning fires (Menut *et al*., 2018).

To confirm the hypothesis of long-range transport biomass burning dominating the boundary layer of West Africa during the wet season for this particular year, a model simulation where biomass burning aerosols (BBA) was turned off was carried out (Figure 4.8). Results from the later show a reduction of aerosol mass fraction in the boundary layer from 4.45 to 1 µg m^{-3} showing clearly the aerosol source of the upwind marine. Likewise, the cities plumes aerosols decrease from 11.52 to 6 µg m^{-3}, reduction almost by half, supporting the finding of Menut *et al*. (2018), which showed that biomass burning aerosol increase the level of pollution of West African cities (Abidjan, Lagos). Nevertheless, COSMO-ART is able to reproduce the observed aerosol mass concentration is possible only when BBA emissions are considered.

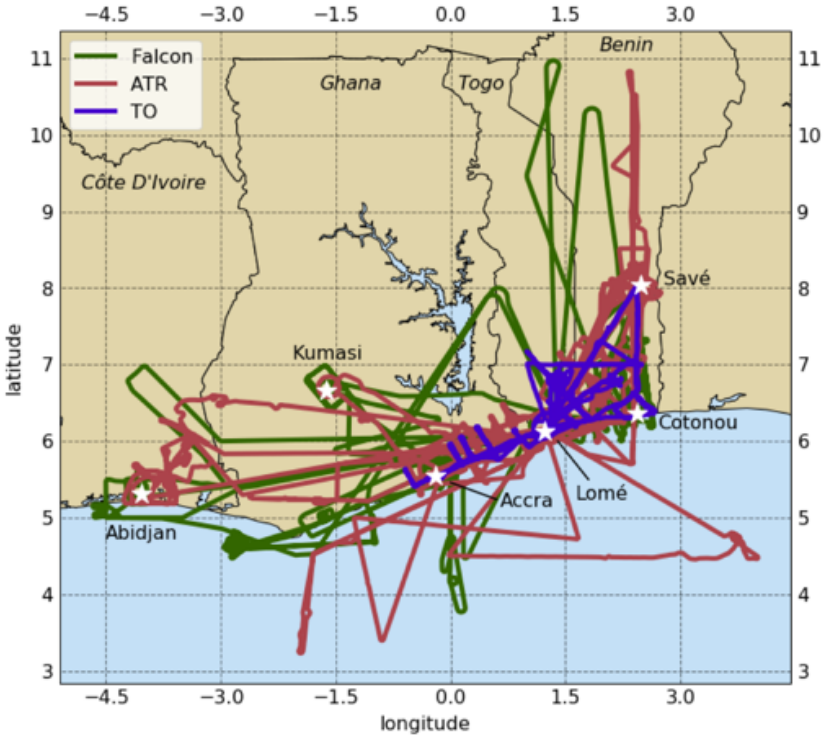

Figure 4.7: Area Map of flight path over West Africa taken by the BAS Twin Otter (TO), DLR Falcon and SAFIRE ATR aircraft during the DACCIWA aircraft campaign from 29th June 2016 to 16th July 2016. (Haslett *et al*., 2019)

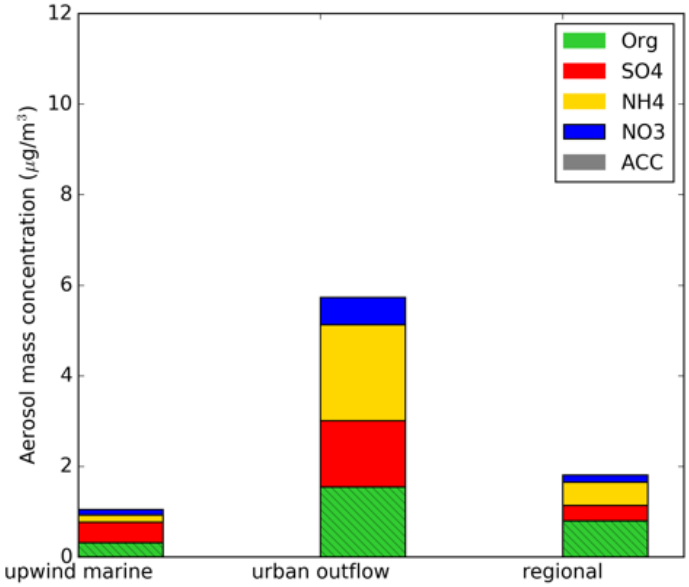

Figure 4.8: Modeled aerosol (including biomass burning emissions) mass and number concentration with BBA turn off in COSMO-ART.

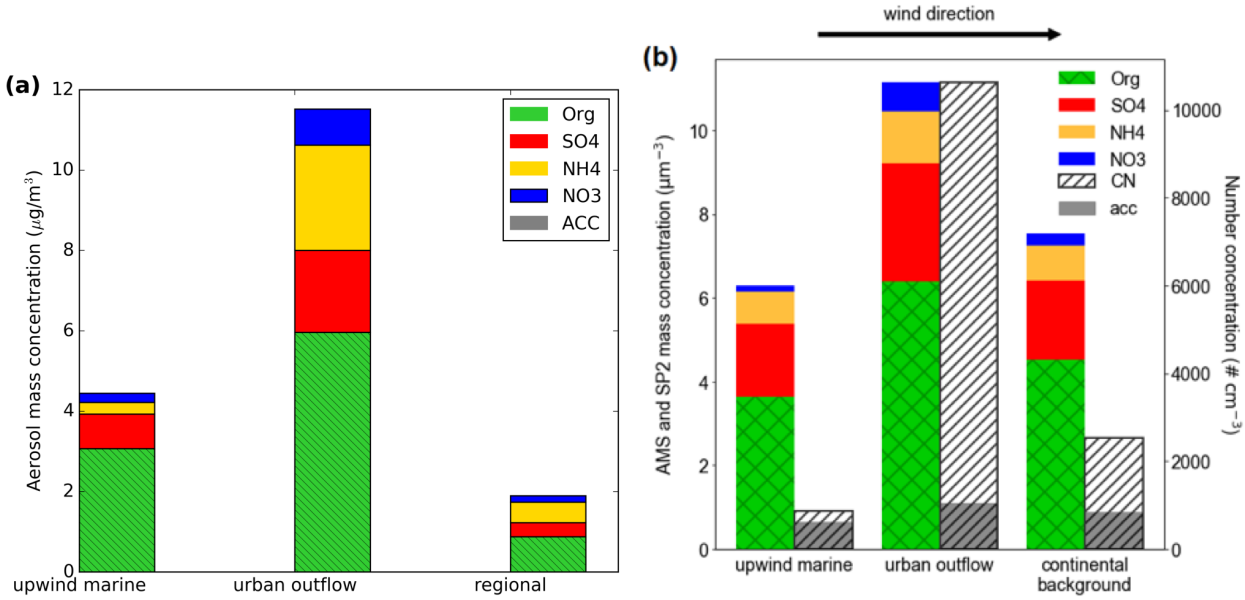

Figure 4.9: Modeled aerosol (including biomass burning emissions) mass and number concentration (a) as compared to the DACCIWA observations (b) (Haslett *et al*., 2019, Adapted).

To further test the model performance regarding the atmospheric composition, AERONET observation is used for comparison with COSMO-ART. In Côte d'Ivoire, there is only one AERONET measurement site in Lamto (Latitude: 6.216; Longitude: -5.016), but the data was not available for the investigation period (July 2016). For that reason, three sites in West Africa, Ilorin (Nigeria), Koforidua (Ghana) and Savè (Benin), for which data is available for the period of interest were used. Figure 4.10 shows the temporal evolution of the total Aerosol Optical Depth (AOD 550nm) for Savè (top), Ilorin (Middle) and Koforidua (bottom) panel as modeled (green) compared to AERONET observation (blue). The investigation period ranges from 1 to 29 July 2016. The simulation used to retrieve the AOD is from the outer domain D1 (5 km resolution). COSMO-ART shows an underestimation of the AOD for Savè and Koforidua whilst a better representation is obtained in Ilorin. Table 4.3 summarizes the statistical scores of the temporal evolution of the AOD for the three sites for the period of investigation. The correlation coefficient between COSMO-ART and AERONET varies from 0.69 (Koforidua) to 0.75 (Ilorin), which illustrates a very good temporal representation of the AOD by the model. Previous studies from N'Datchoh (2015) compared the AOD with RegCM regional model and found an underestimation of AOD in June-July-August-September (JJAS) season. The author stated that the reason was that their model realization did not account for the biomass burning and anthropogenic aerosol. In contrast to their study, all sources of aerosols, natural (dust, sea salt) and anthropogenic (biomass burning, local sources pollution) are accounted for in our model experiment. Another study from Deetz (2017), using COSMO-ART also analyzed the model results of AOD with the AERONET observation. His results revealed an overestimation of the AOD compared to Copernicus Atmosphere Monitoring Service (CAMS) and AERONET for period from June–July 2016. The discrepancies between the latter and

this study are due to the fact that his simulation was performed at 28 km resolution whilst our simulation was performed at 5 km, obviously show better result. AERONET was used at level 1.5 in their realization whilst this study compares model result with observed AOD at level 2.0. Despite the differences found, both studies (this study and Deetz, 2017) highlighted that the northmost station (Ilorin and Savè), show better reproducibility that the southern part (Koforidua). This is an indication that the dust parametrization is much more improved in COSMO-ART. Similarly, to result from this study, Menut *et al*. (2018) analyzed AERONET observations with WRF-CHEM model results in West Africa. For Ilorin, a mean modeled AOD of 0.48 against 0.35 for the AEORNET for a temporal series from 01 to 31 July 2016 was found. A temporal correlation coefficient of 0.28 was estimated from their model result whilst model result from this study estimates the correlation to 0.75 for the period of July 2016.

Table 4.3: Correlations and bias for Aerosol Optical Depth (AOD) between AERONET and COSMO-ART for period ranging from 1 to 29 July 2016.

Site	Observation	Model	R correlation	Bias
Save	0.41	0.25	0.70	-0.11
Koforidua	0.45	0.3	0.69	-0.09
Ilorin	0.34	0.4	0.75	0.02

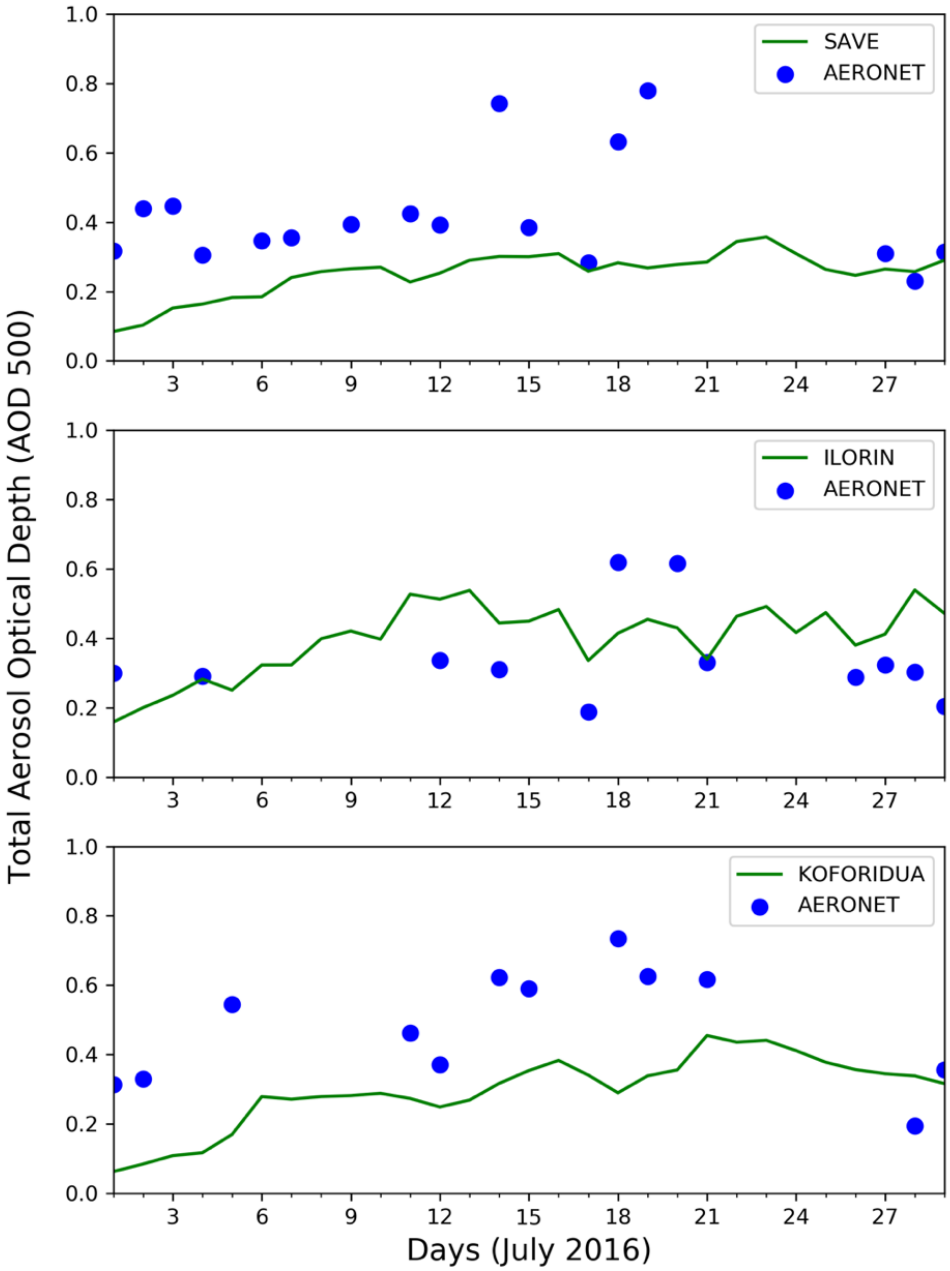

Figure 4.10: Time series of AOD at 500 nm at Savè from COSMO-ART (green, top panel) and AERONET (blue) between 1 to 29 July 2016, same for Ilorin (middle panel) and Koforidua (bottom panel).

4.1.5 Summary of model evaluation

In the latter section, COSMO-ART capability in reproducing the meteorological features and atmospheric composition over West Africa was examined. The model shows some agreement in reproducing the meteorology over the region as far as cloud fraction, temperature, relative humidity and wind field are concerned. The only parameter for which the model shows significant discrepancy is precipitation due to his high variability. And this is a very common problem with almost all models. Regarding the chemical composition over the region, in general the spatial distribution of CO mixing ratio is well reproduced especially over Central Africa where the biomass burning activities occurred. The inconsistency is COSMO-ART shows very high concentration over the whole Nigeria, which result mainly from the emissions dataset. It is worth noting that there is a lot of uncertainties in the anthropogenic emissions dataset used. The simulated aerosols mass concentration agrees with the observed only when BBA are accounted for, except over the regional background (inland) where COSMO-ART failed to simulate the transport of the biomass burning far north. AERONET observation was used to assess COSMO-ART capability in reproducing the AOD for three stations. Good correlation coefficient was found for all the stations, highlighting the model performance in the parametrization of the natural source of aerosol (dust emission, sea salt emissions). Despite the fact that the model underestimates the AOD for two of the three stations (Savè, Koriforidua), it shows better agreement with the observed one compare to other studies (Menut *et al*., 2018; Deetz, 2017). The following section will present the prevailing meteorological and atmospheric condition over West Africa for the investigation period.

4.2 Meteorology and atmospheric features

4.2.1 Meteorological conditions

The meteorological conditions of West Africa in general during June–July 2016 summer monsoon season has been well documented in Knippertz *et al*. (2017); Kalthoff *et al*. (2018) in the framework of DACCIWA observational campaign. In addition to the observations, DACCIWA project includes models' simulations of weather and climate forecast and aerosol/chemistry forecast over the Gulf of Guinea region which also refers to Southern West Africa (8W–8E; 3–12N). Among the models used, there are COSMO-ART, WRF-CHEM, GEOS-CHEM, ECHAM-HAM with different resolutions. The idea was to assess and compare them with observations in order to improve our understanding of the WAM systems as well as provide an update of the atmospheric composition of West Africa regions mainly Coastal region. The reason being that population is increasing as well as industrialization. This study investigates only a subset (Côte d'Ivoire) of the West African domain at country level for detailed studies. However, the outer domain covers the whole West Africa including the Sahelian region and the Eastern Atlantic Ocean. As most of the West African countries mainly located at the Guinea coast, Côte d'Ivoire experiences frequently the occurrence of low-level clouds (LLC), and even shows the highest frequency among region of Guinea coast as shown through satellite observations by van der Linden *et al.* (2015) (Figure 4.11). Obviously, the clouds presence will affect the radiative budget as highlighted by Knippertz *et al*. (2011) and Hill *et al*. (2016). The ability of COSMO-ART to represent the LLC have been assessed over the study domain and compared with previous studies (van der Linden *et al*., 2015). Despite the fact that models have difficulties to reproduce the LLCs (Hannak *et al*., 2017), COSMO-ART is able to reproduce the LLC spatial distribution. Figure 4.11 presents the model result of the LLC occurrence averaged for (05–06 July 2016) case study (top panel) as compared to a JAS climatology seasonally average over 4 years (2007-2011) (bottom panel). According to both COSMO-ART and

observation the bulk of the LLC over Côte d'Ivoire is located below 8 ºN and the frequency of occurrence reached up to 90% as modeled while it reaches up to 50% as observed. This difference is due to the fact that the observation was done for a climatological period (JAS season over four years) whilst, the model study was performed for daily average (05–06 July 2016). In addition, Knippertz *et al*. (2017) pointed out that the LLC are most frequent during the post onset phase of the monsoon (the investigation period). However, the discrepancies between the model and the observation are seen over the ocean where the LLC are overestimated compared to the observations.

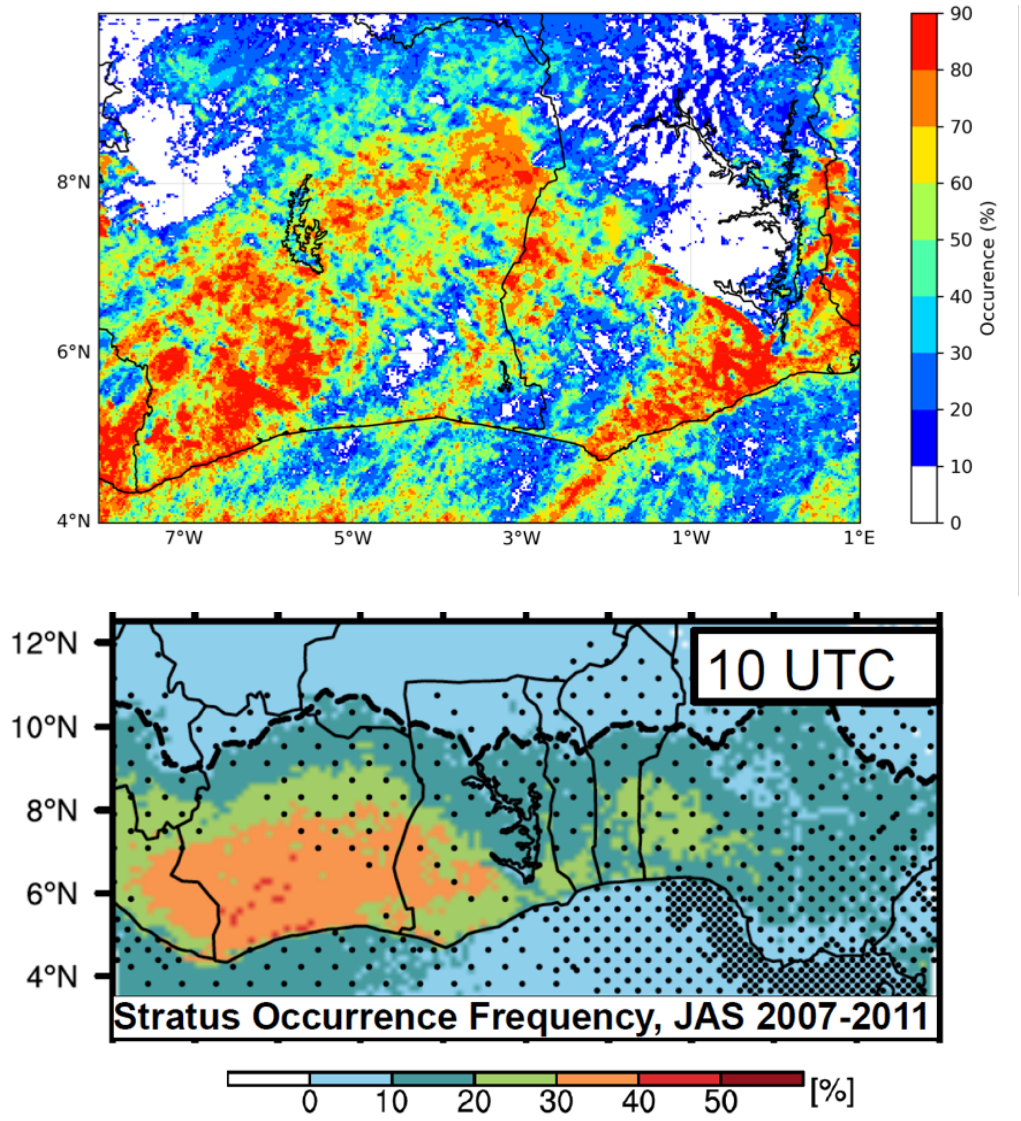

Figure 4.11: Modeled (top panel) and Observed Spatial Distribution of Low-Level Stratus Clouds Occurrence (bottom panel) over West Africa. The Observed was done by van der Linden *et al*. (2015) using satellite observations.

In order to investigate the diurnal cycle of the LLC, longitudinal cross section at 5 ºW is analyzed (Figure 4.12). Latitudinal variation of the LLC shows a reduction above 8 ºN, except at peak hours between 9 and 12 UTC where the LLC cover the whole area from 5 to 11 ºN. The cloud starts developing at night (21 UTC) around 5 ºN and with increasing hours, it expands northward to reach its maximum. After 12 UTC, the LLC clouds fraction decreases with minimum between 15 and 18 UTC. It appears again after 21 UTC. Based on observational measurements, Taylor *et al.* (2019) computed the diurnal cycle of the mean LLC fraction with respect to the latitude but focused more on Togo and Benin (Longitude 0.6 to 2.7 ºE) where the aircraft flew for period ranging from 29th June –17th July 2016. Similarly, to their results, the maximum LLC was detected between 9 and 12 UTC with a peak around 10 UTC with same magnitude. The difference appears in the delay of the cloud formation, which happens to start earlier in our case (after 21 UTC) in contrast to their findings (after 00 UTC). The LLC formation is closely linked to the Atlantic inflow (AI) detected over West Africa as a coast parallel front which developed as a band separating the cool maritime air from the warm airmass of the atmospheric boundary layer (ABL), propagating inland in the afternoon when the ABL convection decays (Grams *et al*., 2010; Adler *et al*., 2017; Deetz *et al*., 2018; Adler *et al*., 2019). A case study of 02 July 2016 analyzed by Deetz (2017) revealed that the AI location is 1º N far north over the eastern part (2.25 ºE) compared to the western part (5.75 ºW) which implies that the AI reaches inland earlier over the western region than the eastern region. The later study showed high meridional wind speed at 250 m in western area (Côte d'Ivoire) compared to the eastern (Benin). As AI is responsible for bringing cold advected air mass inland favorable for the LLC formation, our hypothesis is that it could explain the earlier formation of the LLC in Côte d'Ivoire compared Togo-Benin region.

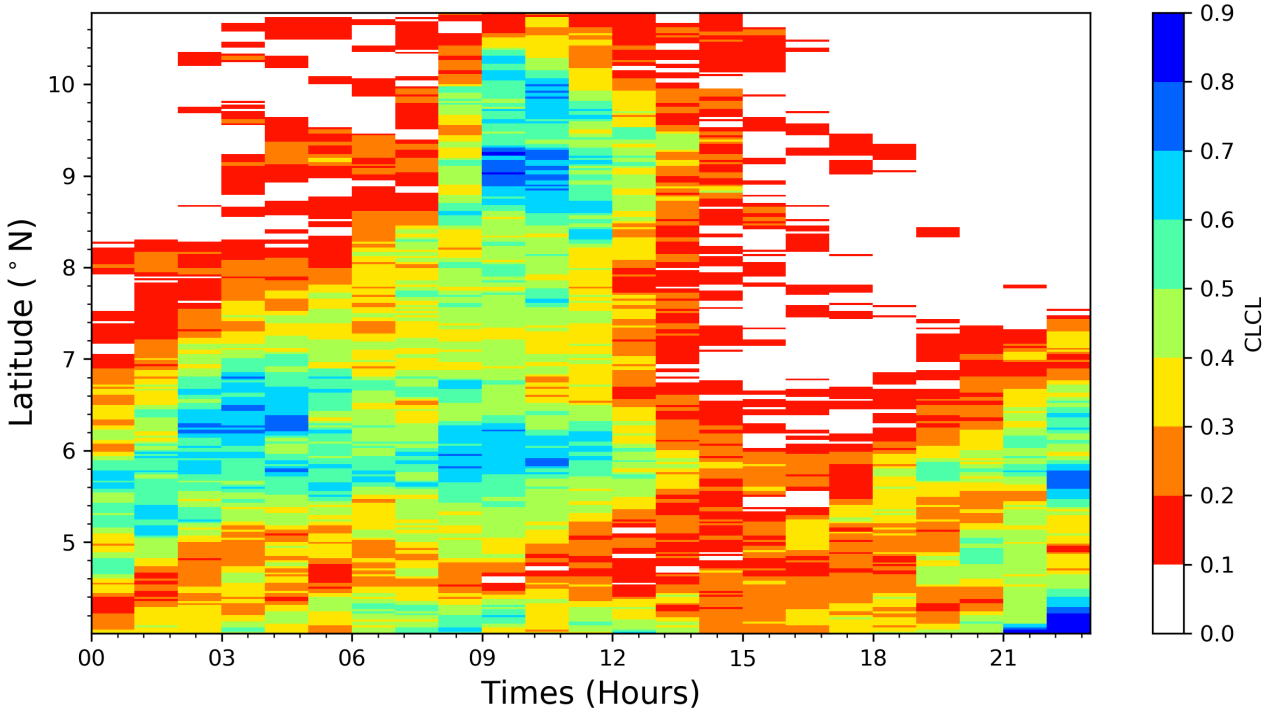

Figure 4.12: Latitudinal variation of LLC diurnal cycle at 5 ºW on 06 July 2016.

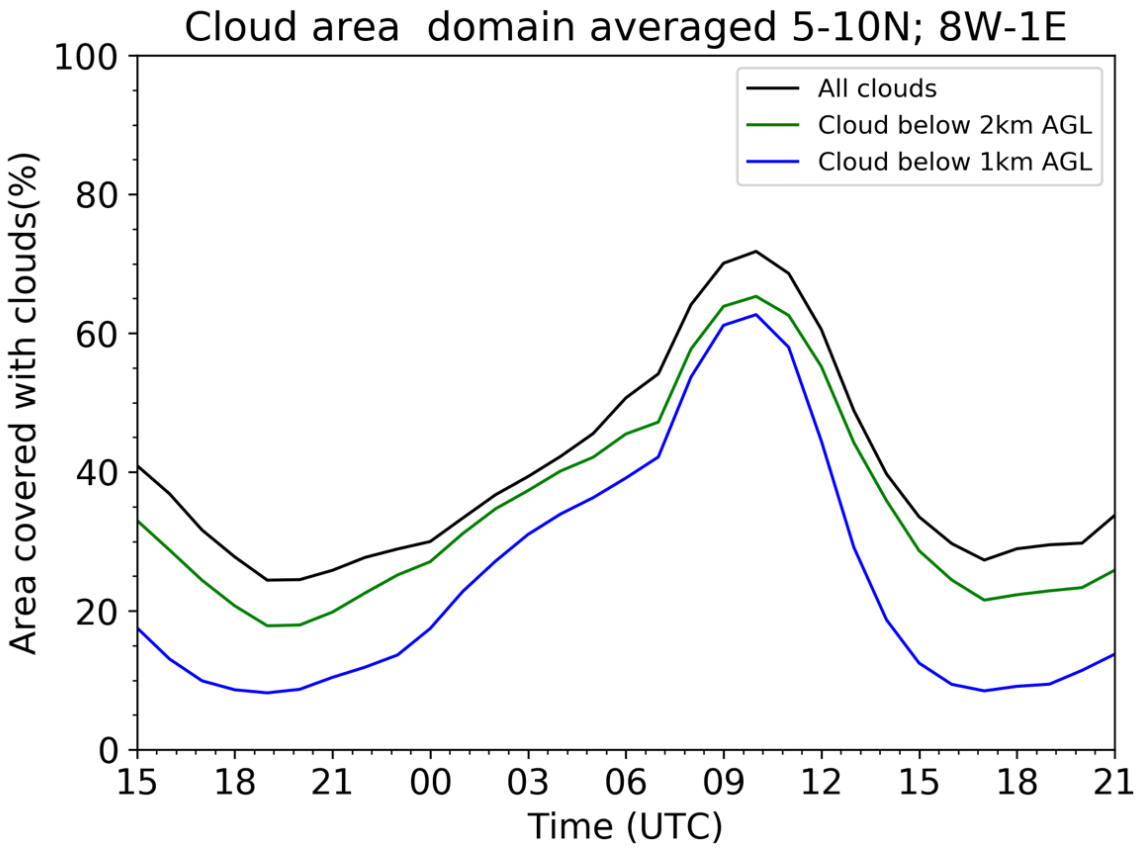

Figure 4.13: Diurnal cycle of mean cloud fraction averaged over the domain (D2) for all clouds (black), cloud below 2 km (green) and cloud below 1 km (blue).

Additionally, studies by Hill *et al*. (2016) suggested that multilayer clouds cover West Africa, thus Figure 4.13 analyses the temporal evolution of area mean cloud fraction at different altitudes above ground level (AGL).

The diurnal cycle of the domain averaged cloud fraction depicts a gradual increase of cloud after 21 UTC to reach a peak value of 70% between 9 UTC and 12 UTC as seen from the latitudinal variation (Figure 4.13). After 12 UTC, it decreases to a minimum of 20% between 15 to 18 UTC. It is worth noting that cloud cover at this specific period of time is dominated by low level cloud (green and blue curves) (Figure 4.13). The difference of percentage between low-level cloud and all clouds is very small, highlighting the abundance of LLC over the region as corroborated by Deetz (2017). In the later, the domain averaged was done over a larger domain (Gulf of Guinea region) whilst in this study, the focus was only Côte d'Ivoire and Ghana. Moreover, results from WRF simulations evaluated using AMMA 2006 observations over the Gulf of Guinea found that the minimum cloud cover was simulated around 18 UTC and the maximum at 9 UTC (Schuster *et al*., 2013) which agrees with our models results.

The total cloud water is investigated from 05 July 2016 18 UTC to 06 July 2016 18 UTC as the cloud formation evolves already from the previous day (Figure 4.14). From 18 UTC of the previous day (05 July 2016), to 00 UTC, there is a clear distinction between south cloudy area and north cloud free area. After 00 UTC, the cloudy region starts expanding northwards to reach a maximum at 12 UTC where the whole domain is covered by clouds. Deetz (2017) highlighted that the AI front airmass is responsible for the propagation of the LLC northward as it penetrates inland. The stratiform clouds layers which refers also to LLC are identified by continuous cloud layers, as seen between 3 UTC to 12 UTC. Between 12 UTC and 15 UTC the transition from stratiform to cumulus clouds (patchy structure) is obvious (Deetz, 2017). Furthermore, the later

study demonstrates that increasing aerosol amount delays the transition from stratiform to cumulus clouds by 1–2 hours.

The prevailing wind conditions during this period of investigation is analyzed. Figure 4.15 presents the meridional vertical transect along 5ºW temporally averaged. The shading color indicates the zonal wind component whilst the black contour shows the meridional wind. The separation between the southerlies wind within the monsoon layer and the easterly wind from the Sahel and Saharan region is clearly seen at around 1.9 km, identified as a top of the monsoon layer according to previous studies (Fink *et al.*, 2017; Deetz, 2017; Kalthoff *et al.*, 2018). The maximum wind speed is located above 10 ºN at mid-tropospheric height.

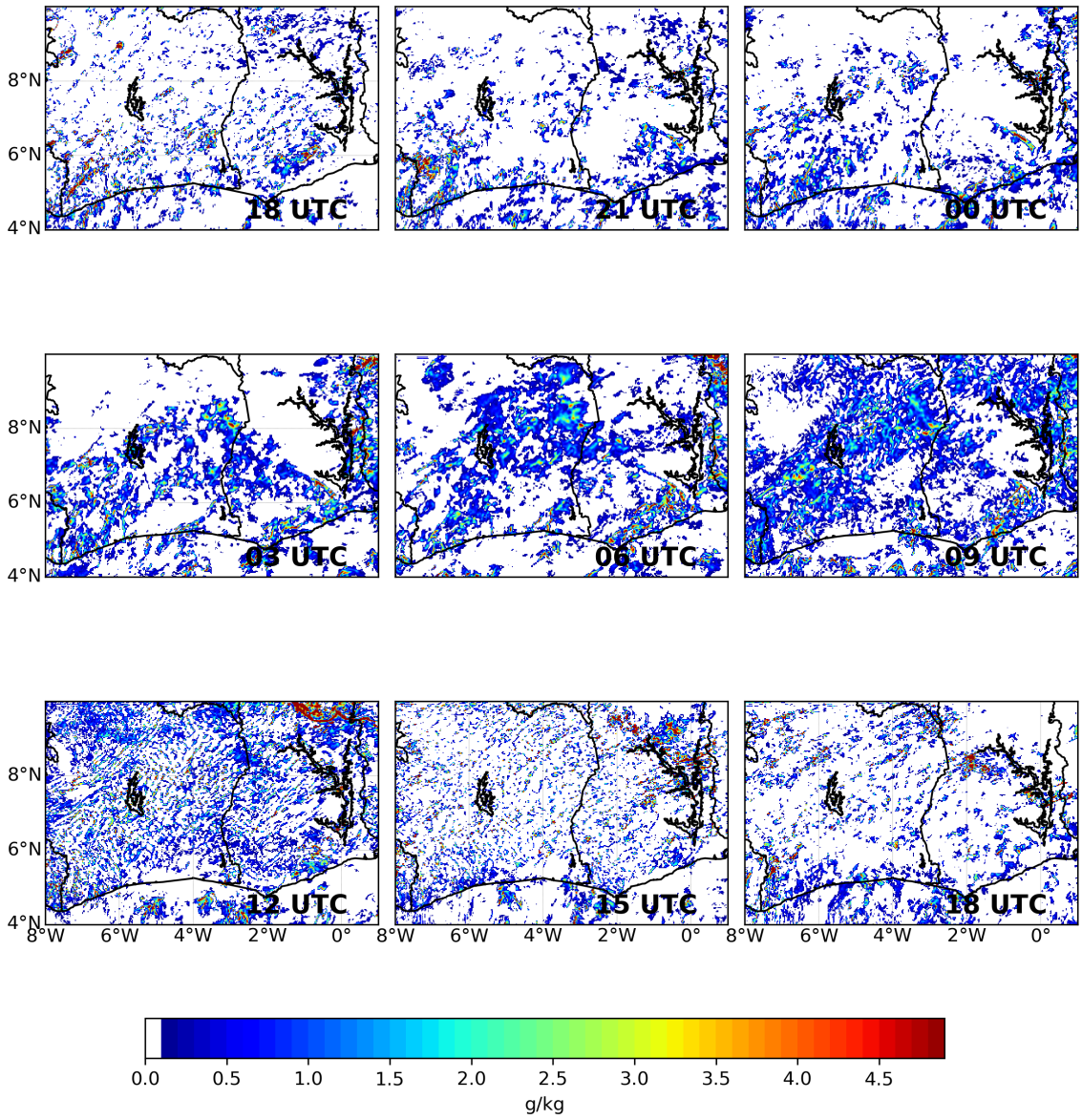

Figure 4.14: Spatial Distribution of Cloud Water from 5 July 18 UTC to 6 July 18 UTC.

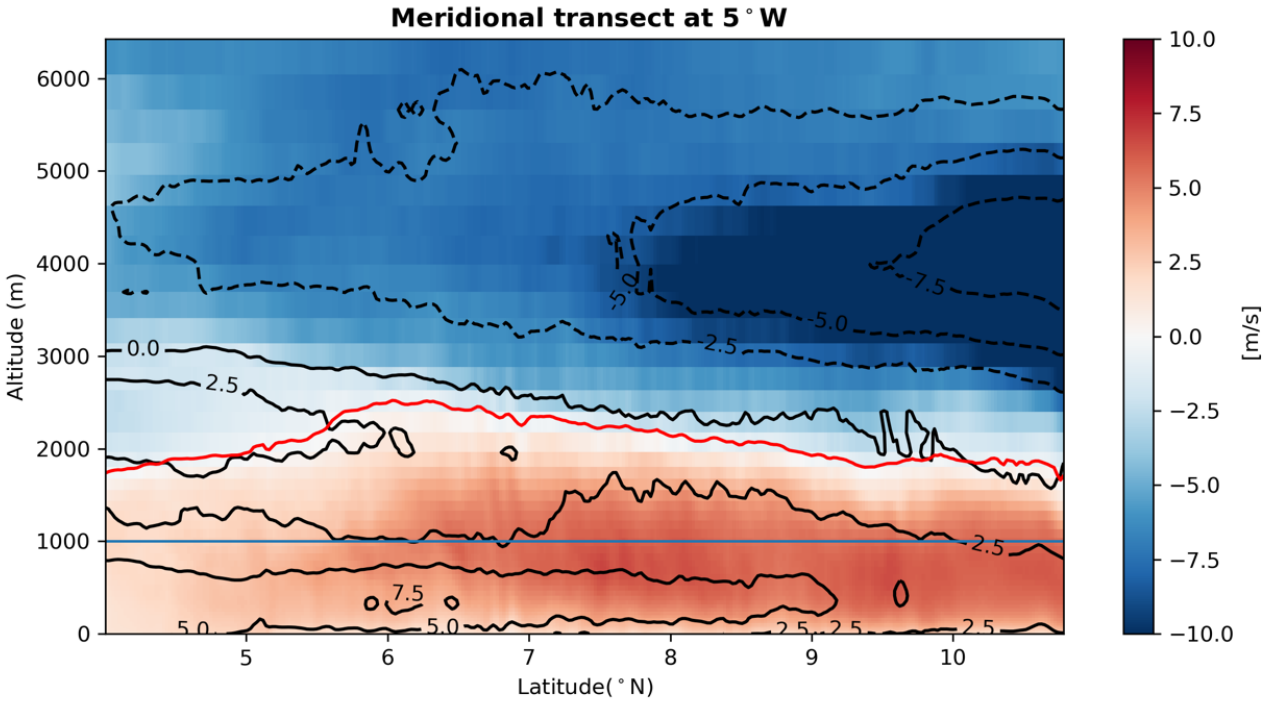

Figure 4.15: Meridional vertical transect along 5ºW temporally averaged. Color shading refers to zonal wind and black contours meridional wind. The red line indicates the height of minimum wind speed as an indicator of the Monsoon Layer Depth (MLD) according to Fink *et al*. (2017).

Over the region, Figure 4.16 presents the streamlines (black) of the wind speed and direction at 700 hPa computed from ECMWF reanalysis temporally averaged for July 2016. The orange shading denotes the CO mixing ratio near the surface, used as a surrogate for biomass burning fires detection. The thick streamlines (weighted by wind speed) highlight the African Easterly Jets in the Northern hemisphere (AEJ-N), and the Southern hemisphere (AEJ-S). The AEJ-S core located between 0° and 5 S° with a wind speed of around 6 m s^{-1} was observed both over the ocean and over land. The core of AEJ-N is located between 10° to 20° N with a maximum wind speed of 11 m s^{-1} around 15° N. A clear high CO concentration is identified over Equatorial Africa between 0° and 10° S where the biomass burning occurs. Its values reaching a maximum of 0.7 ppm. High values of CO concentration, mostly caused by gas flaring over Niger Delta were also visible in Southeastern Nigeria where the oil field industries are located.

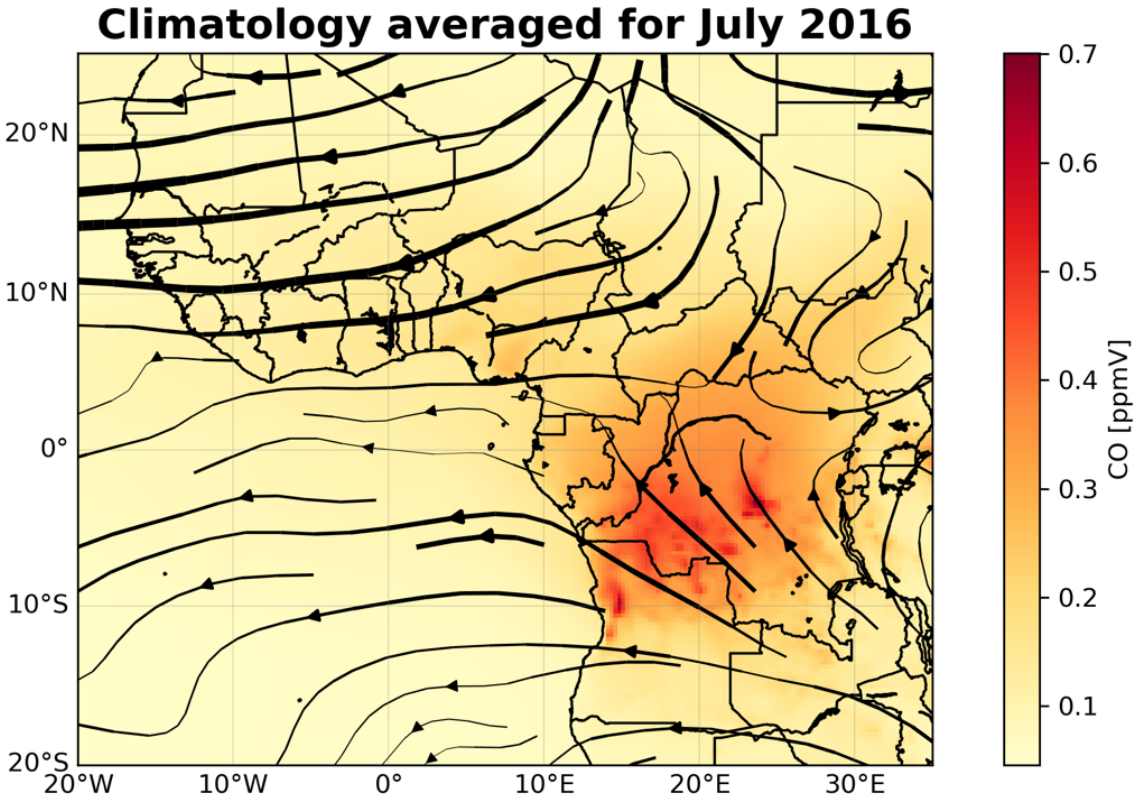

Figure 4.16: Wind speed and direction at 700 hPa (black streamlines) based on ECMWF reanalysis averaged for July 2016, and CO mixing ratio (orange shading) from GFAS.

The atmospheric composition of the study is introduced in the following section, identifying contributions from different sources.

4.2.2 Atmospheric composition

As most of the region over the Gulf of Guinea, Côte d'Ivoire is characterized by a mixture of aerosols from divers sources during this period: long range transport of dust from the Sahelian region and Saharan desert, sea salt from the Atlantic Ocean, long range transport of biomass burning from Central Africa and local anthropogenic aerosols emissions from industry, traffic and domestic fires activities. Figure 4.17 presents the total AOD (contribution from all the aforementioned sources) spatial distribution. High AOD values are observed south of the model domain, highlighting the dominance of the anthropogenic sources. In fact, the industrialized cities over the country are located in the southern part, e.g. Abidjan, as the capital and most populated city, the plume is clearly visible, which is advected northward by southerlies wind from the Gulf of Guinea. In addition, high value of AOD simulated over the Gulf of Guinea is the signature of the biomass burning air mass intrusion (Mari *et al*., 2008; Haslett *et al.*, 2019). Same observation in Ghana where the maximum AOD is seen upwind marine and over the southern cities. Accra plume is obviously seen as well. Over the north (above 8 ºN), the AOD values do not exceed 0.2, indicating the small contribution of the mineral dust over the region for this particular period (July 2016). In order to identify contribution from each source, AOD of local anthropogenic source referring as ANTHRO hereafter, AOD of sea salt and AOD of dust at different altitude are analyzed. Figure 4.18 displays the ANTHRO AOD spatial distribution (a), below 1 km (b), between 1–2 km (c) and above 1.9 km (d). Analyzing ANTHRO AOD distribution at different height, 70% of the AOD is obtained from the lowest layer (below 1 km) close to the source, emphasizing on the local source of pollution. As mentioned earlier, in

addition to the local pollution from anthropogenic activities (traffic, industry), the Gulf of Guinea shows high AOD, as a result of long-range transport of biomass burning aerosols from Central Africa. Above 1.9 km, north of the model domain, moderate AOD is simulated. The reason being that the long-range transport of biomass burning carried a jet is located between 2–4km (Barbosa *et al*., 1999; Mari *et al*., 2008). In the monsoon layer (1–1.9 km), the AOD is present but not as high as below 1km and above 1.9 km. Three cases are possible: The cities plume is transported far in altitude and reach the top of the monsoon layer; Another reason is the large scale of subsidence of Hadley cell over the Atlantic Ocean, West of the African continent, transporting the aerosol load located aloft into the boundary layer over the region (Flamant *et al.*, 2018). However, modeling study by Das *et al.* (2017) illustrated using multi-model that the extent to which the plume is entrained into the marine boundary layer is not consistent from one model to another, as some models show rapid descending plume in contrast to others. (Gordon et al., 2018) using HadGEM model showed that the plume did not descend till 10 ºW as it remain above the cloud between (2–4 km). Nethertheless, significant fraction of these biomass burning aerosol was observed in the monsoon layer over both Atlantic Ocean and continental background. Moreover, models (COSMO-ART and GEOS-Chem) are able to reproduce the aerosol mass concentration in the region only if biomass burning emission is turn on (Haslett *et al*., 2019).

From this study, it has been discovered using both model and observational evidences that clouds play a role in transporting aerosols located aloft into the monsoon layer (Dajuma *et al*., 2019, in review). Individual downward mixing south of the coast of Côte d'Ivoire by mid-level convective clouds has been identified, which appears to be more intense over land due to heating. 20% of the mass located aloft reaches the boundary layer through cloud venting (Dajuma *et al*., 2019, in review).

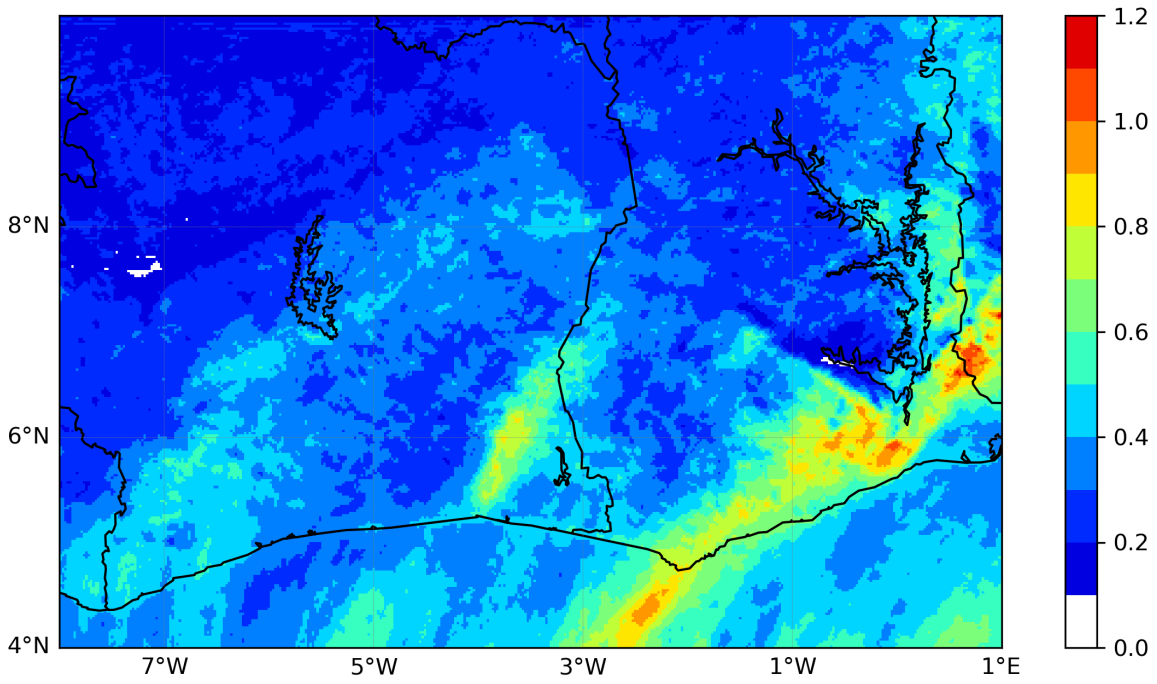

Figure 4.17: Total AOD (dust, biomass burning, local source) spatial distribution.

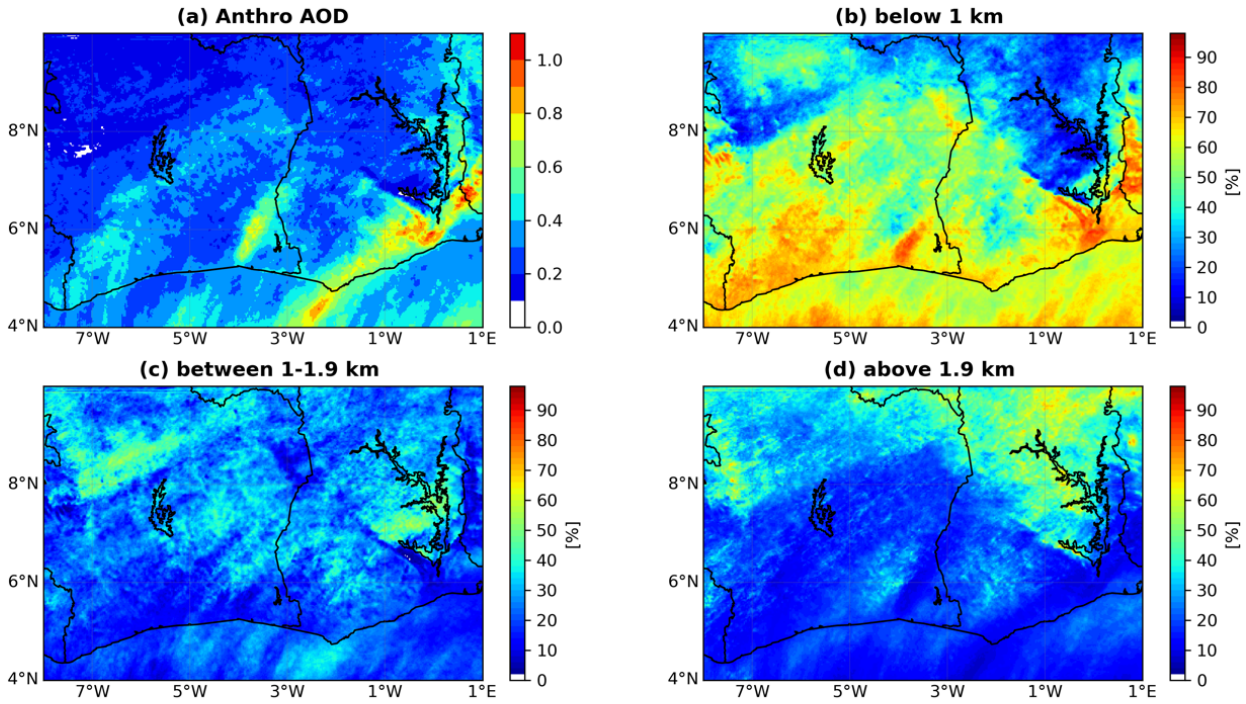

Figure 4.18: (a) Spatial distribution of anthropogenic AOD (b), contribution of AOD below 1km AGL to the total, (c) contribution from layers between 1 and 1.9km AGL and (d) contribution from above 1.9 km AGL.

As performed for ANTHRO AOD, same analyses are done for the sea salt AOD and dust AOD individually. Figures 4. 19 and 4.20 present the dust AOD and sea salt AOD spatial distribution. The contribution of dust AOD is very small at this period of time. 100% is from upper layer (above 1.9 km). From the dust AOD spatial distribution (figure 4.19 panel (a)), the bulk of the dust AOD is located above 8ºN. Generally, the influence of dust over the Gulf of Guinea region is reduced during the post onset phase of the monsoon. Knippertz et al. (2017) demonstrated that the presence of dust retreat to above 8ºN after the onset of the monsoon (22 June–20 July 2018), confirming our findings. The small value observed is due to the fact that, this result pertains to a single day, which appear to be small that particular day (06 July 2016). Furthermore, Deroubaix *et al*. (2018) showed that the dust contribution to the Gulf of Guinea is reduced from 38% in May to only 5 % in July during summer monsoon in 2006.

Regarding the sea salt AOD, obviously the highest simulated values (90%) are seen over the Gulf of Guinea below 1 km (close to the surface). Almost no sea salt is transported beyond the monsoon layer as seen in Figure 4.20 d. However, some AOD below 1 to 1.9 km within the monsoon layer are visible. The maximum value of sea salt AOD reaches 0.09 for this particular period.

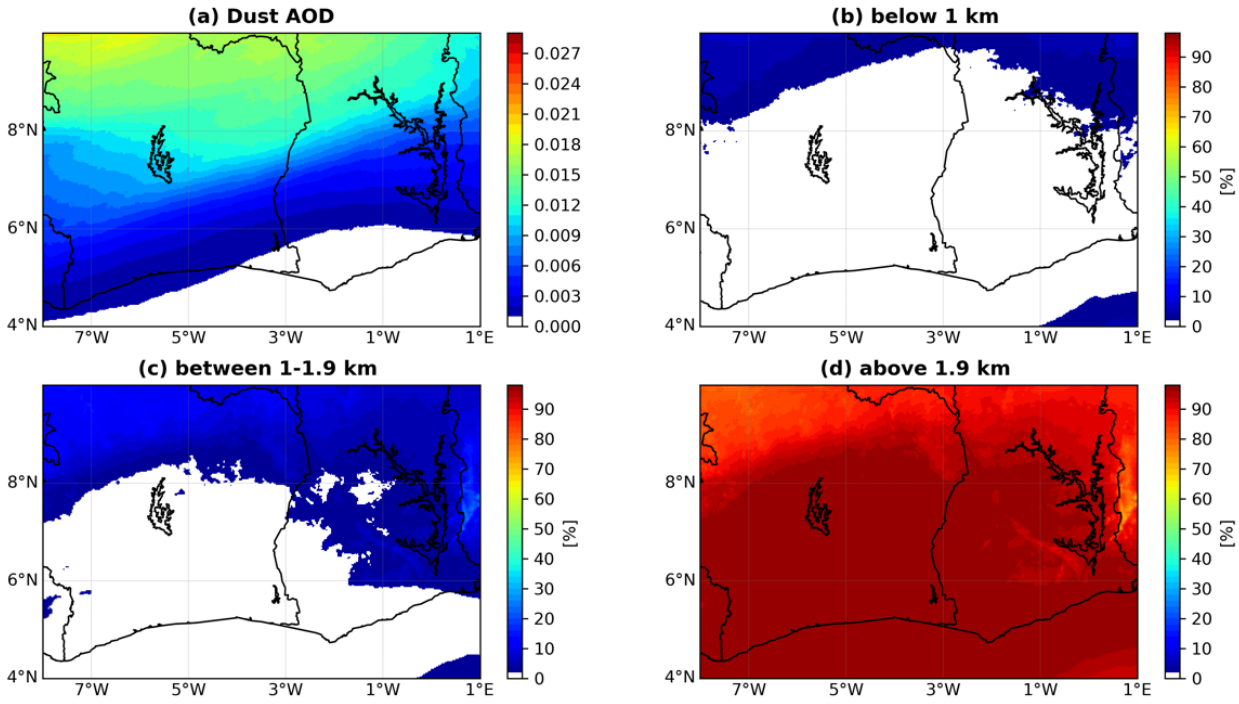

Figure 4.19: Same as Figure 4.18 but for Dust AOD

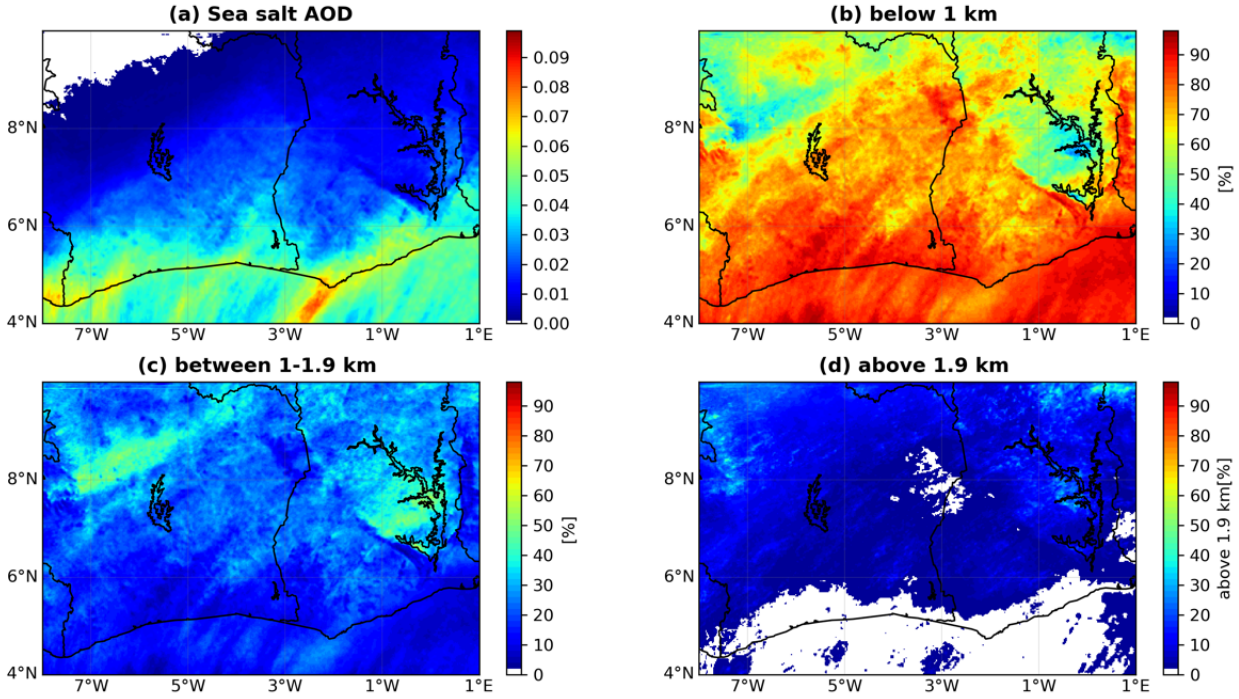

Figure 4.20: Same as Figure 4.18 but for Sea salt AOD

Further investigation of the atmospheric composition is conducted through examining $PM_{2.5}$ contribution from different source (natural, anthropogenic). The anthropogenic sources are categorized into two groups: Local anthropogenic aerosols including traffic, industries, domestic fires for cooking purposes refers hereafter as ANTHRO and long-range transport of biomass burning refers to FIRE hereafter. The peak $PM_{2.5}$ is simulated over cities plumes Abidjan, Accra and Kumasi, as a result of ANTHRO reaching 20 µg m^{-3}. Nethertheless some hotpots of moderate $PM_{2.5}$ values are seen over the whole domain, mainly south of 8 ºN rather than widely spread over the whole domain. From panel (b), 100% of $PM_{2.5}$ above 6 ºN originated from ANTHRO only. The influence of biomass burning is only visible below 6 ºN. This confirms the hypothesis that the FIRE transport northward, after it has been entrained into the boundary layer does not go far (Haslett *et al*., 2019).

The FIRE contribution is more pronounced over the Gulf of Guinea, which results from the long-range transport from Central Africa. However, the local pollution contributes to the aerosol loading over the marine boundary layer. Flamant *et al*. (2018) demonstrated that aged emission from Lomé and Cotonou are seen over the marine boundary layer but did not go far south of the Ocean through simulation with WRF. The authors argued that the plumes are mainly transported northeastward within the boundary layer by the monsoon flow (Knippertz *et al*., 2017). Hence, our simulation shows more organic fraction upwind Accra, Lomé and Cotonou that are seen south of the coast of Abidjan (Côte d'Ivoire). More cities are on the eastern part (Accra, Lomé et Cotonou) compared to the western part (Abidjan). Thus, more contribution from the cities plumes from the east to the Gulf of Guinea than from the west. Whereas the contribution from natural source is less than 10 %, confirming that the low natural impact.

In addition, organic aerosol fraction (sum of all sources) is displayed in Figure 4.22 (a), as one of the most abundant aerosol masses over the region. A separation of the organic aerosol from each source is presented as a pie chart FIRE (biomass) in yellow, natural aerosol in red and ANTHRO in green. As seen from Figure (4.21), it shows similar pattern as the $PM_{2.5}$ aerosol, obviously, it represents a considerable fraction of it. Moreover, organic aerosol is one of the main aerosols from FIRE, therefore its contribution over the Gulf of Guinea is highly present. Thus, biomass burning appears to be one of the major sources of aerosol load over the Gulf of Guinea with 47%, same contribution as anthropogenic aerosol (47.5%) and the least contribution is from the natural source for this period. COSMO-ART seems to underestimate the contribution of FIRE in the regional background as the northward transport of the aerosols is not clearly visible. FIRE contribution is mainly over the cities along the coast and over the marine domain (Gulf of Guinea).

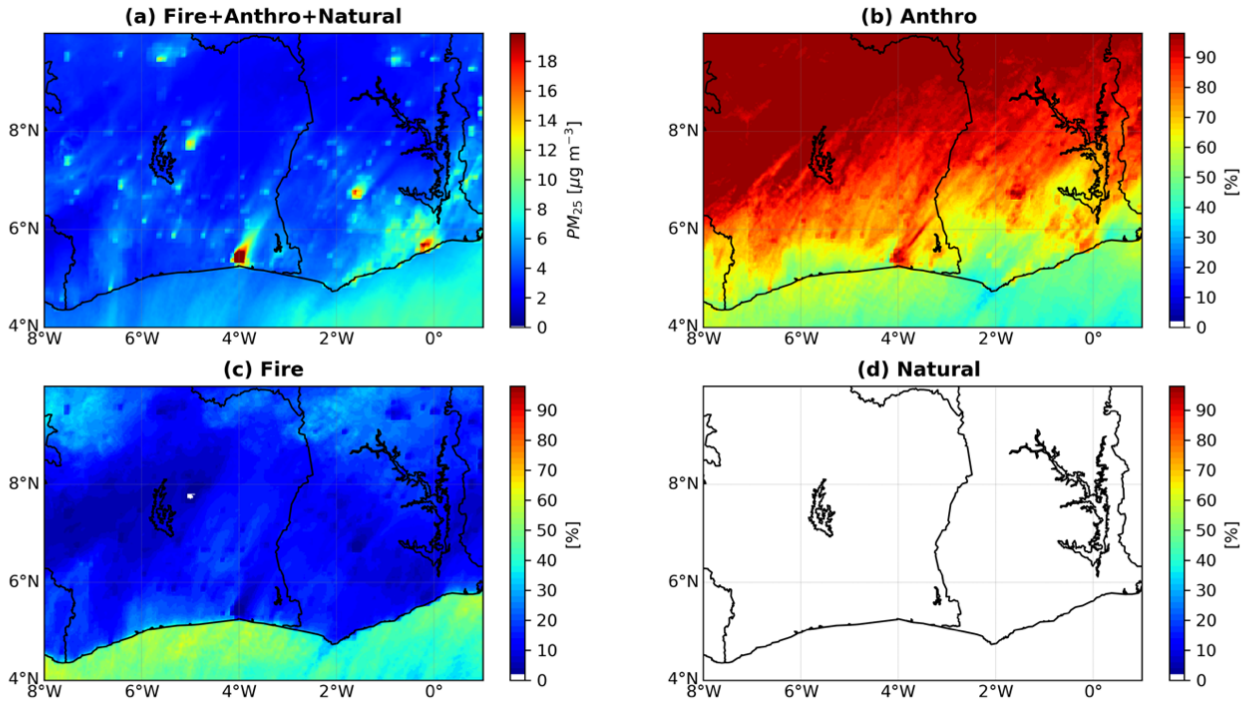

Figure 4.21: a) Spatial distribution of particulate matter PM_{25} sum from all aerosol sources (local pollution, biomass burning, sea salt, dust), contribution of ANTHRO to the total, (c) contribution of FIRE emissions to the total and (d) contribution of natural to the total.

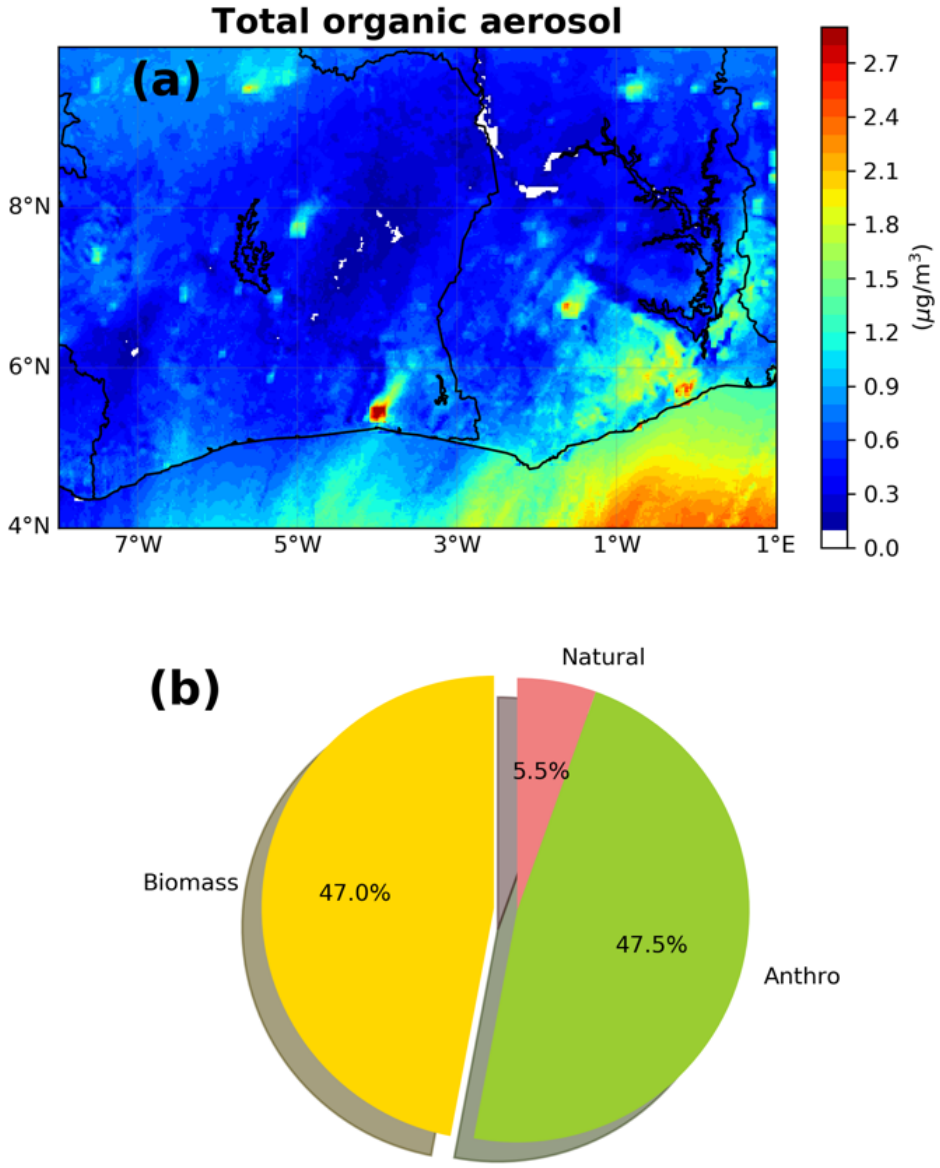

Figure 4.22: (a) Spatial Distribution of Organic aerosol mass concentration over the domain and (b) contribution from different sources (natural, anthropogenic and biomass burning).

Hence, Figure 4.23 illustrates simulated organic aerosol for the outer domain D1 from natural, ANTHRO and FIRE sources. Most of the organic fraction is from anthropogenic and biomass burning sources from our model result. The anthropogenic source of organic aerosols is mainly from the Northern Nigeria and Niger Delta and the cities plume, which are not clearly visible due to the scaling (high values up to 8 $\mu g\ m^{-3}$ over Central Africa). Natural fraction of organic aerosol is very low as seen in the simulation over Domain D2.

In addition to the aerosols, atmospheric composition over West Africa includes traces gases such as ozone, NO_x mainly from anthropogenic activities and CO from both biomass burning and anthropogenic emissions. The diurnal cycle of a coarse aerosol mode is presented with a focus on Abidjan plume in order to determine it evolution during the day and the peak (minimum) hours.

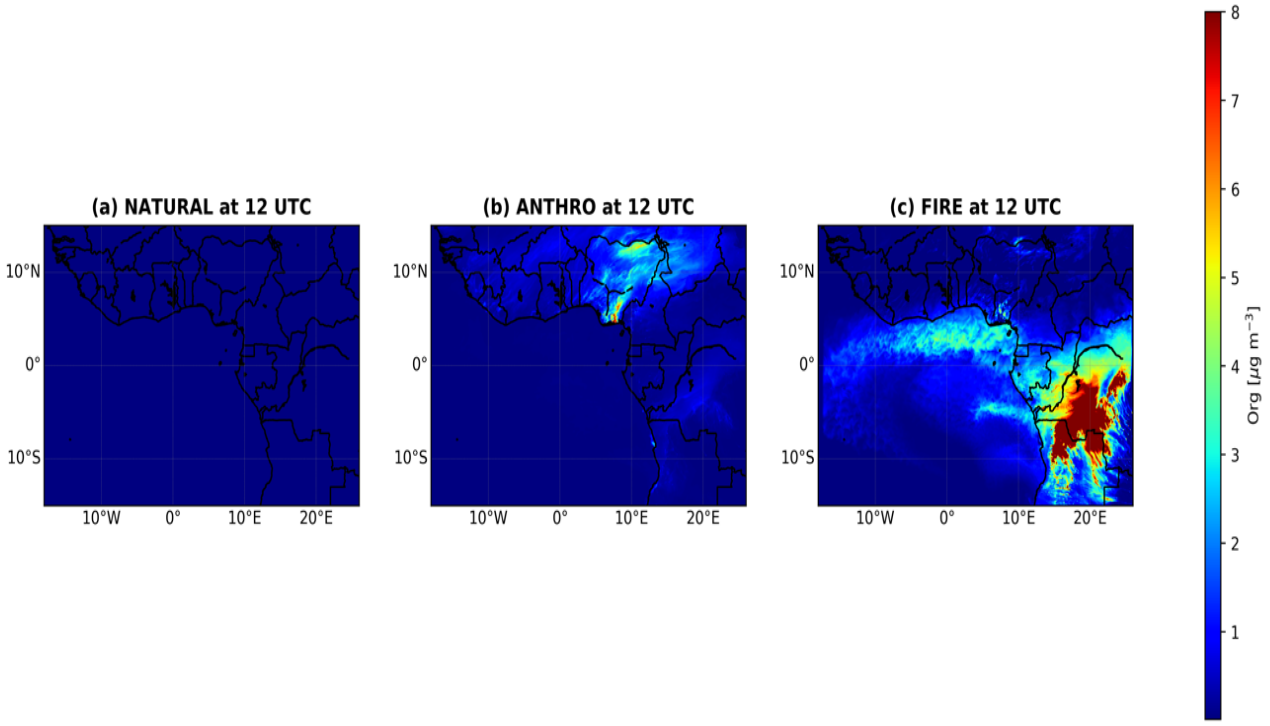

Figure 4.23: Spatial distribution of organic fraction contribution from natural a) anthropogenic b) and biomass burning c) on 06 July 2016.

Additionally, vertical profiles of the trace gases are examined. Figure 4.24 presents the vertical profiles of trace gases CO, Ozone, and NO_x domain averaged. CO mixing ratio shows a constant median value of 220 ppbv within the boundary layer with a quite constant inter-quartile range concentration variation (Figure 4.24a). An increase in CO is observed between 1.2 km and 3km and reached a maximum value of about 350 ppbv around 2 km. This shows the intrusion of the BB plume air masses from Central Africa at that height. Above 3 km CO concentration start decreasing. Ozone profile showed by Figure 4.23b depicts similar characteristic as CO. This pattern agrees with the observation during AMMA campaign (Reeves *et al*., 2010), corresponding to a "S" shaped profile and as well as DACCIWA campaign. The maximum is found around 2 km influences by the air masses from the biomass burning emissions. At this height, the 90th percentile values reach of about 70 ppbv comparable to observed ozone mixing ratios measured at Cotonou on 25 July 2006 during AMMA (Mari *et al*., 2008). The authors argued that peak ozone observed around 650 hPa is the influence of biomass burning aerosols advected into the region and low ozone in the moist air close to the PBL (below 850 hPa). Measurement of ozone profile in Lagos (Sauvage *et al*., 2005) and Cotonou (Mari *et al*., 2008) indicated that biomass burning plumes from Southern hemisphere can have a widespread effect (Reeves *et al*., 2010).

Regarding NO_x mixing ratio, shown in Figure 4.24c, it shows high NO_x in the boundary layer, which revealed urban outflow as the primary source of NO_x in the region and low values far away from the surface with decreasing NO_x concentration upward. However, the possibility of sea breeze effect recirculating urban emissions into the marine boundary layer could have been consistent if we found considerable concentration of NO_x in the marine boundary layer which was not seen in our models results.

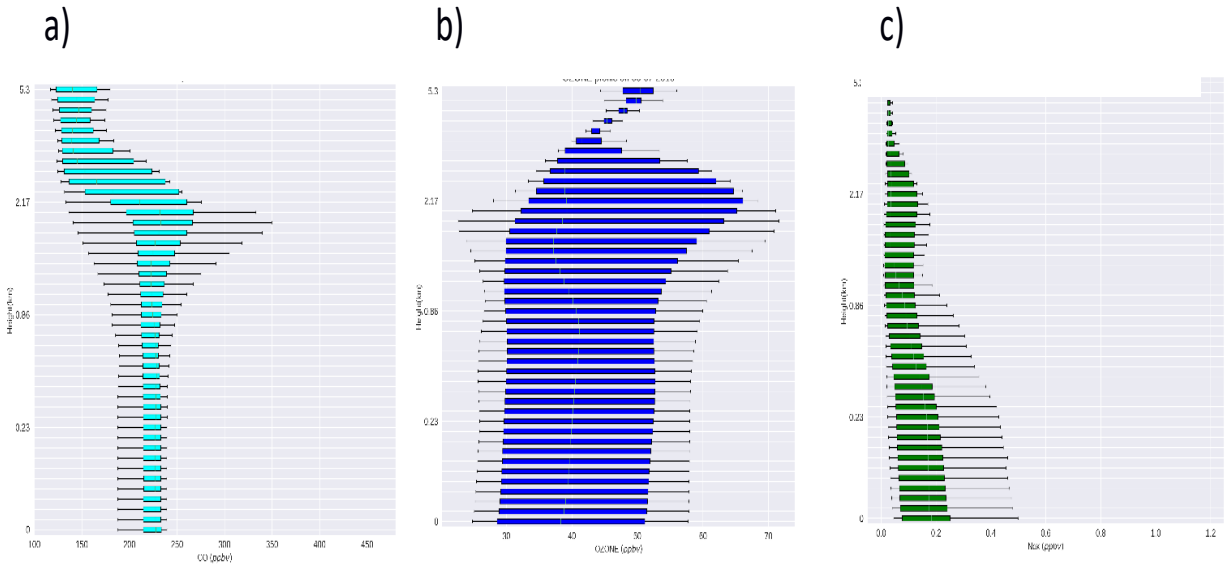

Figure 4.24: CO, Ozone and NO_x mixing ratio vertical profile (up to 5.5 km) of the median concentration, quartiles and 10th and 90th percentiles on 06 July 2016.

The spatial distribution of the surface coarse aerosol mode is presented as a diurnal cycle focusing on Abidjan plume from 00 to 23 UTC on 02 July 2016. The Abidjan's plume is visible as it shows the maximum concentration over the domain Figure (4.25). Peaks values are found early morning before the sunrise, as the aerosols are accumulated below the inversion layer. As soon as the sun rises the heating from the sun reaches the surface leading to the increase of the boundary layer, entraining the mixing of aerosol into upper layer thus, also low aerosol concentration is observed near the surface between 11 and 17 UTC. After the sunset, the PBL decreases, inducing aerosols to again start accumulating close to the surface.

From all above mentioned, local pollution and long-range transport of aerosols are dominant aerosols sources for the period of investigation and COSMO-ART captures the upwind marine aerosol mass concentration as well as that of the city's plumes. However, it fails to capture the contribution of biomass burning in the regional background, thus underestimates the mass concentration over that area. Furthermore, the meteorological condition is a well-established monsoon flows with southerlies wind and rain band shifted from the coastal region to the Sahel (Knippertz *et al*., 2017). Aloft, above the monsoon layer, the wind patterns are easterlies, carrying aerosols westward. The area is dominated by LLC for this particular period, though there are also mid-level and high cloud presents. Consequently, these aerosols affect clouds and radiation, thus modify the energy budget and the clouds microphysics.

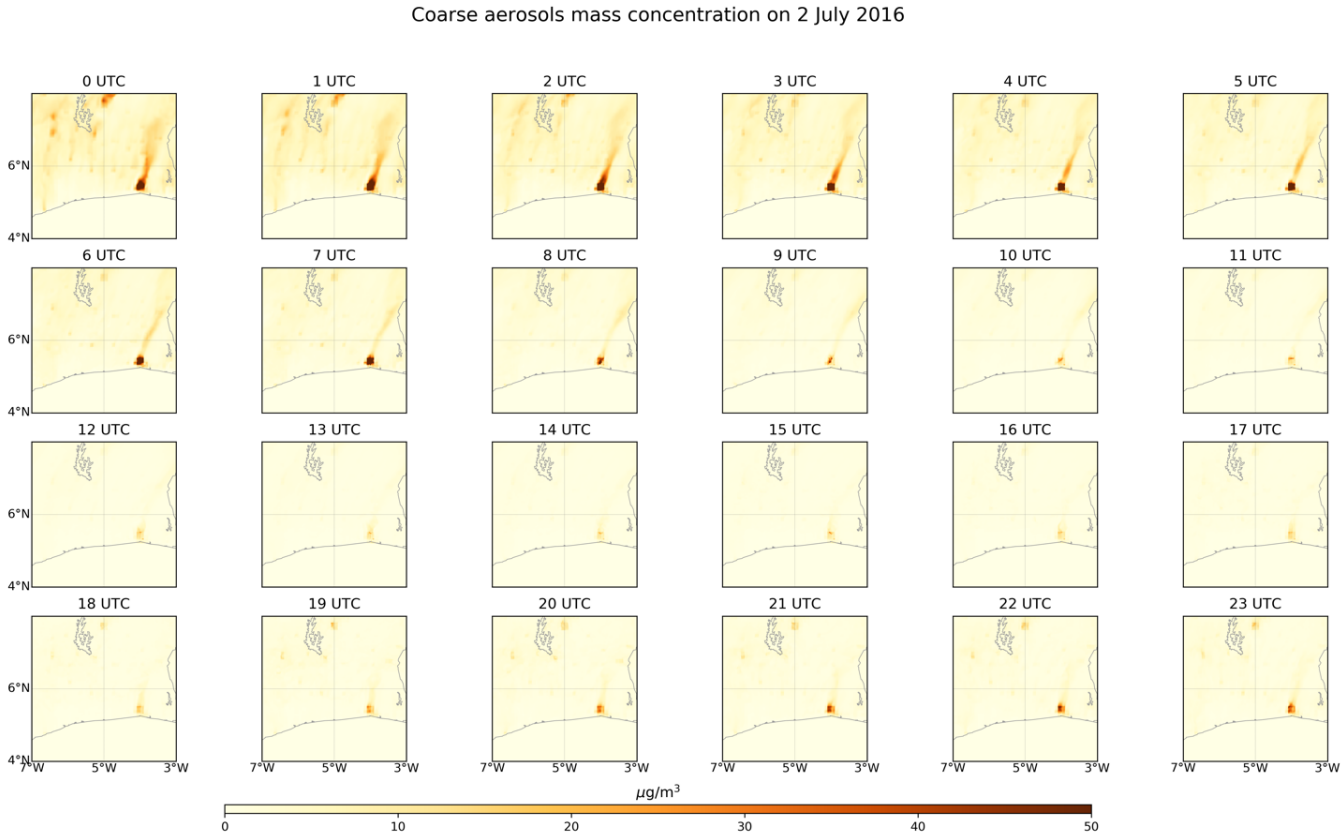

Figure 4.25 Figure 4.25: Temporal evolution of spatial distribution of coarse aerosol mass concentration from 0 to 23 UTC on 02 July 2016.

4.3 Impact of anthropogenic aerosols on the state of the atmosphere

4.3.1 Impact of FIRE (biomass burning emission)

In this section, the impact of FIRE is investigated on both the atmospheric composition and on the meteorological fields. Due to its detrimental effects on the climate through its radiative properties, and its high presence over the Gulf of Guinea region demonstrated through observation and models during the DACCIWA field campaign (Brito *et al*., 2018; Menut *et al*., 2018; Haslett *et al*., 2019), it appears very important to identify firstly the mechanism by which these aerosols mix down and get into the PBL, and then quantify the amount by which it increases the atmospheric composition before examining its adverse effect on the state of atmosphere.

4.3.1.1 Downward mixing of FIRE during the WAM: Case of cloud venting

Cloud venting was discovered for the first time in 1988, as a mean by which cloud transport aerosol and chemical species from the PBL close to the surface into the free troposphere (Ching *et al*., 1988; Cotton *et al*., 1995). A lot of studies (observational and modelling) have demonstrated this phenomenon (e.g. Mari *et al*., 2000; Halland *et al*., 2009). This study investigates rather cloud-induced transport of chemical species and aerosols from FIRE from the mid-level tropospheric layers into the PBL over the Gulf of Guinea and the coastal cities of West Africa. From the one-month simulation conducted in July 2016, one day has been chosen to examine the downward mixing of biomass burning plumes by cloud venting. Focusing on a case study (02 July 2016), the role of convective clouds on the vertical distribution of CO. Figure 4.27 shows the spatial distribution of the simulated near surface (2m) temperature at 12 UTC. At this time of day the temperature is already higher over land than over the ocean. Local temperature maxima are located over cities such as Abidjan and Accra. High temperatures are also simulated in the central part of Ghana near Lake Volta. Modelled

temperatures over the Gulf of Guinea are between 26°C and 28 °C in agreement with observed SST shown in Knippertz et al. (2017). There are clear indications of cold pools related to convective cells developing over the Gulf over Guinea. The hourly analysis of the temperature field (Figure 4.28) shows cold pools appearing around 7 UTC and persisting during the whole day. They are connected to downward motion starting at and above cloud base, bringing air and its constituents from aloft into the PBL.

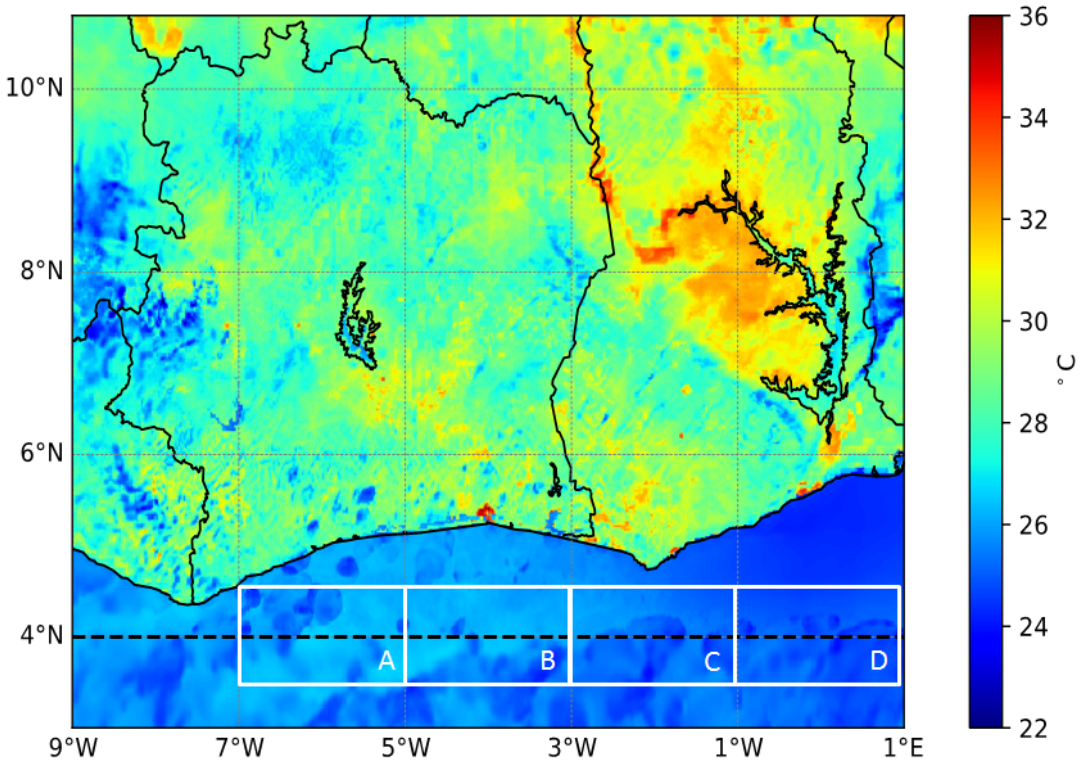

Figure 4.26: 2-m Temperature as simulated by COSMOS-ART over domain D2 on 02 July 2016 at 12 UTC. Note the small-scale cold-pool signatures over the ocean. Different subdomains are defined along 4°N, marked with a dashed line: 7–5°W (A), 5–3°W (B), 3–1°W (C), and 1°W-1°E (D).

Figure 4.27 presents the spatial distribution of cloud and rainfall on 02 July 2016 comparing model results and observation. Satellite retrieved images from EUMETSAT on 02 July 2016 show widespread clouds over SWA and the adjacent ocean, with convective cells located over the Gulf of Guinea south of Cote d'Ivoire at 12 UTC (Figure 4.27b). They produce rain rates of several mm h^{-1} in the course of the afternoon according to GPM-IMERG (Figure 4.27d). the cells over the ocean developed near the border between Côte d'Ivoire and Ghana in the morning hours and propagated slowly westward in the course of the day (Figure 4.28) They form despite anomalously cold coastal waters but may have benefitted from substantially warmer SST along the equator (Knippertz *et al.*, 2017). Mostly moderate precipitation is also observed over land, in central Ghana, around Kumasi as well as along the borders between Côte d'Ivoire with Liberia, Guinea, and Mali.

Total cloud cover and precipitation as simulated by COSMO-ART for 02 July 2016 are shown in Figures 4.27a and c. The whole area is dominated by clouds (Figure 4.27a) with moderate gaps around Lake Volta and over the ocean upwind of Ghana and Côte d'Ivoire. There is reasonable qualitative agreement between the model and observations (Figure 4.27b) but the differences in cloud optical thickness evident from the satellite image make a detailed comparison somewhat difficult. With respect to precipitation, COSMO-ART shows substantially more fine structure than GPM-IMERG. Many localized shower are evident over Côte d'Ivoire and neighboring countries with higher intensities over the hilly terrain in Liberia and along the land-sea breeze convergence parallel to the coast. Larger cells form in the model over the hilly terrain surrounding Lake Volta. The largest and most intense cells are simulated over the ocean with a conspicuous north–south orientation. Despite the differences in resolution there is some good qualitative agreement between model and observations in particular with respect

to the maxima over central Ghana and Liberia. Convection in the north is underestimated and convection over the ocean is overestimated by COSMO-ART in agreement with the cloud biases evident from Figure 4.4. The latter suggests that cloud venting may be somewhat overestimated by COSMO in this specific case, allowing only a rather qualitative assessment.

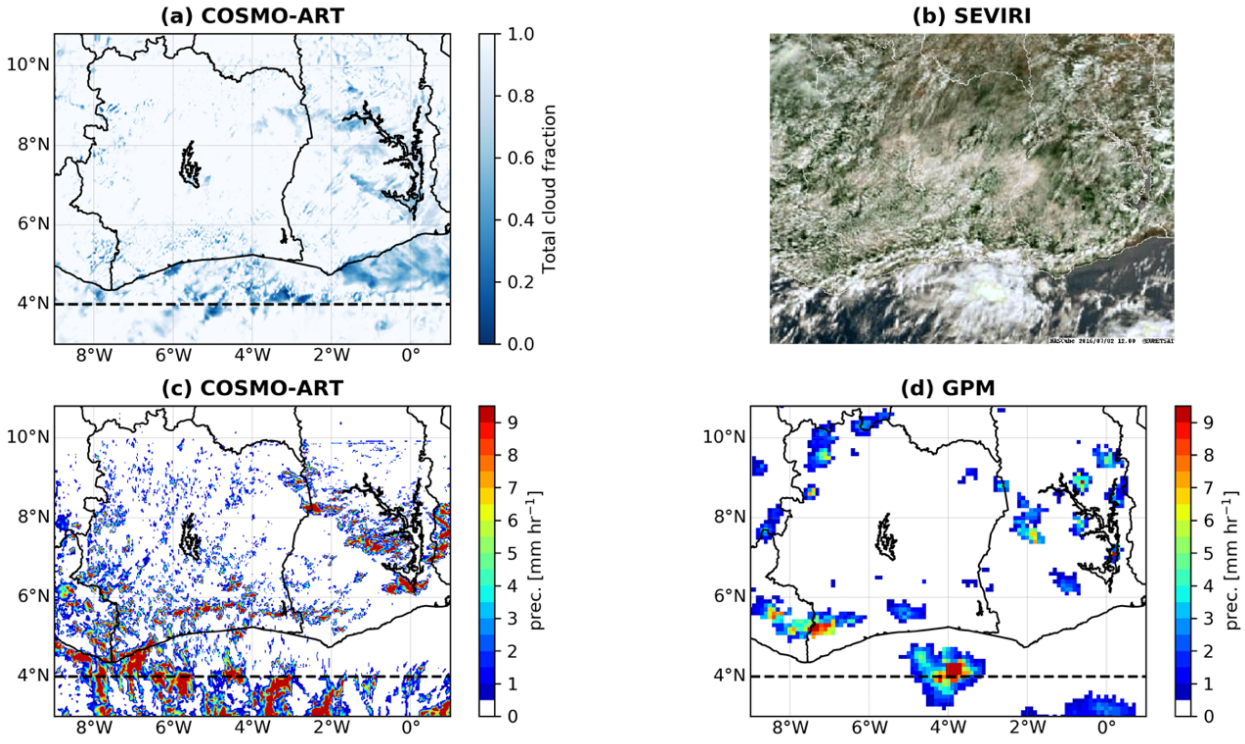

Figure 4.27: Spatial distribution of clouds and rainfall over domain D2 (see Fig. 1) on 02 July 2016. (a) Total cloud fraction simulated by COSMO-ART at 12 UTC. (b) Spinning Enhanced Visible and InfraRed Imager (SEVIRI) cloud visible image from EUMETSAT at 12 UTC (from NAScube http://nascube.univ-lille1.fr). (c) Precipitation rate simulated by COSMO-ART at 18 UTC and (d) corresponding fields from the GPM–IMERG rainfall estimates. The position of the zonal cross-section in Fig. 8 is marked with dashed lines.

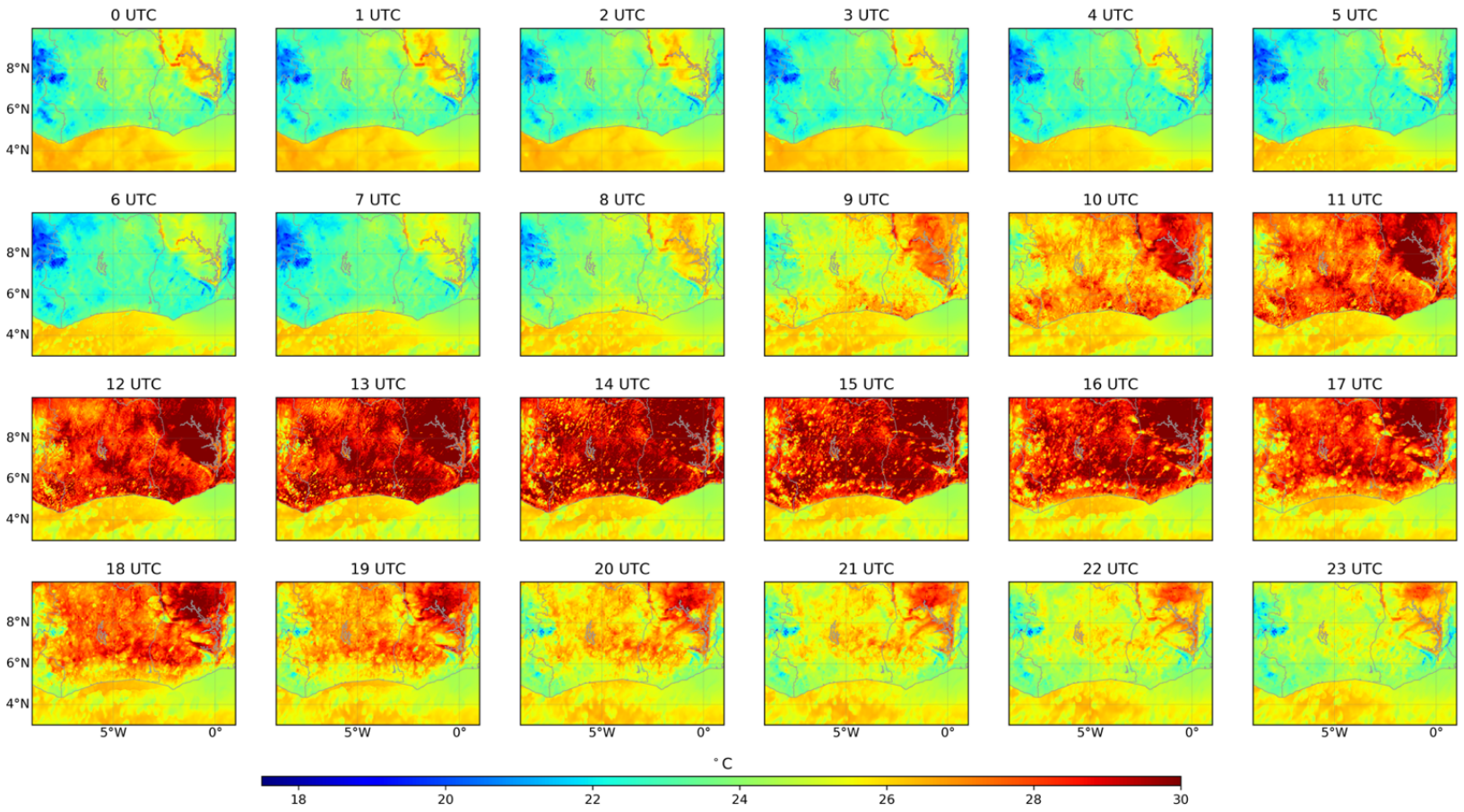

Figure 4.28: Temporal evolution of simulated 2-m temperature spatial distribution on 02 July 2016.

The simulated CO distribution at different level is presented in Figure 4.29 (a) at roughly 500 m in the PBL and (b) at 2900 m at mid-tropospheric height. At 500 m (Figure 4.29a) there is a stark concentration difference between land and ocean with thick pollution plumes over the biomass burning areas in Central Africa (Barbosa *et al*., 1999; Mari **et** *al*., 2008;(Zuidema *et al*., 2016) and over Nigeria. The urban plumes from coastal cities such as Abidjan, Cotonou, Lomé, and Lagos are also visible. These results come from the high anthropogenic emissions used in our study, which have maxima over Nigeria and the big cities along the coast. The simulated hourly CO concentrations (Figure 4.31) reveal that there is a north-eastward transport of CO from the local sources in the PBL further inland with the southerly monsoon flow (Knippertz *et al*., 2017; Deroubaix *et al*., 2018). However, Flamant *et al*. (2018) also showed that parts of the urban pollution re-circulate to the near coastal waters after being mixed into the midlevel easterly or sometimes northeasterly flow. Significantly lower but still considerable CO concentrations are simulated in the marine PBL over the entire eastern tropical Atlantic including the Gulf of Guinea. There is a local enhancement next to the coast stretching from Cameroon to Côte d'Ivoire. At this height level CO is transported with the south-westerly monsoon winds from the Ocean toward SWA coastal cities (see Figure 4.3). Compared to the monthly mean concentration of CO (Figure 4.6), 02 July was characterized by elevated pollution levels, especially over Nigeria.

Aloft at approximately 3 km (Figure. 4.29b) the CO distribution is fundamentally different. Maximum CO concentrations with values of about 400 ppbv are found over the eastern Atlantic Ocean, downstream of the main burning areas in the southern hemisphere. High concentrations stretch far into SWA (e.g. into Burkina Faso), even in areas where 500m concentrations are not all that high as over Côte d'Ivoire. This suggests a relationship to long-range transport of biomass burning plumes. This is

corroborated by much reduced values in a simulation where biomass burning emissions are suppressed (Figure 4.30). The fairly high concentrations at 500m to the west and north of the main plume at 2900m suggest downward mixing into the PBL from aloft. Subsidence within the high-pressure system west of the African continent might also support the downward transport of CO into the boundary layer (Zuidema *et al*., 2016). However, the mechanism is still not clear and we will investigate in the following to what extent oceanic convective clouds support the downward mixing.

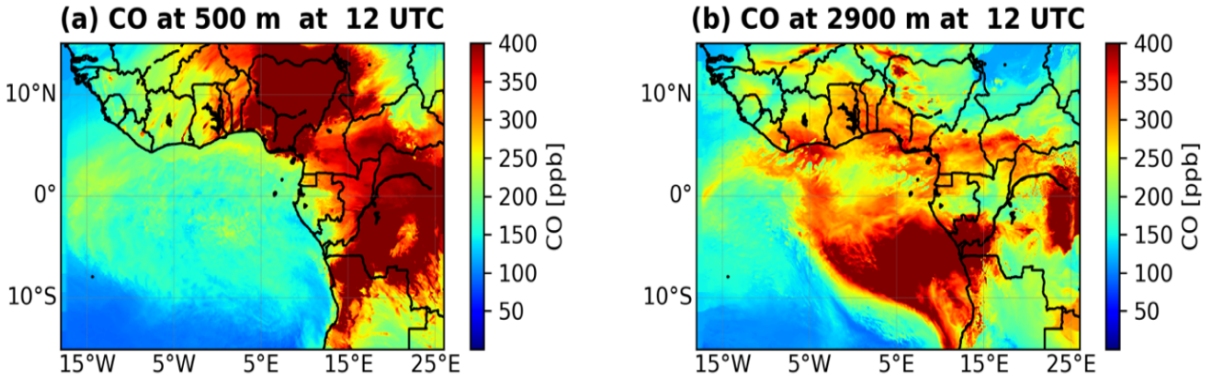

Figure 4.29: CO concentrations on 02 July 2016 at 12 UTC as simulated by COSMO-ART at (a) 500m and (b) 2900 m above ground level with fire emission on.

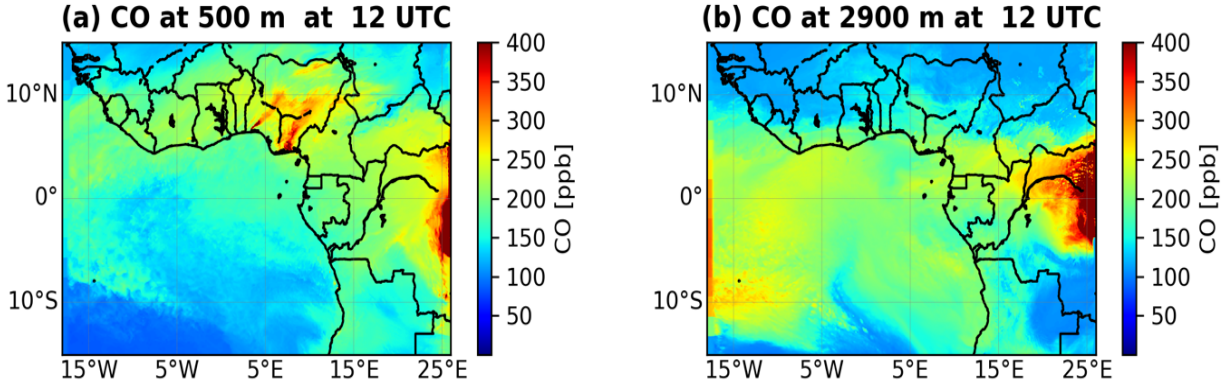

Figure 4.30: CO concentrations on 02 July 2016 at 12 UTC as simulated by COSMO-ART at (a) 500m and (b) 2900 m above ground level with Fire emission off.

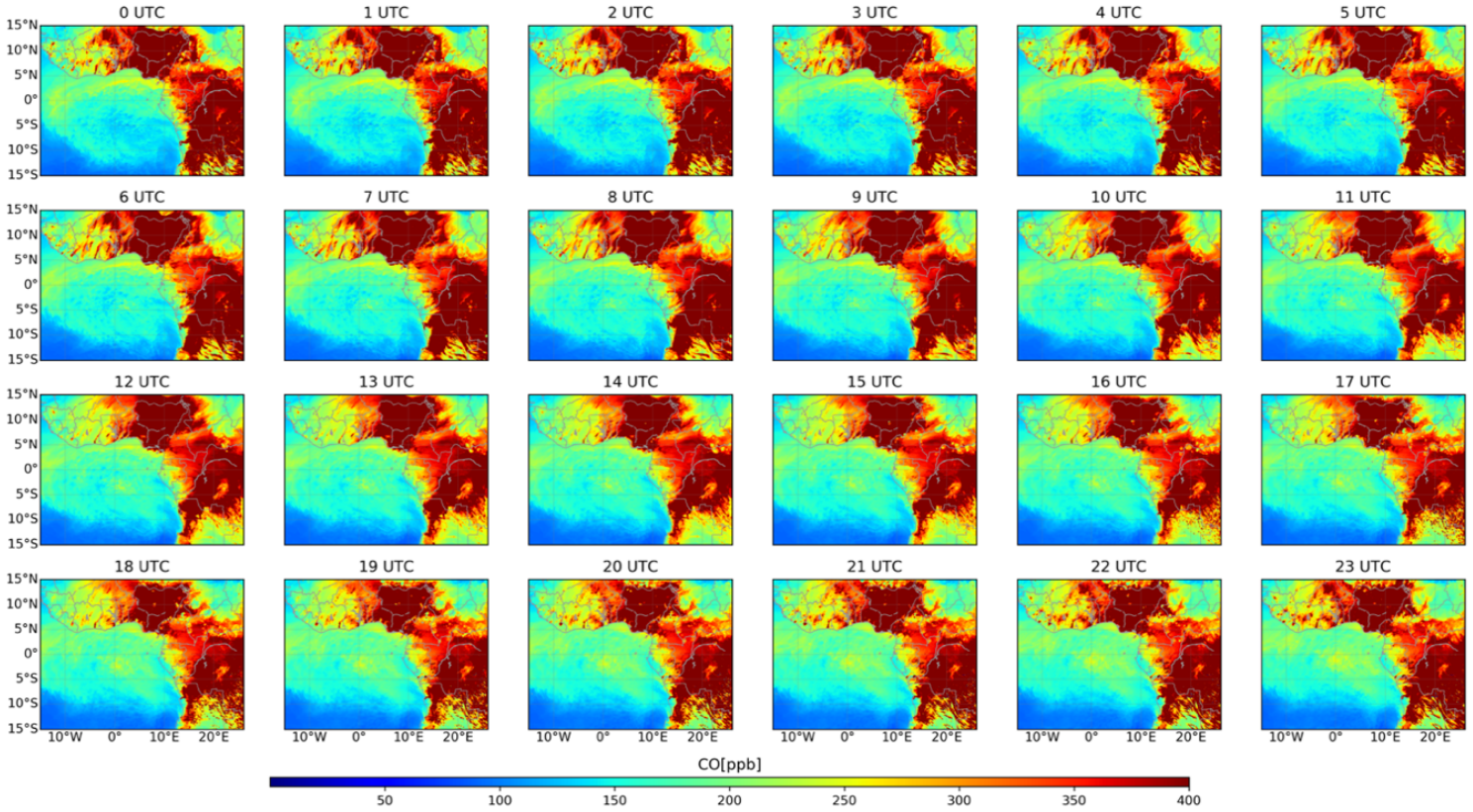

Figure 4.31: Hourly variation of simulated CO surface concentration on 02 July 2016

To test our hypothesis of the role of cloud venting, vertical distributions of CO concentrations and cloud liquid water content from model output are considered (Figure 4.32). Figures 4.32a and 4.32b show simulated zonal cross sections of CO over the Gulf of Guinea at 4°N (i.e. close to the coastal cities of West Africa) over D2 on 02 July 2016 at 12 UTC and 18 UTC, respectively. There is a clear band of high CO concentrations of up to 400 ppbv, mostly between 1 and 3.5km over D2, which is the signature of the long-range biomass burning plumes transport from Central Africa (Mari *et al.*, 2008; Zuidema *et al.*, 2016), possibly affected by larger-scale subsidence.

The belt of high CO concentration is simulated along all longitudes of the domain but is more visible between 10°W to 0° (upwind of Côte d'Ivoire and Ghana) than between 0° E to 5°E. This corroborates the observations that the biomass burning plume is mainly advected in westerly direction (Adebiyi and Zuidema, 2016). In addition, at the height of biomass burning plume, clear patterns with high horizontal concentration gradients are simulated at heights varying from around 1 km up to 4 km. These structures are more pronounced at 18 UTC (Figure 4.32b). They are related to convective clouds simulated and observed (Figure 4.28) over the ocean transporting CO into the PBL from above. Analyzing the simulated diurnal cycle of the vertical distribution of the CO concentration (Figure 4.33) we found that clouds appear after 7 UTC and are persistent throughout the day. Moreover, CO is also visible in the boundary layer and eventually reaches the surface. The meridional cross sections of CO (Figure 4.32a and b) show that concentrations below 1km can reach up to 60% of the maximum located at midlevel height due to downward mixing. Figures 4.32c and d show a meridional vertical cross section of the CO concentration and the specific cloud liquid water content along 6.1°W, close to where convective activity is seen in Figure 4.32a. Areas of high cloud liquid

water content that indicate positive and negative vertical velocities are closely related to the observed patterns in CO.

For comparison meridional cross sections of CO is analyzed corresponding to Figure 4.32c but at 4°W and 1°E over domain D2. At 4°W (Figure 4.32 e) there is much less evidence of convective mixing than at 6.1°W and concentrations in the PBL are reduced. There is, however, a slight increase northward that may come from turbulent mixing or advection into the section. In contrast to that, the cross-section at 1°E (Figure 4.32f) shows a much weaker biomass burning plume in agreement with Figure 4.29b. This appears to be the result of the bulk of the plume travelling westward over the ocean before turning northward into SWA. Also, here, there are indications of a slow decent of the lower boundary of the plume that may come from subsidence or turbulent mixing. Finally, it is also interesting to place the mixing near SWA into the larger regional context. Meridional cross sections along 0° and 10°E but reaching from 10°S to 20°N illustrate the full complexity of the plume evolution. At 0°E (Fig. 4.32g) there is a distinct biomass burning plume centered at 5°S with some indications of northward transport around 1000m AGL and individual mixing events. North of the coast (arrows in Figures 4.32g and h) there is a complicated vertical structure with local near-surface emissions, overhead advection, and vertical mixing to various degrees, particular during the daytime shown here. Farther to the east at 10°E (Figure 4.32h) the situation bears some similarities but the local emissions from Nigeria appear to play a larger role over land.

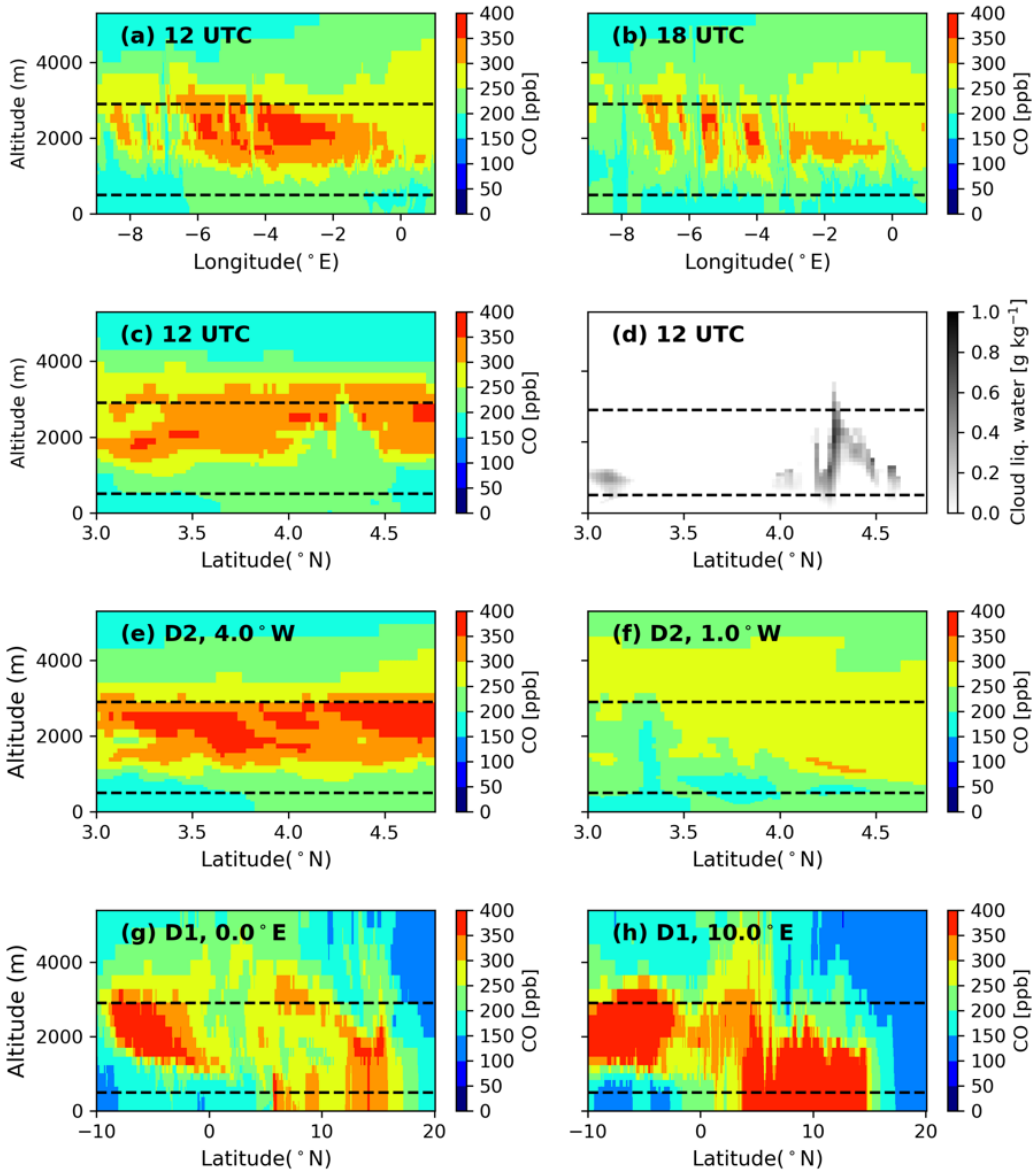

Figure 4.32: CO distributions as simulated by COSMO-ART over domain D1 and D2 (see Fig. 1). Zonal vertical cross-sections at 4°N of the CO concentration at (a) 12 UTC and (b) 18 UTC on 02 July 2016 for domain D2. (c) Meridional vertical cross-section at 12 UTC at 6.1°W and (d) corresponding cloud liquid water content, both for domain D2. (e) and (f) As (c) but for 4°W and 1°E, respectively. (g) and (h) Meridional vertical cross-sections over D1 at 0°E and 10°E, respectively.

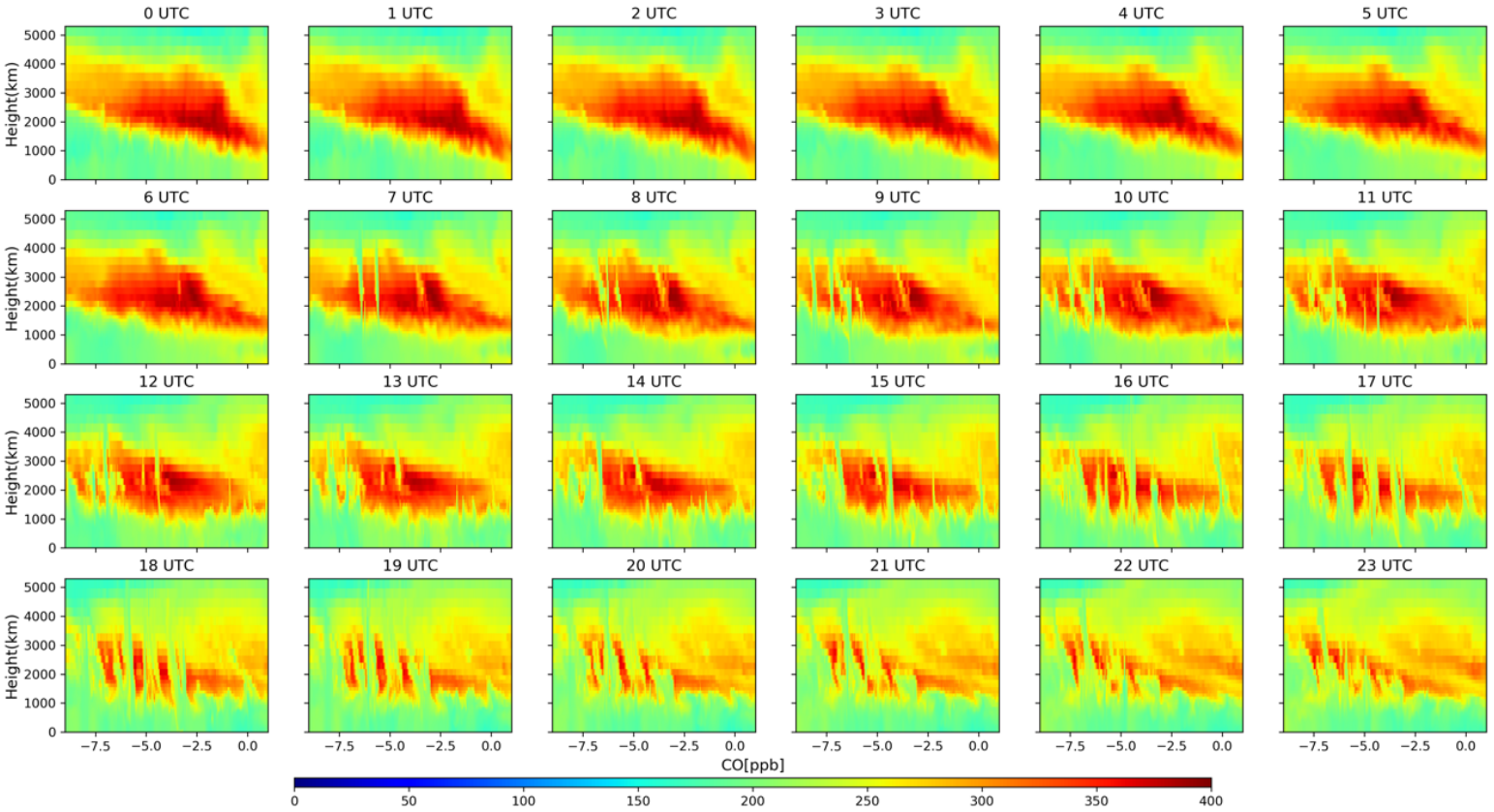

Figure 4.33: Temporal evolution of the zonal vertical cross-sections at 4°N of the CO concentration on 02 July 2016.

In order to quantify the downward mixing of the biomass burning plume into the PBL by cloud venting over the Gulf of Guinea idealized numerical experiments were carried out. For the simulations initialized at 02 July 2016 at 00 UTC initial profiles of the tracer were prescribed within the domains D1 and D2. Directly at the lateral boundaries the tracer concentrations were set to zero and kept constant during the time integration. This was done to assess the horizontal transport of the tracer. The idealized tracer has a concentration of 1 ppmv between 2 and 4 km and is zero elsewhere. Chemical reactions as well as dry deposition are neglected. With this configuration the standard simulation is repeated for each case. This procedure allows to quantify the percentage of mass being mixed into the boundary layer by cloud venting that was originally located between 2 and 4 km above ground. The simulations were carried out for two days. Figure 4.34 shows the percentage of mass located between 2 and 4 km, below 1 km, and the sum of the two. All values are averaged between 9°W and 1°E.

Over land, i.e. between 5 and 10°N, (Figure 4.34d) the vertical exchange reaches 2 km in the late morning hours. The mixing process stops when the convective boundary layer breaks down and then continues again the next morning. Tracer mass is lost due to advection out of the domain by the AEJ as shown by the declining red line. Over the ocean at 5° and 0°S (Figures 4.34a and b), where mostly shallow cumuli are present, the concentration in the layer between 2 and 4 km stays almost constant. The increase of the concentration in the layer below 1 km is mostly due to horizontal transport, either from CO that is mixed into the PBL farther south or over Central Africa itself before a westward transport. This leads to a net increase in the sum of the two layers reaching above 100% at the end of the two periods considered in Figure 4.34. Over the Gulf of Guinea between 4 and 4.7°N there is a clear decrease of CO in the layer between 2 and 4 km and an increase of mass below 1 km.

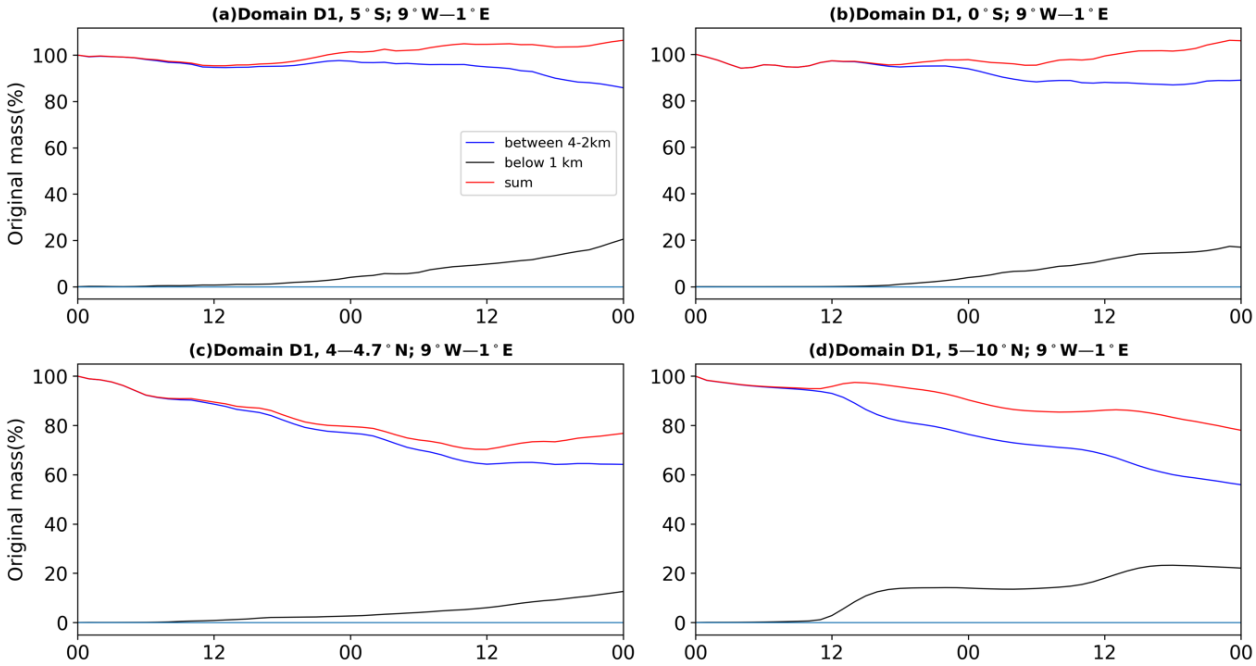

Figure 4.34: Time evolution of the idealized tracer experiment on 02 and 03 July 2016 over Domain D1. Shown are changes in original mass in % between 2 and 4km (blue), below 1km (black), and the sum between the two (red). Fields are averaged from 9°W–1°E along (a) 5°S (southeastern Atlantic), (b) 0° (equatorial cold tongue), (c) 4–4.7°N (Gulf of Guinea), and (d) 5–10°N (inland SWA).

As the temperature of the sea surface stays constant over the course of the day and the boundary layer usually stays rather shallow, this increase is due to downward mixing due to convective clouds as illustrated above.

Figure 4.35 shows results for the model domain D2 and for the areas A–D indicated in Figure 4.27. In this configuration, the marked decrease of the tracer concentration in the layer between 2 and 4 km above surface is partly due to the vertical mixing induced by convective clouds and partly due to the advection of low concentrations from the lateral boundary. The latter is indicated by a consistently faster depletion from east to west, i.e. from D to A. The former is evident from marked individual mixing events, leading to bumps in the below 1km layer. This is a strong indication that cloud venting does in fact contribute to mixing biomass burning aerosol into the PBL.

To investigate this further, Figure 4.36 shows the final mixing state in the layer below 1km after two days of integration, i.e. the right-hand-side intercept of the black curves in Figure 4.34 but for steps of 1° latitude. Plotted against SSTs for the same longitudinal range, a clear correspondence is evident. Both mixing and SSTs have a marked minimum around 2°S. To the south of this SSTs increase moderately but the CO mass fraction is largely enhanced (>27%), while to the north SSTs are strongly increased but not so much the mass mixing (14–17%). This is likely a reflection of the much larger CO concentrations aloft in the southern area (see Figure 4.29). The possibly more effective cloud venting in the north is not able to compensate this effect.

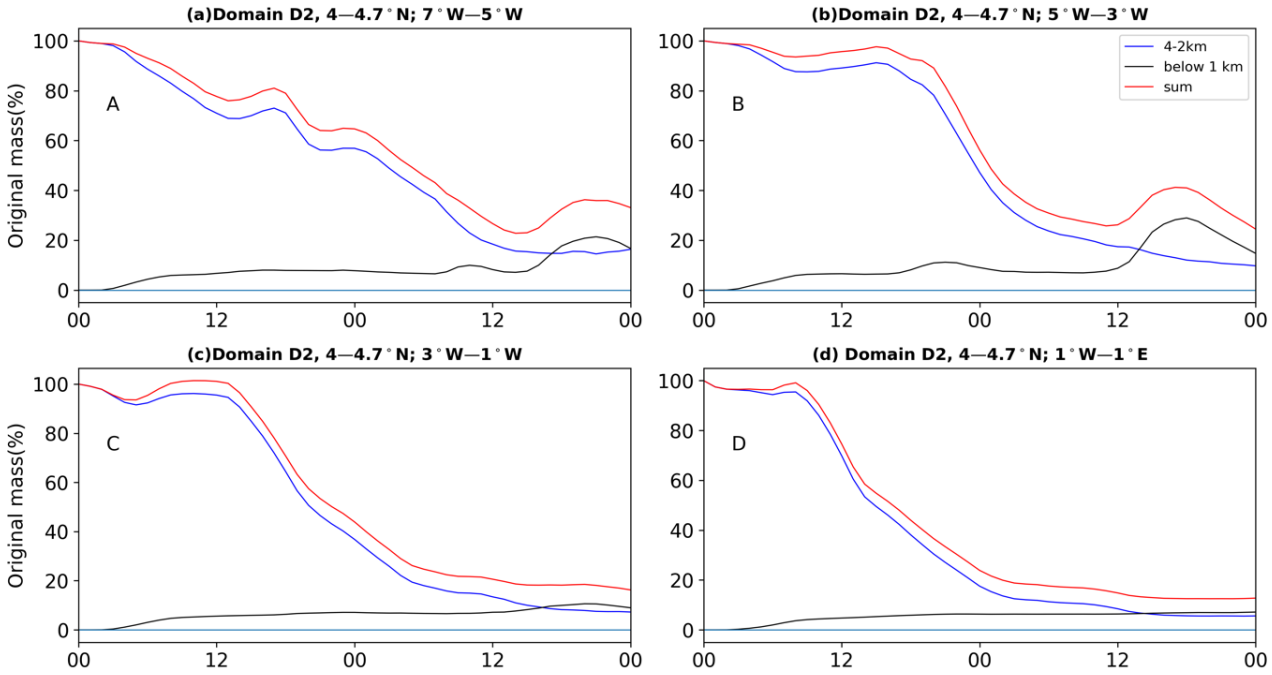

Figure 4.35:Time evolution of the idealized tracer experiment on 02 and 03 July 2016 over Domain D2. Shown are changes in original mass in % between 2 and 4km (blue), below 1km (black) and the sum between the two (red). Fields are averaged from 4 – 4.7°N along subdomains according to Figure 4.27 (a) A, (b) B, (c) C and (d) D.

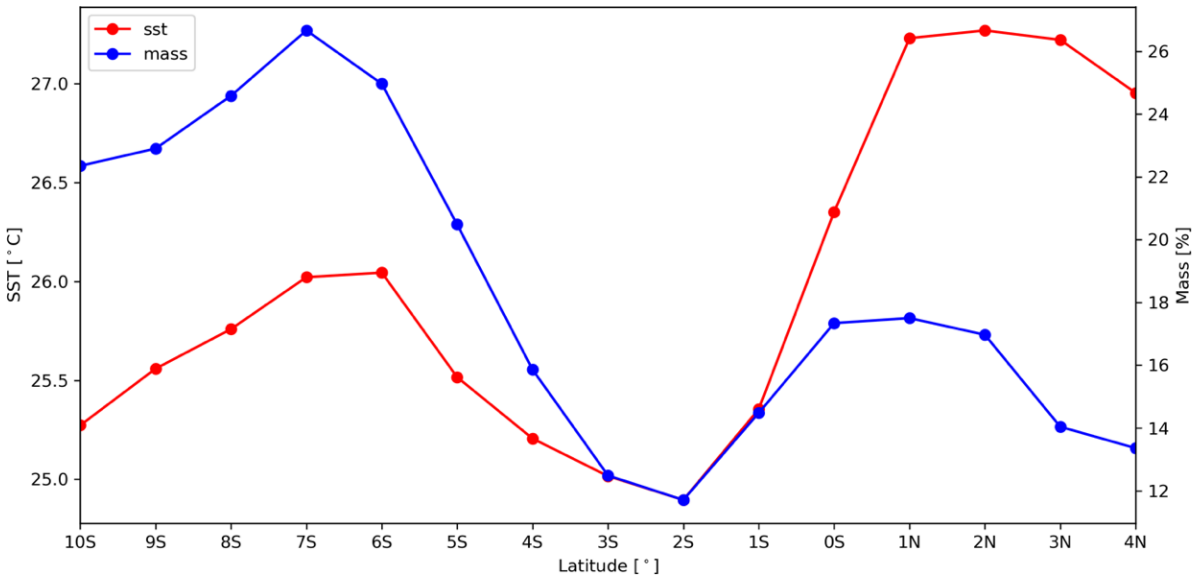

Figure 4.36: Relationship between sea surface temperatures (SST) and vertical mixing of CO. CO masses in % (in blue) correspond to the values for the below 1-km layer at the end of the time window shown in Figure 4.33 but for steps of one degree latitude. SSTs (in red) are from the Advanced Very High-Resolution Radiometer (AVHRR) and were averaged in the same way as the CO fields.

In summary, it appears that convective clouds are responsible of downward mixing of biomass burning aerosols from aloft into the PBL below 1km up to 20% which could be dangerous for people leaving near the coastal regions as far as health is concerned. In fact, Menut *et al*. (2018) showed that these aerosols (FIRE) are mainly organic aerosol and primary particulate matter (PM). It is well documented that PM, penetrate the thoracic region of the respiratory system as they are small enough and inhalable (Bae and Hong, 2018). These FIRE emissions will obviously have some impact on the meteorology which will be introduced the next section.

4.3.1.2 Impact on clouds

Figure 4.37 shows the domain joint histogram of clouds droplets number concentrations against the cloud effective radius (a) for FIRE case scenario and (b) for NO FIRE case scenario referring to simulation with FIRE turn off. The simulation is performed for domain D2, where aerosol radiation and aerosol cloud interaction are considered.

The cloud droplet number concentrations (CDNC) increase in presence of biomass burning aerosols (fire case) compared to the case where biomass burning aerosols are neglected (No fire case). This is due to the abundance of aged accumulation mode aerosols in the fire case. This increase in CDNC is accompanied by a shift in the cloud effective radius towards smaller values. This finding verifies the Twomey effect, which suggest that in a polluted case, more aerosols lead to smaller cloud droplets size formation with high number concentration. This implies that FIRE aerosols modify the cloud radiative forcing, which could have great impact on the atmospheric condition over the area of interest. From our models results, 27% of CDNC increase is observed over the Gulf of Guinea (3-4°N; 9°W-1°E) and 7.5 % increase over D2 domain averaged for the whole day. Our results corroborate with the findings of Rosenfeld *et al.* (2019) showing that FIRE emissions have an effect on cloud droplet size distribution over the

Ocean. The impacts of FIRE on cloud optical properties observed through our simulations indicate almost no change in the cloud liquid water (Figure 4.38). Low values of aerosols water are simulated with an increase from surface to a peak value around 1 km, and then sharply decrease above 1km towards zero.

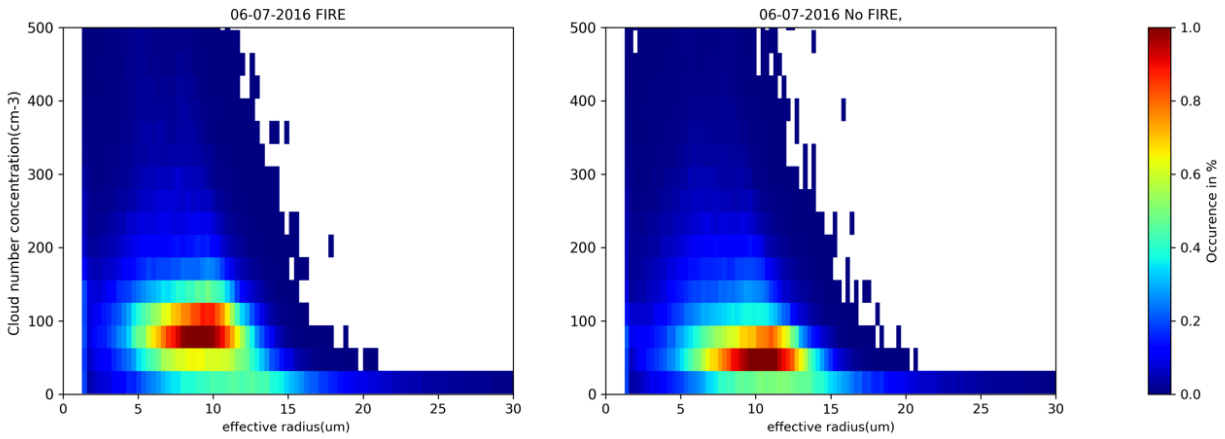

Figure 4.37: Domain joint histogram of cloud droplet number concentration against cloud effective radius calculated for all the grids points for FIRE case (left) and No FIRE (right).

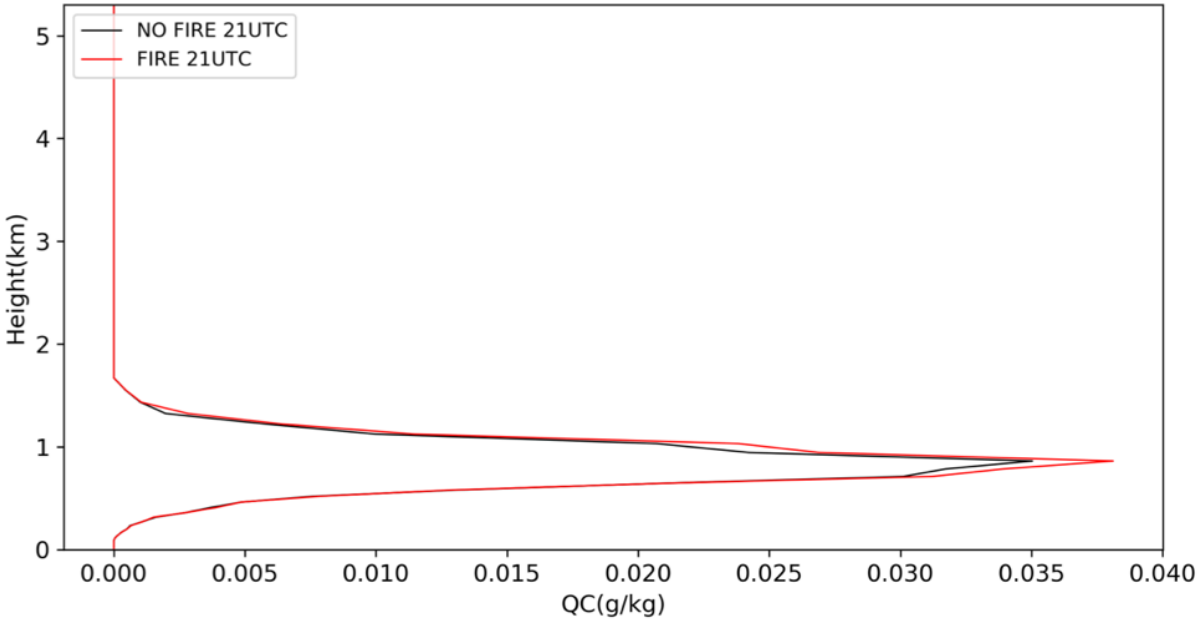

Figure 4.38: Cloud liquid water vertical profile domain averaged on 06 July 2016.

4.3.1.3 Impact on radiation

Figure 4.39 shows the temporal variation surface shortwave (SW) radiation difference (Fire – No Fire) averaged over the Ocean (top panel) and over domain D2 (bottom panel). The temporal variation of SW difference shows a diurnal cycle, minimal during the night and increases during the day with a peak value around 12 UTC. Biomass burning aerosols radiative forcing for free cloud pixels can reach up to 65 W/m^2 (25 W/m^2) domain average over the ocean (over the whole domain D2) whilst it reached 50 W/m^2 (20 W/m^2) over the Ocean (land) for cloudy pixels. It has been highlighted that FIRE layers reduce the amount of solar energy reaching the surface, cooling the near surface air and also increase the diffuse radiation fraction over a large area affected by Fire smoke (Moreira *et al*., 2017). Areas affected by large intrusions of Fire aerosols experience an increase of aerosols optical thickness which exceed 1. Walter *et al*. (2016) investigating the impact of forest fires in Canada during July 2010 using COSMO-ART found that downwelling surface shortwave radiation is reduced up to 50%. In Brazil Amazon and Zambian savanna sites established during a large-scale atmospheric experiment, Schafer *et al*. (2002) found a relative reduction in total irradiance at surface ranging from 16% for an aerosol optical thickness (500 nm) of 1.0 for the Brazilian sites to an average rate of 22% for the African sites. For cloudy pixels (in presence of clouds), the aerosols radiative forcing reached up to 50 W/m^2 (20 W/m^2) over the ocean (over the whole domain D2). As the cloud optical depth is larger than that of the aerosol, in presence of clouds, it reduces the aerosol radiative properties. The decrease of surface SW radiation was expected, as aerosols directly reflect or scatter radiation, thus leading to a cooling effect, which in turn reduces the atmospheric stability and, thus, the surface fluxes called semi-direct effects. This result agrees with the findings of Thornhill *et al*. (2018). The FIRE effect on precipitation is very small with a slight decrease of 2.7%

(Figure 4.40) which in contrast to other studies shows significant reduction of precipitation (14.5%) (Thornhill *et al*., 2018). The latter study was conducted for 30 years whereas our precipitation average is done over 2 days (05–06 July 2016). Another reason is precipitation band for this period shifted from the coast to the Sahel, thus very little precipitation events occurs during this period, though COSMO-ART shows precipitation for almost the whole month of July 2016. The reason for choosing this period is that this study aims to quantify the impact of aerosols on clouds and radiation, and the post onset period (22 June–20 July 2016) was characterized by frequent clouds covers over the Gulf of Guinea region according to (Knippertz *et al*., 2017). However, long-term simulation is necessary to really validate the precipitation over the region and quantify the possible impact of Fire on precipitation over the Gulf of Guinea region.

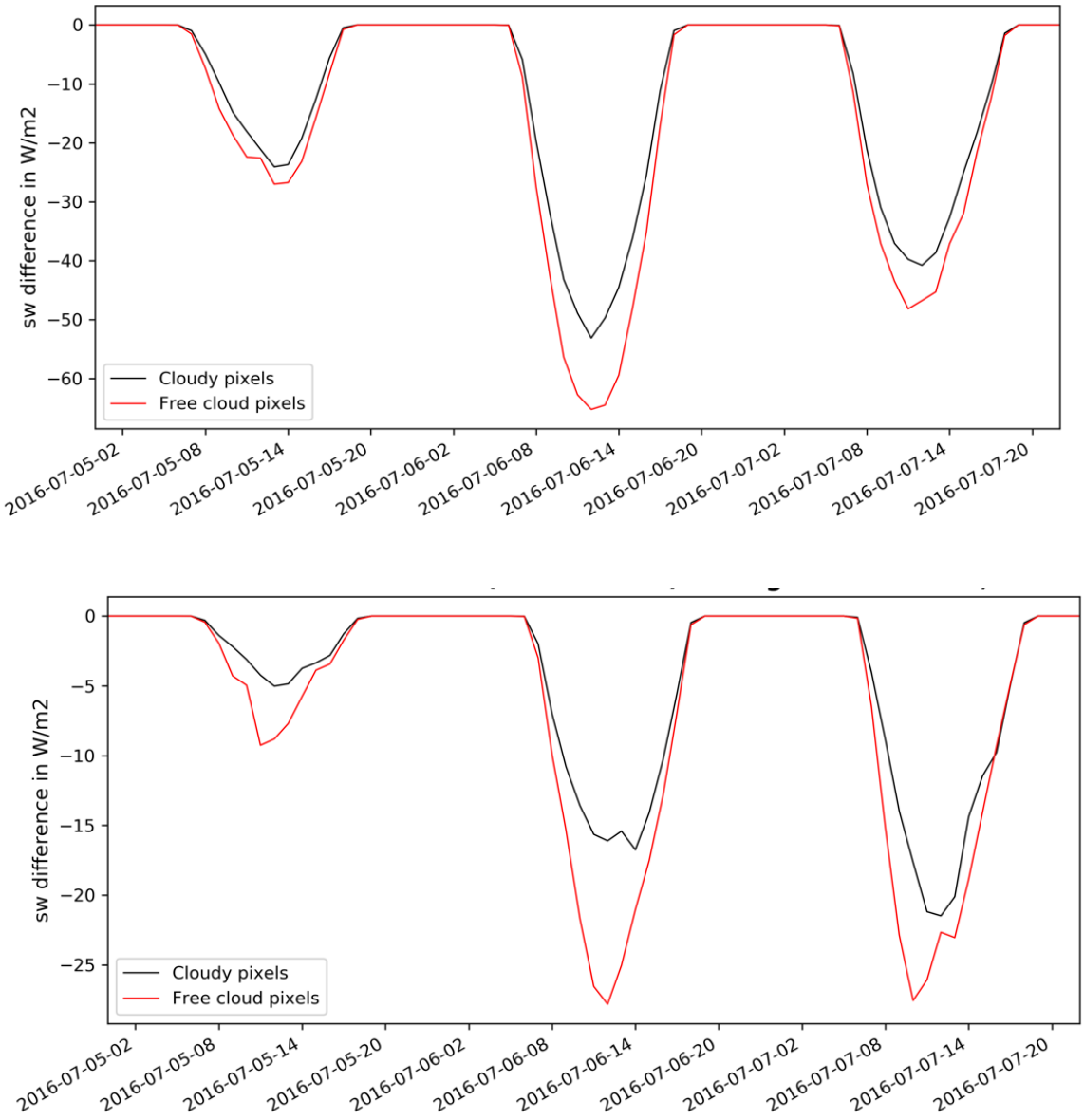

Figure 4.39: Temporal evolution of surface SW radiation domain averaged over the Ocean (top panel) and over Land (bottom panel) from 05-07 July 2016.

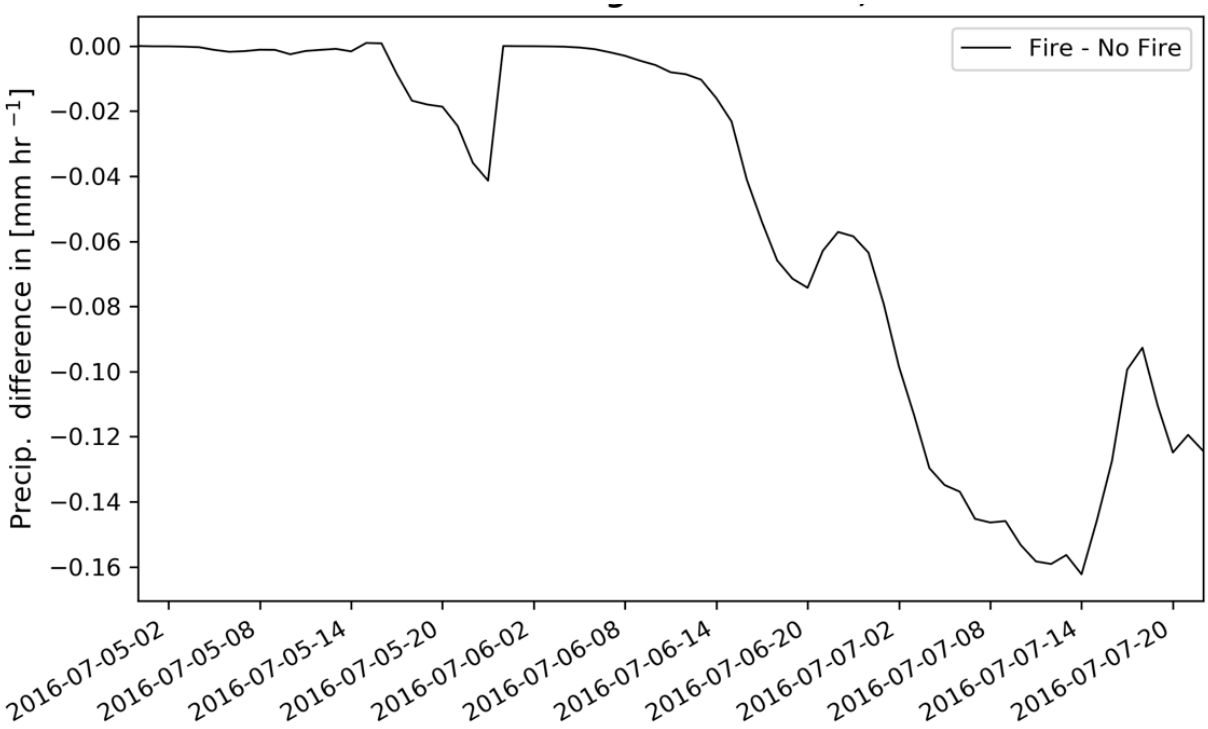

Figure 4.40: Temporal variation of precipitation mean difference between Fire and No Fire experiments.

4.3.1.4 Impact on atmospheric composition

In addition to the investigation of the impact of FIRE on the meteorology over the domain, their relative contribution to the atmospheric composition is also examined. The spatial distribution of the surface Organic aerosol (OC) concentration ($\mu g/m^3$) is presented in Figure 4.41, over both domains, D1 and D2. The two panels (Figures 4.41 b and d) depict the contribution of FIRE in the organic fraction concentration. It is marked by high values (12 $\mu g/m^3$) over Central Africa where FIRE occurs (Figure 4.41b). Moderate values of OC concentration (4 $\mu g/m^3$) can be observed over the Gulf of Guinea, as the biomass burning plume above the monsoon layer is advected westward by a jet across the Eastern Atlantic Ocean and the Gulf of Guinea, and coastal cities over West Africa during this period of the year (Chatfield *et al*., 1998; Mari *et al*., 2008). After being transported into the monsoon layer through cloud venting (Dajuma *et al*., 2019, in review) or subsidence (Flamant *et al*., 2018), it is carried by the monsoon flow northward (Knippertz *et al*., 2017; Deroubaix *et al*., 2019). These simulated OC concentrations over the Gulf of Guinea and their influences on coastal cities are more visible on D2 (Figure 4.41d) simulated with high resolution (2.5 km). When the FIRE emission is turned off, the most visible plume result from local pollution activities taking place over Lagos and the Niger Delta in southern Nigeria (Figure 4.41a). The cities plumes (Abidjan, Accra) are also visible with low values (Figure 4.41c) but increase when FIRE is considered (Figure 4.41d). This supports the finding that FIRE increases the level of pollution over coastal cities over West Africa (Menut *et al*., 2018). It is worth noting that OC concentration is underestimated by our model mainly inland, but it still performs quite well over the marine domain. Figure 4.42 shows the vertical profile of OC averaged over the marine domain and over the whole domain D2. Two distinct layers are depicted from the aerosol vertical profile in the Fire case. It shows less

variation in the PBL below 1 km and start increasing with altitude due to the intrusion of air mass from FIRE. Measurements during AMMA campaign demonstrated that accumulation aerosols mode increases after the monsoon onset over West Africa, thus dominates Aitken mode during the post monsoon period (Matsuki *et al*., 2010). Haslett *et al*. (2019) from observation highlighted the dominance of accumulation mode in the background concentration over Gulf of Guinea regions. Above 2 km where the maximum FIRE is located, it starts decreasing quickly. The profile of organic aerosol in NO FIRE case does not vary much with increasing height, showing a quite constant profile. The domain averaged mean organic aerosol mass concentration increases of about 2 $\mu g\ m^{-3}$ from NO FIRE to FIRE case at the surface which is not negligible.

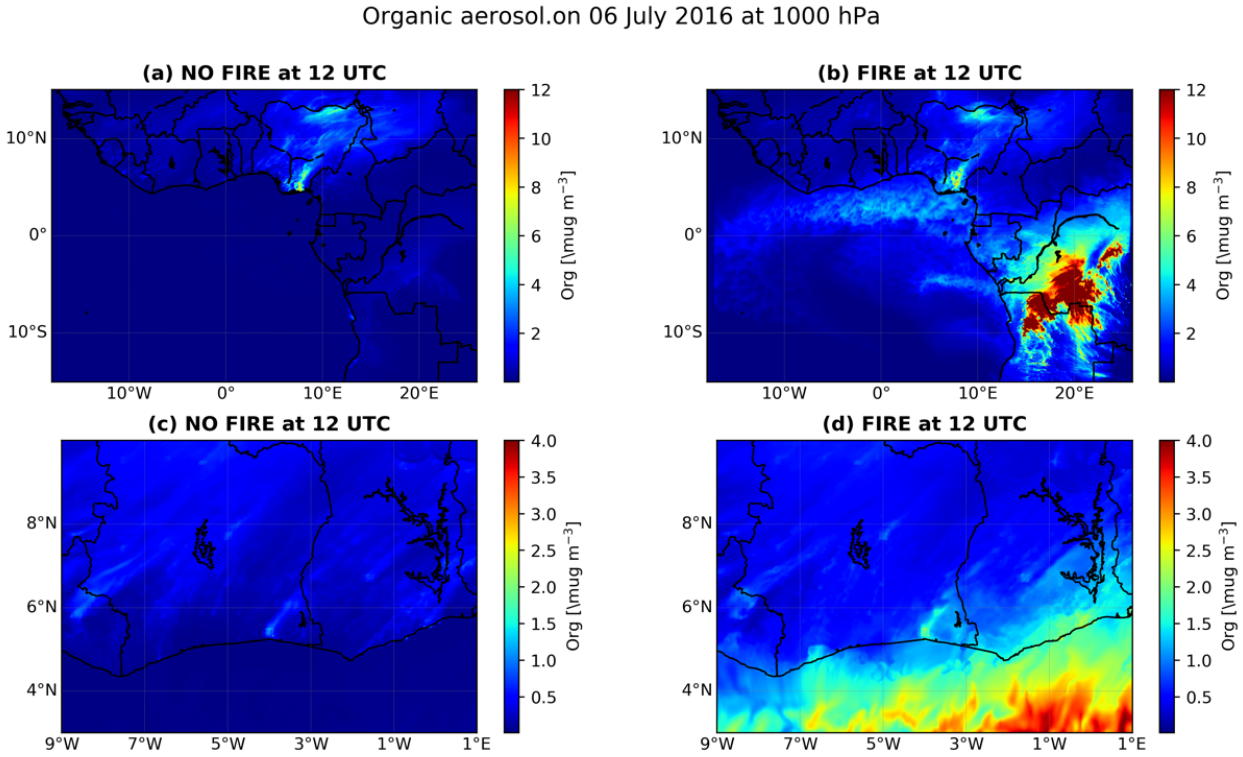

Figure 4.41: Simulated surface organic aerosol spatial distribution over domain D1 (a, b) respectively with NO FIRE (a) and FIRE (b), and over Domain D2 (c, d) respectively with NO FIRE (c) and FIRE (d).

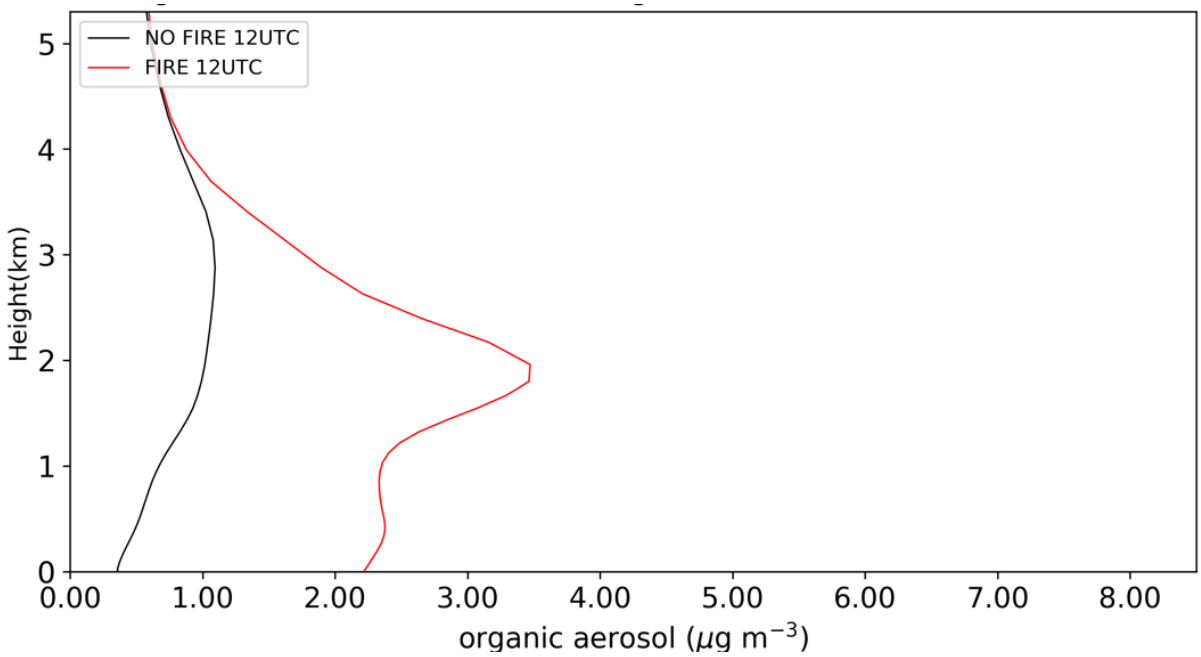

Figure 4.42: Vertical profile of organic aerosols fraction averaged over Domain D2 on 06 July 2016.

This study agrees with the findings that aerosols from smoke (biomass burning) are mainly composed of organic carbon (Zhang *et al*., 2009). Lin *et al*. (2014) using model simulation showed that 34% of the AOD change was attributed to organic carbon over Indochina, whilst the contribution of black carbon to AOD was about 4% from biomass burning emissions. Our study analyses the impact of FIRE on the anthropogenic AOD and find out that 36% of increase of AOD is attributed to biomass burning aerosols (in general), though it is mainly dominated by organic aerosols. Table 4.4 summarizes the effects of FIRE on both meteorological field and aerosols and chemical species. Figure 4.43 presents the diurnal cycle of the AOD averaged over Domain D2 on 06 July 2016 for FIRE (red) and NO FIRE (black). The temporal variation of AOD box averaged over D2 is analyzed. AOD depicts a diurnal cycle, with high values during night and early morning due to the absence of convection. Aerosols accumulate at night and early morning due to the absence of insolation, source of turbulence mixing. After 8 UTC, the AOD starts decreasing with increasing PBL due to vertical mixing till 17 UTC where the sunset occurs. High AOD values is observed during the night and lower values during the day, closely linked to the diurnal cycle of the PBL depth. The two AOD (Fire and No Fire) show similar pattern. The only difference is AOD is high in Fire case compared to No Fire case due to the biomass burning aerosols. It is worth noting that the simulated AOD for the anthropogenic aerosols, thus does not include AOD from dust and sea salt. The reason being that the impact of anthropogenic aerosol (biomass burning aerosols) is investigated. Figure 4.44 presents the spatial distribution of the simulated AOD as a difference between FIRE and No FIRE. Obviously, the increase of AOD as a result of FIRE is more pronounced over the Ocean (upwind marine) and south of the model domain (coastal cities) will a value up to (0.4) than inland (above 7 ºN), showing a great influence of FIRE on the coastal cities. There is a south-north

decreasing gradient of AOD FIRE influence due to the extent to which the monsoon flow transports the biomass burning plume northward. Our study revealed a closed link between the AOD and the FIRE emissions as suggested by Reddington *et al*. (2015). Thornhill *et al*. (2018) found a 71% increase of AOD as a result of biomass burning but the result was computed for long-term. The signature of FIRE is confirmed through the AOD analysis.

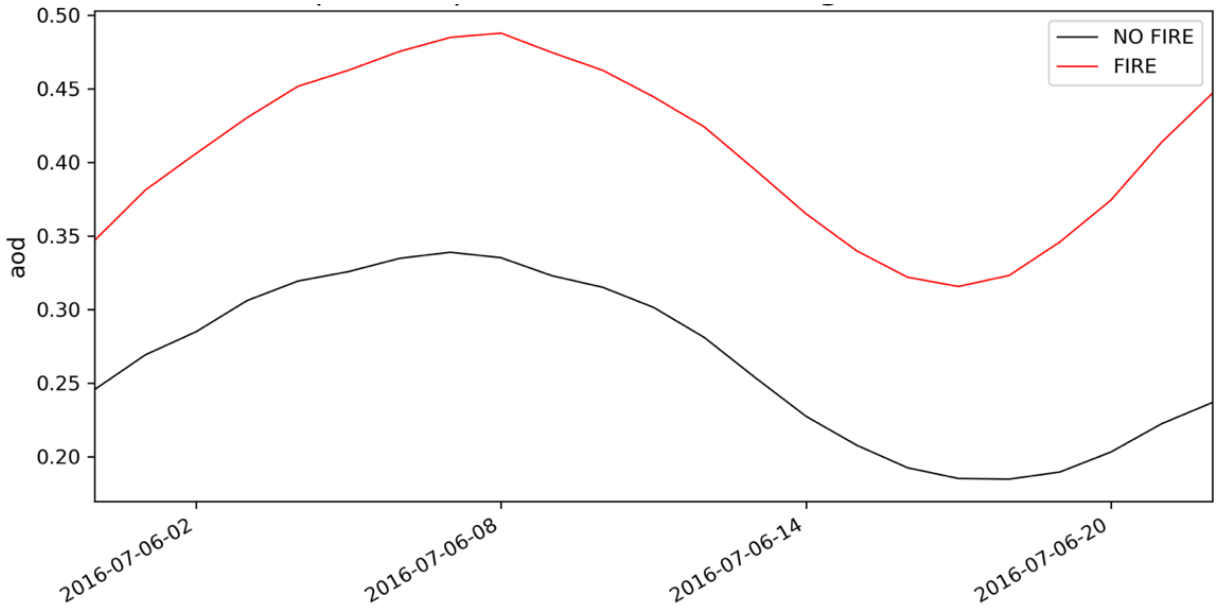

Figure 4.43: Time series of simulated AOD for FIRE case (red) and NO FIRE (black) averaged over domain D2.

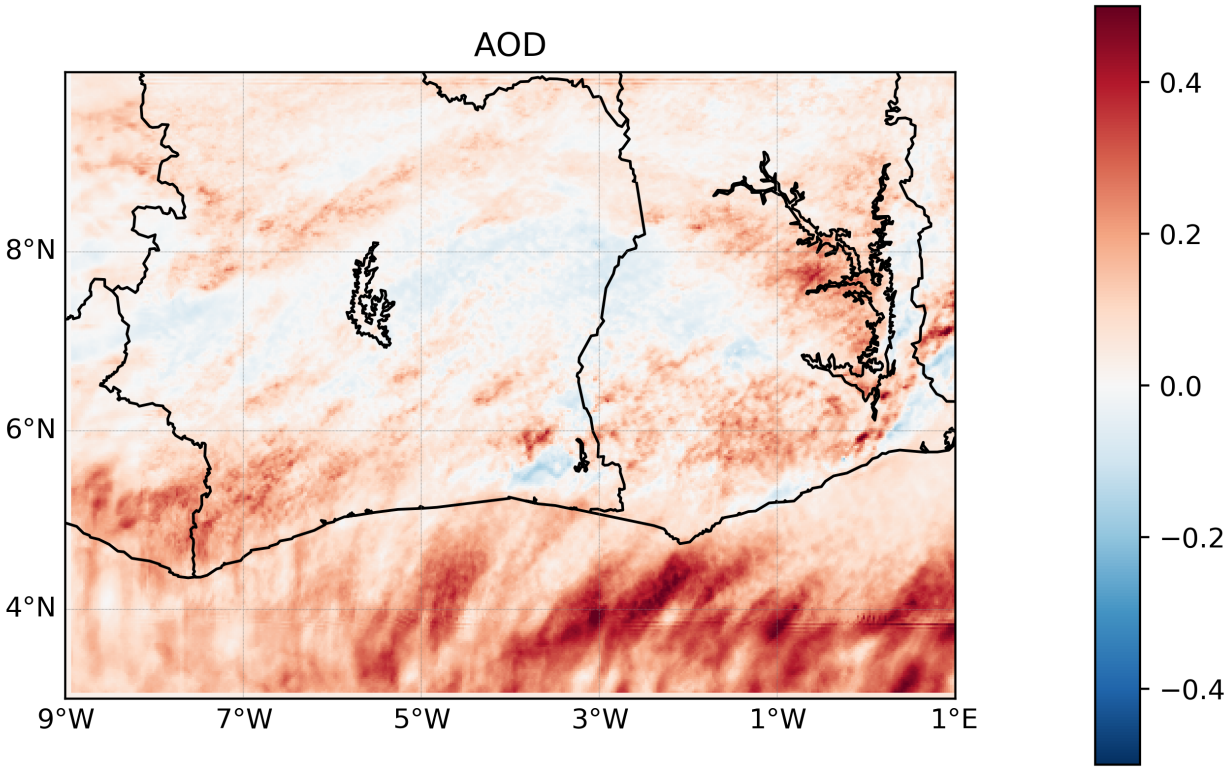

Figure 4.44: Spatial distribution of simulated AOD difference (FIRE -No FIRE).

Furthermore, a temporal evolution of particulate matter (PM) and chemical species are presented in Figures 4.45 and 4.46. The results are computed for Abidjan and Accra, as the two coastal cities of our inner domain (D2). Both trace gases and PM show an increase due to FIRE in Abidjan and Accra. The peak of the $PM_{2.5}$ and PM_{10} concentrations corresponding to 80 (30) $\mu g/m^3$ for Abidjan (Accra) are found early morning around 5–6 UTC before the sunrise and start decreasing right after to a minimum of 9 (6) $\mu g/m^3$ around 14 UTC. Regarding the PM_1, the concentration is slightly lower than that of $PM_{2.5}$ and PM_{10} with minimum (maximum) values around 7 (70) for Abidjan and 1 (27) $\mu g/m^3$ for Accra. From the beginning of sunset, it starts increasing at night, suggesting that the height of the PBL has reduced and less vertical mixing occurs. CO mixing ratio shows similar behavior as the PM, but for the ozone, it shows opposite phase to the CO (Figure 4.46). Maxima are simulated during daytime around 14 UTC with peak of 43 ppb (50 ppb) in Abidjan (Accra), and minimum value of 17 ppb for both cities around 5–6 UTC early morning. CO peaks in Abidjan are very high for the first simulated day and reaches 800 ppbv, whilst that of Accra is around 500 ppbv. Our model suggests that Abidjan is more polluted than Accra. In fact, in term of population, Abidjan is twice the population of Accra (5 against 2.3 millions of inhabitants (UNO, 2018)), and moreover, there is a very high correlation between population and the anthropogenic emissions in Africa (Keita, 2018). The increase of PM over Abidjan and Accra is estimated to 6 to 7 $\mu g/m^3$ for our case study (5–6 July 2016). This result agrees with the findings of Menut et al. (2018) who found 5 $\mu g/m^3$ increase of PM_{10} due to FIRE emission but in contrast our model shows high values of PM_{10}. The authors used WRF-CHEM and simulated period ranging from May to July 2014 at 60 km resolution and found peak values in Abidjan around 30 $\mu g/m^3$ whilst our simulation found peak value of 78 $\mu g/m^3$ in Abidjan. Regarding ozone concentration,

the peak value reaches 50 ppbv and is in the same order of magnitude than the one predicted by WRF-CHEM (100 µg/m^3 ~ 51 ppbv). The contribution of FIRE to ozone is estimated to 14 ppbv (equivalent to 27.4 µg/m^3) in Abidjan whilst, Menut *et al*. (2018) found an increase of 10– 20 µg/m^3. CO increase of around 78 ppbv (~152 µg/m^3) and is similar to the CO increase simulated by WRF-CHEM of 150 µg/m^3. Our results are in good agreement with the findings of Menut *et al*. (2018) despite some discrepancies in the simulated PM_{10} and CO.

Table 4.4 summarizes the contribution of FIRE to atmospheric composition over the study domain and their effects on radiation, cloud and precipitation. The mean value for the AOD is 0.26 (0.4) in No FIRE (FIRE) equivalent to an increase of 36%. Mostly, CO and O_3 and aerosols (i.e. Organic aerosols, Black Carbon) experience an increase due to biomass burning. The consequent effects are also visible on the meteorology, by reduction of direct surface and top of Atmosphere SW and increase of clouds droplets number concentration followed by a decrease of the size of the droplets. However, the impact on precipitation remains small.

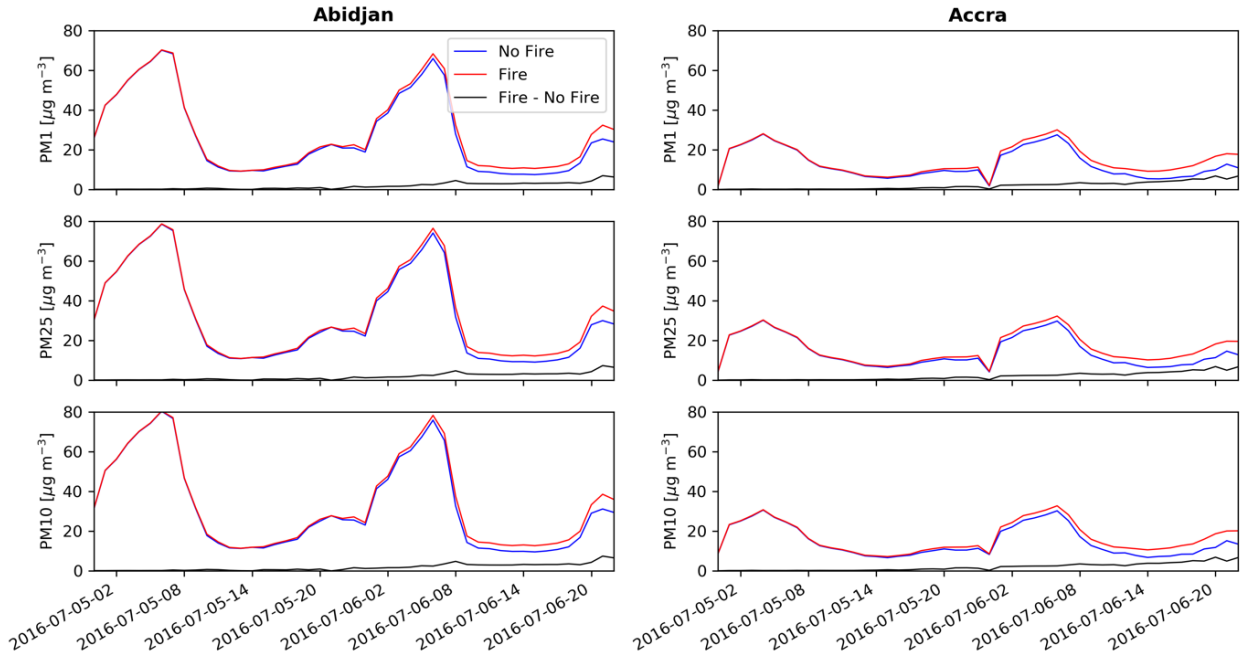

Figure 4.45: Time series of PM_1, $PM_{2.5}$ and PM_{10} surface concentration in Accra and Abidjan for simulation with FIRE (red), No FIRE (blue) and the difference (FIRE -No FIRE) (black).

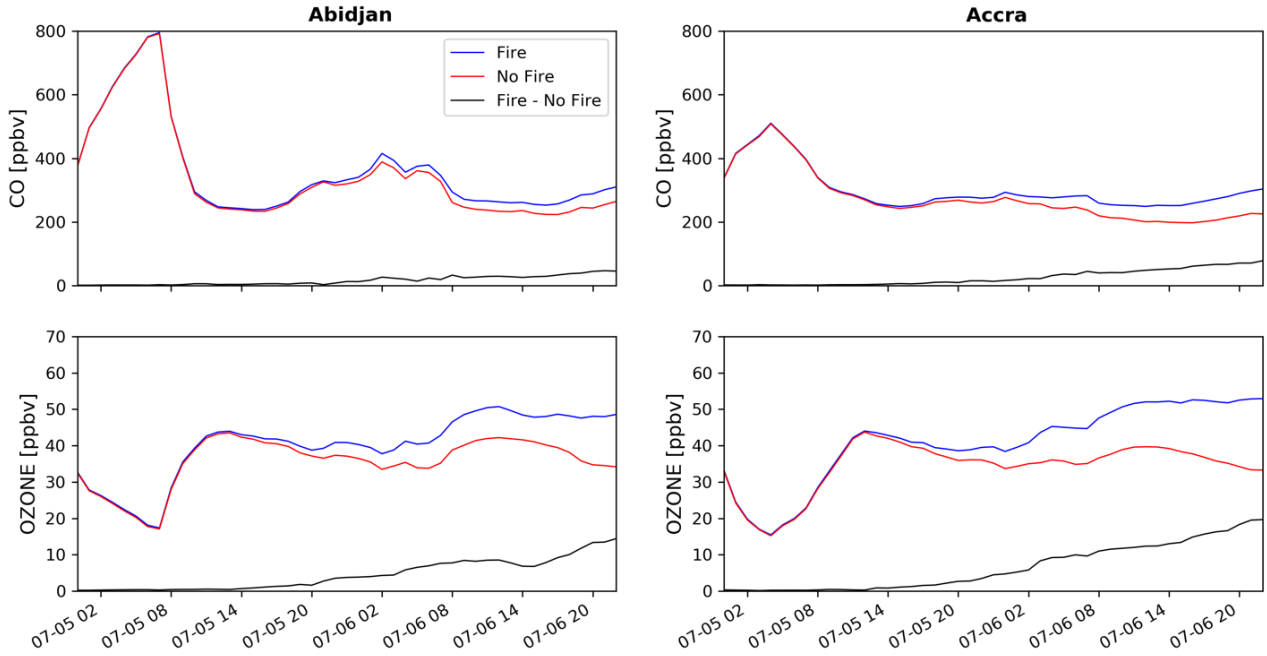

Figure 4.46: Same as Figure 4.45 but for O_3 and CO.

Table 4.4: Table of daily mean values for FIRE and NO FIRE case and the difference between them. The percentage change in the table is computed as (F-NF/F). The mean is computed over the domain D2.

Field	Fire	No Fire	Difference	% change (F-NF/F)
AOD	0.4	0.26	0.14±0.01	36
SW down surface (W m^{-2})	83.43	89.95	-6.51±0.0	-7.81
TOA net downward SW (W m^{-2})	184.61	190.28	-5±0.0	-3.07
CDNC	132	120	12±0.00	9
Precipitation (mm day^{-1})	4.15	4.26	-0.11±0.01	-2.68
CO (ppb)	225	199	26±1	11.5
O_3 (ppb)	39	33	6±0.3	16

F stands for FIRE case; NF: stands for NO FIRE case

4.3.2 Impact of local pollution (anthropogenic emissions)

In West Africa, most of studies has focused on natural dust aerosols impact on the climate over the region (Ogunjobi *et al*., 2007; Konaré *et al*., 2008; Solmon *et al*., 2008; Stanelle *et al*., 2010; Raji *et al*., 2017; N'Datchoh *et al*., 2018). Biomass burning aerosol on African air pollution has attracted attention but mainly during the dry season over the northern hemisphere (N'Datchoh *et al*., 2015; Swap *et al*., 2002). Whereas during wet season (summer monsoon), the biomass burning shift from northern to southern hemisphere and appears to be transported toward West Africa (Mari *et al*., 2008; Haslett *et al*., 2019). It is obvious that biomass burning increases to the level of pollution over coastal cities in West Africa (Menut *et al*., 2018; this study), however less study has focused on the impact of local pollution on the meteorology due to scarcity of observational network. Though, emissions of anthropogenic pollutants are predicted to triple over the next century (Lamarque *et al*., 2010; Liousse *et al*., 2014) due to rapid population growth, urbanization and increase of industrialization. Figure 4.47 illustrates the impact of ANTHRO on direct surface SWA radiation. The impact of ANTHRO on radiation over land dominates as it represents the major source of pollution in the region mainly for this period of time. The reduction reaches up to 50 W m^{-2} for the anthropogenic whilst it is 20 W m^{-2} for the FIRE emissions. The FIRE emission dominates more over ocean and over coastal cities as demonstrated in the previous section. Moreover, a spatial distribution of the difference (ANTHRO – No ANTHRO) of surface meteorological quantities (shortwave radiation, longwave radiation and temperature) temporally averaged. A clear signal is visible from the spatial distribution of difference of downward SW and temperature, with decrease over the whole domain due to absorption and scattering. Maximum increase of SW reaches up to 50 W m^{-2}. Consequently, temperature also decreases generally over the whole domain except

northwest of Côte d'Ivoire where less cloud was observed. According to Thornhill *et al*. (2018), the increase of surface temperature where clouds are less allows more SW radiation through and the extinction due to the aerosol's emission is lower. Their results were related to biomass burning emissions whilst here, it is about anthropogenic (local pollution) emissions. Additionally, it is found that by removing cloudy pixels from the calculation of radiation difference, the decrease of radiation is higher than when it is computed with all pixels (including cloudy areas) (see Figure 4.39). The decreases is estimated to about 0.5 ºC. The temperature anomalies observed in the surroundings of the Lake Volta (Figure 4.48e) is due to the fixed SST applied (Deetz, 2017). The latter lead to no temperature change over the Gulf of Guinea after calculating the temperature difference (Figures 4.48e and 4.48f). Regarding the longwave radiation (Figures 4.48c, d), the signal is not clear whether it is an increase or decrease as seen for the SW radiation. There is a mixture of both increasing and decreasing longwave radiation, which make it difficult to detect the impact on longwave (LW) radiation. Moreover, the difference of outgoing LW radiation appears to be very small (-5 to 5 W m^{-2}). Our hypothesis is that the effect is too small, so this patchy pattern is probably due some secondary effects (i.e. water vapor). Previous studies (Deetz *et al*., 2018) shows a high relative humidity in the monsoon layer which affect the AOD in West Africa coastal region. Similarly to our study, the authors found that the effects of aerosols on the longwave radiation is not significant whilst a decrease of 50 W m^{-2} with respect to the SW radiation is observed and followed by a reduction of less than 1 K of temperature.

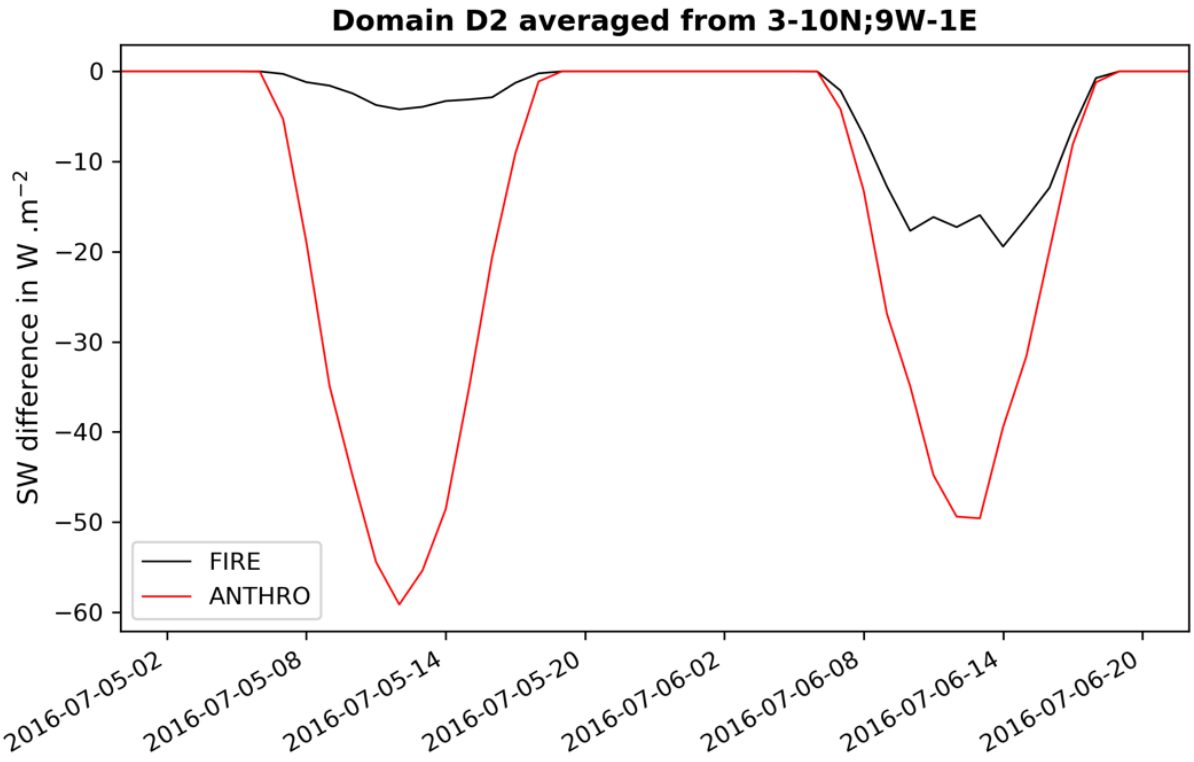

Figure 4.47: Temporal evolution of direct surface SW difference (ANTHRO -No ANTHRO) averaged over domain D2 (3°-10°N; 9°W-1°E) in red and (FIRE -No FIRE) in black.

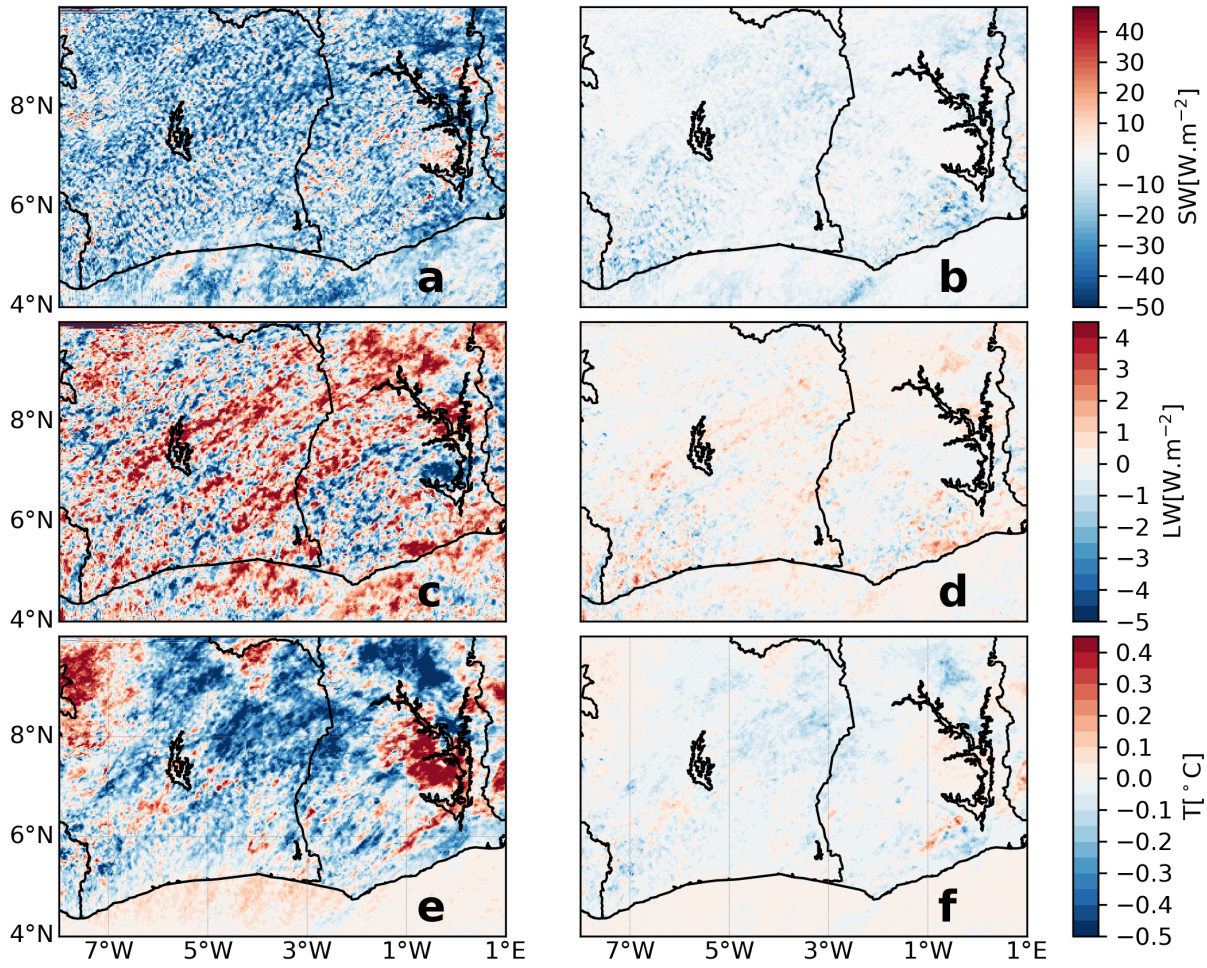

Figure 4.48: Spatial distribution of surface meteorological quantities as difference between ANTHRO and No ANTHRO including cloudy area (a, c, e) and cloud-free area (b, d, f).

The impact on anthropogenic aerosols on cloud microphysics is also examined (Figure 4.49). The clouds droplets number concentration (CDNC) varies from (0–200 cm^{-3}) for ANTHRO scenario, whilst it does not exceed 50 cm^{-3} for No ANTHRO scenario. A median cloud size of 10 μm (12 μm) for ANTHRO (No ANTHRO) scenario is obtained. The abundance of CDNC in the ANTHRO scenario suggests that the anthropogenic aerosols are the main contributor of CDNC in the region during this period of time. This is evident as the natural source appears to be very less during this period. The dust fraction is very small and barely reach the region below 8ºN after the monsoon onset (Knippertz *et al*., 2017). Regarding sea salt aerosols, though they are advected by the monsoon flow into the region and efficient as cloud condensation nuclei (CCN), their contribution is small compared to that of anthropogenic aerosols over the region. Several sources (industry, energy and heat production, road, rail and air traffic, flaring, residential, domestic fires, waste burning) of aerosols are considered as anthropogenic aerosols. For instance, in West Africa, the traffic fleet contributes significantly to pollutants emission in the atmosphere as there are mainly unmaintained second-hand vehicles and moreover make use of poor fuel quality with a very high Sulphur content (1500–3000 ppm) compared to European standard 50 ppm (UNEP, 2017). Assamoi and Liousse (2010) found that most of the two-wheeled vehicles, specific to Africa continent are highly polluting as they use a mixture of gasoline and oil (two-stroke engine). For instance, sulfate aerosols are very efficient as CCN, as well as secondary organic aerosols which appear to dominate the atmosphere in the region confirmed both by model results (this study) and observation (Haslett *et al*., 2019; Brito *et al*., 2018).

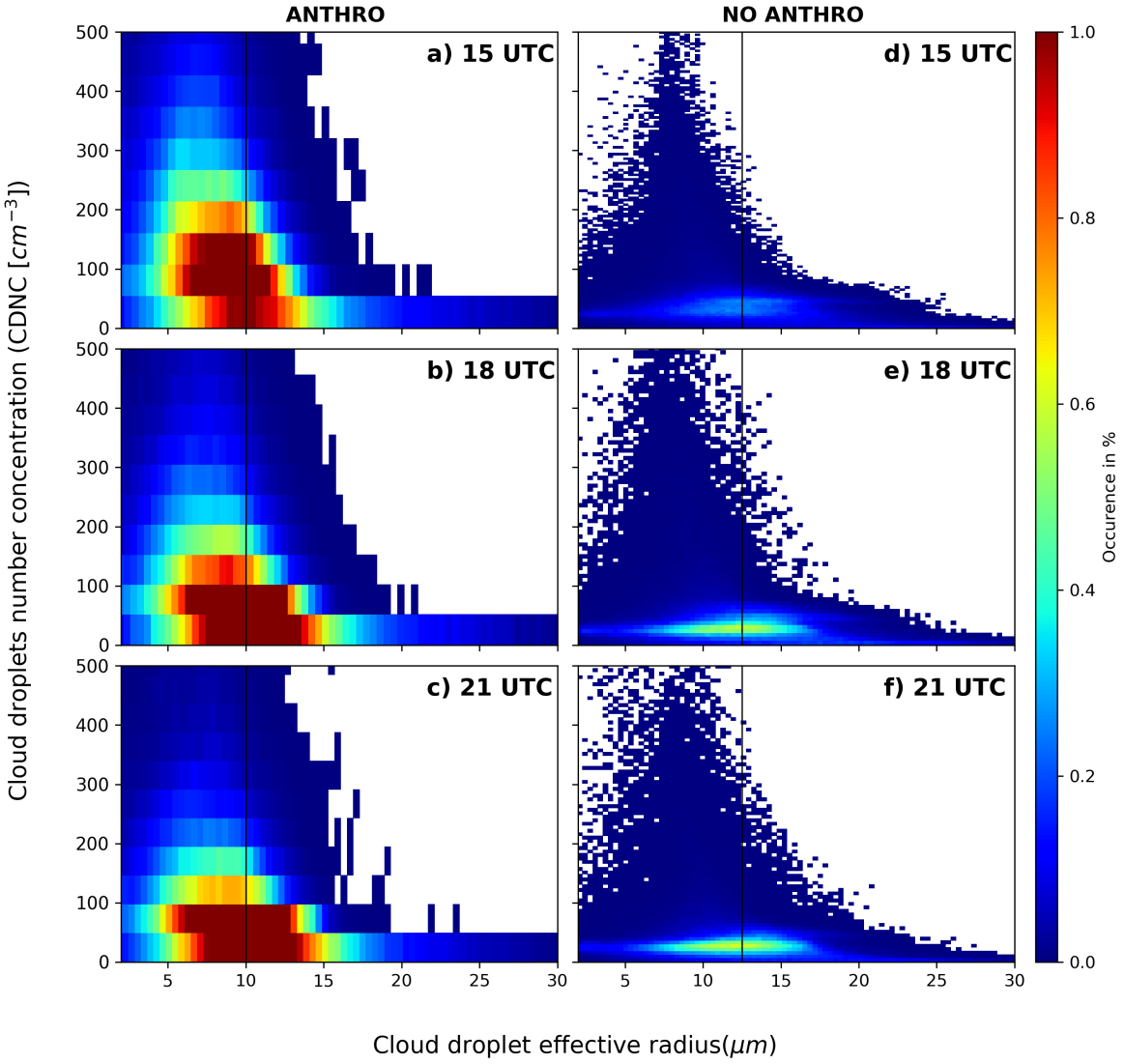

Figure 4.49: Domain joint histogram of clouds droplets number concentration (CDNC) and cloud effective radius calculated for grid points with CDNC > 1 cm^{-3} for different times during the day. Comparison between simulation between ANTHRO (left panel) and No ANTHRO (right panel).

Figure 4.50 shows the empirical cumulative distribution function of CDNC, cloud droplets size, cloud water and precipitation temporally averaged on 06 July 2016. Comparison between ANTHRO and No ANTHRO is analyzed. The ecdf reveals an increase of CDNC as simulated by the joint histogram (Figure 4.49) as a result of anthropogenic activities and a clear reduction of cloud droplets size (effective radius). It also reveals a decrease of cloud water and no significant change in precipitation. Our finding agrees well with that of Deetz *et al*. (2018), which used also COSMO-ART with respect to the CDNC, the effective radius and precipitation. However, the authors found that aerosols increase do not change significantly the cloud water content whilst our study found a slight decrease in cloud water as a result of aerosol increase. Study from Toll *et al*. (2019) revealed through direct observational evidence that anthropogenic aerosols cause a relatively weak decrease of water in polluted cloud compared to unpolluted cloud. According to the author is caused by enhanced evaporation of cloud water. Nevertheless, increasing aerosols could lead to increase of cloud water caused by suppressed rainfall formation which is not the case in this study. Both processes cancel each other in some cases. This buffered mechanism was highlighted in a study by Xue and Feingold (2006). Figure 4.51 presents the simulated spatial distribution of wind speed difference between ANTHRO and No ANTHRO at 925 hPa. It reveals a clear signal of aerosol-induced a decrease of wind speed decreases which was highlighted by Deetz *et al*. (2018). The authors stated that the cooling effect due to aerosol increase induces a reduction of the ocean-land temperature gradient. This will result in a weakening of the monsoon flow. The wind speed reduction is estimated to 1.2 m s^{-1}.

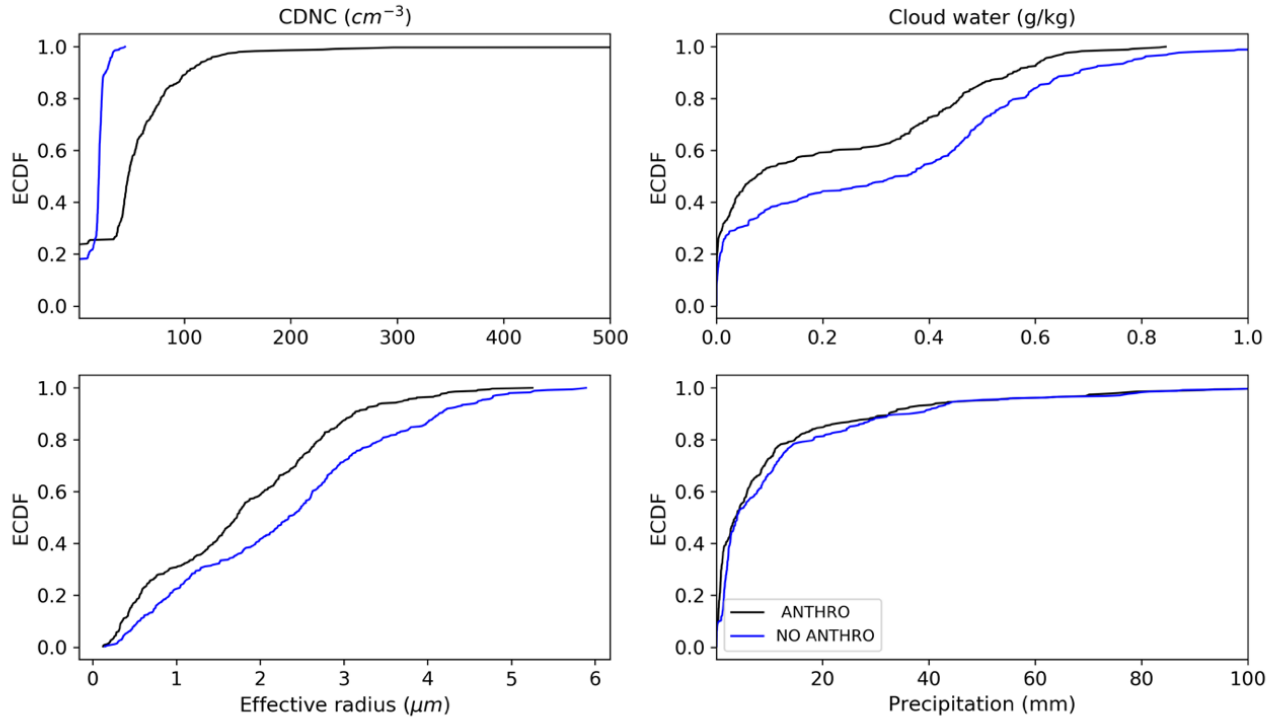

Figure 4.50: Simulated ecdf for ANTHRO scenario (black) and No ANTHRO (blue) temporally averaged on 06 July 2016.

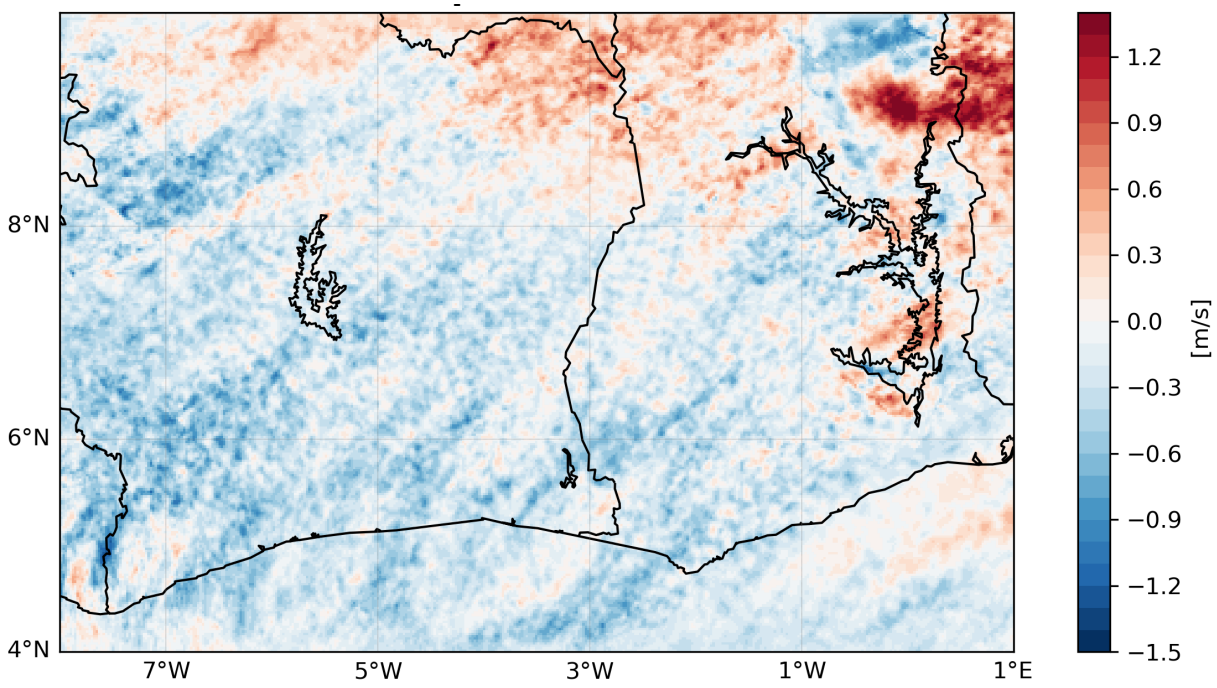

Figure 4.51: Spatial distribution of wind difference (ANTHRO – No ANTHRO) as simulated by COSMO-ART based on daily averaged.

4.3.3 AIE and ADE sensitivity simulations

Another experiment is analyzed, consisting of the use of scaling factors to modify aerosols concentration in order to identify their effect on the meteorology (Montgomery, 2005; Deetz, 2017). In case our study, the effect will be examined on radiation and clouds properties. According to the authors, this method is efficiency in separating signal of Aerosol direct effects (ADE) from Aerosol indirect effects (AIE).

For our study, F_{ADE}=0.1; F_{AIE}=0.1 is used as a clean case and F_{ADE}=1.0; F_{AIE}=1.0 as the reference case and F_{ADE}=1.5; F_{AIE}=1.5 as the polluted case following Deetz (2017). Figure 4.52 presents the joint histogram of CDNC and cloud droplets size as compared between the clean and the reference case. 5 μm difference is observed in the median size of the cloud droplet between the clean case (15 μm) and the reference case (10 μm). The increase in the CDNC is also visible. This finding is in agreement with previous studies and verify the Twomey effect. Figure 4.53 presents the temporal variation of the difference of (polluted – clean); (reference – clean) and (polluted – reference) for a domain averaged over D2. These differences display peak values around 13–14 UTC where the peak solar radiation is observed. Obviously, the (polluted – clean) case exhibits the highest value with a reduction of about -46 W m^{-2}, followed by the difference between reference and clean case reaching up to -38 W m^{-2}. The polluted and reference case shows a difference of -9 W m^{-2}. Through our model simulation, the ADE give a clear signal in contrast to AIE.

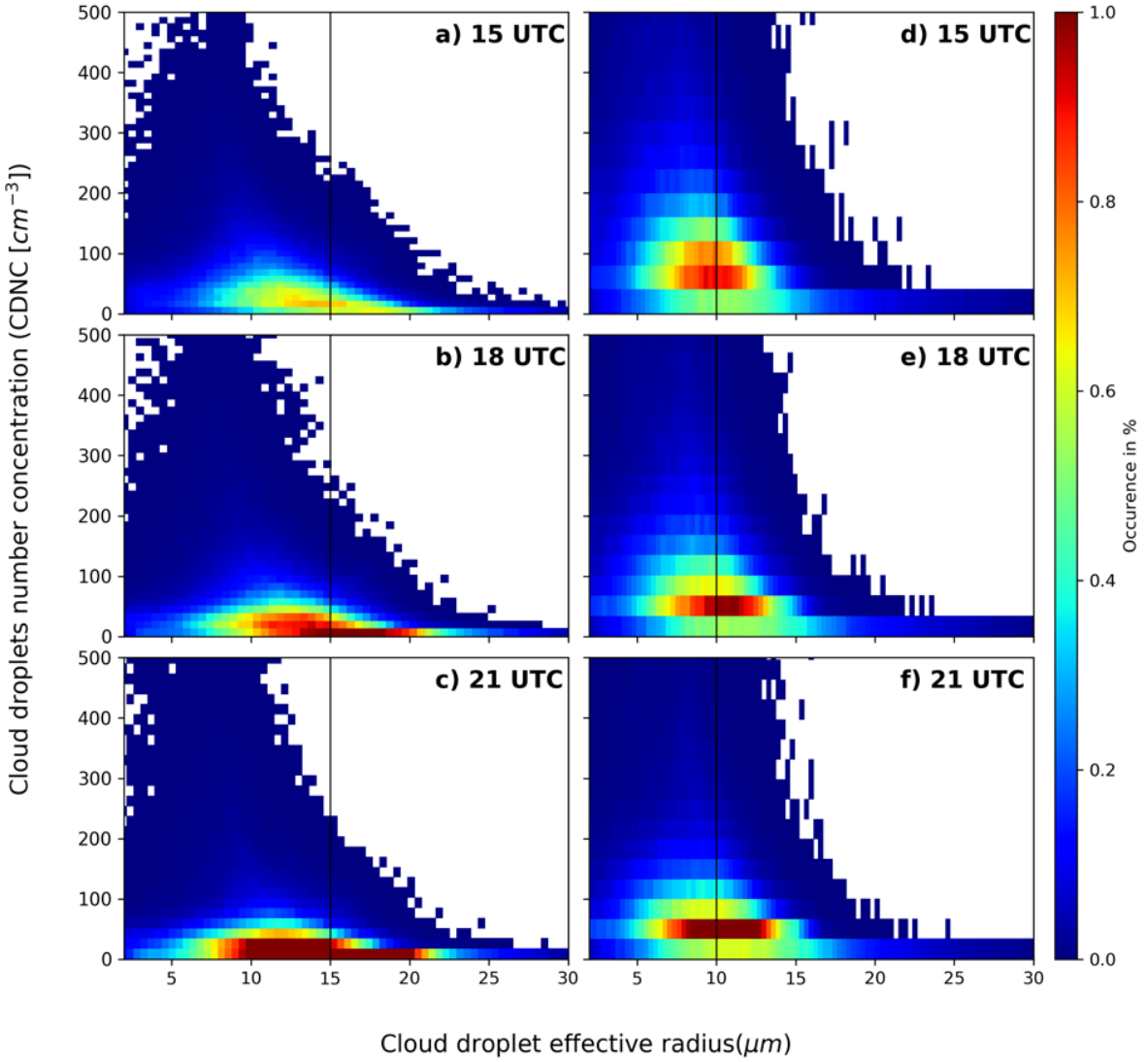

Figure 4.52: Joint histogram of the CDNC and cloud droplet radius. Comparison between clean case (left panel) and reference case (right panel).

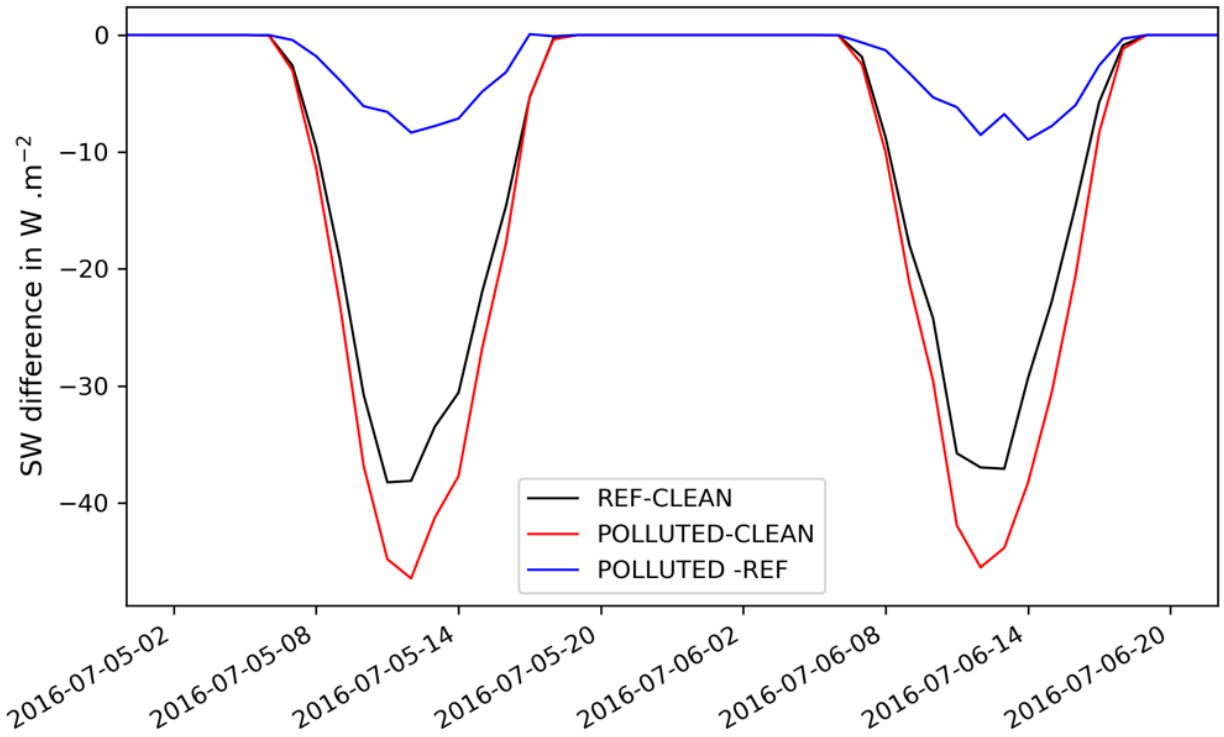

Figure 4.53: Temporal evolution of difference of surface SW radiation between polluted and clean case (red), polluted and reference case (blue) and reference and clean case (black). The calculated was done average over Domain D2.

4.4 Evaluation of Emission with COSMO-ART and Observations.

Anthropogenic emissions are subjected to many uncertainties in their calculations and no reliable data sources in West Africa. Many anthropogenic emissions exist mainly global anthropogenic emissions which are used to assess the impact of anthropogenic aerosols on the atmospheric. The most popular one is EDGAR dataset which was used for this study. In the framework of DACCIWA, in order to determine accurately the atmospheric composition over the region, an Africa-specific set of emission dataset was developed (Keita, 2018). This emissions data was also used in COSMO-ART simulation and compared with simulations conducted with EDGAR dataset and observational aircraft measurements. It is worth noting that DACCIWA emissions dataset is more recent (2015) whilst EDGAR was for year 2010. Figure 4.54 presents the anthropogenic emissions from EDGAR and DACCIWA for organic carbon (OC), Black Carbon (BC), Carbon monoxide (CO) and nitrogen dioxide (NO_2) averaged over the domain D2. DACCIWA shows high emissions compared to EDGAR for all the species mentioned above, specially the organic fraction OC and the NO_2 differences are too large. Obviously, large source of uncertainties is reflected in the difference between the two emission datasets. Figure 4.55 illustrates simulated ozone concentration with COSMO-ART using different anthropogenic emissions (EDGAR, DACCIWA) and DACCIWA aircraft observation in a vertical, longitudinal and latitudinal profiles below 1.2 km. There is a good agreement between observed and simulated ozone with DACCIWA emissions compared to EDGAR emissions. The latter overestimates the ozone concentration with respect to the longitude and latitude but the verticals profiles are well matched for both inventories. With an initial value of 30 ppb for both simulated and observed ozone, the observed (simulated) ozone concentration decreases between 200 and 400 m with minimum value of 22.5 (26) ppb and starts increasing to reach a value

of 22 (30 for DACCIWA and 33 for EDGAR) ppb above 400m and remain relatively constant till 1200 m. The longitudinal profile is well predicted by COSMO-ART than the latitudinal profile. A difference of 4 ppb is seen between the observed EDGAR values whilst it is 1 ppb for the DACCIWA. The latitudinal variation shows a sharp decrease around 6 ºN in both inventories and observation but an increase precedes this sharp decrease simulated by both inventories which is not seen in the observation. The model prediction of ozone is quite good and is below the World Health Organization (WHO) 8 hour mean limit of 100 µg m^{-3} (51 ppbv) during this time. Figure 4.56 presents the longitudinal and latitudinal profiles of NO_x compared between DACCIWA observation and COSMO-ART simulations with EDGAR and DACCIWA. Regarding the longitudinal profile, the simulation with EDGAR inventory is very low whilst simulation with DACCIWA inventory underestimates the observation NO_x but with small difference. With respect to the latitudinal variation, the NO_x values are very low upwind marine, and shows a sharp increase from 5.55º N northward reflecting the coastal cities sources.

The DACCIWA inventory still performs better than the EDGAR one. This is obvious because from the comparison of the NO_2 emissions dataset between them (Figure 4.54), the difference was too large, thus it is reflected into the COSMO-ART output. The vertical profile of aerosols (OC, NH_4, NO_3 and SO_4) from aircraft measurement is compared to our model results (Figure 4.56). All the aerosol concentration is underestimated except the nitrate (NO_3). Generally, NO_3 concentration has always been very difficult to validate with observational measurement (B. Vogel, personal communication). The instrument that measures NO_3 heat the air the flow is used to measure the NO_3 lost. The difference between the observed and the simulated NO_3 is close 0.5 µg/m^3. The other aerosols (OC, NH_4 and SO_4) show a relatively constant

profile whilst the observation is quite variable. Regarding the organic carbon (OC), the simulated concentration is two and half times lower than the actual concentration. This is also evident as OC from EDGAR dataset is very low compared to DACCIWA emission (Figure 4.54). The inorganic aerosols (SO_4 and NH_4) are underpredicted but much less for the ammonium than the sulfate. The difference ammonium is around 0.5 $\mu g/m^3$ whereas, it is 1.25 $\mu g/m^3$ for the sulfate. Overall, all the aerosols are not well represented by COSMO-ART simulation but this simulation was done using only EDGAR emissions. Simulations of gas species with DACCIWA emissions proved a better performance of COSMO-ART than with the EDGAR emission. Thus, further simulation has to be done to confirm the robustness and accuracy of the simulated atmospheric composition over the region with COSMO-ART using DACCIWA emissions, which seems to provide better results than EGDAR emissions.

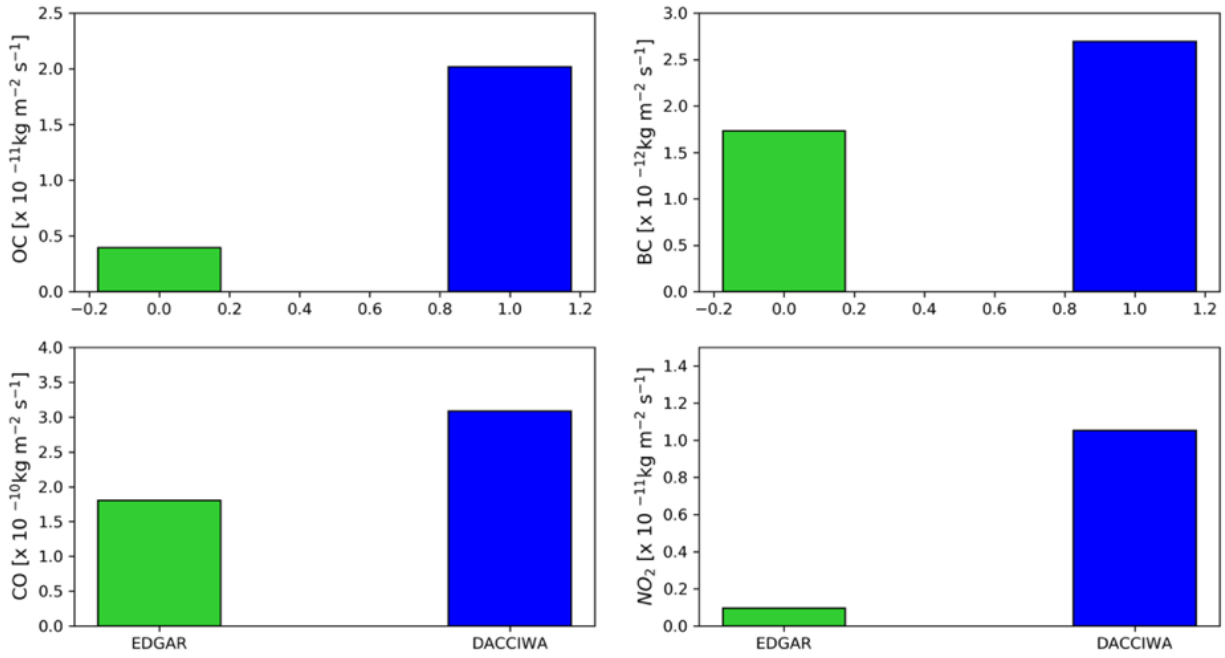

Figure 4.54: Comparison between EDGAR and DACCIWA emissions dataset averaged over Domain D2.

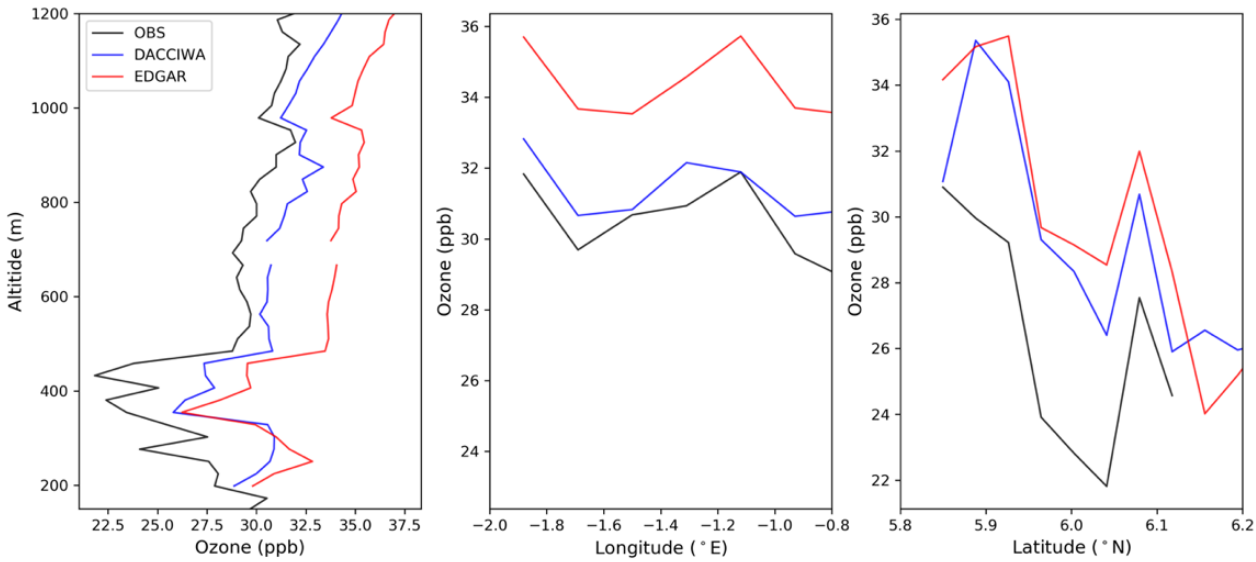

Figure 4.55: Comparison of DACCIWA aircraft observation (black) to COSMO-ART output using two different anthropogenic emissions, EDGAR (red) and DACCIWA (blue).

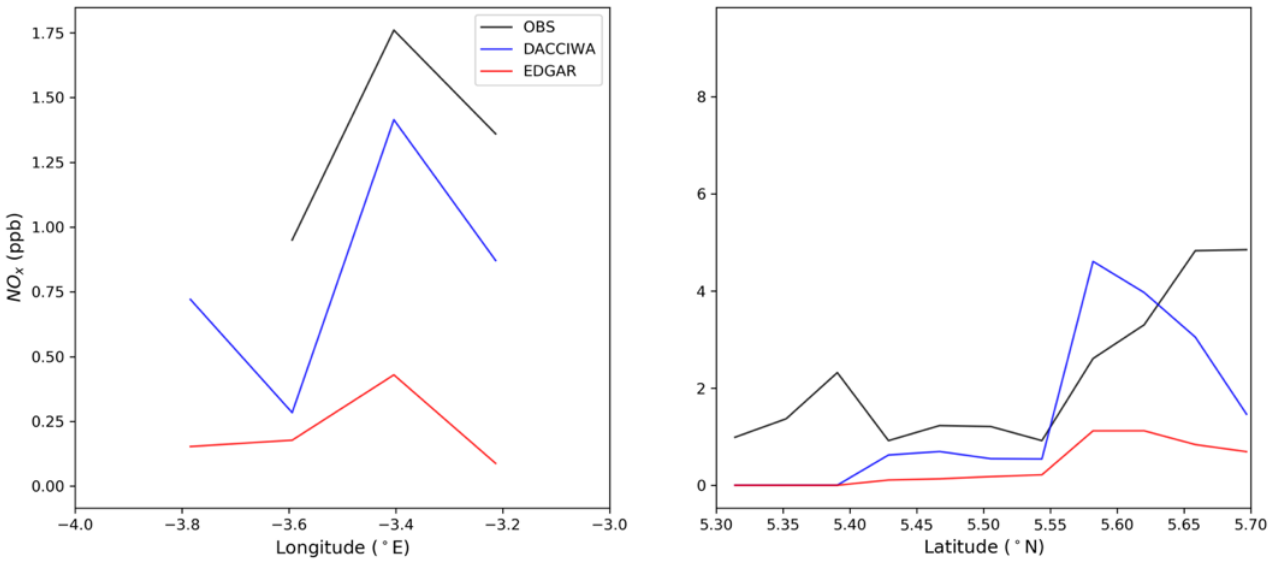

Figure 4.56: Longitudinal and latitudinal profile of NO_x compared between DACCIWA observation (black) and COSMO-ART results with EDGAR (red) and DACCIWA (blue).

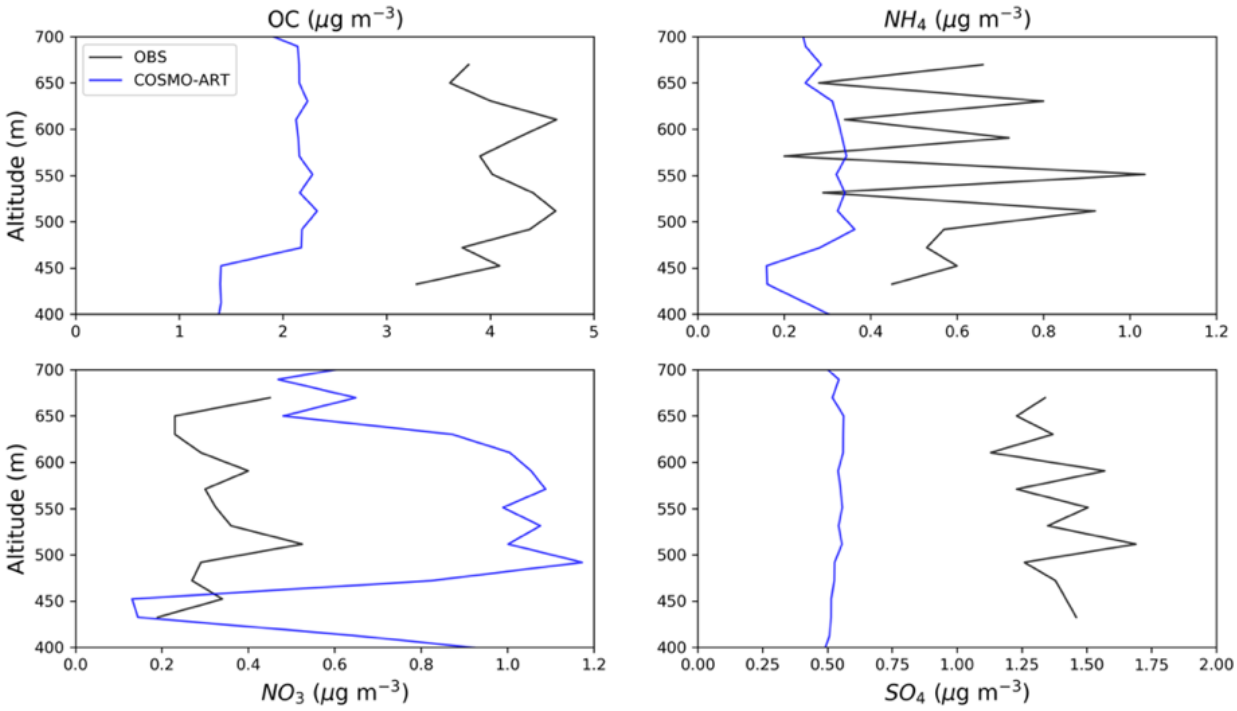

Figure 4.57: Vertical profile of simulated OC, NH_4, NO_3 and SO_4 compared with DACCIWA aircraft observation.

Moreover, CO concentration is also evaluated against DACCIWA emissions for both inventories (Figure 4.58). Both inventories simulations with COSMO-ART overestimate the CO concentration but more in DACCIWA than EDGAR. This is expected because EDGAR emission presents less CO than DACCIWA (Figure 4.54). The 25^{th} (75^{th}) percentile values are respectively 126 (175), 150 (205) and 180 (220) for the observed CO, EDGAR and DACCIWA simulated CO. The median values are respectively 160, 180, 205 for the observed CO, EDGAR and DACCIWA simulated CO. Thus, the CO different between DACCIWA (EDGAR) simulated and observed one with respect to the median is 45 (20) ppb. COSMO-ART has the tendency of overestimating the CO concentration. Deetz, 2017 found an overestimation of CO forecast in Savè and hypothesized that it is due to an overestimation of the CO anthropogenic emission (EDGAR) in his study. But the author stated that the CO was reduced after a sensitivity study performed over the entire domain. From our study, both emissions EDGAR and DACCIWA carried a lot of uncertainties, though DACCIWA shows best performance for the overall gas species except CO concentration. More investigation is need to understand in detail the reason behind the overestimation of CO by COSMO-ART.

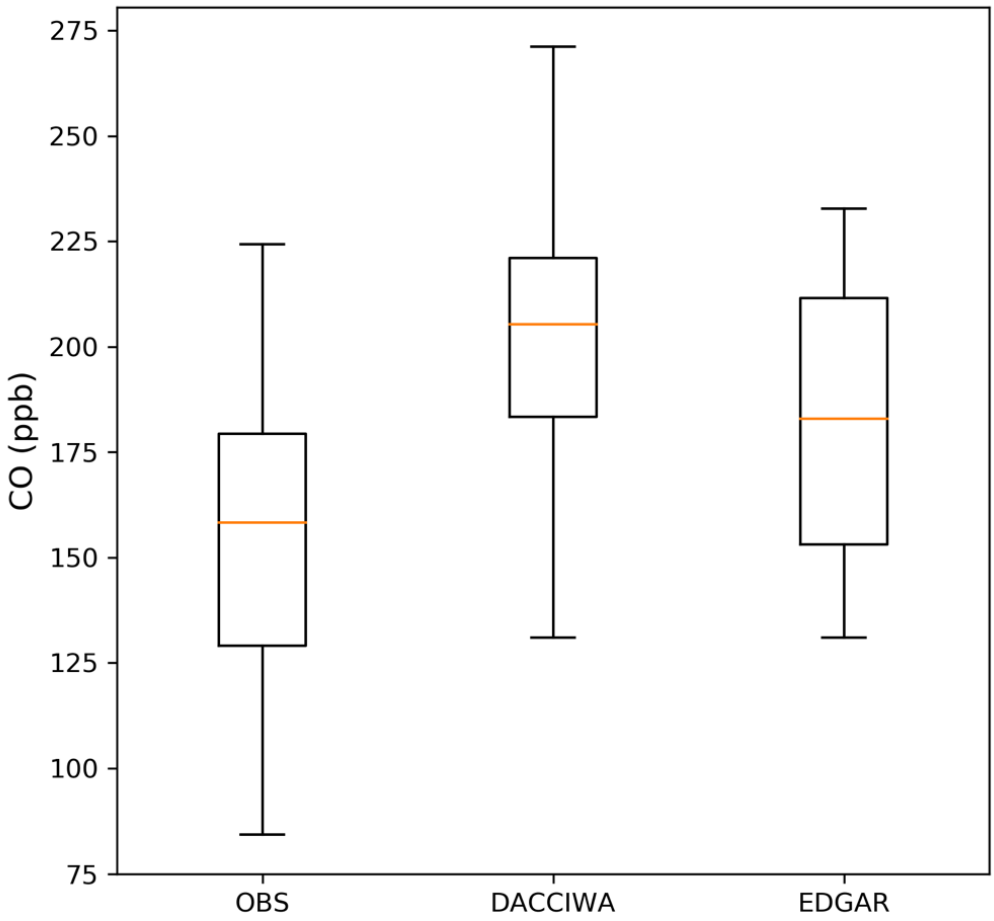

Figure 4.58: Box plots of CO Observation from concentration measured from the aircraft and simulated by DACCIWA and EDGAR on 06 July 2016.

4.5 Assessment of the impact of increasing pollutants on the atmosphere.

This section is dedicated to the impact of future emissions inventories RCP for year 2050 on the atmospheric composition as well as clouds and radiation. Simulation have been run for year 2016 (present) and 2050 (future). The ratio between RCP 2050 and 2010 has been spatially determined for the study domain and used to scale the DACCIWA anthropogenic emissions. RCP 2.6 and 8.5 were used. By definition, RCP 2.6 refers to a so-called "peak" scenario with the radiative forcing level reaching a value of around 3.1 W m^{-2} mid-century, returning to 2.6 W m^{-2} by 2100 (van Vuuren *et al*., 2007). RCP 8.5 refers to a scenarios of increasing greenhouse gas emissions over time leading to high greenhouse gas concentration levels (Riahi *et a*l., 2007). Figures 4.59 and 4.60 present the 2016 and 2050 emissions and the ratio 2050/2016 of CO, SO_2 and OC over domain D1 respectively for RCP 2.6 and RCP 8.5. Analysis Figure 4.59, there are differences of the simulated pollutants using RCP 2.6. For instance, CO and SO_2 show an increase over the entire West Africa which is more pronounced over the Gulf of Guinea coastal area. Whilst the increase in OC shifted from south to north from 2016 to 2050. Therefore, there is not straight forward relationship between the changes of pollutant within the RCP. Generally, a tendency of increase of all the pollutants with is more over the Sahel region that over the Gulf of Guinea. The ratio is respectively 5, 3, and range from 2–2.5 over most of the Sahel countries for SO_2, CO, and OC whilst it ranges from 1–1.5 for the Gulf of Guinea countries (Côte d'Ivoire, Ghana, Togo, Benin and Nigeria) for CO and OC and SO_2 but for SO_2 Benin and Nigeria experience more increase (2–2.5). As far as RCP 8.5 is concerned, figure 4.60 shows similar pattern with respect to CO and OC but slightly increase than RCP 2.6 with a ratio ranging from 2–2.5 for with a ratio. However, the increase is uniformly distributed over the whole West Africa domain (both over Sahel and Gulf of Guinea). In contrast, SO_2 experience an

increase of 3.5–4 over the entire Gulf of Guinea countries except western part of Cote d'Ivoire, Burkina Faso and Mali, where the increase ratio is 2.5. From above mentioned, it appears that the changes of pollutant from one RCP depend on the region. Mostly all, the pollutants experience more change (increasing ratio) from RCP 2.6 to 8.5 over the Gulf of Guinea whilst over the Sahel it is shows opposite trend.

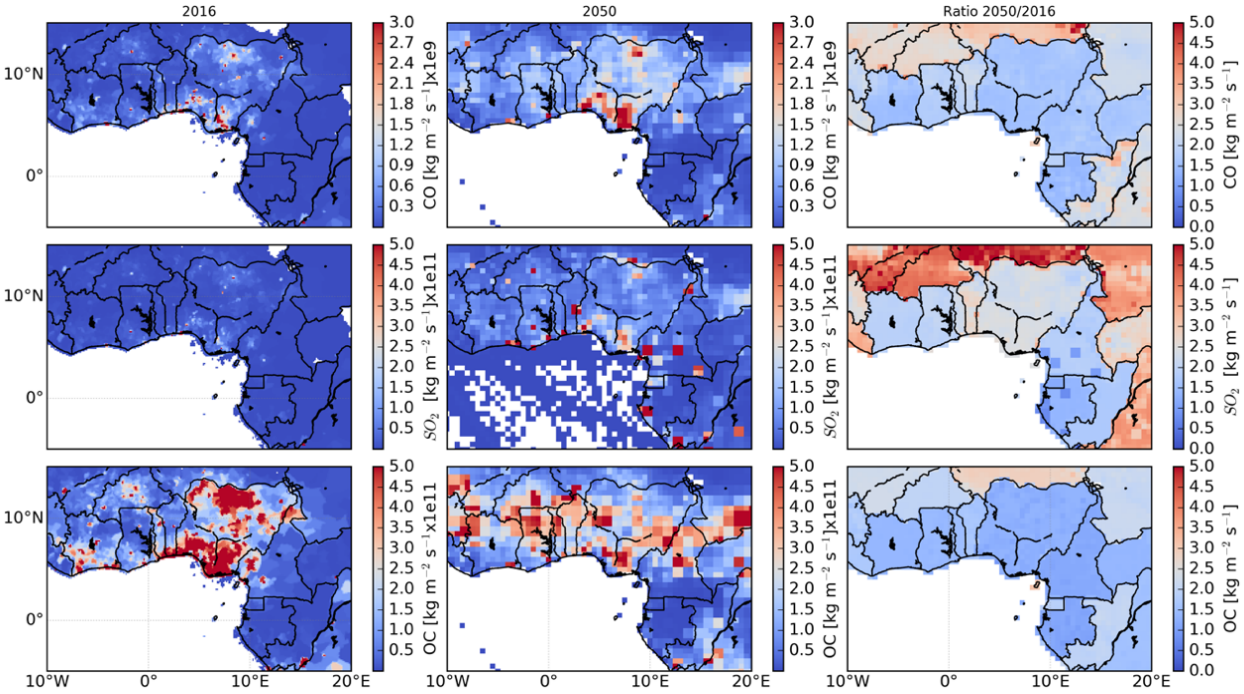

Figure 4.59: Spatial distribution of RCP 2.6 emission for CO, SO_2 and OC for Domain D1 for year 2016 (first panel), year 2050 (second panel) and the ratio 2050/2016 for the third panel.

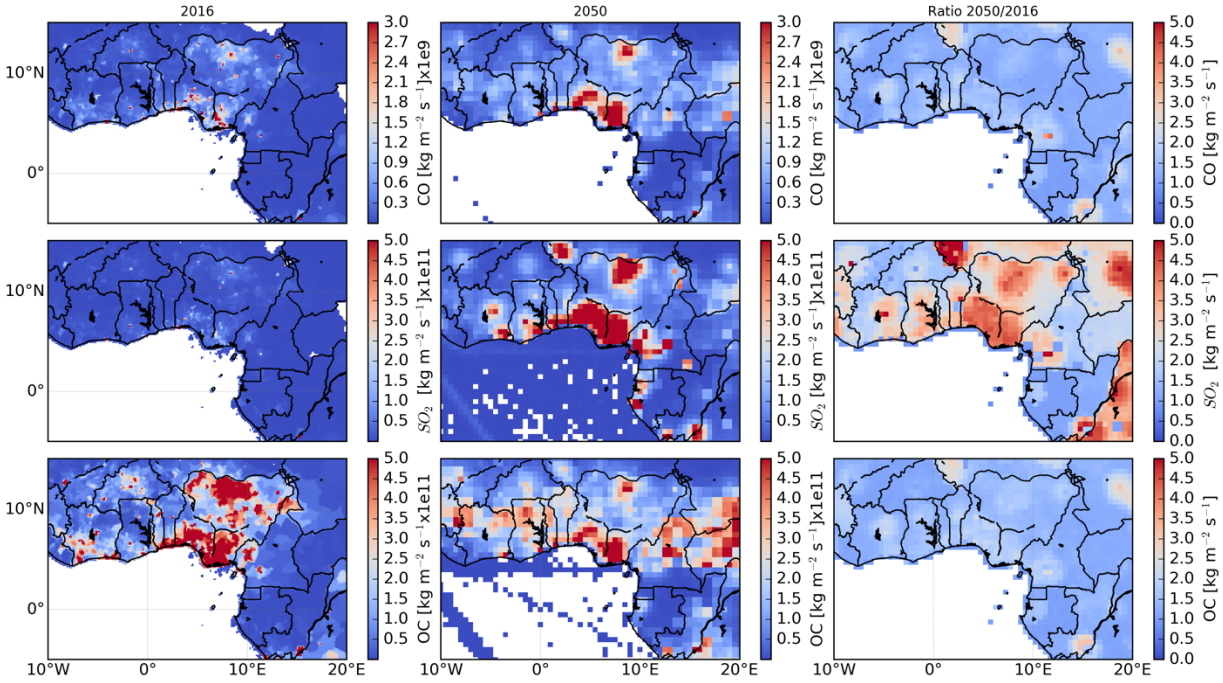

Figure 4.60: Same as Figure 4.6 for RCP 8.5 scenario.

Simulations performed with present and future pollutant concentration (RCP 2.6 and 8.5) over the region are analyzed. Figures 4.61 and 4.62 show the spatial distribution of CO mixing ratio in 2016, 2050 for RCP 2.6 and RCP 8.5. All the variables are considered at surface level.

Under both RCP, CO experiences an increase generally over the entire West Africa domain at almost the same magnitude. But the difference is seen over the Sahel where RCP 2.6 shows large increase than RCP 8.5. This result is in phase with the prediction that CO will increase more over Sahel under RCP 2.6 and moderately under RCP 8.5 (see Figures 4.59 and 4.60). The CO increase is about 30 ppb under both scenarios and the percentage change vary from 20 to 30% with peak values more south, mainly over cities along the coast and the Niger Delta in Nigeria.

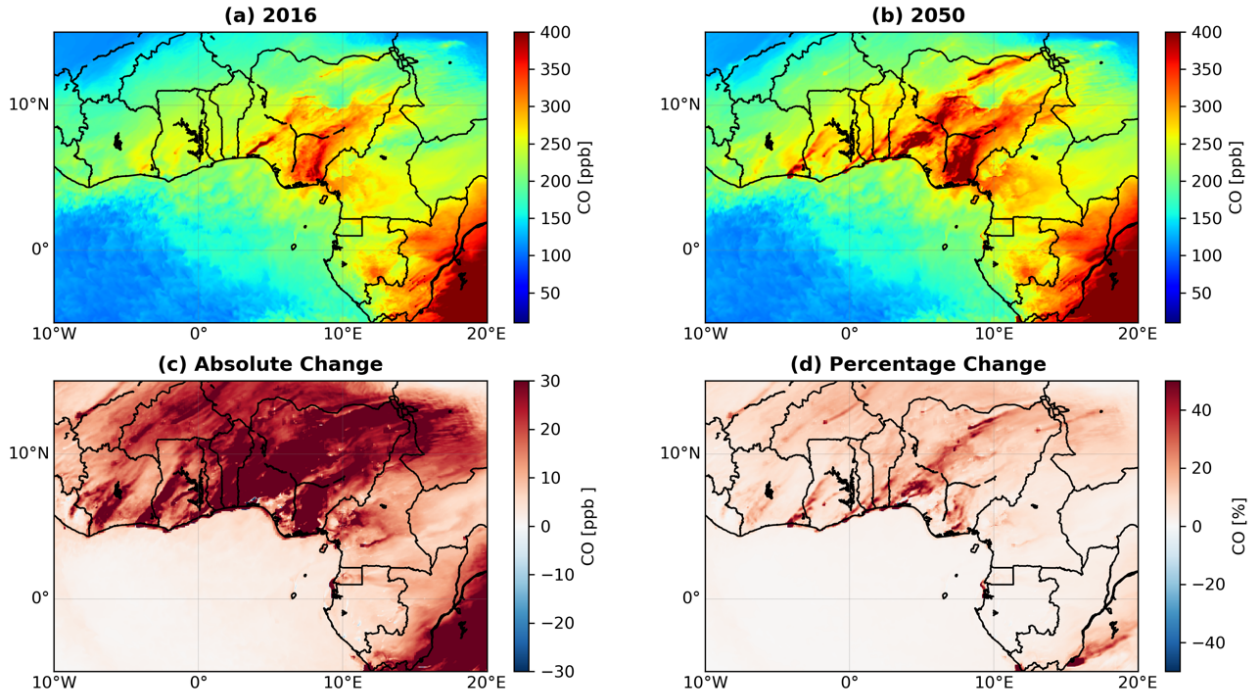

Figure 4.61: Spatial distribution of mean CO concentration under RCP 2.6 for year 2016 (a), 2050 (b), absolute difference between 2050 and 2016 (c) and the change in percentage (d).

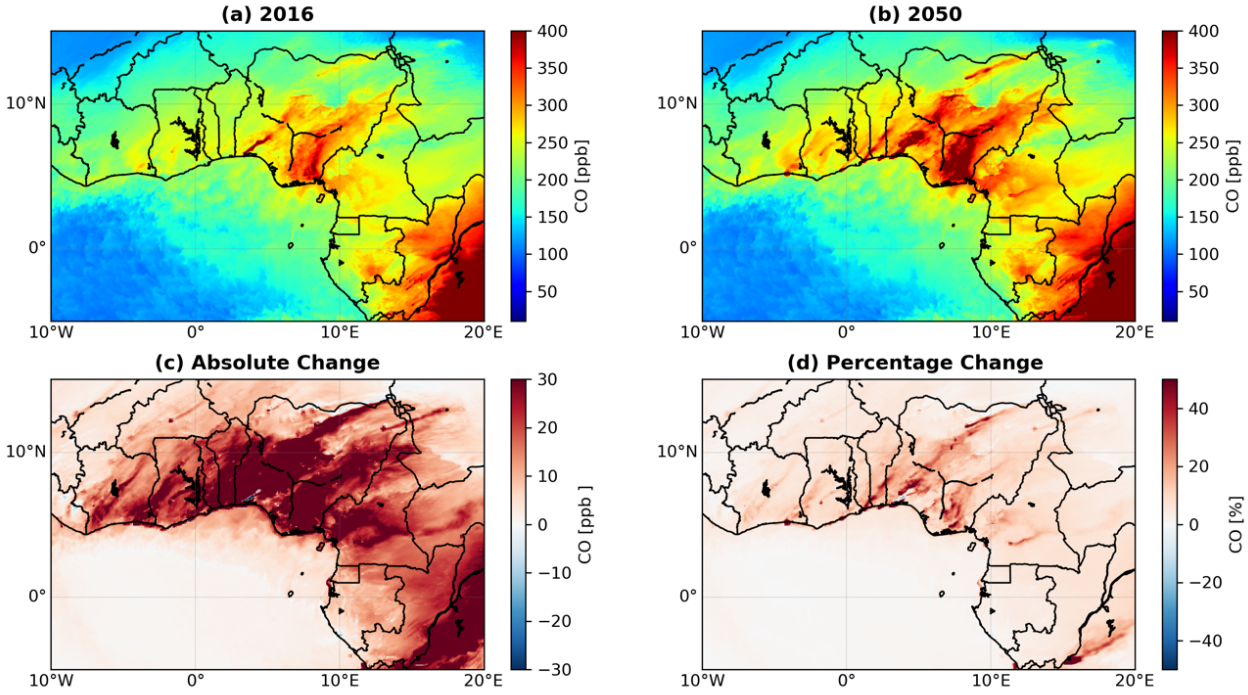

Figure 4.62: Same Figure as Figure 4.60 but for RCP 8.5.

Figures 4.63 and 4.64 present the mean OC concentration for both RCP 2.6 and 8.5. Under both scenarios, similar pattern is observed for OC concentration and predict an increase over the entire domain up to 100% change. From 2016 to 2050, OC increase spreads more inland and over Sahel region. Figures 4.65 and 4.66 analyzed the Black Carbon (BC) concentration under RCP 2.6 and 8.5. Interestingly, BC is predicted to decrease over Nigeria (mostly central and northern part), Ghana (mostly central and northern part) and Niger (northern part), whilst for the rest of the area (Côte d'Ivoire, Togo, Benin, southern Niger), an increase is predicted. This observation is reflected under both RCP scenarios. Moreover, the decrease is more under RCP 8.5, as the entire Niger experiences a decrease of BC. Focusing on Lagos and the Niger Delta, some contrasting patterns of increase and decrease are observed under both RCP scenarios. The absolute change varies from -10 to 10 ($\mu g\ m^{-3}$) and the percentage change from -50 to 50% for both RCPs. The analysis of the spatial distribution reveals an increase of the pollutant over the entire West Africa, expect for BC where some region will experience a decrease.

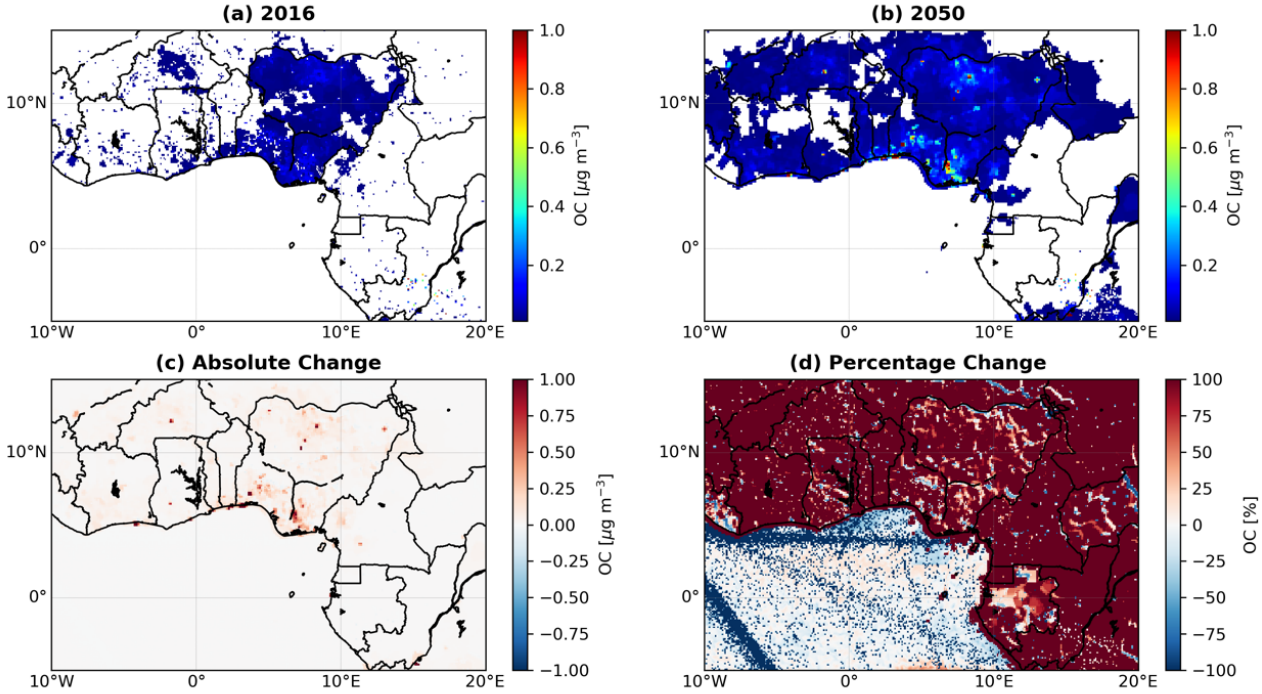

Figure 4.63: Spatial distribution of mean OC concentration under RCP 2.6 for year 2016 (a), 2050 (b), absolute difference between 2050 and 2016 (c) and the change in percentage (d).

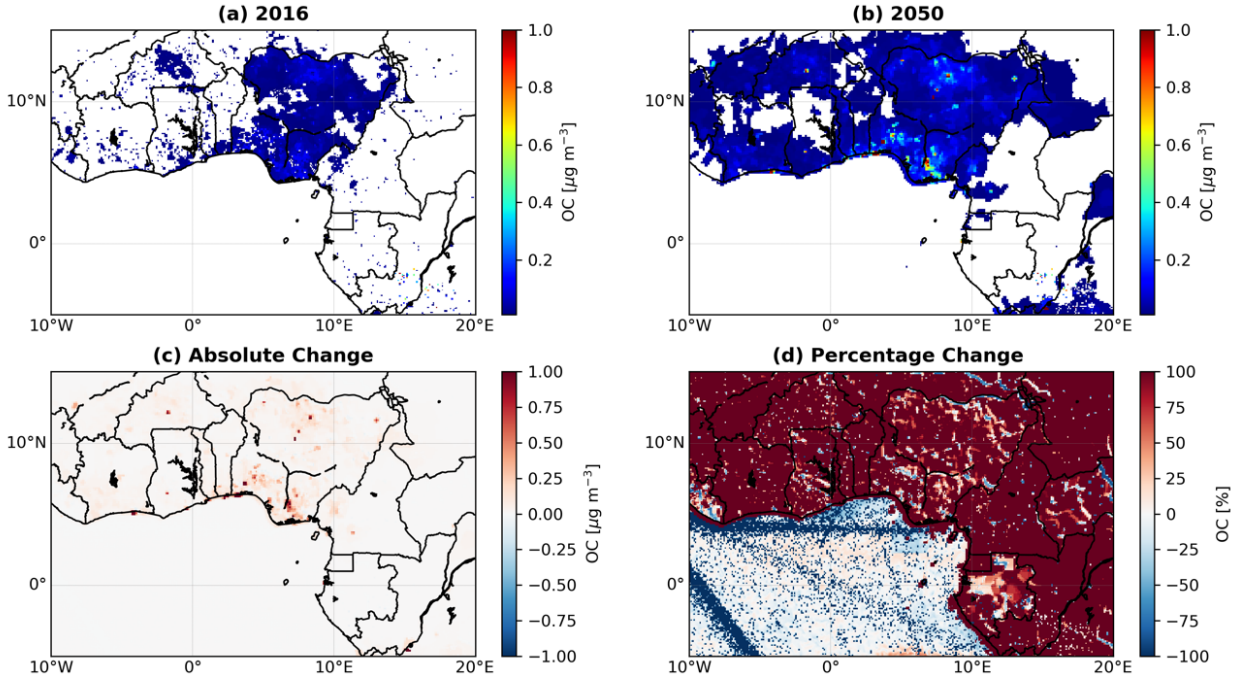

Figure 4.64: Same as Figure 4.63 but for RCP 8.5.

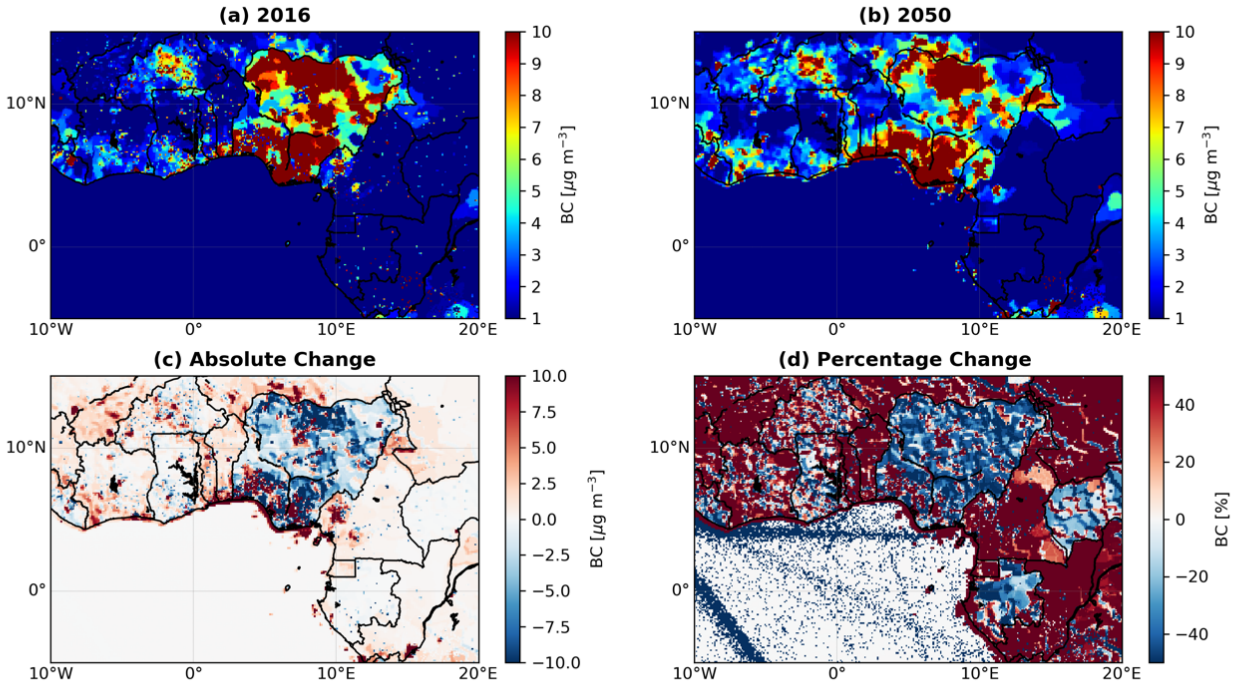

Figure 4.65: Spatial distribution of mean Black Carbon (BC) concentration under RCP 2.6 for year 2016 (a), 2050 (b), absolute difference between 2050 and 2016 (c) and the change in percentage (d).

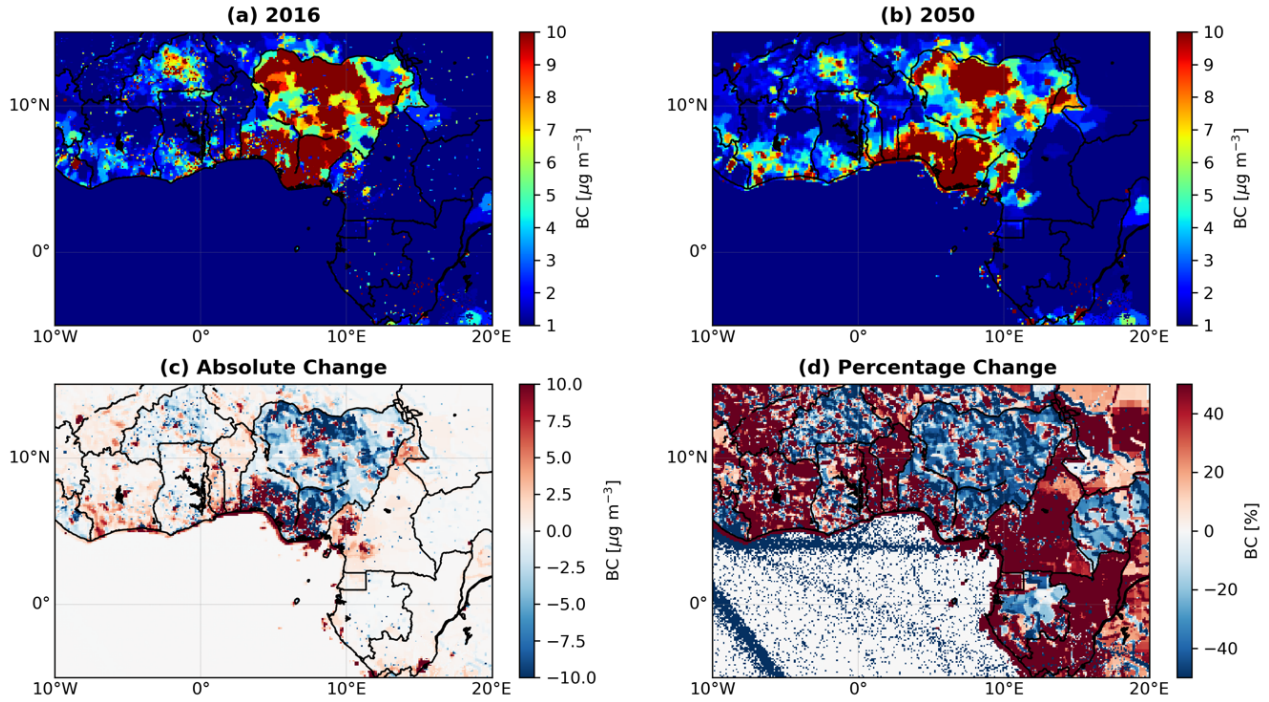

Figure 4.66: Same as Figure 4.65 but for RCP 8.5

The temporal variation of pollutants over four cities in Côte d'Ivoire and Ghana is examined. Two coastal cities as Abidjan (Côte d'Ivoire) and Accra (Ghana), a rural city, located at approximately hundreds of miles north of Abidjan named Lamto and a metropolitan area Kumasi, located in Southwestern Ghana, considered as a supersite due to its topographical feature during the DACCIWA field campaign Figure 4.67 presents the change in ozone concentration under present (2016), future scenarios RCP 2.6 and RCP 8.5. The WHO guideline for the ozone is 50 ppbv (equivalent approximately to 100 $\mu g\ m^{-3}$). The maximum (minimum) ozone concentration in Abidjan and Accra is 27 (20) ppbv for the present day, whilst an increase is predicted under both scenarios RCP 2.6 and 8.5 of about 5 ppbv. However, RCP 2.6 shows some peaks values up 40 ppbv and seems to predict more ozone that RCP 8.5 in Abidjan. Focusing on Accra, RCP 8.5 predicts more ozone than RCP 2.6 with peaks values reaching 50 ppbv (8 hours WHO limit) occurring on 05 July 2016. In Kumasi and Lamto the maximum (minimum) ozone concentration is 23 (17) ppbv for the present day, whilst an increase is predicted under both scenarios RCP 2.6 and 8.5 of about 5 ppbv but only for Kumasi. Regarding Lamto, the concentration of ozone remains unchanged between present and 2050 under both RCP scenarios. This emphasis on the relatively polluted situation in coastal cities (Abidjan, Accra) than inland area (Kumasi and Lamto).

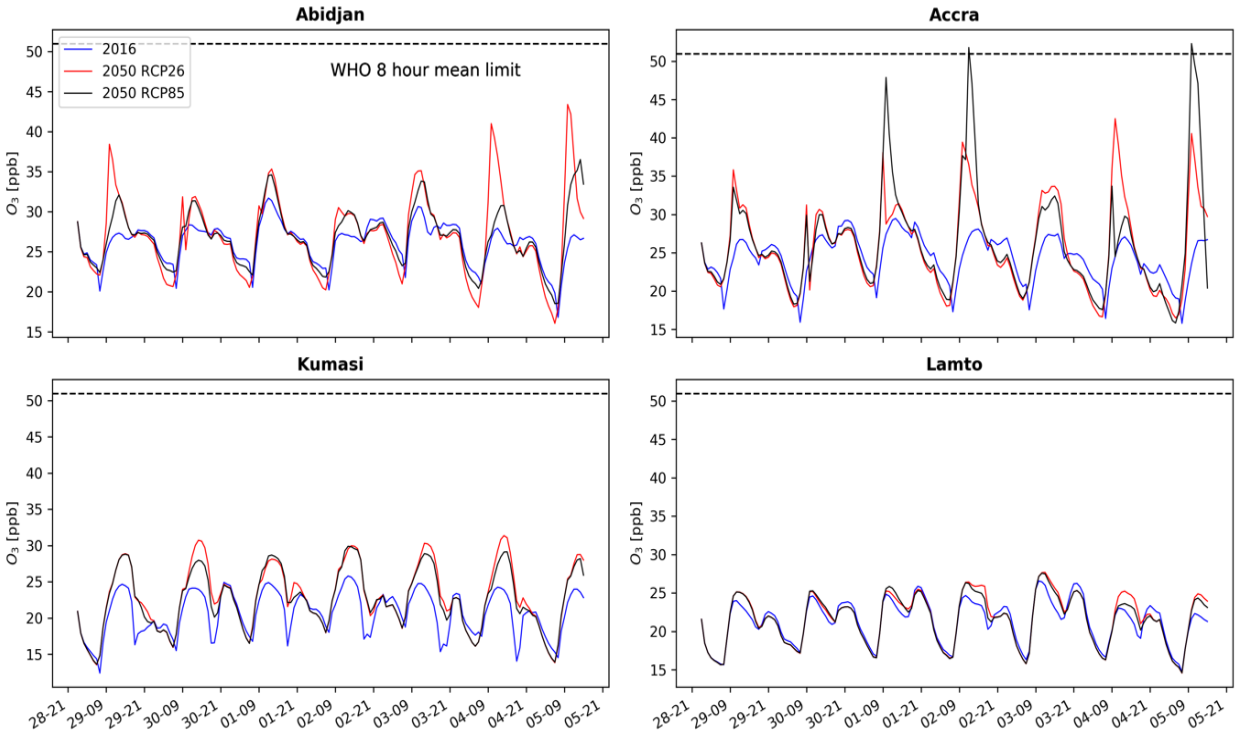

Figure 4.67: Temporal variation in ozone concentrations from 29 June to 05 July 2016 in four West African cities. The time series is computed for year 2016 (blue), year 2050 RCP 2.6 (red) and year 2050 RCP 8.5 (black). The black dash lines show the WHO guidelines of 50 ppbv (equivalent approximately to 100 µg m^{-3}).

Figure 4.68 and Figure 4.69 show the time series for CO and NO_2 respectively. In Abidjan, the variation of CO remains unchanged between present day and RCP 8.5 2050, whilst the RCP 2.6 2050 predicts a significant increase of about 200 ppbv. Maximum (minimum) CO concentration for the present day is around 400 (180) ppb. Same values for Accra but a bit less in Kumasi with maximum (minimum) of about (350) 200 ppb.

In contrast, for Accra and Kumasi, CO is predicted to increase under both RCP scenarios but more under RCP 2.6 than 8.5. Focusing on Lamto, no significant change of CO concentration is predicted and shows less variability with constant value around 200 ppb. Regarding the NO_2 variation, Figure 4.69 depicts a constant mean NO_2 concentration of around 4 ppb and predicts an increase under both scenarios, exceeding the WHO annual limit of 21 ppb in Accra, whilst in Abidjan the increase is predicted only under RCP 2.6. NO_2 concentration remain unchanged under RCP 8.5 in Abidjan. No change is observed under both RCP scenarios in Kumasi and almost zero concentration is found in Lamto. It is worth noting that WHO limit is exceeded only over coastal cities which emphasis on their level of pollution.

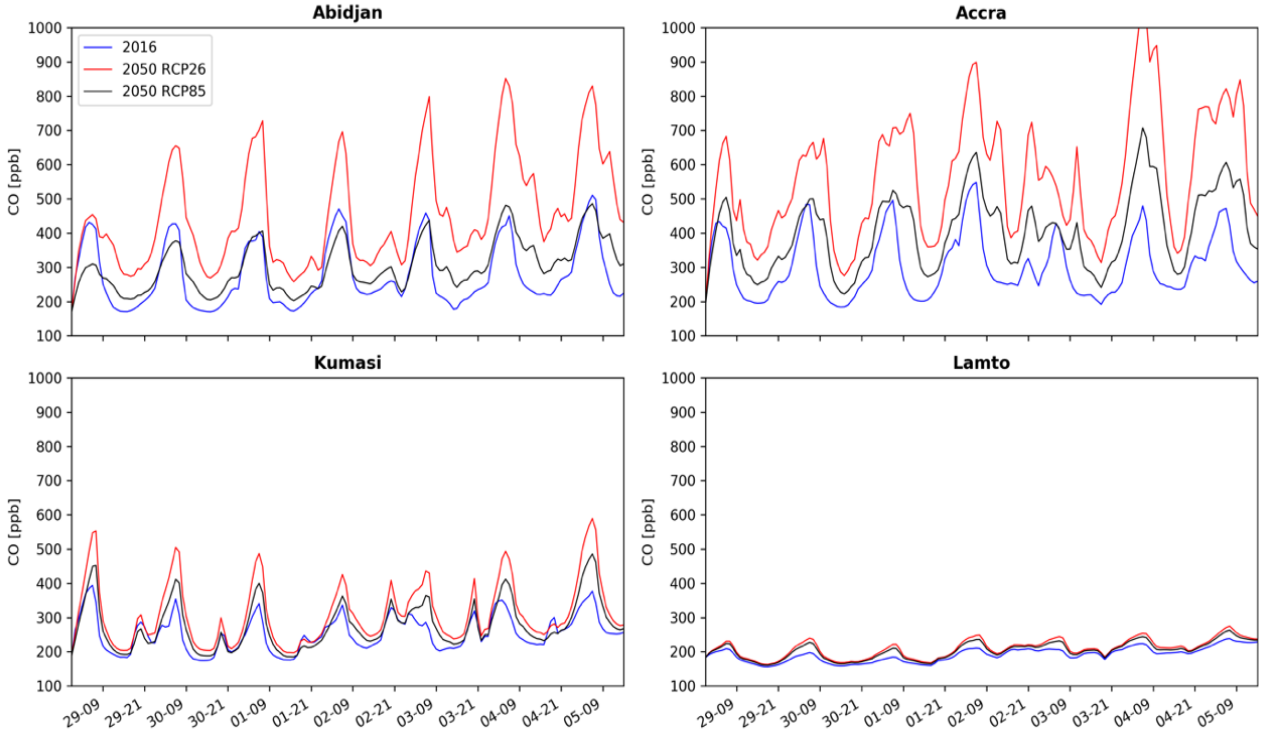

Figure 4.68: Same as Figure 4.67 but for CO.

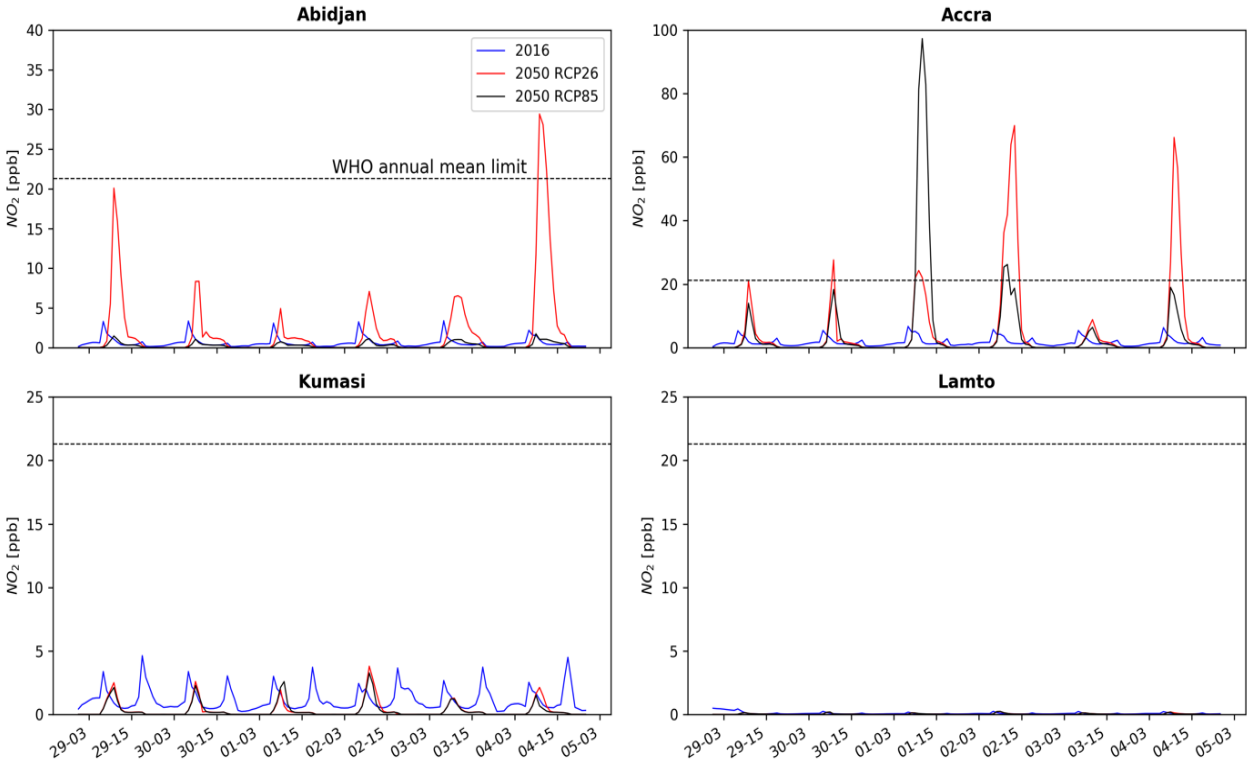

Figure 4.69: Same as Figure 4.67 but for NO_2.

CHAPTER FIVE

CONCLUSION AND RECOMMENDATIONS

5.1 Conclusion

This study focused on southern West Africa region to identify the current atmospheric composition and quantify the impact of aerosols on the clouds and radiative properties using high resolution regional climate model COSMO-ART, with a full aerosol and chemistry. This research was mainly oriented based on the availability of data and get support from DACCIWA project with respect to observational data and investigation period. Actually, DACCIWA community has identified some days with particular features, relevant for detailed cases studies. COSMO-ART has already been tested in West Africa, investigating two particular dust events during AMMA campaign (Stanelle *et al*., 2010), and is among the models used to forecast the air quality over West Africa during DACCIWA field campaign (Deetz, 2017). Therefore, it has undergone lot of model development to suit the condition of West Africa with regard to the atmospheric composition and meteorology. For computational cost constrains, the model simulation was run for period between 29 June and 31 July 2016, but the period of investigation targets the aircraft observational period (29June –16 July 2016) in order to compared model result of atmospheric composition vertical profile over the study area. The peculiarity of this work is that it quantifies the impact of both local anthropogenic aerosols (ANTHRO) and long-range biomass burning transport (FIRE) from Central Africa on the radiation and clouds microphysical properties over West Africa, which has not yet been fully investigated.

First of all, the ability to COSMO-ART to reproduce clouds features, atmospheric composition, meteorology (wind, temperature, precipitation) was assessed. Results show that COSMO-ART reproduces well the diurnal cycle of near surface temperature

and relative humidity in Abidjan with correlation coefficient of 0.87, 0.86 respectively. COSMO-ART has a tendency of slightly overestimates the temperature with a RMSE of 0.74 ºC. Regarding the precipitation, COSMO-ART shows large differences with the observed ones from DACCIWA. COSMO-ART shows precipitation for the whole month of July though the precipitation was restricted to only period from 25–30 July 2016 (recovery phase according to Knippertz *et al*., 2017). Furthermore, it does not capture peak rainfall events observed over the cities except for Accra. Overall, from the statistical analysis of metrics in order to determine the performance of COSMO-ART in forecasting rainfall over the area, it is deduced that the model displays a random forecast.

With respect to the wind speed and direction, COSMO-ART broadly agrees with ERA-Interim reanalysis, although COSMO-ART revealed a strong monsoon flow (overestimation of 1.4 m s^{-1} compared to ERA-Interim) and a stronger midlevel export from Central Africa. Regarding cloud cover, COSMO-ART reproduces areas of maximum and minimum clouds but overestimates it over the Gulf of Guinea. As far as atmospheric composition is concerned, COSMO-ART agrees well with all the observed daily particulate matter (PM) in Abidjan except for PM_1, for which the model overestimated it by 7 µg/m^3. Compared to observation, the simulated spatial distribution of CO represents quite well areas of high values such as Central Africa where biomass burning takes place. However, the model overestimates CO concentration over Nigeria as a result of anthropogenic as a result of anthropogenic emissions used by the model. In the PBL, high CO concentration, have been identified over the Gulf of Guinea close to the coastal cities of West Africa. Investigating the aerosol composition over three regimes in West Africa: upwind marine, urban cities plumes and the regional background, COSMO-ART reproduces quite well the aerosol mass concentration in

upwind marine and cities outflow but underestimates the aerosols composition in the regional background. The aerosol mass fraction is underestimated by 5.5 µg m^{-3}. Moreover, the agreement between the model and the observation is fulfilled only when biomass burning aerosols is considered in the model simulation. AERONET observation was used to evaluate COSMO-ART. The model showed a good temporal correlation for all the stations ranging from 0.69 to 0.75. Regarding the spatial distribution of the nocturnal low-level stratus (NLLS), a good representation is found between COSMO-ART and satellites-based climatology of NLLS by Van der Linden *et al*. (2015). The shortcoming is that the model shows high cloud fraction over the Gulf of Guinea and present a high frequency of occurrence 90% against 50% for the observation. The wind profile over the region during this time period is easterly at 700 hPa and southerlies within the monsoon layer. The top height of the monsoon layer is simulated to 1.9 km as defined by Fink *et al*. (2017), and agree with the observation (Kalthoff *et al*., 2018).

The atmospheric composition over the study domain is investigated. Simulated AOD from different sources (natural, anthropogenic) is examined. The AOD is dominated by anthropogenic plumes from the coastal cites which are transported mainly northward within the monsoon flow. Above it, the high AOD is observed as a result of the intrusion of airmass from long-range transport of biomass burning. As evident, over the Gulf of Guinea, the AOD is also high as a signature of biomass burning. The mineral dust AOD is generally low during this period of time. Sea salt is restricted only to the monsoon layer.

A detailed modeling case study (02 July 2016) revealed a downward mixing of aerosols from mid-tropospheric height into the PBL by convective clouds located over the Gulf of Guinea. Cold pools are found in the model over the Gulf of Guinea as a consequence

of convective cells. These cells were observed in satellite rainfall estimates but not quite as intense as in the model. Cross sections of CO concentration and cloud liquid water over the Gulf of Guinea give clear evidence that precipitating clouds are responsible of injecting the biomass burning plume from the mid-troposphere into the PBL. The meridional cross section of CO reveals that right below 1km, concentration can reach up to 60% of the maximum located at midlevel height due to downward mixing. The vertical transport moves biomass burning aerosol and trace gases from the westward moving main pollution layer at 2–4km, into the monsoon layer from where southerly flow can carry it into the region and increase local pollution levels there (Haslett *et al.*, 2019). In addition, an idealized tracer experiment shows that the leakage of biomass burning CO from the 2–4 km layer to below 1 km is on the order of 20% but varies depending on the SST.

The impact of biomass burning aerosols on the cloud microphysics, precipitation, radiation over the investigated domain are investigated. 27% increase of cloud droplets number concentration (CDNC) is found over the Gulf of Guinea and 7.5% over the region by domain averaging on a daily basis. Regarding the cloud water, there is almost no change as a result of biomass burning aerosols. Biomass burning aerosols induce a decrease of surface SW radiation up to 65 (50) W/m^2 spatially averaged over the Gulf of Guinea (3–4°N; 9°W–1°E) for cloud free pixels (cloudy pixels), whereas 25 (20) W/m^2 is found for domain D2 (3–10°N; 9°W–1°E). This emphasis the high contribution of Fire emission over the Gulf of Guinea compared to inland, as simulated by COSMO-ART. The impact on precipitation is small and estimated to 2.7% decrease. Furthermore, the impact of biomass burning aerosol on the atmospheric composition is analyzed. 36% increase of anthropogenic AOD due to FIRE emission. 6 to 7 $\mu g/m^3$ increase for PM_{10}, 78 ppbv (~152 $\mu g/m^3$) for CO and 14 ppbv (equivalent to 27.4 $\mu g/m^3$) for ozone in

Abidjan. Anthropogenic aerosols represent the major source of aerosols over the area, as it occurs throughout the year. Therefore, it appears important to quantify the impacts on the cloud properties, temperature and radiation. The decrease of surface SW radiation reaches 60 W m^{-2} due to local anthropogenic aerosol against 20 W m^{-2} due to biomass burning. The calculation was computed based on spatial average of D2. It is clearly evident that local anthropogenic aerosols have more impact compared to biomass burning aerosols, but the latter obviously increase to the burden of local pollution occurring over the region. While temperature decreases as a result of anthropogenic aerosols, the impact on longwave (LW) radiation is not clear and seems to be insignificant. Our hypothesis is that secondary effect might be responsible for the change in the LW radiation. Regarding the CDNC, 90% of the CDNC result from anthropogenic aerosols. A clear decrease towards small radius from No ANTHRO (12 µm) to ANTHRO (10 µm) is simulated. No change in precipitation is detected as a result of anthropogenic aerosols whereas, a slight decrease of cloud water is observed due to enhanced evaporation of cloud water in polluted case. This is confirmed through observational studies by Toll *et al*. (2019). Moreover, a weakening of the monsoon flow related to anthropogenic aerosols is found and agrees with the findings of Deetz *et al*. (2018).

Aerosol sensitivity experiment was examined by scaling the aerosol mass and number concentration through some factor (0.1, 1.0 and 1.5) after Deetz, (2017). The difference scaling refers to clean, reference and polluted case. The CDNC varies from

0 to 200 cm^{-3} for the reference case whereas, it remains below 100 cm^{-3} for the clean case. A shift from 15 µm to 10 µm of the droplet median size from the clean to the reference case is simulated, verifying the Twomey effect. A reduction of 46 W m^{-2}, 36 W m^{-2} and 9 W m^{-2} are obtained respectively from polluted to clean case, reference to

clean case and polluted to reference case, showing the sensitivity of aerosol change to clouds and radiative properties.

An evaluation of emission inventories over West Africa is assessed using COSMO-ART and validate with DACCIWA field campaign observation. As the development of anthropogenic aerosols emission is subjected to a lot of uncertainties, two emission datasets were used to conduct this study. A global emission dataset (EDGAR, 2010), and a regional emission dataset (DACCIWA, 2015), specific to African region.

Result shows underestimation of the EDGAR emission compared to DACCIWA for Black Carbon (BC), CO and even large difference for organic carbon fraction and NO_2. Simulation with DACCIWA emission shows better agreement with observation than with EDGAR emission for the gas species. However, shortcomings in simulating CO mixing ratio, and the aerosol mass concentration are detected. Both inventories overestimates CO concentration. All the aerosols (OC, NH_4, SO_4) are underestimated by COSMO-ART except for NO_3. The difference is large for OC and SO_4 whereas, it is less for NH_4. The difference in OC is reflected from the anthropogenic inventories. The simulated aerosol was performed with EDGAR emission, therefore, there is a need to investigate the model performance with the DACCIWA emission.

Anthropogenic aerosol is predicted to increase in the future over West Africa is no regulation is taken (Larmarque *et al*., 2010; Liousse *et al*., 2014). Therefore, it is important to investigate the impact of increasing pollutant concentration on the atmospheric composition over West Africa. All RCP scenarios shows increase of aerosols and gas pollutants but more or less with different magnitude from one area to another. For instance, high increase in the Sahel than the Gulf of Guinea for RCP 2.6 whereas same increasing trend is observed for RCP 8.5 over all the region except for SO_2 where eastern part of the Gulf of Guinea experiences high increase up to 5 times

the present day. Using the RCP2.6 and 8.5 to run COSMO-ART simulation, results reveals an increase over the whole domain of about 20% and more pronounced in Nigeria with change up to 40%. Focusing on RCP 2.6, the increase expands to Sahel region, whilst in RCP 8.5, it is restricted to Gulf of Guinea region. Regarding OC, 100% increase is predicted over the region under both scenarios, whereas for BC, some areas will experience an increase whilst a decrease is predicted in Nigeria, Niger, and Western Ghana. Furthermore, temporal variation of ozone is predicted to exceed the WHO limit (51 ppbv) in 2050 under RCP 8.5 in Accra whilst in Abidjan, Kumasi and Lamto, it will be below the limit. The NO_x limit is predicted to also exceed the WHO annual limit of 20 ppbv in both Abidjan and Accra. The WHO limit is exceeded only in coast cities, showing their high values and more variability, whilst the cities located more inland do experience less increase (i.e. Kumasi) and almost no increase for NO_x in Lamto.

5.2 Limitations and Recommendations

The most important limitations of this work are anthropogenic emissions and the period of simulation which is restricted to only a month due to high computational cost. The former refers to both EDGAR and DACCIWA inventories. Although all the emission datasets carry uncertainties, DACCIWA emissions presents better results regarding the chemical composition in the region and is recommended to be used for further investigation of the atmospheric composition over West Africa for more robust results. The investigation period is a limitation for this study. Longer simulation is needed get more robust statistic and compare with other models. Moreover, it is important to investigate the implication of biomass burning in the West Africa Monsoon (WAM) dynamics as it appears to affect the region during the investigation period. Regarding the cloud venting detected over the Gulf of Guinea, biomass burning contain a lot of

aerosols which do sediment and can be washed out by rainfall into the ocean. Thus, further investigation is necessary to know the magnitude of this process.

Both increasing local pollution and remote aerosols sources such as biomass burning from Central Africa increase the aerosol burden over West Africa in general. As a consequence, poor air quality exposes the population to serious health risk (Adon *et al*., 2019), particularly people living in the coastal cities.

This study recommends the followings:

(i) a need to implement management plans and policies to increase the adaptive capacity and mitigate the effect of anthropogenic induced air pollution in coastal cities in West Africa. For instance, an air quality monitory network should be established in order to regulate air quality over the region over the long term. This will help fill the existing data gap in West Africa regarding the atmospheric composition and should be used for data assimilation for better air quality forecast over West Africa. Also, it will help for the awareness of the population of areas of high pollution, thus reduces respiratory illness such as asthma.

(ii) Local population should shift from using wood and charcoal for the cooking purpose to the use of electricity or gas in order to reduce local emissions.

(iii) Regarding transportation, the traffic fleet in (Yopougon, Abidjan) city is dominated by old cars (Doumbia *et al*., 2018). Regulations should be implemented to ban the use of old cars as well as improve the public transportation systems, which are major sources of pollutants.

(iv) Moreover, there is a need to implement transboundary agreements in policies making, for example by collaborating with countries in Central Africa to

reduce their emissions from vegetation fires, as suggested by the DACCIWA policy brief (Evans *et al.*, 2019).

(v) As this study focused on the wet season, simulation during the dry season is needed to compare result of anthropogenic aerosol influence the state of the atmosphere during that period and compare with that of the wet season. It will also help appreciate the contribution of mineral dust on clouds properties with appears to be more abundant during that period.

(vi) Finally, the impact of future aerosol increase on clouds and radiation need to be addressed as anthropogenic aerosol is projected to increase which significantly affect radiation and increase clouds number.

REFERENCES

Abdul-Razzak, H., and Ghan, J. (2000). A parametrization of aerosol activation 2. Multiples aerosol types. *Journal of Geophysical Research*, *105*, 6837–6844.

Ackerman, S. A., Holz, R. E., Frey, R., Eloranta, E. W., Maddux, B. C., and McGill, M. (2008). Cloud detection with MODIS. Part II: Validation. *Journal of Atmospheric and Oceanic Technology*, *25*(7), 1073–1086. https://doi.org/10.1175/2007JTECHA1053.1

Adebiyi, A. A., and Zuidema, P. (2016). The role of the southern African easterly jet in modifying the southeast Atlantic aerosol and cloud environments. *Quarterly Journal of the Royal Meteorological Society*. https://doi.org/10.1002/qj.2765

Adjiri, O. A., Mafou, C. K., and Konan, P. K. (2015). Impact de la décharge d ' Akouédo (Abidjan - Côte d ' Ivoire) sur les populations : étude socio-économique et environnementale [Impact of Akouedo landfill (Abidjan - Côte d ' Ivoire) on the populations : socio-economic and environmental study], *13*(4), 979–989.

Adler, B., Babia, K., Kalthoff, N., Lohou, F., Lothon, M., Dione, C., Pedruzo-Bagazgoitia, X., and Andersen, H. (2019). Nocturnal low-level clouds in the atmospheric boundary layer over southern West Africa: An observation-based analysis of conditions and processes. *Atmospheric Chemistry and Physics*, *19*(1), 663–681. https://doi.org/10.5194/acp-19-663-2019

Adler, B., Kalthoff, N., and Gantner, L. (2017). Nocturnal low-level clouds over southern West Africa analysed using high-resolution simulations. *Atmospheric Chemistry and Physics*. https://doi.org/10.5194/acp-17-899-2017

Adon, A. J., Liousse, C., Doumbia, E. T., and Baeza-squiban, A. (2019). Physico-chemical characterization of urban aerosols from specific combustion sources in West Africa at Abidjan in Côte d ' Ivoire and Cotonou in Benin in the frame of

DACCIWA program, (June), 1–69.

Afeti, G. M., and Resch, F. J. (2000). Physical characteristics of Saharan dust near the Gulf of Guinea. *Atmospheric Environment*, *34*(8), 1273–1279. https://doi.org/10.1016/S1352-2310(99)00296-4

Albrecht, B. a. (1989). Fractional Cloudiness. *Science*, *245*, 1227–1230. https://doi.org/10.1126/science.245.4923.1227

Andreae, M. O., and Merlet, P. (2001). Emission of trace gases and aerosols from biomass burning. *Global Biogeochemical Cycles*, *15*(4), 955–966. https://doi.org/10.1029/2000GB001382

Assamoi, E. M., and Liousse, C. (2010). A new inventory for two-wheel vehicle emissions in West Africa for 2002. *Atmospheric Environment*, *44*(32), 3985–3996. https://doi.org/10.1016/j.atmosenv.2010.06.048

Athanasopoulou, E., Vogel, H., Vogel, B., Tsimpidi, A. P., Pandis, S. N., Knote, C., and Fountoukis, C. (2013). Modeling the meteorological and chemical effects of secondary organic aerosols during an EUCAARI campaign. *Atmospheric Chemistry and Physics*, *13*(2), 625–645. https://doi.org/10.5194/acp-13-625-2013

Awadzi, T., and Breuning-Madsen, H. (2011). Harmattan dust deposited in Ghana within 2000–2005. *West African Journal of Applied Ecology*, *11*(1). https://doi.org/10.4314/wajae.v11i1.45723

Babic, K., Adler, B., Kalthoff, N., Andersen, H., Dione, C., and Lohou, F. (2019). The observed diurnal cycle of low-level stratus clouds over southern West Africa : a case study, (2012), 1281–1299.

Bae, S., and Hong, Y. C. (2018). Health effects of particulate matter. *Journal of the Korean Medical Association*, *61*(12), 749–755. https://doi.org/10.5124/jkma.2018.61.12.749

Bahino, J., Yoboué, V., Galy-Lacaux, C., Adon, M., Akpo, A., Keita, S., Liousse, C., Gardrat, E., Chiron, C., Ossohou, M., Gnamien, S., and Djossou, J. (2017). Spatial distribution of gaseous pollutants (NO2, SO2, NH3, HNO3 and O3) in Abidjan, Cote d'Ivoire. *Atmos. Chem. Phys. Discuss*. https://doi.org/10.5194/acp-2017-724

Bangert, M. J. (2012). Interaction of Aerosol , Clouds , and Radiation on the Regional Scale.

Bangert, M., Nenes, A., Vogel, B., Vogel, H., Barahona, D., Karydis, V. A., Kumar, P., Kottmeier, C., and Blahak, U. (2012). Saharan dust event impacts on cloud formation and radiation over Western Europe. *Atmospheric Chemistry and Physics*, *12*(9), 4045–4063. https://doi.org/10.5194/acp-12-4045-2012

Barbosa, P. M., Stroppiana, D., Grégoire, J. M., & Pereira, J. M. C. (1999). An assessment of vegetation fire in Africa (1981-1991): Burned areas, burned biomass, and atmospheric emissions. *Global Biogeochemical Cycles*. https://doi.org/10.1029/1999GB900042

Benedetti, A., Reid, J. S., Knippertz, P., Marsham, J. H., Di Giuseppe, F., Rémy, S., Basart, S., Boucher, O., Brooks, I. M., Menut, L., Mona, L., Laj, P., Pappalardo, G., Wiedensohler, A., Baklanov, A., Brooks, M., Colarco, P. R., Cuevas, E., Da Silva, A., Escribano, J., Huneeus, N., Jorba, O., Kazadzis, S., Kinne, S., Popp, T., Quinn, P. K., Sekiyama, T. T., Tanaka, T., and Terradellas, E. (2018). Status and future of numerical atmospheric aerosol prediction with a focus on data requirements. *Atmospheric Chemistry and Physics*. https://doi.org/10.5194/acp-18-10615-2018

Binkowski, F. S., and Shankar, U. (1995). The Regional Particulate Matter Model 1. Model description and preliminary results. *Journal of Geophysical Research*, *100*(95).

Brito, J., Freney, E., Dominutti, P., Borbon, A., Haslett, S. L., Batenburg, A. M., Colomb, A., Dupuy, R., Denjean, C., Burnet, F., Bourriane, T., Deroubaix, A., Sellegri, K., Borrmann, S., Coe, H., Flamant, C., Knippertz, P., and Schwarzenboeck, A. (2018). Assessing the role of anthropogenic and biogenic sources on PM 1 over southern West Africa using aircraft measurements. *Atmos. Chem. Phys*. https://doi.org/10.5194/acp-18-757-2018

Burpee, R. W. (1972). The Origin and Structure of Easterly Waves in the Lower Troposphere of North Africa. *Journal of the Atmospheric Sciences*. https://doi.org/10.1175/1520-0469(1972)029<0077:TOASOE>2.0.CO;2

Camara, M., Jenkins, G., and Konare, A. (2010). Impacts of dust on West African climate during 2005 and 2006. *Atmospheric Chemistry and Physics Discussions*, *10*(2), 3053–3086. https://doi.org/10.5194/acpd-10-3053-2010

CCMS. (2015). No. Retrieved June 10, 2017, from https://svn-ccsm-inputdata.cgd.ucar.edu/trunk/inputdata/lnd/clm2/rawdata/pftlanduse.3minx3%0Dmin.simyr2000.c110913/

Chaboureau, J. P., Tulet, P., and Mari, C. (2007). Diurnal cycle of dust and cirrus over West Africa as seen from Meteosat Second Generation satellite and a regional forecast model. *Geophysical Research Letters*, *34*(2). https://doi.org/10.1029/2006GL027771

Chatfield, R. B., Vastano, J. A., Li, L., Sachse, G. W., and Connors, V. S. (1998). The Great African Plume from biomass burning: Generalizations from a three-dimensional study of TRACE A carbon monoxide. *Journal of Geophysical Research: Atmospheres*, *103*(D21), 28059–28077. https://doi.org/10.1029/97JD03363

Chen, G., Xue, H., Feingold, G., and Zhou, X. (2012). Vertical transport of pollutants

by shallow cumuli from large eddy simulations. *Atmospheric Chemistry and Physics*, *12*(23), 11319–11327. https://doi.org/10.5194/acp-12-11319-2012

Ching, J. K. S., Shipley, S. T., and Browell, E. V. (1988). Evidence for cloud venting of mixed layer ozone and aerosols. *Atmospheric Environment (1967)*. https://doi.org/10.1016/0004-6981(88)90030-3

Clerbaux, C., George, M., Turquety, S., Walker, K. A., Barret, B., Bernath, P., Boone, C., Borsdorff, T., Cammas, J. P., Catoire, V., Coffey, M., Coheur, P. F., Deeter, M., De Mazière, M., Drummond, J., Duchatelet, P., Dupuy, E., De Zafra, R., and Wiacek, A. (2008). CO measurements from the ACE-FTS satellite instrument: Data analysis and validation using ground-based, airborne and spaceborne observations. *Atmospheric Chemistry and Physics*, *8*(9), 2569–2594. https://doi.org/10.5194/acp-8-2569-2008

Cook, K. H. (1999). Generation of the African easterly jet and its role in determining West African precipitation. *Journal of Climate*. https://doi.org/10.1175/1520-0442(1999)012<1165:GOTAEJ>2.0.CO;2

Costantino, L., and Bréon, F. M. (2013). Aerosol indirect effect on warm clouds over South-East Atlantic, from co-located MODIS and CALIPSO observations. *Atmospheric Chemistry and Physics*, *13*(1), 69–88. https://doi.org/10.5194/acp-13-69-2013

Cotton, W. R., Alexander, G. D., Hertenstein, R., Walko, R. L., McAnelly, R. L., and Nicholls, M. (1995). Cloud venting - A review and some new global annual estimates. *Earth Science Reviews*, *39*(3–4), 169–206. https://doi.org/10.1016/0012-8252(95)00007-0

Dai, Y., Dickinson, R. E., and Wang, Y.-P. (2004). A Two-Big-Leaf Model for Canopy Temperature, Photosynthesis, and Stomatal Conductance. *America Meteorogical*

Society, 2281–2299.

Dajuma, A., Ogunjobi, K. O., Vogel, H., Knippertz, P., Silué, S., Datchoh, E. T. N., Yoboué, V., and Vogel, B. (2019). Cloud-venting induced downward mixing of the Central African biomass burning plume during the West Africa summer monsoon, (July 2016), 1–31.

Das, S., Dey, S., and Dash, S. K. (2016). Direct radiative effects of anthropogenic aerosols on Indian summer monsoon circulation. *Theoretical and Applied Climatology*, *124*(3–4), 629–639. https://doi.org/10.1007/s00704-015-1444-8

Das, S., Harshvardhan, H., Bian, H., Chin, M., Curci, G., Protonotariou, A. P., Mielonen, T., Zhang, K., Wang, H., and Liu, X. (2017). Biomass burning aerosol transport and vertical distribution over the South African-Atlantic region. *Journal of Geophysical Research*, *122*(12), 6391–6415. https://doi.org/10.1002/2016JD026421

Dee, D. P., Uppala, S. M., Simmons, A. J., Berrisford, P., Poli, P., Kobayashi, S., Andrae, U., Balmaseda, M. A., Balsamo, G., Bauer, P., Bechtold, P., Beljaars, A. C.M., van de Berg, L., Bidlot, J., Bormann, N., and Vitart, F. (2011). The ERA-Interim reanalysis: Configuration and performance of the data assimilation system. *Quarterly Journal of the Royal Meteorological Society*, *137*(656), 553–597. https://doi.org/10.1002/qj.828

Deetz, K. (2017). Assessing the Aerosol Impact on Southern West African Clouds and Atmospheric Dynamics.

Deetz, K., and Vogel, B. (2017). Development of a new gas-flaring emission dataset for southern West Africa. *Geoscientific Model Development*, *10*(4), 1607–1620. https://doi.org/10.5194/gmd-10-1607-2017

Deetz, K., Vogel, H., Haslett, S., Knippertz, P., Coe, H., and Vogel, B. (2018). Aerosol

liquid water content in the moist southern West African monsoon layer and its radiative impact. *Atmospheric Chemistry and Physics*, *18*(19), 14271–14295. https://doi.org/10.5194/acp-18-14271-2018

Deetz, K., Vogel, H., Knippertz, P., Adler, B., Taylor, J., Coe, H., Bower, K., Haslett, S., Flynn, M., Dorsey, J., Crawford, I., Kottmeier, C. and Vogel, B. (2018c). Numerical simulations of aerosol radiative effects and their impact on clouds and atmospheric dynamics over southern West Africa. *Atmospheric Chemistry and Physics*, *18*(13), 9767–9788. https://doi.org/10.5194/acp-18-9767-2018

DeMott, P. J., Sassen, K., Poellot, M. R., Baumgardner, D., Rogers, D. C., Brooks, S. D., Prenni, A. J., and Kreidenweis, S. M. (2003). African dust aerosols as atmospheric ice nuclei. *Geophysical Research Letters*, *30*(14), 26–29. https://doi.org/10.1029/2003GL017410

Deroubaix, A., Flamant, C., Menut, L., Siour, G., Mailler, S., Turquety, S., Briant, R., Khvorostyanov, D., and Crumeyrolle, S. (2018). Interactions of atmospheric gases and aerosols with the monsoon dynamics over the Sudano-Guinean region during AMMA. *Atmospheric Chemistry and Physics*, *18*(1), 445–465. https://doi.org/10.5194/acp-18-445-2018

Deroubaix, A., Menut, L., Flamant, C., Brito, J., Denjean, C., Dreiling, V., Fink, A., Jambert, C., Kalthoff, N., Knippertz, P., Ladkin, R., Mailler, S., Maranan, M., Pacifico, F., Piguet, B., Siour, G., and Turquety, S. (2019). Diurnal cycle of coastal anthropogenic pollutant transport over southern West Africa during the DACCIWA campaign. *Atmospheric Chemistry and Physics*, *19*(1), 473–497. https://doi.org/10.5194/acp-19-473-2019

Dickinson, R. E. (1984). Modeling evapotranspiration for three-dimensional global climate models. *Climate Processes and Climate Sensitivity*, *29*, 58–72.

Diedhiou, A., Janicot, S., Viltard, A., De Felice, P., and Laurent, H. (1999). Easterly wave regimes and associated convection over West Africa and tropical Atlantic: Results from the NCEP/NCAR and ECMWF reanalyses. *Climate Dynamics*, *15*(11), 795–822. https://doi.org/10.1007/s003820050316

Dione, C., Lohou, F., Lothon, M., Adler, B., Babić, K., Kalthoff, N., Pedruzo-Bagazgoitia, X., Bezombes, Y., and Gabella, O. (2019). Low-level stratiform clouds and dynamical features observed within the southern West African monsoon. *Atmospheric Chemistry and Physics*, *19*(13), 8979–8997. https://doi.org/10.5194/acp-19-8979-2019

Djossou, J., Léon, J. F., Barthélemy Akpo, A., Liousse, C., Yoboué, V., Bedou, M., Bodjrenou, M., Chiron, C., Galy-Lacaux, C., Gardrat, E., Abbey, M., Keita, S., Bahino, J., N'Datchoh, E. T., Ossohou, M., and Awanou, C. N. (2018). Mass concentration, optical depth and carbon composition of particulate matter in the major southern West African cities of Cotonou (Benin) and Abidjan (Côte d'Ivoire). *Atmospheric Chemistry and Physics*, *18*(9), 6275–6291. https://doi.org/10.5194/acp-18-6275-2018

Doumbia, M., Toure, N. E., Silue, S., Yoboue, V., Diedhiou, A., and Hauhouot, C. (2018). Emissions from the road traffic of West African cities: Assessment of vehicle fleet and fuel consumption. *Energies*, *11*(9), 1–16. https://doi.org/10.3390/en11092300

E. Ite, A., and J. Ibok, U. (2013). Gas Flaring and Venting Associated with Petroleum Exploration and Production in the Nigeria's Niger Delta. *American Journal of Environmental Protection*, *1*(4), 70–77. https://doi.org/10.12691/env-1-4-1

Edgar. (2010). EDGAR - Emission Database for Global Atmospheric Research. *Global Emissions EDGAR v4.2 (November 2011)*. https://doi.org/10.2904/EDGARv4.2

Elvidge, C. D., Zhizhin, M., Baugh, K., Hsu, F. C., and Ghosh, T. (2016). Methods for global survey of natural gas flaring from visible infrared imaging radiometer suite data. *Energies*, *9*(1). https://doi.org/10.3390/en9010014

Elvidge, C. D., Ziskin, D., Baugh, K. E., Tuttle, B. T., Ghosh, T., Pack, D. W., Erwin, E. H., and Zhizhin, M. (2009). A fifteen year record of global natural gas flaring derived from satellite data. *Energies*, *2*(3), 595–622. https://doi.org/10.3390/en20300595

Emmons, L. K., Walters, S., Hess, P. G., Lamarque, J.-F., Pfister, G. G., Fillmore, D., Granier, C., Guenther, A., Kinnison, D., Laepple, T., Orlando, J., Tie, X., Tyndall, G., Wiedinmyer, C., Baughcum, S. L., and Kloster, S. (2009). MOZART-4 description Geoscientific Model Development Discussions Description and evaluation of the Model for Ozone and Related chemical Tracers, version 4 (MOZART-4) MOZART-4 description MOZART-4 description. *Geosci. Model Dev. Discuss*.

Engelstaedter, S., and Washington, R. (2007). Temporal controls on global dust emissions: The role of surface gustiness. *Geophysical Research Letters*, *34*(15). https://doi.org/10.1029/2007GL029971

Evans, M. J., Knippertz, P., Aristide, A., and Allan, R. P. (2019). Policy-relevant findings of the DACCIWA, (April). https://doi.org/10.5281/zenodo.1476843

Fan, J., Wang, Y., Rosenfeld, D., and Liu, X. (2016). Review of aerosol-cloud interactions: Mechanisms, significance, and challenges. *Journal of the Atmospheric Sciences*, *73*(11), 4221–4252. https://doi.org/10.1175/JAS-D-16-0037.1

Feichter, J., Roeckner, E., Lohmann, U., and Liepert, B. (2004). Nonlinear aspects of the climate response to Greenhouse gas and aerosol forcing. *Journal of Climate*,

17(12), 2384–2398. https://doi.org/10.1175/1520-0442(2004)017<2384:NAOTCR>2.0.CO;2

Fiedler, S., Stevens, B., Gidden, M., Smith, S. J., Riahi, K., and Van Vuuren, D. (2019). First forcing estimates from the future CMIP6 scenarios of anthropogenic aerosol optical properties and an associated Twomey effect. *Geoscientific Model Development*, *12*(3), 989–1007. https://doi.org/10.5194/gmd-12-989-2019

Fink, A. H., Engel, T., Volker, E., van der Linden, R., Schneidewina, M., Redl, R., Afiesimama, E., Thiaw, W. M., Yorke, C., and Evans, M. (2017). Meteorology of tropical West Africa: The forecasters' handbook. *Meteorology of Tropical West Africa: The Forecasters' Handbook*, 1–468. https://doi.org/10.1002/9781118391297

Flamant, C., Deroubaix, A., Chazette, P., Brito, J., Gaetani, M., Knippertz, P., Fink, A. H., de Coetlogon, G., Menut, L., Colomb, A., Denjean, C., Meynadier, R., Rosenberg, P., Dupuy, R., Dominutti, P., Duplissy, J., Bourrianne, T., Schwarzenboeck, A., Ramonet, M., and Totems, J. (2018). Aerosol distribution in the northern Gulf of Guinea: local anthropogenic sources, long-range transport, and the role of coastal shallow circulations. *Atmospheric Chemistry and Physics*, *18*(16), 12363–12389. https://doi.org/10.5194/acp-18-12363-2018

Flamant, C., Knippertz, P., Fink, A. H., Akpo, A., Brooks, B., Chiu, C. J., Coe, H., Danuor, S., Evans, M., Jegede, O., Kalthoff, N., Konaré, A., Liousse, C., Lohou, F. and Yoboué, V. (2018). The Dynamics–Aerosol–Chemistry–Cloud Interactions in West Africa Field Campaign: Overview and Research Highlights. *Bulletin of the American Meteorological Society*, *99*(1), 83–104. https://doi.org/10.1175/bams-d-16-0256.1

Flamant, C., Lavaysse, C., Todd, M. C., Chaboureau, J. P., and Pelon, J. (2009). Multi-

platform observations of a springtime case of Bodélé and Sudan dust emission, transport and scavenging over West Africa C. *Royal Meteorological Society*, *135*(February), 413–430. https://doi.org/10.1002/qj

Fountoukis, C., and Nenes, A. (2005). Continued development of a cloud droplet formation parameterization for global climate models. *Journal of Geophysical Research D: Atmospheres*, *110*(11), 1–10. https://doi.org/10.1029/2004JD005591

Freitas, S. R., Longo, K. M., and Andreae, M. O. (2006). Impact of including the plume rise of vegetation fires in numerical simulations of associated atmospheric pollutants. *Geophysical Research Letters*, *33*(17). https://doi.org/10.1029/2006GL026608

Gal-chen, T., and Somerville, R. C. J. (1975). On the Use of a Coordinate Transformation for the Solution of the Navier-Stokes Equations Considerable progress has been made in the last decade toward a better numerical solution of the Navier-Stokes equations without topography . The simulation of fluid. *Journal Of Computational Physics*, *228*, 209–228.

Ginoux, P., Prospero, J. M., Torres, O., and Chin, M. (2004). Long-term simulation of global dust distribution with the GOCART model: Correlation with North Atlantic Oscillation. In *Environmental Modelling and Software* (Vol. 19, pp. 113–128). https://doi.org/10.1016/S1364-8152(03)00114-2

GlobCover. (2009). GlobCover Land Cover Map - European Space Agency GlobCover Project. Retrieved June 10, 2017, from http://www.gelib.com/globcover-2009.htm

Gordon, H., Field, P. R., Abe, S. J., Dalvi, M., Grosvenor, D. P., Hill, A. A., Johnson, B. T., Miltenberger, A. K., Yoshioka, M., and Carslaw, K. S. (2018). Large simulated radiative effects of smoke in the south-east Atlantic. *Atmospheric Chemistry and Physics*, *18*(20), 15261–15289. https://doi.org/10.5194/acp-18-

15261-2018

Grams, C. M., Jones, S. C., Marsham, J. H., Parker, D. J., Haywood, J. M., and Heuveline, V. (2010). The Atlantic inflow to the Saharan heat low: Observations and Modelling. *Quarterly Journal of the Royal Meteorological Society*, *136*(SUPPL. 1), 125–140. https://doi.org/10.1002/qj.429

Grythe, H., Ström, J., Krejci, R., Quinn, P., and Stohl, A. (2014). A review of sea-spray aerosol source functions using a large global set of sea salt aerosol concentration measurements. *Atmospheric Chemistry and Physics*, *14*(3), 1277–1297. https://doi.org/10.5194/acp-14-1277-2014

Gu, Y., Liou, K. N., Jiang, J. H., Su, H., and Liu, X. (2012). Dust aerosol impact on North Africa climate: A GCM investigation of aerosol-cloud-radiation interactions using A-Train satellite data. *Atmospheric Chemistry and Physics*, *12*(4), 1667–1679. https://doi.org/10.5194/acp-12-1667-2012

Guenther, A. B., Jiang, X., Heald, C. L., Sakulyanontvittaya, T., Duhl, T., Emmons, L. K., and Wang, X. (2012). The Model of Emissions of Gases and Aerosols from Nature version 2.1 (MEGAN2. 1): an extended and updated framework for modeling biogenic emissions. *Geoscientific Model Development*, *5*(6), 1471–1492.

Guo, L., Highwood, E. J., Shaffrey, L. C., and Turner, A. G. (2013). The effect of regional changes in anthropogenic aerosols on rainfall of the East Asian Summer Monsoon. *Atmospheric Chemistry and Physics*, *13*(3), 1521–1534. https://doi.org/10.5194/acp-13-1521-2013

Halland, J. J., Fuelberg, H. E., Pickering, K. E., and Luo, M. (2009). Identifying convective transport of carbon monoxide by comparing remotely sensed observations from TES with cloud modeling simulations. *Atmospheric Chemistry and Physics*, *9*(13), 4279–4294. https://doi.org/10.5194/acp-9-4279-2009

Hannak, L., Knippertz, P., Fink, A. H., A., K., and G., P. (2017). AMERICAN METEOROLOGICAL This is a preliminary PDF of the author-produced. *America Meteorogical Society*. https://doi.org/10.1175/JCLI-D-16-0451.1

HAO, W. M., and LIU, M. H. (1994). SPATIAL AND TEMPORAL DISTRIBUTION OF TROPICAL BIOMASS BURNING. *GLOBAL BIOGEOCHEMICAL CYCLES*. https://doi.org/10.1029/94GB02086

Haslett, S. L., Taylor, J. W., Deetz, K., Vogel, B., Babić, K., Kalthoff, N., Wieser, A,. Dione, C., Lohou, F., and Coe, H. (2018). The radiative impact of out-of-cloud aerosol hygroscopic growth during the summer monsoon in southernWest Africa. *Atmospheric Chemistry and Physics Discussions*, 1–25. https://doi.org/10.5194/acp-2018-805

Haslett, S. L., Taylor, J. W., Evans, M., Morris, E., Vogel, B., Dajuma, A., Brito, J., Batenburg, A. M., Borrmann, S., Schneider, J., Schulz, C., Denjean, C., Bourrianne, T., Knippertz, P., Dupuy, R., Schwarzenböck, A., Sauer, D., Flamant, C., Dorsey, J., Crawford, I., and Coe, H. (2019). Remote biomass burning dominates southern West African air pollution during the monsoon. *Atmospheric Chemistry and Physics Discussions*, *3*(April), 1–23. https://doi.org/10.5194/acp-2019-38

Hill, P. G., Allan, R. P., Chiu, J. C., and Stein, T. H. M. (2016). Journal of Geophysical Research : Atmospheres and comparison to climate models. *Journal of Geophysical Research : Atmospheres*, 1–23. https://doi.org/10.1002/2016JD025246.Received

Hourdin, F., Musat, I., Guichard, F., Ruti, P. M., Favot, F., Filiberti, M. A., Pham, M. A.Ï., Grandpeix, J. Y., Polcher, J. A. N., Marquet, P., Boone, A., Lafore, J. P., Redelsperger, J. L., Dell'Aquila, A., Doval, T. L., Traore, A. K., and Gallée, H.

(2010). Amma-Model intercomparison project. *Bulletin of the American Meteorological Society*, *91*(1), 95–104. https://doi.org/10.1175/2009BAMS2791.1

Huang, J., Adams, A., Wang, C., and Zhang, C. (2013). Black Carbon and West African Monsoon precipitation : observations and simulations Accessed Annales Geophysicae Black Carbon and West African Monsoon precipitation : observations and simulations. *Annales Geophysicae*, 4171–4181.

Huang, X., Ding, A., Liu, L., Liu, Q., Ding, K., Niu, X., Nie, W., Xu, Z., Chi, X., Wang, M., Sun, J., Guo, W., and Fu, C. (2016). Effects of aerosol-radiation interaction on precipitation during biomass-burning season in East China. *Atmospheric Chemistry and Physics*, *16*(15), 10063–10082. https://doi.org/10.5194/acp-16-10063-2016

Huffman, G., Adler, R. F., Bolvin, D. T., Gu, G., Nelkin, E. J., Bowman, K. P., Stocker, E., and Wolff, D. (2007). The TRMM multi-satellite precipitation analysis: Quasi-global, multi-year, combined-sensor precipitation estimates at fine scale. *J. Hydrometeor.*, *8*, 28–55.

Huffman, G. J., Bolvin, D. T., Braithwaite, D., Hsu, K., Joyce, R., Kidd, C., Nelkin, E. J., Sorooshian, S., and Xie, P. (2018). NASA Global Precipitation Measurement (GPM) Integrated Multi-satellitE Retrievals for GPM (IMERG). *Algorithm Theoretical Basis Document (ATBD)*, (February), 1–31. https://doi.org/https://pmm.nasa.gov/resources/documents/gpm-integrated-multi-satellite-retrievals-gpm-imerg-algorithm-theoretical-basis-

HWSD. (2012). *Harmonized world soil database*. *Food and Agriculture Organization*. https://doi.org/10.1192/bjp.112.483.211-a

IPCC. (2013). *Climate change 2013: the physical science basis: Working Group*. *Fifth Assessment Report of the Intergovernmental Panel on Climate Change* (Vol. 5).

Jacobsen, I., and Heise, E. (1982). A new economic method for the computation of the surface temperature in numerical models. *Contributions to Atmospheric Physics*, *55*.

Janicot, S., Thorncroft, C. D., Ali, A., Asencio, N., Berry, G., Bock, O., Bourles, B., Caniaux, G., and Chauvin, F. (2008). ReviewAMMA field experiment in 2006.pdf, 2569–2595.

Jenkins, G. S., Pratt, A. S., and Heymsfield, A. (2008). Possible linkages between Saharan dust and tropical cyclone rain band invigoration in the eastern Atlantic during NAMMA-06. *Geophysical Research Letters*, *35*(8), 1–7. https://doi.org/10.1029/2008GL034072

Jiang, Y., Lu, Z., Liu, X., Qian, Y., Zhang, K., Wang, Y., and Yang, X. Q. (2016). Impacts of global open-fire aerosols on direct radiative, cloud and surface-albedo effects simulated with CAM5. *Atmospheric Chemistry and Physics*, *16*(23), 14805–14824. https://doi.org/10.5194/acp-16-14805-2016

Kaiser, J. W., Heil, A., Andreae, M. O., Benedetti, A., Chubarova, N., Jones, L., Morcrette, J. J., Razinger, M., Schultz, M. G., Suttie, M., and Van Der Werf, G. R. (2012). Biomass burning emissions estimated with a global fire assimilation system based on observed fire radiative power. *Biogeosciences*. https://doi.org/10.5194/bg-9-527-2012

Kalthoff, N., Lohou, F., Brooks, B., Jegede, G., Adler, B., Babić, K., Dione, C., Ajao, A., Amekudzi, L. K., Aryee, J. N. A., Ayoola, M., Bessardon, G., Danuor, S. K., Handwerker, J., Kohler, M., Lothon, M., Pedruzo-Bagazgoitia, X., Smith, V., Sunmonu, L., Wieser, A., Fink, A. H., and Knippertz, P. (2018). An overview of the diurnal cycle of the atmospheric boundary layer during the West African monsoon season: Results from the 2016 observational campaign. *Atmospheric*

Chemistry and Physics. https://doi.org/10.5194/acp-18-2913-2018

Kaufman, Y. J., Koren, I., Remer, L. A., Rosenfeld, D., and Rudich, Y. (2005). The effect of smoke, dust, and pollution aerosol on shallow cloud development over the Atlantic Ocean. *Proceedings of the National Academy of Sciences*, *102*(32), 11207–11212. https://doi.org/10.1073/pnas.0505191102

Keita, S. (2018). Emissions anthropiques des gaz et particules issus ds combustions en Afrique: élaboration d'inventaire et évaluation d'incertitudes.

Keita, S., Liousse, C., Yoboué, V., Dominutti, P., Guinot, B., Borbon, A., Haslett, S. L., Bouvier, L., Colomb, A., Ossohou, M., N'Datchoh, E. T., and Roblou, L. (2017). Aerosol and VOC emission factor measurements for African anthropogenic sources. *Atmospheric Chemistry and Physics Discussions*, (October), 1–40. https://doi.org/10.5194/acp-2017-944

Kerkweg, A., Wurzler, S., Reisin, T., and Bott, A. (2003). On the cloud processing of aerosol particles: An entraining air-parcel model with two-dimensional spectral cloud microphysics and a new formulation of the collection kernel. *Quarterly Journal of the Royal Meteorological Society*, *129*(587 PART A), 1–18. https://doi.org/10.1256/qj.02.52

Klemp, J. B., and Wilhelmson, R. B. (1978). The SImulation of Three-DImensional Convective Storm Dynamics. *Journal of the Atmospheric Sciences*, *35*, 1070–1096.

Kniffka, A., Knippertz, P., and Fink, A. H. (2019). The role of low-level clouds in the West African monsoon system. *Atmospheric Chemistry and Physics*, *19*(3), 1623–1647. https://doi.org/10.5194/acp-19-1623-2019

Knippertz, P., Coe, H., Chiu, J. C., Evans, M. J., Fink, A. H., Kalthoff, N., Liousse, C., Mari, C., Allan, R. P., Brooks, B., Danour, S., Jegede, O. O., Lohou, F., and

Marsham, J. H. (2015). The dacciwa project: Dynamics-aerosol-chemistry-cloud interactions in West Africa. *Bulletin of the American Meteorological Society*, *96*(9), 1451–1460. https://doi.org/10.1175/BAMS-D-14-00108.1

Knippertz, P., Fink, A. H., Deroubaix, A., Morris, E., Tocquer, F., Evans, M. J., Flamant, C., Gaetani, M., Lavaysse, C., Meynadier, R., Deetz, K., Maranan, M., Rosenberg, P. D., and Schlueter, A. (2017). A meteorological and chemical overview of the DACCIWA field campaign in West Africa in June-July 2016. *Atmospheric Chemistry and Physics*, *17*(17), 10893–10918. https://doi.org/10.5194/acp-17-10893-2017

Knippertz, P., Fink, A. H., Schuster, R., Trentmann, J., Schrage, J. M., and Yorke, C. (2011). Ultra - low clouds over the southern West African monsoon region, *38*(August), 1–7. https://doi.org/10.1029/2011GL049278

Knippertz, P., and Todd, M. C. (2012). Mineral dust aerosols over the Sahara: Meteorological controls on emission and transport and implications for modeling. *Reviews of Geophysics*, *50*(1). https://doi.org/10.1029/2011RG000362

Köhler, H. (1936). The nucleus in and the growth of hygroscopic droplets. *Transactions of the Faraday Society*, *32*(0), 1152–1161. https://doi.org/10.1039/TF9363201152

Konare, A., Zakey, A. S., Solmon, F., Giorgi, F., Rauscher, S., Ibrah, S., and Bi, X. (2008). A regional climate modeling study of the effect of desert dust on the West African monsoon. *Journal of Geophysical Research Atmospheres*, *113*(12), 1–15. https://doi.org/10.1029/2007JD009322

Lafore, J.-P., Flamant, C., Guichard, F., Parker, D. J., Bouniol, D., Fink, A. H., Giraud, V., Gosset, M., Hall, N., Höller, H., Jones, S. C., Protat, A., Roca, R., Roux, F., Saïd, F., and Thorncroft, C. (2011). Progress in understanding of weather systems in West Africa. *Atmospheric Science Letters*, *12*(1), 7–12.

https://doi.org/10.1002/asl.335

Lamarque, J. F., Hess, P., Emmons, L., Buja, L., Washington, W., and Granier, C. (2005). Tropospheric ozone evolution between 1890 and 1990. *Journal of Geophysical Research D: Atmospheres*, *110*(8), 1–15. https://doi.org/10.1029/2004JD005537

Lana, A., Bell, T. G., Simó, R., Vallina, S. M., Ballabrera-Poy, J., Kettle, A. J., Dachs, J., Dachs, J., Bopp, L., Saltzman, E. S., Stefels, J., Johnson, J. E., and Liss, P. S. (2011). An updated climatology of surface dimethlysulfide concentrations and emission fluxes in the global ocean. *Global Biogeochemical Cycles*, *25*(1), 1–17. https://doi.org/10.1029/2010GB003850

Lau, K. M., Kim, K. M., Sud, Y. C., and Walker, G. K. (2009). A GCM study of the response of the atmospheric water cycle of West Africa and the Atlantic to Saharan dust radiative forcing. *Annales Geophysicae*, *27*(10), 4023–4037. https://doi.org/10.5194/angeo-27-4023-2009

Lau, W. K. M., Kim, K. M., Shi, J. J., Matsui, T., Chin, M., Tan, Q., Peters-Lidard, C., and Tao, W. K. (2017). Impacts of aerosol–monsoon interaction on rainfall and circulation over Northern India and the Himalaya Foothills. *Climate Dynamics*, *49*(5–6), 1945–1960. https://doi.org/10.1007/s00382-016-3430-y

Laurent, B., Marticorena, B., Bergametti, G., Léon, J. F., and Mahowald, N. M. (2008). Modeling mineral dust emissions from the Sahara desert using new surface properties and soil database. *Journal of Geophysical Research Atmospheres*, *113*(14), 1–20. https://doi.org/10.1029/2007JD009484

Lee, S. S. (2012). Effect of aerosol on circulations and precipitation in deep convective clouds. *Journal of the Atmospheric Sciences*, *69*(6), 1957–1974. https://doi.org/10.1175/JAS-D-11-0111.1

Lee, S. S., and Feingold, G. (2013). Aerosol effects on the cloud-field properties of tropical convective clouds. *Atmospheric Chemistry and Physics*, *13*(14), 6713–6726. https://doi.org/10.5194/acp-13-6713-2013

Lemburg, A., Bader, J., and Claussen, M. (2019). Sahel rainfall – Tropical Easterly Jet relationship on synoptic to intraseasonal time scales. *Monthly Weather Review*, 1733–1752. https://doi.org/10.1175/mwr-d-18-0254.1

Li, M., Wang, T., Xie, M., Zhuang, B., Li, S., Han, Y., and Chen, P. (2017). Impacts of aerosol-radiation feedback on local air quality during a severe haze episode in Nanjing megacity, eastern China. *Tellus, Series B: Chemical and Physical Meteorology*, *69*(1), 1–16. https://doi.org/10.1080/16000889.2017.1339548

Liepert, B. G., Feichter, J., Lohmann, U., and Roeckner, E. (2004). Can aerosols spin down the water cycle in a warmer and moister world? *Geophysical Research Letters*, *31*(6), n/a-n/a. https://doi.org/10.1029/2003gl019060

Lin, C. Y., Zhao, C., Liu, X., Lin, N. H., and Chen, W. N. (2014). Modelling of long-range transport of Southeast Asia biomass-burning aerosols to Taiwan and their radiative forcings over East Asia. *Tellus, Series B: Chemical and Physical Meteorology*, *66*(1). https://doi.org/10.3402/tellusb.v66.23733

Liousse, C., Assamoi, E., Criqui, P., Granier, C., and Rosset, R. (2014). Explosive growth in African combustion emissions from 2005 to 2030. *Environmental Research Letters*. https://doi.org/10.1088/1748-9326/9/3/035003

Liu, Y. (2005). Atmospheric response and feedback to radiative forcing from biomass burning in tropical South America. *Agricultural and Forest Meteorology*, *133*(1–4), 40–53. https://doi.org/10.1016/j.agrformet.2005.03.011

Lu, Z., Liu, X., Zhang, Z., Zhao, C., Meyer, K., Rajapakshe, C., Wu, C., Yang, Z., and Penner, J. E. (2018). Biomass smoke from southern Africa can significantly

enhance the brightness of stratocumulus over the southeastern Atlantic Ocean. *Proceedings of the National Academy of Sciences*, *115*(12), 2924–2929. https://doi.org/10.1073/pnas.1713703115

Majewski, D., and Schrodin, R. (1994). *Short Description of the Europa-modell (EM) and Deutschland-modell (DM) of the Deutscher Wetterdienst (DWD) as at October 1994*. Deutschen Wetterdienstes.

Mallet, M., Pont, V., Liousse, C., Gomes, L., Pelon, J., Osborne, S., Haywood, J., Roger, J. C., Dubuisson, P., Mariscal, A., Thouret, V., and Goloub, P. (2008). Aerosol direct radiative forcing over Djougou (northern Benin) during the African Monsoon Multidisciplinary Analysis dry season experiment (Special Observation Period-0). *Journal of Geophysical Research Atmospheres*, *113*(23), 1–16. https://doi.org/10.1029/2007JD009419

Marais, E. A., and Wiedinmyer, C. (2016). Air Quality Impact of Diffuse and Inefficient Combustion Emissions in Africa (DICE-Africa). *Environmental Science and Technology*. https://doi.org/10.1021/acs.est.6b02602

Marenco, A. (1990). Study of tropospheric ozone in china, *24*(2), 2.

Mari, C. H., Cailley, G., Corre, L., Saunois, M., Attié, J. L., Thouret, V., and Stohl, A. (2008). Tracing biomass burning plumes from the Southern Hemisphere during the AMMA 2006 wet season experiment. *Atmospheric Chemistry and Physics*, *8*(14), 3951–3961. https://doi.org/10.5194/acp-8-3951-2008

Mari, C., Jacob, D. J., and Bechtold, P. (2000). Transport and scavenging of soluble gases in a deep convective cloud. *Journal of Geophysical Research Atmospheres*. https://doi.org/10.1029/2000JD900211

Mårtensson, E. M., Nilsson, E. D., de Leeuw, G., Cohen, L. H., and Hansson, H. (2003). Laboratory simulations and parameterization of the primary marine aerosol

production. *Journal of Geophysical Research: Atmospheres*, *108*(D9).

Marticorena, B., Haywood, J., Coe, H., Formenti, P., Liousse, C., Mallet, M., and Pelon, J. (2011). Tropospheric aerosols over West Africa: Highlights from the AMMA international program. *Atmospheric Science Letters*, *12*(1), 19–23. https://doi.org/10.1002/asl.322

Mathon, V., Laurent, H., and Lebel, T. (2002). Mesoscale Convective System Rainfall in the Sahel. *Journal of Applied Meteorology*. https://doi.org/10.1175/1520-0450(2002)041<1081:MCSRIT>2.0.CO;2

Matsuki, A., Quennehen, B., Schwarzenboeck, A., Crumeyrolle, S., Venzac, H., Laj, P., and Gomes, L. (2010). Temporal and vertical variations of aerosol physical and chemical properties over West Africa: AMMA aircraft campaign in summer 2006. *Atmospheric Chemistry and Physics*, *10*(17), 8437–8451. https://doi.org/10.5194/acp-10-8437-2010

Mellor, G. L., and Yamada, T. (1974). A Hierarchy of Turbulence Closure Models or Planetary Boundary Layers. *Journal of the Atmospheric Sciences*, *31*, 1791–1806.

Menut, L., Flamant, C., Turquety, S., Deroubaix, A., Chazette, P., and Meynadier, R. (2018). Impact of biomass burning on pollutant surface concentrations in megacities of the Gulf of Guinea. *Atmospheric Chemistry and Physics*, *18*(4), 2687–2707. https://doi.org/10.5194/acp-18-2687-2018

Miller, R. L., Tegen, I., and Perlwitz, J. (2004). Surface radiative forcing by soil dust aerosols and the hydrologic cycle. *Journal of Geophysical Research D: Atmospheres*, *109*(4), 1–24. https://doi.org/10.1029/2003JD004085

Milton, S. F., Greed, G., Brooks, M. E., Haywood, J., Johnson, B., Allan, R. P., Slingo, A., and Grey, W. M. F. (2008). Modeled and observed atmospheric radiation balance during the West African dry season: Role of mineral dust, biomass burning

aerosol, and surface albedo. *Journal of Geophysical Research Atmospheres*, *113*(23), 1–24. https://doi.org/10.1029/2007JD009741

Mironov, D., Heise, E., Kourzeneva, E., Ritter, B., Schneider, N., and Terzhevik, A. (2010). Implementation of the lake parameterisation scheme FLake into the numerical weather prediction model COSMO. *Boreal Environment Research*, *15*(2), 218–230.

Monahan, E. C., Spiel, D. E., and Davidson, K. L. (1986). A model of marine aerosol generation via whitecaps and wave disruption. In *Oceanic whitecaps* (pp. 167–174). Springer.

Montgomery, D. (2005). Design and Analysis of Experiment. John Wiley and Sons. New York.

Moreira, D. S., Longo, K. M., Freitas, S. R., Yamasoe, M. A., Mercado, L. M., Rosário, N. E., Gloor, E., Viana, R. S. M., Miller, J. B., Gatti, L. V., Wiedemann, K. T., Domingues, L. K. G., and Correia, C. C. S. (2017). Modelling the radiative effects of smoke aerosols on carbon fluxes in Amazon. *Atmospheric Chemistry and Physics Discussions*, (September 2010), 1–48. https://doi.org/10.5194/acp-2016-1147

Myhre, G., Shindell, D. T., Bréon, F. M., Collins, W. D., Fuglestvedt, J., Huang, J., Koch, D., Larmarque, J-F., Lee, D., Mendoza, B., Nakajima, T., Robock, A., Stephens, G., Takemura, T., and Zhang, H. (2013). *Anthropogenic and natural radiative forcing: Positive feedbacks*. *Journal of Marine Science and Engineering* (Vol. 6). https://doi.org/10.3390/jmse6040146

N'Datchoh, E. T., Diallo, I., Konaré, A., Silué, S., Ogunjobi, K. O., Diedhiou, A., and Doumbia, M. (2018). Dust induced changes on the West African summer monsoon features. *International Journal of Climatology*, *38*(1), 452–466.

https://doi.org/10.1002/joc.5187

N'Datchoh, E. T., Konaré, A., Diedhiou, A., Diawara, A., Quansah, E., Assamoi, P., and . (2015). Effects of climate variability on savannah fire regimes in West Africa. *Earth System Dynamics*, *6*(1), 161–174. https://doi.org/10.5194/esd-6-161-2015

NasCube. (2016). N. Retrieved August 30, 2018, from http://nascube.univ-lille1.fr

Nicholson, S. E. (2008). On the factors modulating the intensity of the tropical rainbelt over West Africa. *INTERNATIONAL JOURNAL OF CLIMATOLOGY*, *689*(July 2008), 673–689. https://doi.org/10.1002/joc

Ogunjobi, K., Ajayi, V., Balogun, I., Omotosho, J., and He, Z. (2007). The synoptic and optical characteristics of the harmattan dust spells over Nigeria. *Theoretical and Applied Climatology*, *93*(1–2), 91–105. https://doi.org/10.1007/s00704-007-0332-2

Ogunjobi, K. O., He, Z., and Simmer, C. (2008). Spectral aerosol optical properties from AERONET Sun-photometric measurements over West Africa, *88*, 89–107. https://doi.org/10.1016/j.atmosres.2007.10.004

Ogunjobi, K. O., Oluleye, A., and Ajayi, V. O. (2012). A long-term record of aerosol index from TOMS observations and horizontal visibility in sub-Saharan West Africa. *International Journal of Remote Sensing*, *33*(19), 6076–6093. https://doi.org/10.1080/01431161.2012.676689

Olaniyan, E., Afiesimama, E., Oni, F., and Lawal, K. A. (2015). Simulating the Daily Evolution of West African Monsoon Using High Resolution Regional Cosmo-model: A Case Study of the First Half of 2015 over Nigeria. *Journal of Climatology & Weather Forecasting*, *03*(03). https://doi.org/10.4172/2332-2594.1000142

Pani, S. K., Wang, S. H., Lin, N. H., Lee, C. Te, Tsay, S. C., Holben, B. N., Janjai, S., Hsiao, T. C., Chuang, M. T., and Chantara, S. (2016). Radiative effect of

springtime biomass-burning aerosols over northern indochina during 7-SEAS/BASELInE 2013 campaign. *Aerosol and Air Quality Research*, *16*(11), 2802–2817. https://doi.org/10.4209/aaqr.2016.03.0130

Parker, D. J., Burton, R. R., Diongue-Niang, A., Ellis, R. J., Felton, M., Taylor, C. M., Thorncroft, C. D., Bessemoulin, P., and Tompkins, A. M. (2005). The diurnal cycle of the West African monsoon circulation. *Quarterly Journal of the Royal Meteorological Society*, *131*(611), 2839–2860. https://doi.org/10.1256/qj.04.52

Peng, J., Hu, M., Guo, S., Du, Z., Zheng, J., Shang, D., Levy Z., M., Zeng, L., Shao, M., Wu, Y- Z., Wang, Y., Glen, C. R., Collins, D. R., Molina, M. J., and Zhang, R. (2016). Markedly enhanced absorption and direct radiative forcing of black carbon under polluted urban environments. *Proceedings of the National Academy of Sciences*, *113*(16), 4266–4271. https://doi.org/10.1073/pnas.1602310113

Penner, J. E., Andreae, M., Annegarn, H., Barrie, L., Feichter, J., Hegg, D., Jayaraman, A., Leaitch, R., Murphy, D., Nganga, J., Pitari, G., and Zhang, Y. (2011). Aerosols, their Direct and Indirect Effects. *Climate Change 2001: The Physical Science Basis. Contribution of Working Group 1 to the Third Assesment Report of the Intergovernmental Panel on Climate Change*, 291–336.

Penner, J. E., Dickinson, R. E., and O'Neill, C. A. (1992). Effects of aerosol from biomass burning on the global radiation budget. *Science*, *256*(5062), 1432–1434. https://doi.org/10.1126/science.256.5062.1432

Pereira, E. B., Martins, F. R., Abreu, S. L., Couto, P., Stuhlmann, R., and Colle, S. (1999). Effects of burning of biomass on satellite estimations of solar irradiation in Brazil. *Solar Energy*, *68*(1), 91–107. https://doi.org/10.1016/S0038-092X(99)00044-4

Platnick, S., Meyer, K. G., King, M. D., Wind, G., Amarasinghe, N., Marchant, B.,

Arnold, G. T., Zhang, Z., Hubanks, P. A., Holz, R. E., Yang, P., Ridgway, W. L., and Riedi, J. (2017). The MODIS Cloud Optical and Microphysical Products: Collection 6 Updates and Examples from Terra and Aqua. *IEEE Transactions on Geoscience and Remote Sensing*, *55*(1), 502–525. https://doi.org/10.1109/TGRS.2016.2610522

Quaas, J., Boucher, O., Dufresne, J. L., and Le Treut, H. (2004). Impacts of greenhouse gases and aerosol direct and indirect effects on clouds and radiation in atmospheric GCM simulations of the 1930-1989 period. *Climate Dynamics*, *23*(7–8), 779–789. https://doi.org/10.1007/s00382-004-0475-0

Raji, K. B., Ogunjobi, K. O., and Akinsanola, A. A. (2017). Radiative effects of dust aerosol on West African climate using simulations from RegCM4. *Modeling Earth Systems and Environment*, *3*(1), 34. https://doi.org/10.1007/s40808-017-0295-y

Ramaswamy, V. (1998). Aerosol Radiative forcing and model responses.

Real, E., Orlandi, E., Law, K. S., Fierli, F., Josset, D., Cairo, F., Schlager, H., Borrmann, S., Kunkel, D., Volk, C. M., McQuaid, J. B., Stewart, D. J., Lee, J., Lewis, A. C., Hopkins, J. R., Ravegnani, F., Ulanovski, A., and Liousse, C. (2010). Cross-hemispheric transport of central African biomass burning pollutants: Implications for downwind ozone production. *Atmospheric Chemistry and Physics*, *10*(6), 3027–3046. https://doi.org/10.5194/acp-10-3027-2010

Reddington, C. L., Butt, E. W., Ridley, D. A., Artaxo, P., Morgan, W. T., Coe, H., and Spracklen, D. V. (2015). Air quality and human health improvements from reductions in deforestation-related fire in Brazil. *Nature Geoscience*, *8*(10), 768–771. https://doi.org/10.1038/ngeo2535

Redelsperger, J. L., Thorncroft, C. D., Diedhiou, A., Lebel, T., Parker, D. J., and Polcher, J. (2006). African Monsoon Multidisciplinary Analysis: An international

research project and field campaign. *Bulletin of the American Meteorological Society*, *87*(12), 1739–1746. https://doi.org/10.1175/BAMS-87-12-1739

Reeves, C. E., Formenti, P., Afif, C., Ancellet, G., Attié, J. L., Bechara, J., Borbon, A. , Cairo, F., Crumeyrolle, S., Flamant, C., Hamburger, T., Methven, J., Murphy, J. G., Richter, A., Schwarzenboeck, A., and Thouret, V. (2010). Chemical and aerosol characterisation of the troposphere over West Africa during the monsoon period as part of AMMA. *Atmospheric Chemistry and Physics*, *10*(16), 7575–7601. https://doi.org/10.5194/acp-10-7575-2010

Reynolds, R. W., Smith, T. M., Liu, C., Chelton, D. B., Casey, K. S., and Schlax, M. G. (2007). Daily high-resolution-blended analyses for sea surface temperature. *Journal of Climate*, *20*(22), 5473–5496. https://doi.org/10.1175/2007JCLI1824.1

Riahi, K., Grübler, A., and Nakicenovic, N. (2007). Scenarios of long-term socio-economic and environmental development under climate stabilization. *Technological Forecasting and Social Change*, *74*(7), 887–935. https://doi.org/10.1016/j.techfore.2006.05.026

Rieger, D., Bangert, M., Kottmeier, C., Vogel, H., and Vogel, B. (2014). Impact of aerosol on post-frontal convective clouds over Germany. *Tellus B: Chemical and Physical Meteorology*, *66*(1), 22528. https://doi.org/10.3402/tellusb.v66.22528

Rieger, D., Steiner, A., Bachmann, V., Gasch, P., Förstner, J., Deetz, K., Vogel, B. and Vogel, H. (2017). Impact of the 4 April 2014 Saharan dust outbreak on the photovoltaic power generation in Germany. *Atmospheric Chemistry and Physics*. https://doi.org/10.5194/acp-17-13391-2017

Rinke, R. (2008). Parametrisierung des Auswaschens von Aerosolpartikeln durch Niederschlag. KIT-Bibliothek.

Ritter, B., and Geleyn, J.-F. (1992). A Comprehensive Radiation Scheme for Numerical

Weather Prediction Models with Potential Appilcations in Climate Simulations. *Monthly Weather Review*, *120*, 303–325.

Roeckner, E., Stier, P., Feichter, J., Kloster, S., Esch, M., and Fischer-Bruns, I. (2006). Impact of carbonaceous aerosol emissions on regional climate change. *Climate Dynamics*, *27*(6), 553–571. https://doi.org/10.1007/s00382-006-0147-3

Rosenfeld, D., Rudich, Y., and Lahav, R. (2002). Desert dust suppressing precipitation: A possible desertification feedback loop. *Proceedings of the National Academy of Sciences*, *98*(11), 5975–5980. https://doi.org/10.1073/pnas.101122798

Rosenfeld, D., Zhu, Y., Wang, M., Zheng, Y., Goren, T., and Yu, S. (2019). Aerosol-driven droplet concentrations dominate coverage and water of oceanic low-level clouds. *Science*, *363*(6427), eaav0566. https://doi.org/10.1126/science.aav0566

Salah, Z., Shalaby, A., Steiner, A. L., Zakey, A. S., Gautam, R., and Abdel Wahab, M. M. (2018). Study of aerosol direct and indirect effects and auto-conversion processes over the west african monsoon region using a regional climate model. *Advances in Atmospheric Sciences*, *35*(2), 182–194. https://doi.org/10.1007/s00376-017-7077-3

Salzmann, M., Weser, H., and Cherian, R. (2014). Robust response of Asian summer monsoon to anthropogenic aerosols in CMIP5 models. *Journal of Geophysical Research*, *119*(19), 11,321-11,337. https://doi.org/10.1002/2014JD021783

Sauvage, B., Thouret, V., Cammas, J.-P., Gheusi, F., Athier, G., and Nédélec, P. (2005). Tropospheric ozone over Equatorial Africa: regional aspects from the MOZAIC data. *Atmospheric Chemistry and Physics Discussions*, *4*(3), 3285–3332. https://doi.org/10.5194/acpd-4-3285-2004

Schafer, J. S., Eck, T. F., Holben, B. N., Artaxo, P., Yamasoe, M. A., and Procopio, A. S. (2002). Observed reductions of total solar irradiance by biomass-burning

aerosols in the Brazilian Amazon and Zambian Savanna. *Geophysical Research Letters*, *29*(17), 4-1-4–4. https://doi.org/10.1029/2001gl014309

Schrage, J. M., and Fink, A. H. (2012). Nocturnal Continental Low-Level Stratus over Tropical West Africa: Observations and Possible Mechanisms Controlling Its Onset. *Monthly Weather Review*. https://doi.org/10.1175/MWR-D-11-00172.1

Schulz, M., Textor, C., Kinne, S., Balkanski, Y., Bauer, S., Berntsen, T., Berglen, T., Boucher, O., Iversen, T., Montanaro, V., Myhre, G., Reddy, S., Stier, P., and Takemura, T. (2006). Radiative forcing by aerosols as derived from the AeroCom present-day and pre-industrial simulations. *Atmospheric Chemistry and Physics*, *6*(12), 5225–5246. https://doi.org/10.5194/acp-6-5225-2006

Schuster, R., Fink, A. H., and Knippertz, P. (2013). Formation and Maintenance of Nocturnal Low-Level Stratus over the Southern West African Monsoon Region during AMMA 2006. *Journal of the Atmospheric Sciences*. https://doi.org/10.1175/JAS-D-12-0241.1

Segal, Y., and Khain, A. (2006). Dependence of droplet concentration on aerosol conditions in different cloud types: Application to droplet concentration parameterization of aerosol conditions. *Journal of Geophysical Research Atmospheres*, *111*(15), 1–11. https://doi.org/10.1029/2005JD006561

Seifert, A., and Beheng, K. D. (2001). A double-moment parameterization for simulating autoconversion, accretion and selfcollection. *Atmospheric Research*, *59–60*, 265–281. https://doi.org/10.1016/S0169-8095(01)00126-0

Seifert, A., and Beheng, K. D. (2006). A two-moment cloud microphysics parameterization for mixed-phase clouds. Part 1: Model description. *Meteorology and Atmospheric Physics*. https://doi.org/10.1007/s00703-005-0112-4

Seiler, Wolfgang. and Crutzen, P. J. (1980). Estimates of Gross and Net Fluxes of

Carbon Between. *Climatic Change*, *2*, 207–247.

Seinfeld, J. H., Bretherton, C., Carslaw, K. S., Coe, H., and Demott, P. J. (2016). Improving our fundamental understanding of the role of aerosol − cloud interactions in the climate system. *Proceedings of the National Academy of Sciences*, *113*(21), 5781–5790. https://doi.org/10.1073/pnas.1514043113

Seinfeld, J. H., and Pandis, S. N. (2008). *(A Wiley-Interscience publication) Seinfeld, John H._ Pandis, Spyros N-Atmospheric chemistry and physics _from air pollution to climate change-Wiley (1998)* (Third).

Seinfeld, J. H., Pandis, S. N., and Noone, K. (1998). Atmospheric chemistry and physics: from air pollution to climate change. *Physics Today*, *51*, 88.

Shao, Y. (2004). Simplification of a dust emission scheme and comparison with data. *Journal of Geophysical Research D: Atmospheres*, *109*(10), 1–6. https://doi.org/10.1029/2003JD004372

Shao, Y., Wyrwoll, K. H., Chappell, A., Huang, J., Lin, Z., McTainsh, G. H., Mikami, M., Tanaka, T. Y., Wang, X., and Yoon, S. (2011). Dust cycle: An emerging core theme in Earth system science. *Aeolian Research*, *2*(4), 181–204. https://doi.org/10.1016/j.aeolia.2011.02.001

Smith, M. H., Park, P. M., and Consterdine, I. E. (1993). Marine aerosol concentrations and estimated fluxes over the sea. *Quarterly Journal of the Royal Meteorological Society*, *119*(512), 809–824. https://doi.org/10.1002/qj.49711951211

Smoydzin, L., Teller, A., Tost, H., Fnais, M., and Lelieveld, J. (2012). Impact of mineral dust on cloud formation in a Saharan outflow region. *Atmospheric Chemistry and Physics*, *12*(23), 11383–11393. https://doi.org/10.5194/acp-12-11383-2012

SODEXAM. (2017). Société d'Exploitation et de Developpement Aeroportuaire, Aeronautique et Meteorologique, *special report*.

Sokolik, I. N., and Toon, O. B. (1999). Incorporation of mineralogical composition into models of the radiative properties of mineral aerosol from UV to IR wavelengths. *Journal of Geophysical Research Atmospheres*, *104*(D8), 9423–9444. https://doi.org/10.1029/1998JD200048

Solmon, F., Mallet, M., Elguindi, N., Giorgi, F., Zakey, A., and Konaré, A. (2008). Dust aerosol impact on regional precipitation over western Africa, mechanisms and sensitivity to absorption properties. *Geophysical Research Letters*, *35*(24). https://doi.org/10.1029/2008GL035900

Solomos, S., Kallos, G., Kushta, J., Astitha, M., Tremback, C., Nenes, A., and Levin, Z. (2011). An integrated modeling study on the effects of mineral dust and sea salt particles on clouds and precipitation. *Atmospheric Chemistry and Physics*, *11*(2), 873–892. https://doi.org/10.5194/acp-11-873-2011

Stanelle, T., Vogel, B., Vogel, H., Bäumer, D., and Kottmeier, C. (2010). Feedback between dust particles and atmospheric processes over West Africa during dust episodes in March 2006 and June 2007. *Atmospheric Chemistry and Physics*, *10*(22), 10771–10788. https://doi.org/10.5194/acp-10-10771-2010

Stevens, B., and Feingold, G. (2009). Untangling aerosol effects on clouds and precipitation in a buffered system. *Nature*, *461*(7264), 607–613. https://doi.org/10.1038/nature08281

Stockwell, W. R., Middleton, P., Chang, J. S., and Xiaoyan Tang. (1990). The second generation regional acid deposition model chemical mechanism for regional air quality modeling. *Journal of Geophysical Research*, *95*(D10).

Sultan, B., and Janicot, S. (2003). The West African monsoon dynamics. Part II: The "preonset" and "onset" of the summer monsoon. *Journal of Climate*. https://doi.org/10.1175/1520-0442(2003)016<3407:TWAMDP>2.0.CO;2

Swap, R. J., Annegarn, H. J., Suttles, J. T., Haywood, J., Helmlinger, M. C., Hely, C., Hobbs, P. V., Holben, B. N., Maenhaut, W., Piketh, S. J., Platnick, S., Thompson, A. M., Ward, D., and Yokelson, R. (2002). The Southern African Regional Science Initiative (SAFARI 2000): Overview of the dry season field campaign. *South African Journal of Science*, *98*(3–4), 125–130.

Tanaka, T. Y., and Chiba, M. (2006). A numerical study of the contributions of dust source regions to the global dust budget. *Global and Planetary Change*, *52*(1–4), 88–104. https://doi.org/10.1016/j.gloplacha.2006.02.002

Tao, W. K., Chen, J. P., Li, Z., Wang, C., and Zhang, C. (2012). Impact of aerosols on convective clouds and precipitation. *Reviews of Geophysics*, *50*(2). https://doi.org/10.1029/2011RG000369

Taylor, J. W., Haslett, S. L., Bower, K., Flynn, M., Crawford, I., Dorsey, J., Choularton, T., Connolly, P. J., Hahn, V., Voigt, C., Lee, J. D., Vaughan, A. R., Hill, P. G., Brooks, B., Catoire, V., Knippertz, P., and Coe, H. (2019). Aerosol influences on low-level clouds in the West African monsoon. *Atmospheric Chemistry and Physics Discussions*, (Llc), 1–45. https://doi.org/10.5194/acp-2019-40

Tegen, I., Hollrig, P., Chin, M., Fung, I., Jacob, D., and Penner, J. (1997). Contribution of different aerosol species to the global aerosol extinction optical thickness: Estimates from model results. *Journal of Geophysical Research Atmospheres*, *102*(20), 23895–23915.

Teller, A., and Levin, Z. (2006). The effects of aerosols on precipitation and dimensions of subtropical clouds; a sensitivity study using a numerical cloud model. *Atmospheric Chemistry and Physics Discussions*, *5*(4), 7211–7245. https://doi.org/10.5194/acpd-5-7211-2005

Thorncroft, C. D., and Blackburn, M. (1999). Quarterly journal. *Royal Meteorological*

Society, *125*.

Thorncroft, C. D., and Hoskins, B. J. (1994). An idealized study of African easterly waves. I: A linear view. *Quarterly Journal of the Royal Meteorological Society*, *120*(518), 953–982. https://doi.org/10.1002/qj.49712051809

Thornhill, G. D., Ryder, C. L., Highwood, E. J., Shaffrey, L. C., and Johnson, B. T. (2018). The effect of South American biomass burning aerosol emissions on the regional climate. *Atmospheric Chemistry and Physics*, *18*(8), 5321–5342. https://doi.org/10.5194/acp-18-5321-2018

Tiedtke, M. (1989). A Comprehensible Mass FLux Schem for Cumulus Parametrization in Large-Scale Models. *America Meteorogical Society*, *117*, 1779–1799.

Toll, V., Christensen, M., Quaas, J., and Bellouin, N. (2019). Weak average liquid-cloud-water response to anthropogenic aerosols. *Nature*, *572*(7767), 51–55. https://doi.org/10.1038/s41586-019-1423-9

Tulet, P., Mallet, M., Pont, V., Pelon, J., and Boone, A. (2008). The 7-13 March 2006 dust storm over West Africa: Generation, transport, and vertical stratification. *Journal of Geophysical Research Atmospheres*, *113*(23), 1–13. https://doi.org/10.1029/2008JD009871

Twomey, S. (1977). The Influence Of Pollution on the Shortwave Albedo of CLouds. https://doi.org/10.1175/1520-0469(1977)034<1149:TIOPOT>2.0.CO;2

UNEP. (2017). *Fuel Sulphur Levels: Global Status*. Retrieved from https://wedocs.unep.org/bitstream/handle/20.500.11822/17543/MapWorldSulphur_March2017.pdf?

Unger, N., Menon, S., Shindell, D. T., and Koch, D. M. (2010). Impacts of aerosol indirect effect on past and future changes in tropospheric composition. *Atmospheric Chemistry and Physics Discussions*, *9*(1), 4691–4725.

https://doi.org/10.5194/acpd-9-4691-2009

UNO. (2018). The World's Cities in 2018. https://doi.org/10.18356/c93f4dc6-en

van der Linden, R., Fink, A. H., and Redl, R. (2015a). Satellite-based climatology of low-level continental clouds in southern West Africa during the summer monsoon season. *Journal of Geophysical Research*. https://doi.org/10.1002/2014JD022614

Van Der Werf, G. R., Randerson, J. T., Giglio, L., Collatz, G. J., Mu, M., Kasibhatla, P. S., Morton, D. C., Defries, R. S., Jin, Y., and Van Leeuwen, T. T. (2010). Global fire emissions and the contribution of deforestation, savanna, forest, agricultural, and peat fires (1997-2009). *Atmospheric Chemistry and Physics*, *10*(23), 11707–11735. https://doi.org/10.5194/acp-10-11707-2010

van Vuuren, D. P., den Elzen, M. G. J., Lucas, P. L., Eickhout, B., Strengers, B. J., van Ruijven, B., Wonink, S., and van Houdt, R. (2007). Stabilizing greenhouse gas concentrations at low levels: an assessment of reduction strategies and costs. *Climatic Change*, *81*(2), 119–159. https://doi.org/10.1007/s10584-006-9172-9

Vogel, B., Hoose, C., Vogel, H., and Kottmeier, C. (2006). A model of dust transport applied to the Dead Sea Area. *Meteorologische Zeitschrift*, *15*(6), 611–624. https://doi.org/10.1127/0941-2948/2006/0168

Vogel, B., Vogel, H., Bäumer, D., Bangert, M., Lundgren, K., Rinke, R., and Stanelle, T. (2009). The comprehensive model system COSMO-ART – Radiative impact of aerosol on the state of the atmosphere on the regional scale. *Atmospheric Chemistry and Physics*, *9*(22), 8661–8680. https://doi.org/10.5194/acp-9-8661-2009

Walter, C., Freitas, S. R., Kottmeier, C., Kraut, I., Rieger, D., Vogel, H., and Vogel, B. (2016). The importance of plume rise on the concentrations and atmospheric impacts of biomass burning aerosol. *Atmospheric Chemistry and Physics*, *16*(14), 9201–9219. https://doi.org/10.5194/acp-16-9201-2016

Wang, J., Wang, S., Jiang, J., Ding, A., Zheng, M., Zhao, B., Wong, D. C., Zhou, W., Zheng, G., Wang, L., Pleim, J. E., and Hao, J. (2014). Impact of aerosol-meteorology interactions on fine particle pollution during China's severe haze episode in January 2013. *Environmental Research Letters*, *9*(9). https://doi.org/10.1088/1748-9326/9/9/094002

Wang, Y., Jiang, J. H., and Su, H. (2015). Atmospheric responses to the redistribution of anthropogenic aerosols. *Journal of Geophysical Research*, *120*(18), 9625–9641. https://doi.org/10.1002/2015JD023665

Whitby, E. R., and McMurry, P. H. (1997). Modal aerosol dynamics modeling. *Aerosol Science and Technology*, *27*(6), 673–688. https://doi.org/10.1080/02786829708965504

Whitby, K. T. (1978). The physical characteristics of sulfur aerosols. In *Sulfur in the Atmosphere* (pp. 135–159). Elsevier.

Wicker, L. J., and Skamarock, W. C. (2002). Time-splitting methods for elastic models using forward time schemes. *Monthly Weather Review*, *130*(8), 2088–2097. https://doi.org/10.1175/1520-0493(2002)130<2088:TSMFEM>2.0.CO;2

Wu, M. L. C., Reale, O., Schubert, S. D., Suarez, M. J., Koster, R. D., and Pegion, P. J. (2009). African easterly jet: Structure and maintenance. *Journal of Climate*. https://doi.org/10.1175/2009JCLI2584.1

Xue, H., and Feingold, G. (2006). Large-eddy simulations of trade wind cumuli: Investigation of aerosol indirect effects. *Journal of the Atmospheric Sciences*, *63*(6), 1605–1622.

Yoshioka, M., Mahowald, N. M., Conley, A. J., Collins, W. D., Fillmore, D. W., Zender, C. S., and Coleman, D. B. (2007). Impact of desert dust radiative forcing on sahel precipitation: Relative importance of dust compared to sea surface temperature

variations, vegetation changes, and greenhouse gas warming. *Journal of Climate*, *20*(8), 1445–1467. https://doi.org/10.1175/JCLI4056.1

Zängl, G., Reinert, D., Rípodas, P., and Baldauf, M. (2015). The ICON (ICOsahedral Non-hydrostatic) modelling framework of DWD and MPI-M: Description of the non-hydrostatic dynamical core. *Quarterly Journal of the Royal Meteorological Society*, *141*(687), 563–579. https://doi.org/10.1002/qj.2378

Zhang, Q., Jimenez, J. L., Canagaratna, M. R., Allan, J. D., Coe, H., Ulbrich, I., Alfarra, M. R., Takami, A., Dzepina, K., Docherty, K., DeCarlo, P. F., Bahreini, R., Cottrell, L., Griffin, R. J., Rautiainen, J., Sun, J. Y., Zhang, Y. M., and Worsnop, D. R. (2007). Ubiquity and dominance of oxygenated species in organic aerosols in anthropogenically-influenced Northern Hemisphere midlatitudes. *Geophysical Research Letters*, *34*(13), 1–6. https://doi.org/10.1029/2007GL029979

Zhang, S., Wang, M., Ghan, S. J., Ding, A., Wang, H., Zhang, K., Neubauer, D., Lohmann, U., Ferrachat, S., Takeamura, T., Gettelman, A., Morrison, H., Lee, Y. H., Shindell, D. T., Partridge, D. G., Stier, P., Kipling, Z., and Fu, C. (2015). On the characteristics of aerosol indirect effect based on dynamic regimes in global climate models. *Atmospheric Chemistry and Physics Discussions*, *15*(17), 23683–23729. https://doi.org/10.5194/acpd-15-23683-2015

Zhang, X., and Kondragunta, S. (2008). Temporal and spatial variability in biomass burned areas across the USA derived from the GOES fire product. *Remote Sensing of Environment*, *112*(6), 2886–2897. https://doi.org/10.1016/j.rse.2008.02.006

Zhang, Y., Fu, R., Yu, H., Qian, Y., Dickinson, R., Silva Dias, M. A. F., da Silva Dias, P. L. and Fernandes, K. (2009). Impact of biomass burning aerosol on the monsoon circulation transition over Amazonia. *Geophysical Research Letters*, *36*(10), 1–6. https://doi.org/10.1029/2009gl037180

Zhao, C., Liu, X., Leung, L. R., and Hagos, S. (2011). Radiative impact of mineral dust on monsoon precipitation variability over West Africa. *Atmospheric Chemistry and Physics*, *11*(5), 1879–1893. https://doi.org/10.5194/acp-11-1879-2011

Zhao, S., Zhang, H., Feng, S., and Fu, Q. (2015). Simulating direct effects of dust aerosol on arid and semi-arid regions using an aerosol-climate coupled system. *International Journal of Climatology*, *35*(8), 1858–1866. https://doi.org/10.1002/joc.4093

Zuidema, P., Redemann, J., Haywood, J., Wood, R., Piketh, S., Hipondoka, M., and Formenti, P. (2016). Smoke and clouds above the southeast Atlantic: Upcoming field campaigns probe absorbing aerosol's impact on climate. *Bulletin of the American Meteorological Society*, *97*(7), 1131–1135. https://doi.org/10.1175/BAMS-D-15-00082.1